Mode identification of oscillations of Delta Scuti stars using multicolor photometry and high resolution spectroscopy

A thesis submitted to the Faculty of Science
University of Colombo
for the Degree of Doctor of Philosophy
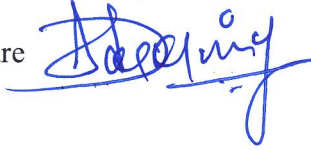
Janaka Adassuriya

March 2021

Declaration

This thesis is my original work and has not been submitted previously for a degree at this or any other university / institute. To the best of my knowledge it does not contain any material published or written by another person, except as acknowledged in the text.

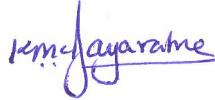Author's name: Janaka Adassuriya

Signature _____   Date 08/03/2021

This is to certify that this dissertation is based on the work carried out by Mr. Janaka Adassuriya under our supervision. The dissertation has been prepared according to the format stipulated and is of acceptable standard.

Certified by:

Supervisor 1   Prof. K. P. S. C. Jayaratne
                   Astronomy and Space Science Unit
                   Department of Physics
                   University of Colombo
                   Colombo 03
                   Sri Lanka

Signature _____   Date 2021/03/08

Supervisor 2   Dr. Shashikiran Ganesh
                   Astronomy & Astrophysics Division
                   Physical Research Laboratory
                   Navarangpura
                   Ahmedabad 380009
                   India

Signature _____   Date 08/03/2021

Acknowledgements

Abstract

Delta Scuti stars are pulsating stars. They are transitional objects where asteroseismology could help to study the physics of the stellar interior. The pulsation drives by an opacity mechanism with periodicities, typically of a few hours. The central or shell hydrogen burning stage Delta Scuti stars are placed where the classical instability strip crosses the main sequence of the Hertzsprung-Russell diagram. Both radial and non-radial pulsations occur in Delta Scuti stars. With the increase of ground-based, and most importantly, the advent of space-based photometry, this particular class of stars became better studied with their complex frequency spectra. The high-quality continuous space-based light curves mainly reveal the pulsation frequencies of both pressure modes (p-mode) and gravity modes (g-mode). These modes should be identified through mode identification.

The analysis of high temporal resolution ground and space-based photometric observations of SZ Lyncis, a binary star one of whose components is high amplitude Delta Scuti, is presented. UBVR photometric observations were obtained from Mt. Abu Infrared Observatory (24.65° N, 72.78° E) in India and Fairborn Observatory (31.68° N, 110.88° W) in Arizona. In addition, the archival observations from the Wide Angle Search for Planets (WASP) project were used. Furthermore, the continuous, high-quality light curve from the TESS project was extensively used for the analysis. The well-resolved light curve from Transiting Exoplanet Survey Satellite (TESS) reveals the presence of 23 frequencies with four independent modes, 13 harmonics of the primary pulsation frequency of 8.296943 ± 0.000002 d^{-1}, and their combinations. The frequency 8.296 d^{-1} is identified as the fundamental radial mode primarily by the amplitude ratio method. The estimated pulsation constant using the frequency 8.296 d^{-1} also claims the existence of this fundamental mode. The frequencies 14.535 d^{-1}, 32.620 d^{-1}, and 4.584 d^{-1} are newly discovered for SZ Lyn. Out of these three, 14.535 $d^{-1}$and 32.620 d^{-1} are identified as non-radial low order p-modes, and 4.584 d^{-1} could indicate presence of a g-mode in SZ Lyn. The ultimate purpose of frequency determination and mode identification is to derive accurate physical parameters of SZ Lyn. The optimization of the generated stellar pulsation models with the observed frequencies produced a set of physical parameters to represent SZ Lyn. The theoretical models correspond to 7500 K $\leq T_{eff} \leq$ 7800 K and

log (g) = 3.81 ± 0.06. The mass of SZ Lyn estimated using evolutionary sequences is close to 1.7–2.0 $M_\odot$. The period-density relation calculates a mean density (ρ) of 0.1054 ± 0.0016 g cm^{-3}.

Five more Delta Scuti stars observed by the Kepler mission were also analyzed for frequencies and thereby identified the oscillation modes. KIC 4077032 and KIC 8623953 have contrasting frequency spectra and thus emphasize the diversity of the Delta Scuti group. Though the fundamental radial mode is the highest amplitude dominant mode, KIC 4077032 shows a secondary amplitude mode as its fundamental mode. On the other hand, KIC 8623953 has the highest amplitude for the fundamental mode, and this mode does not agree with the well-established range of the pulsation constant (Q) of the fundamental mode of Delta Scuti stars. The splitting of frequencies due to rotation was identified in both KIC 9700322 and KIC 11754974. This rotational splitting confirmed the availability of $l = 2$ quintuplet mode in KIC 9700322 and KIC 11754974. Furthermore, the rotational periods were determined to be 6.19 days and 3.83 days for KIC 9700322 and KIC 11754974, respectively. On the contrary, KIC 9845907 is a purely radial pulsator where all frequencies fit into $l = 0$ modes. In common, large numbers of harmonics and linear combinations of these independent frequencies are also present in all five Kepler targets.

The spectroscopic observation of SZ Lyn was carried out at the Mount Abu Observatory from October to December 2016. Although the low-resolution spectroscopy of SZ Lyn is insufficient to resolve the low amplitude frequencies, the fundamental radial mode is prominently recovered from the spectroscopic data.

Contents

List of Tables

List of Figures

Abbreviations and Notations

AAVSO   American Association of Variable Star Observers

APT   Automatic Photoelectric Telescope

BJD   Barycentric Julian Date

CCD   Charge Couple Device

DEC   Declination

DFT   Discrete Fourier Transformation

EW   Equivalent Width

FOV   Field of View

FWHM   Full Width at Half Maxima

GAIA   Astrometric observatory

HADS   High Amplitude Delta Scuti Stars

HELAS   European Helio and Asteroseismology Network

HJD   Heliocentric Julian Date

HR Diagram   Hertzsprung–Russell diagram

IRAF   Image Reduction and Analysis Facility

JD   Julian Date

KIC   Kepler Input Catalogue

LAMOST   Large Sky Area Multi-Object Fiber Spectroscopic Telescope

LDC   Limb Darkening Coefficient

LS   Lomb–Scargle

MAST   Mikulski Archive for Space Telescopes

RA   Right Ascension

TESS   Transiting Exoplanet Survey Satellite

WASP   Wide Angle Search for Planets

TDC   Time dependent convection

STScI	Space Telescope Science Institute
MESA	Modules for Experiments in Stellar Astrophysics
LC	Long Cadence
SC	Short Cadence
ppm	Parts Per Million
$\odot$	Sun
Z	Chemical Composition
α_{MTL}	Mixing Length Parameter
Fe/H	Chemical Abundance
pc	Parsecs
f_{ov}	Overshooting Parameter
mas	milliarcseconds

Chapter 1

Introduction

1.1 Stellar pulsation

Formation of a star is achieved by the hydrostatic equilibrium condition where the force of gravity attracts the matter towards the center and radiation pressure against it. Nevertheless, purely convective stars do exists. The hydrostatic equilibrium condition causes a stable luminosity and temperature over a long time period. Any departure from this equilibrium will immediately lead to a strong reaction for restoring the equilibrium state. However, in the latter part of the stars when central hydrogen burns out, this equilibrium condition is disturbed and begins to behave abnormally. As a result, the pulsation occurs in the stars. The recent evidence suggests that all stars are pulsating to some extent during their stellar evolution. It is known that there is no prominent variability in brightness in the case of the closest star, the Sun. However, it exhibits oscillations to some extent. The solar oscillation is caused by trapping acoustic waves below the photosphere (Ulrich, 1970). This oscillation does not penetrate the deeper solar sphere and has an oscillation period of 5 minutes of the very high frequency of 3333 μHz. This high frequency may not be clearly seen in an amplitude spectrum due to a low signal-to-noise ratio that falls below the detecting threshold. The first pulsating star, o Ceti, was discovered in 1596 by David Fabricius (Gaspani, 1998). o Ceti was later called 'Mira' ('wonderful') to describe its unusual behavior. In 1784, the most crucial discovery of stellar pulsation, the observation of periodic light variations in the yellow supergiant, δ Cephei, was discovered. δ Cephei has a pulsation period of 5 days, 8 hours, and 37 minutes and exhibits magnitude variations of ±1 magnitude. Since then, there has been an increase in the number of known pulsating stars with a corresponding increase in our understanding of stellar pulsation (Kurtz et al., 2015, Bowman and Kurtz, 2018, Niemczura et al., 2015). A classification of pulsation stars is given in Table 1.1. The main types of pulsating stars and their respective locations in the Hertzsprung-Russell (H-R) diagram are shown in Figure 1.1.

Table. 1.1 Selected classes of pulsating stars

Type	Period	Radial or Non-radial
Mira variables	100 - 1000 d	Radial
δ Cephei stars	1 - 100 d	Radial
RR Lyrae stars	0.3 - 3 d	Radial
δ Scuti stars	0.3 - 6 h	Radial and Non-radial
β Cephei stars	2 - 7 h	Radial and Non-radial
Rapidly oscillating Ap (roAp) stars	5 - 25 min	Radial and Non-radial
Slowly Pulsating B (SPB) stars	0.5 - 3 d	Radial and Non-radial
Solar-like oscillators	3 - 15 min	Radial and Non-radial
γ Doradus stars	0.3 - 1.5 d	Radial and Non-radial

In general, pulsating stars are not found on the main sequence of the HR diagram, where most of the stars spend their lifetime. The pulsating stars mainly lie on the instability strip (see Figure 1.1), where stars are shifting from the main sequence at the later stage of their lifetime. Pulsation is a transient phenomenon where the stars show higher brightness variations apart from their insignificant oscillations in the other evolutionary stages.

This variability was thought to be caused by star spots, tidal effects of binaries or to modulation by eclipsing binaries until 1914, when Harlow Shapley suggested that this variability may be due to the internal physical process of the star.
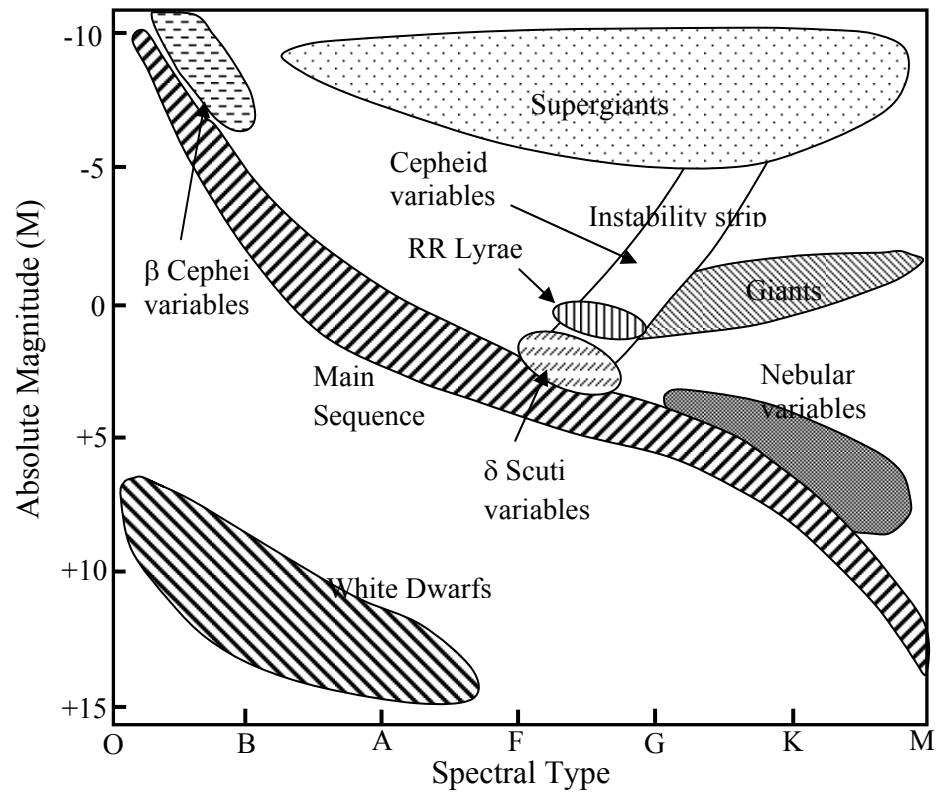
Figure 1.1 Main types of pulsating stars in Hertzsprung-Russell (H-R) diagram.

1.1.1 Thermodynamics of the pulsations

There is an analogy between the thermodynamics of a heat engine and of a star. For a mass of stellar gas, the first law of thermodynamics in equation 1.1 states that the heat energy provided to the mass element goes into the increase of the internal energy and into the work done.

$$\oint \delta Q^{\downarrow} = \oint \delta U + \oint \delta W^{\uparrow} \qquad 1.1$$

Let us consider the first law of thermodynamics on the mass element. The thermal energy supplied ($\downarrow$) to the system goes into increase in internal energy (δU) and work done to the outside ($\uparrow$). The internal energy is zero over the cycle and therefore the work done is positive ($\uparrow$). The condition is sustaining the pulsation. The entropy δS, the function of the state of the mass element over a cycle is given by;

$$\delta S = \oint \frac{\delta Q^{\downarrow}}{T} = 0 \qquad 1.2$$

The equation 1.2 means that if temperature T is constant over the cycle, there is no work done. Therefore assume temperature is perturbed by ΔT from the average temperature T_0;

$$T(t) = T_0 + \Delta T(t) \qquad 1.3$$

The first order approximation of the entropy over cycle;

$$0 = \oint \frac{\delta Q^{\downarrow}}{T_0 + \Delta T} \approx \oint \frac{\delta Q^{\downarrow}}{T_0} \left[1 - \frac{\Delta T}{T_0} \right] \qquad 1.4$$

Similarly,
$$\oint \delta Q^{\downarrow} \approx \oint \delta Q^{\downarrow} \frac{\Delta T}{T_0}$$

Then the positive work done;

$$\delta W^{\uparrow} = \oint \frac{\Delta T}{T_0} \delta Q^{\downarrow} \qquad\qquad 1.5$$

From equation 1.5, in order to produce positive work done, the $\delta W^{\uparrow} > 0$, i.e,;

$$\delta Q^{\downarrow} > 0 \text{ with } \Delta T > 0 \quad \text{or} \quad \delta Q^{\downarrow} < 0 \text{ with } \Delta T < 0 \qquad\qquad 1.6$$

Therefore for positive work done; both $\delta Q^{\downarrow}$ and ΔT have the same sign. The heat must be provided when increasing the temperature and released when temperature reduced. The conditions in equation 1.6 are the general terms of explaining the process of a pulsating star. Either one condition or both in equation 1.6 could be satisfied in pulsating stars as some layers may absorb heat while the other layers may release. The condition for pulsation is that the total work over the star is positive so that;

$$\text{Total Work} \approx \oint \frac{\Delta T}{T_0} \delta Q^{\downarrow} dM_r > 0 \qquad\qquad 1.7$$

In order to sustain the pulsation, there should be a continuous energy fed to the system via some mechanism. During the compression by pulsation, T increases and the production of nuclear energy increase so that the first condition of 1.6 will be satisfied. The star expands beyond its equilibrium point and return back by the gravity of the above layers. The different layers acts differently, as one layer gains heat and do positive work for the driving pulsation, other layers release heat on pulsation and damp the pulsation. This is analogy to a heat – engine mechanism. The important part of the heat – engine is the valves operating at specific times. In a star this could be done by partial ionizing layers through opacity (κ). Hence this mechanism is called κ - mechanism (Baker & Kippenhahn, 1962, 1965) (Zhevakin, 1963).

1.1.2 Partial ionization zones

Hydrogen (H) and Helium (He) are the main elements constituting the partial ionization zones of a star. In addition, Iron (Fe) is also contributing at higher temperatures. The Hydrogen partial ionization zone is a broad region which occurs at $(1.0 - 1.2) \times 10^4$ K.

$$H \leftrightarrow H^+ + e^-$$

$$He \leftrightarrow He^+ + e^-$$
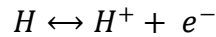
The second helium ionization occurs much deeper in the stellar interior at $(4.5 - 5.0) \times 10^4$ K and excited ions of metals such as Fe occurs at $(1.5 - 2.0) \times 10^5$ K (Pamyatnykh, 1999).

$$He^+ \leftrightarrow He^{++} + e^-$$

The location of the layers of partial ionization zones of hydrogen and helium entirely depends on the effective temperature of the star. The depth of the partial ionization zone decides the pulsation of a star. For a star hotter than $T_{eff} = 7500$ K, the partial ionization zones of hydrogen and helium are located close to the surface. Comparatively a star cooler than $T_{eff} = 5500$ K, these layers are close to the center of the star as seen in Figure 1.2.

The mass layer above the partial ionization is too thin for the stars of effective temperature hotter than 7500 K causing not enough mass to drive the oscillations. In comparison, the stars cooler than 5500 K have a very large convective layer above the partial ionization zone and more effectively radiate the energy preventing the building up heat and pressure beneath the driving pulsation layer again causing no pulsation. Therefore, the appropriate temperature range for pulsation is very narrow. This region of the Hertzsprung–Russell (HR) diagram is known as the instability strip (see Figure 1.1)
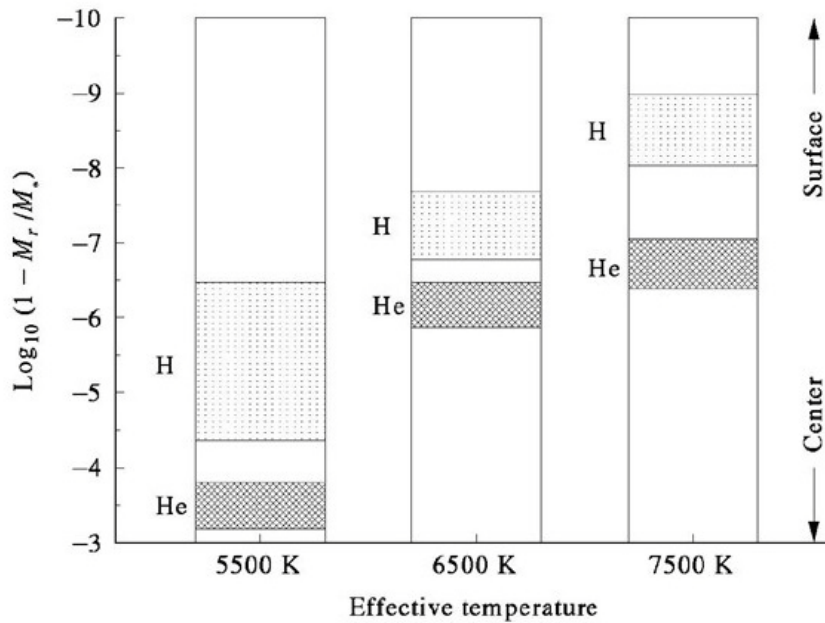
Figure 1.2. Partial ionization zones of hydrogen and helium in a star with different effective temperatures. The vertical axis is the logarithmic mass fraction from the center to the surface of the star relative to the sun. Adopted from Steven R. Majewski.

1.1.3   Opacity (κ)

The opacity of stellar matter determines the rate of penetration of radiation through the gas layers of a star. The opacity parameter is critical in stellar astrophysics as it is the main parameter to explain the absorption and emission spectroscopy, stellar pulsation, etc. In addition, the opacity of stellar matter is essential to model the stellar evolution and to generate synthetic spectra. Opacity tables were produced by OPAL (Rogers & Iglesias, 1998) and the Opacity Project (OP) by an international collaboration (Seaton, 2005) to fulfill the needs of synthetic stellar modeling. Stellar opacities (Maeder, 2009) are mainly due to

- Line absorption or bound - bound transitions
- Electron scattering
- Photoionization or bound - free transitions, including H⁻ absorption
- Free - Free transitions

7

The opacity increases significantly at particular temperature regions of stellar matter which is identified as opacity ridges or bumps. These bumps are the important points in stellar oscillations as they act as valves for stellar compression and expansion. These bumps are due to ionizations of hydrogen, helium and heavy metals such as iron. Figure 1.3 illustrates the opacity distribution as a function of temperature and density (Pamyatnykh 1999). The solid lines indicate the Zero Age Main Sequence (ZAMS) models of masses 1.8 – 40 M_{sun}. The opacity bumps due to hydrogen, helium and heavy metals are shown H, He and Z respectively. OPAL opacity tables (Rogers & Iglesias 1996) were used to generate by Pamyatnykh, (1999) to produce the Figure 1.3.
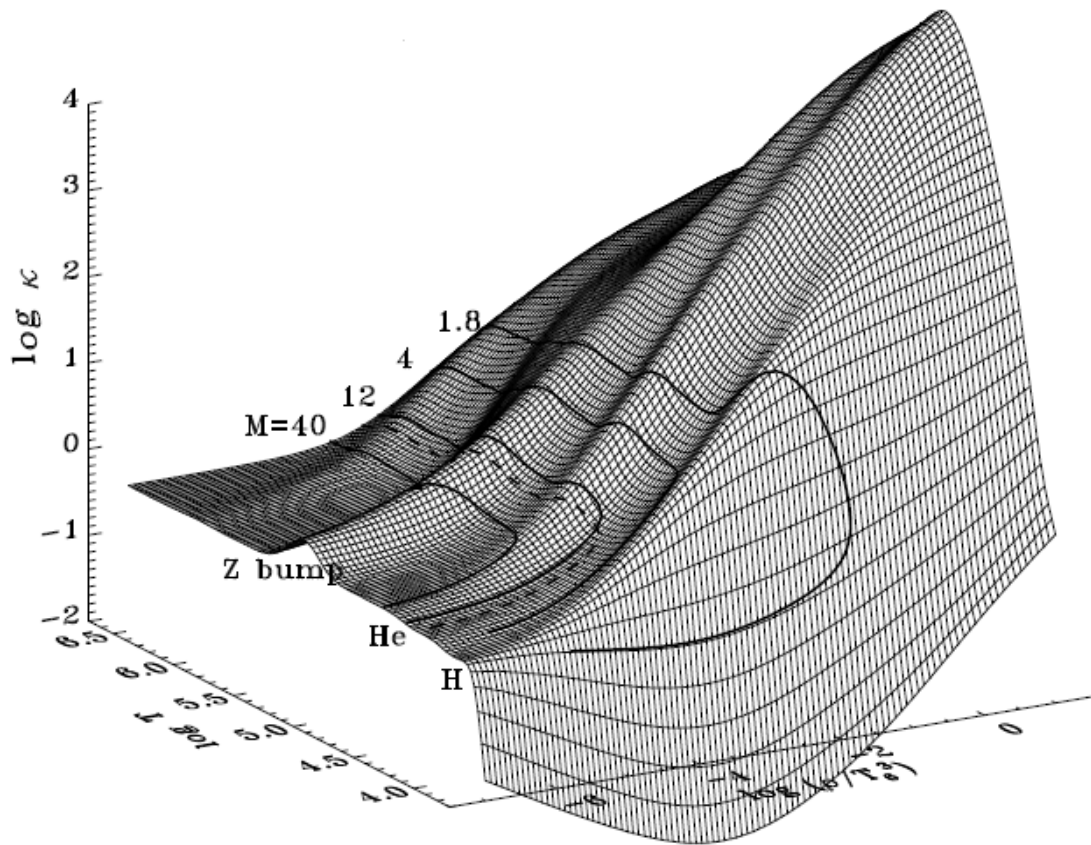
Figure 1.3. Opacity versus $\log T$ and $\log\left(\frac{\rho}{T_6^3}\right)$ for the stellar masses of $1.8 - 40$ M_{sun} $T_6 = T/10^6$. Figure and caption from Pamyatnykh, 1999.

The Kramers law for bound-free and free-free transition is given by

$$\kappa \propto \frac{\rho}{T^{3.5}} \qquad\qquad 1.8$$

The proportionality constant depends on heavy element content of a star. Considering compression of a star since the temperature increases, the opacity, κ, decreases in most region according to the equation 1.8. For a non-pulsating star, the compression increases the density (ρ) and temperature (T) but equation 1.8 shows the opacity is more sensitive to the temperature so that increase in temperature decrease the opacity, κ. This means the $\delta Q^{\downarrow} < 0$ with $\Delta T > 0$, i.e., condition 1.6 is not satisfied and so in general there is no pulsation.

The regions of the stellar interior where the partial ionization occurs can act as a valve mechanism and increases the opacity with temperature T. During the compression these partial ionization zones absorb part of the heat energy and further ionize hydrogen and helium rather than contributing to increase the temperature. In this way increasing in density produce higher opacity of the layer. Therefore temperature remains low allowing more heat to flow from adjacent layers keeping $\delta Q^{\downarrow} > 0$ with $\Delta T > 0$ which satisfies the first condition of 1.6. Since the opacity increases, the retained energy makes an expansion, allowing T and κ decrease, satisfying the second condition of 1.6 to pulsate the star.

1.2 Asteroseismology

A devastating earthquake in the city of Lisbon, Portugal in the year 1755, started the modern era of seismology (Davison, 1936). The Greek word "seismo" means shaking or shock. Nowadays we have a thorough knowledge of earthquakes by means of seismology. The first sign of that a similar behavior would be possible in stars was given by Eddington in 1926 (Eddington, 1988) introducing the possibility of stellar pulsation. The internal Constitution of the Stars published by him in 1926 raised a question;

"At first sight it would seem that the deep interior of the Sun and stars is less accessible to scientific investigation than any other region in the universe. Our telescopes may probe farther and farther into the depths of space; but how can we ever obtain certain knowledge of that which is hidden behind substantial barriers? What appliance can pierce through the outer layers of a star and test the conditions within?"

In such a background, later in mid of 20th century, a new concept, asteroseismology, had arisen, developing the theories (Ledoux & Walraven 1958) of stellar oscillations that can explain the interior of the stars in an unprecedented way.

The pressure waves, more simply sound waves, are produced inside the stars due to gigantic energy production by nuclear fusion reactions. These sound waves are trapped inside as they cannot come out due to the vacuum of space. When the waves travel inside, standing waves are created with different frequencies. This is similar to the standing waves created by musical instruments. Astronomers are listening to these stellar musical tones from faraway to investigate the stellar interior.

Acoustic waves are pressure waves. The compressions and rarefactions of air produce these waves. The acoustic waves are not directed at the center of the star as the lower part of the wave is in higher temperature and the upper part of the wave in lower temperature. At higher temperature region, the acoustic speed is higher and thus, the wave is refracted to the upper atmosphere. The refracted waves again bounce off from the surface, trapping the acoustic energy within the star, as shown in Figure 1.4c. The waves of different modes penetrate to various depths. Hence, the detection of as many modes as possible provides the sound speed distribution resulting in the construction of the temperature profile of the stellar interior. Thus asteroseismology is the only way to extract the internal properties and structure of stars.

1.2.1 Three dimensional oscillations in Stars

Stars are three dimensional and their oscillation nodes have three orthogonal directions. The three directions are r – *the radial distance,* θ - *latitude and* ϕ - *longitude*. The nodes are concentric shells at constant r, cones of constant θ and

planes of constant ϕ. For 3-D stars there are three quantum indices to specify the modes, n is related to the number of radial modes known as overtone of the mode, l is the degree of the mode (number of surface nodes) and m is the azimuthal order (|m| is the number of surface nodes that are lines of longitudes). The displacements in r, θ and ϕ directions are given by the following equations (Aerts et al., 2010).

$$S_r = a(r)Y_l^m(\theta, \emptyset)\, e^{(-i2\pi\nu t)} \hspace{4cm} 1.9$$

$$S_\theta = b(r)\frac{\partial Y_l^m(\theta,\emptyset)}{\partial \theta}\, e^{(-i2\pi\nu t)} \hspace{3.5cm} 1.10$$

$$S_\emptyset = b(r)\frac{\partial Y_l^m(\theta,\emptyset)}{\partial \emptyset}\, e^{(-i2\pi\nu t)} \hspace{3.5cm} 1.11$$

Where $a(r)$ and $b(r)$ are amplitudes, ν is the oscillation frequency and $Y_l^m(\theta, \emptyset)$ are spherical harmonics given by

$$Y_l^m(\theta, \emptyset) = (-1)^m \sqrt{\frac{(2l+1)}{4\pi}\frac{(l-m)!}{(l+m)!}}\; P_l^m(\cos\theta)e^{(im\emptyset)} \hspace{2cm} 1.12$$

Where $P_l^m(\cos\theta)$ are Legendre polynomials and $c_{lm} = \sqrt{\frac{(2l+1)(l-m)!}{4\pi\,(l+m)!}}$ is defined as normalization constant.

1.2.2 Radial modes

The simplest mode of oscillations is a radial mode with all indices, n, l and m being zero. The fundamental mode is the contraction and expansion of the star radially, making the center of the star node and the surface anti-node (Figure 1.4a and Figure 1.4b). The first overtone in radial mode is caused by a concentric shell within the star. The concentric shell does not move; the waves above and below this shell oscillate in anti-phase. The line going through the center in Figure 1.4c schematically illustrates the behavior of a radial mode. The radial pulsation is illustrated in Figure 1.4a and Figure 1.4b.
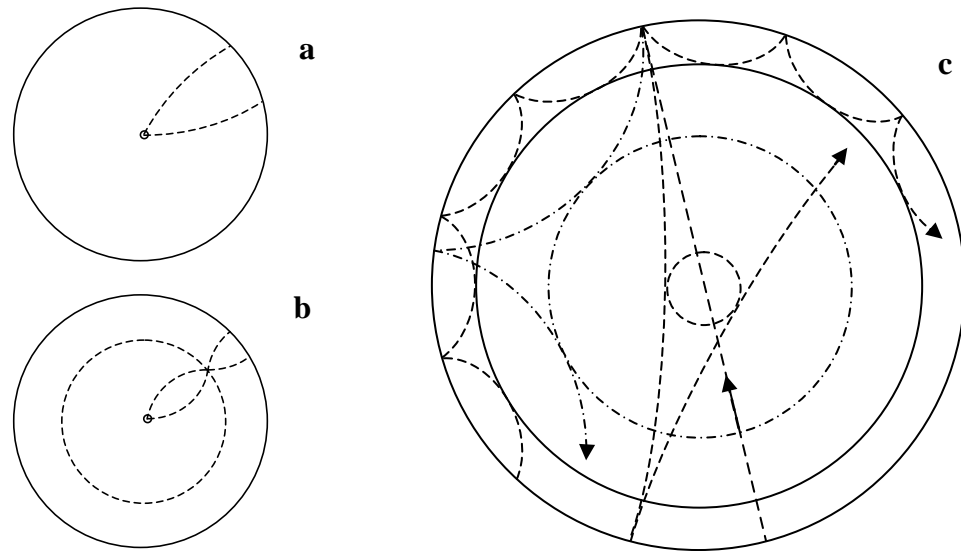
Figure 1.4. The propagation of sound waves inside a star in radial and non-radial mode. 1.4a represent s the fundamental radial node and 1.4b is an overtone. The non-radial standing wave patterns penetrate from surface to different depths are shown in 1.4c.

The interpretation of radial modes and overtones is given by the quantum number n. Therefore, $n = 0$ is the fundamental radial node which is the dominant vibration mode of a star and represented by Figure 1.4a. In addition, it is possible to have radial overtones (see Figure 1.4b) which are denoted as $n = 1, 2, 3$, etc. The presence of overtones can be interpreted as double mode pulsators. The overtones appearing in an oscillating star are similar to those in an organ pipe with one end closed and the other end open. However, the ratio of the fundamental and harmonics are completely different. The fundamental and overtones of one end closed organ pipe and the radial displacements of the eigenfunction of a star are shown in Figure 1.6. The ratio of the fundamental and first harmonic for the one end closed pipe is 0.33 while these ratios for a Delta Scuti type pulsating star is 0.77, and for Cephieds, this is 0.71 (Aerts et al., 2010) which are drastically different. This difference is due to the non-uniform temperature and density profiles inside the stars. The fundamental mode penetrates to the center of a pulsating star. Therefore, determining the fundamental pulsation period is very important since it can be used to figure out the average density more precisely.

1.2.3 Non-radial modes

The non-radial oscillations are represented by the values of degree $l \geq 1$ and the combinations of m. The solutions existing for $l \geq 1$ in equation 1.12 are known as non-radial modes. The non-radial waves or surface waves propagate, avoiding the star's center while penetrating to the different depths. In Figure 1.4c, the waves penetrating to shallow depths produce surface disturbances resulting in higher degree modes of l. The wave penetrating closer to the center and reflected back by the smallest circle in Figure 1.4c is a low degree (l=2) non-radial oscillation. In this way, the higher degree modes penetrate to shallow depths, and low degree modes penetrate deeper. Therefore, identifying independent modes of frequencies as much as possible leads to determining the interior profile of a star.

Non-radial propagation is explained by the superposition of sound waves, as illustrated in Figure 1.5. This is similar to the light rays reflected with the higher refractive index. The sound waves penetrating the star are affected by increasing temperature and density. The waves with higher sound speed are continuously refracted, and in a particular depth, the sound wave reflection occurs. These reflection depths are called the turning radii, r_1 and r_2 in Figure 1.5, and higher order degrees of l have higher turning radius ($r_2 > r_1$) and hence are more sensitive in determining of the surface parameters. The simplest non-radial mode is $l = 1$ and $m = 0$ called dipole mode. In this mode, the star is divided into two oscillation regions by the equator. The northern hemisphere expands while the southern hemisphere contracts and vice versa maintaining the equator as a node. In such a way, the star oscillates in dipole mode keeping the center of mass at the same place so that preserving Newton's laws. The star is a compressible gas ball. Therefore, it can oscillate, keeping the center of mass unchanged (Christensen-Dalsgaard, 1976). However, in order to have non-radial mode of $l \geq 1$, there should be at least a one radial mode within the star. The quantum index of $l = 2$ and $m = 0$ is a quadruple mode consisting of two surface nodes. In equations 1.9 and 1.12, the azimuthal parameter, $m \neq 0$ gives a phase factor which is a time-dependent component to the solutions. The rotation effect deviates the spherical symmetry of a star and frequencies are degenerate giving the multiplet of $m = 2l + 1$ which give rise frequencies corresponding to $m = $ -2, -1, 0, +1, +2 for $l = 2$ mode. The sign convention of positive m's denotes by prograde motion (same direction of

13

rotation of star) and negative m's is for retrograde motion (opposite direction of star rotation). The first few spherical harmonics of equation 1.12 which illustrate the non-radial modes are shown in Fig. 1.7.
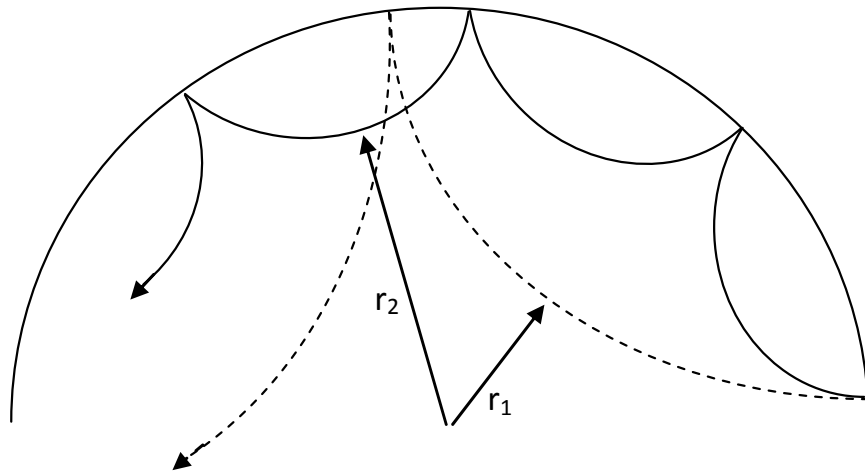
Figure 1.5. The propagation of acoustic waves for two different degrees of l of same frequency inside a star. The continuous line path penetrates to shallow depth (r_2) which corresponds to higher degree of l while the dashed line path penetrates to deeper depth (r_1) corresponds to lower degree of l.
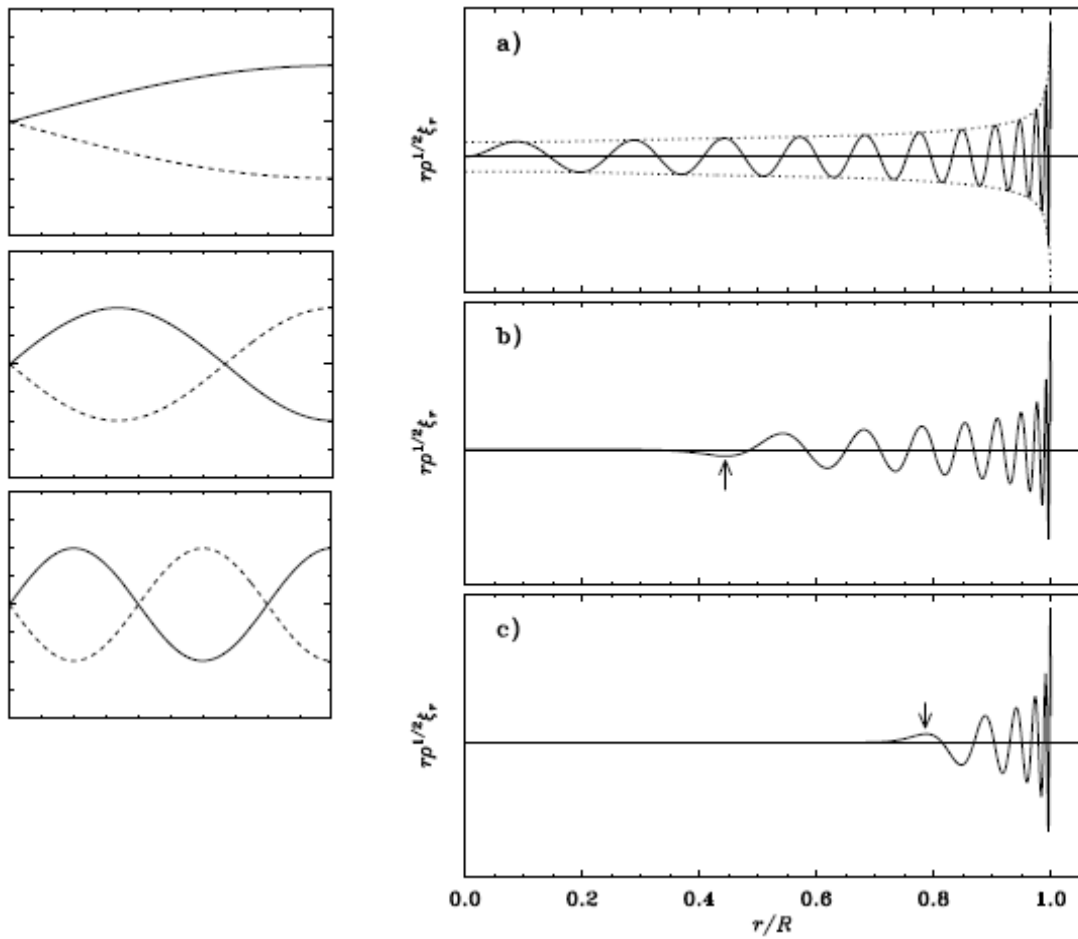
Figure 1.6. The first three oscillation modes in one end closed pipe (Left panel) and scaled radial displacement eigenfunctions, on an arbitrary scale, for selected p modes in a solar model, with a) $l = 0$, $n = 23$, $v = 3310$ μHz; b) $l = 20$, $n = 17$, $v = 3375$ μHz; c) $l = 60$, $n = 10$, $v = 3234$ μHz. In panels b) and c) the arrows mark the asymptotic location of the turning points. Figure and caption of 3.21 of Asteroseismology (2010) is reproduced with the permission from Springer. Note that the radial displacements ε_r is analogues to equation 1.9 in this document.
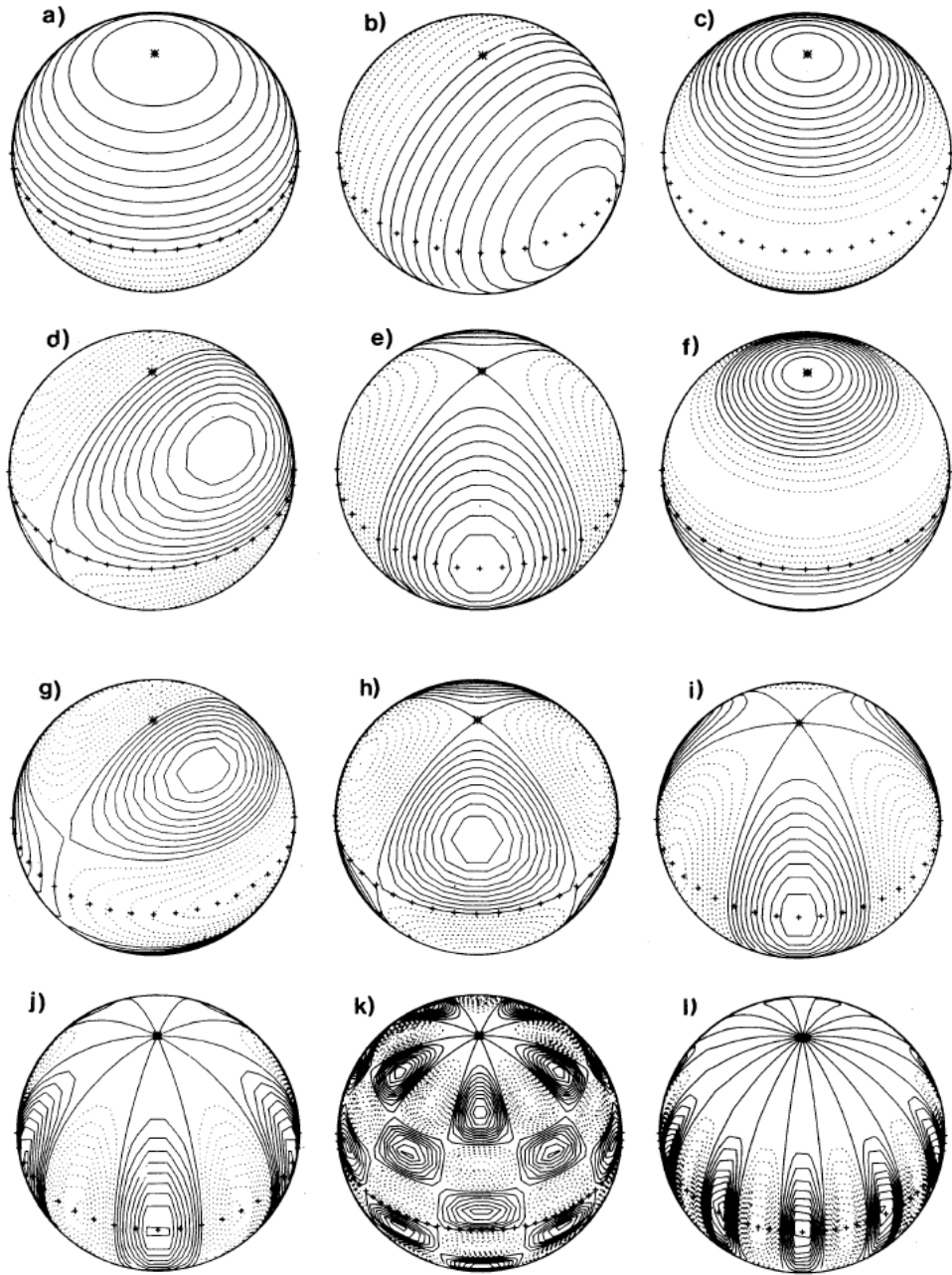
Figure 1.7. Contour plots of the real part of spherical harmonics Y_l^m equation 1.4. Positive contours are indicated by continuous lines and negative contours by dashed lines. The $\theta = 0$ axis has been inclined by 45° towards the viewer, and is indicated by the star. The equator is shown by "++++". The following cases are illustrated: a) $l = 1, m = 0$; b) $l = 1, m = 1$; c) $l = 2, m = 0$; d) $l= 2, m = 1$; e) $l = 2, m = 2$; f) $l = 3, m = 0$; g) $l = 3, m = 1$; h) $l = 3, m = 2$; i) $l = 3, m = 3$; j) $l = 5, m = 5$; k) $l = 10, m = 5$; l) $l = 10, m = 10$. The image and caption are reproduced from Fig. 2.1 of "Analysis of oscillation data" with the authorization of Christensen-Dalsgaard.

1.2.4 Pressure waves (p-mode) and Gravity waves (g-mode)

The internal waves of a star are basically of two types. The pressure is the primary restoring force in a perturbed star from its equilibrium. The gas motion in these perturbations is radial, similar to the radiation pressure procedure by nuclear reaction. These waves are acoustic waves and known as pressure waves or p-mode as shown in Figure 1.4c. The frequencies of the p-modes are increased with the increase of radial nodes. The p-modes are more sensitive to the surface conditions of the star and the asymptotic relation implies that these frequencies are equally spaced. The p-mode frequencies are given by equation 1.13 (Tassoul 1980, 1990).

$$V_{n,l} = \Delta v \left(n + \frac{l}{2} + \alpha \right) + \epsilon_{n.l} \qquad\qquad 1.13$$

where n is the overtone and l is the degree of the mode, α is a constant of order unity and $\epsilon_{n.l}$ is the small correction. Δv is the large frequency separation which is defined as the inverse of the sound travel time from core to the surface of the star and back, given by

$$\Delta v = \left(2 \int_0^R \frac{dr}{V(r)} \right)^{-1} \qquad\qquad 1.14$$

where $v(\text{r})$ is the speed of sound and R is the radius of the star.

The gravity waves are transverse and primary restoring force is buoyancy and gas motions are horizontal. The frequencies of g-modes due to internal gravity waves are decreased with the increase of radial nodes. g-modes are mostly located at the center of the star and hence more sensitive to the conditions at the core of the star. The frequencies of g – modes are given by

$$\Pi_{n,l} = \frac{\Pi_0}{\sqrt{l(l+1)}} (n + \epsilon) \qquad\qquad 1.15$$

where *n* and *l* are the overtone and degree of the mode, ϵ is small constant and Π_0 is given by

$$\Pi_0 = 2\pi^2 \left(\int \frac{N}{r} dr \right)^{-1} \qquad 1.16$$

where *N* is the Brunt-Vaisala frequency given by;

$$N^2 = \frac{g}{\varrho} \frac{d(\Delta\varrho)}{dr} \qquad 1.17$$

so that $\frac{d(\Delta\varrho)}{dr} > 0 \longrightarrow$ stable, $\frac{d(\Delta\varrho)}{dr} < 0 \longrightarrow$ unstable, with respect to the convection. The above conditions define whether the fluid layer stays within the equilibrium or deviates from it.

1.3 Delta Scuti stars

The Delta Scuti stars (DSS) are situated where the classical instability strip crosses the main sequence (MS) in the Hertzsprung-Russell (HR) diagram. In general, these stars are either on the main sequence or post main sequence branch which corresponds to the core hydrogen or shell hydrogen burning stage, respectively. The pulsation period and the masses are in the range of 0.02 – 0.25 days (Breger & Montgomery, 2001) and 1.5 – 2.5 $M_\odot$ (Aerts et al., 2010), respectively. Therefore DSS are known as short period pulsators compared to RR Lyrae, β Cephei and Gamma Dor stars. The spectral type is between F2 V and A2 V and effective temperature approximately between 6400 K $\leq T_{eff} \leq$ 8600 K (Breger & Montgomery, 2001, Rodriguez & Breger 2001, Uytterhoeven et al., 2011). DSS show complex oscillation spectra composed of p-mode and g-mode and mixed modes of low overtone (Handler, 2012, Kurtz et al., 2014). Both radial and non-radial oscillations occur in DDS. The observed amplitudes can go from magnitude to millimagnitude scale. The stars with higher magnitude variations are called High Amplitude Delta Scuti Stars (HADS). The asteroseismic potential of DDS is enormous but could so far not be fully exploited. Even though hundreds of pulsation modes have been detected in some Delta Scuti stars, a little has been learned on their interior structures through

asteroseismology. Therefore, the importance of observations in long time base and multi-site is always advantageous in filling the information and knowledge gaps in this particular type of pulsating stars.

The DDS are important in stellar evolution because of their presence in the transition region of HR diagram. The placement of DDS stars in the HR diagram within the instability strip is shown in Figure 1.8.
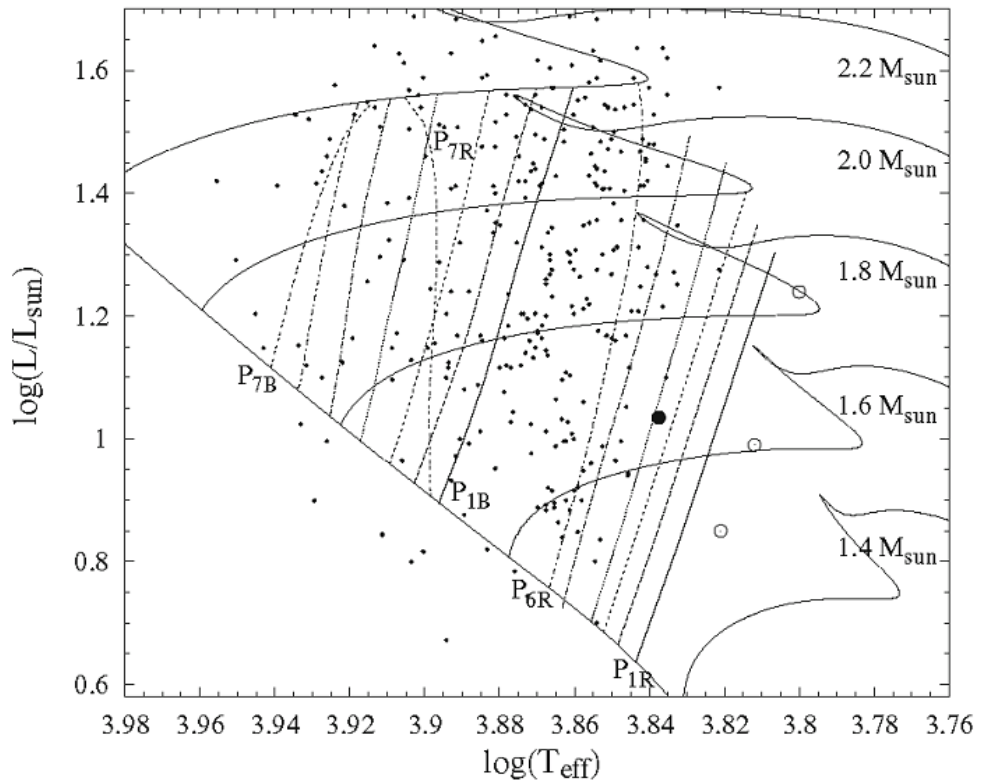
Figure 1.8. Blue and red edges of the Delta Scuti theoretical instability strip. Lines are our TDC results for radial modes from p1 to p7 for models with α = 1.8. The small points correspond to observations. For comparison, we also give the red edges for the fundamental radial mode obtained by Xionget et al., (2001) (⊙) and by Houdek (2000) (•). The image and caption adopted from Dupret et al., (2005).

The low- mass Delta Scuti stars (M ≤ 1.0 M⊙) closer to the red edge in instability strip have radiative cores and thick convective envelopes. The high mass stars (M ≥ 2.0 M⊙) have larger convective core and radiative envelopes (Bowman, 2017). The

instability regions of the Delta Scuti and the lower mass γ Dor stars are predicted to overlap in the HR diagram (Dupret et al., 2004, 2005; Houdek & Dupret, 2015). These stars, simultaneously pulsating in p - modes excited by the κ mechanism and gravity (g - modes) modes excited by the convective flux blocking (modulation) mechanism, are commonly referred as hybrid stars. The high precision photometry by Kepler mission revealed that many Delta Scuti stars are hybrid stars (Grigahcene et al., 2010; Uytterhoeven et al., 2011; Balona & Dziembowski, 2011).

Through a detailed analysis of amplitude spectra, p-modes, g-modes and their combinations and harmonics are possible to recover. Subsequently, recovered frequencies can be subjected to mode identification procedure to determine *n, l* and *m*. However, the analysis could be more complicated when the amplitude spectra are non-linear due to the mode coupling between pulsation modes and non- linear due to the harmonics and combination frequencies that create forest-like amplitude spectra. The DDS can have a wide range of p-mode oscillations consisting of a closely packed frequency spectrum. For example, KIC 4077032 and KIC 8623953 discussed in Chapter 7 have frequency spectra where regular frequency spacing could not be seen. In the single wavelength band observation like Kepler and TESS (see Figure 2.12), the mode identification completely depends on the frequency spacing and rotational splitting (Gupil et al., 2000). Delta Scuti stars are generally slow rotators typically, v sin i < 30 km/s[-1] (Breger & Montgomery, 2001), which means the recovery of frequency splitting in the amplitude spectra is challenging due to the noise frequencies and artificial effect of Fourier transformation. Despite the complexity, the high precision long time-based Kepler targets of Delta Scuti stars have been extensively analyzed by Reed et al., (2011); Breger et al., (2011); Murphy et al., (2013). In contrast with other pulsation stars, Delta Scuti stars are not yet fully exploited and therefore, more scientific investigations are still needed to be done.

Chapter 2

Instruments and Observations

Observations discussed in this dissertation were obtained from ground-based as well as space-borne observatories. A detailed instrumental profile of these observatories has been included in this chapter. In addition, the summary of the observations from the Mount Abu Observatory are also provided along with a detailed description of the photometric and spectroscopic data reduction on a high amplitude Delta Scuti star, SZ Lyn.

2.1 Mount Abu Infrared observatory

The observations were carried out at Mount Abu Infrared observatory. The observatory is located near the town of Mount Abu in the state of Rajasthan, India. The observatory is at 24:39:09 N, 72:46:47 E and an altitude of 1680 meters with typical astronomical seeing of ~ 1.2 arc seconds and is adjacent to Guru Shikhar, the highest peak of the Aravalli Range.

2.1.1 1.2 m Telescope

The main telescope is equatorial mounted open truss and fork type and has a 1.2 m parabolic primary (f/3) and 300 mm hyperbolic secondary making a Cassegrain focus of f/13. The effective focal length is 15.6 m and the plate scale is 13.6''/mm that remains linear over the telescope field of view of 10 arc minutes diameter (Shah, 2005). The detector is Liquid Nitrogen cooled 1296 x 1152 CCD operating at a temperature of -120 degrees C, with a field of view of 6.4 x 5.7 arc minutes. Liquid nitrogen cooled heads offer the ultimate performance in terms of sensitivity and dynamic range. Dark current of the chip is reduced to levels of only a few electrons per pixel by cooling the CCD to approximately -120C. The liquid nitrogen cooled heads contain a CCD mounted in a vacuum-sealed housing to minimize heat loss. The CCD is connected by a cold "finger" to a container filled with liquid nitrogen. This process effectively cools the CCD to -120 °C., reducing dark current to the absolute minimum. The filter set is the UBVRI standard photometric filters.
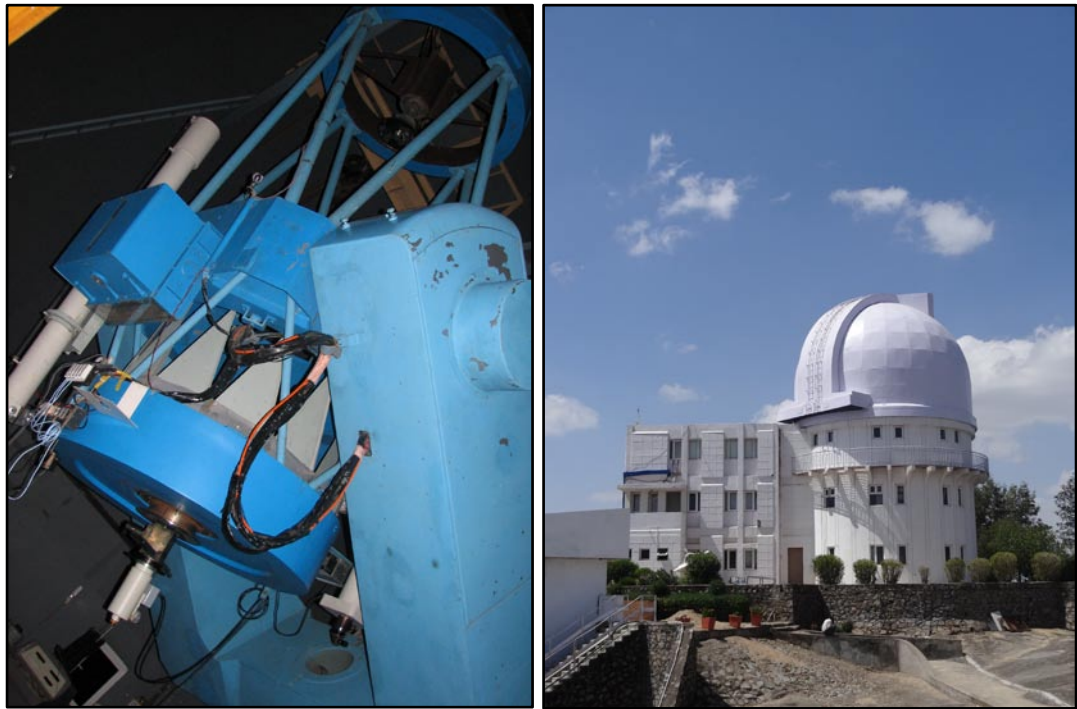
Figure 2.1**.** 1.2 m telescope with LN2 cooled CCD camera at Mount Abu (Left).
View of the observatory and dome from outside (Right).
.

2.1.2 50 cm CDK Reflector

The Corrected Dall-Kirkham (CDK) has a 50 cm Prolate Ellipsoid, f/3 primary mirror
and 19 cm spherical secondary mirror with an effective focal ratio of f/6.8. The
telescope is a fork mounted equatorial type reflector. The detector is 1024 x 1024
electrons multiplying (EM) CCD with a typical cooling of -80 C and negligible read-
noise. The higher frame rate per second and negligible read out noise (< 1 electron
with EM gain) are ideal for observing short period variable stars with very high time
resolution. The large CCD array provides a field of view 13 X 13 arc minutes square
which is an advantageous to observe large field in a single frame. In addition to the
standard UBVRI filters, a set of Polaroid sheets oriented at 0°, 45°, 90° and 135° are
also included in the system. The telescope and the dome are fully automated through
the network and can be operated remotely from PRL main campus with all
functionalities including weather monitoring (Ganesh et al., 2013).
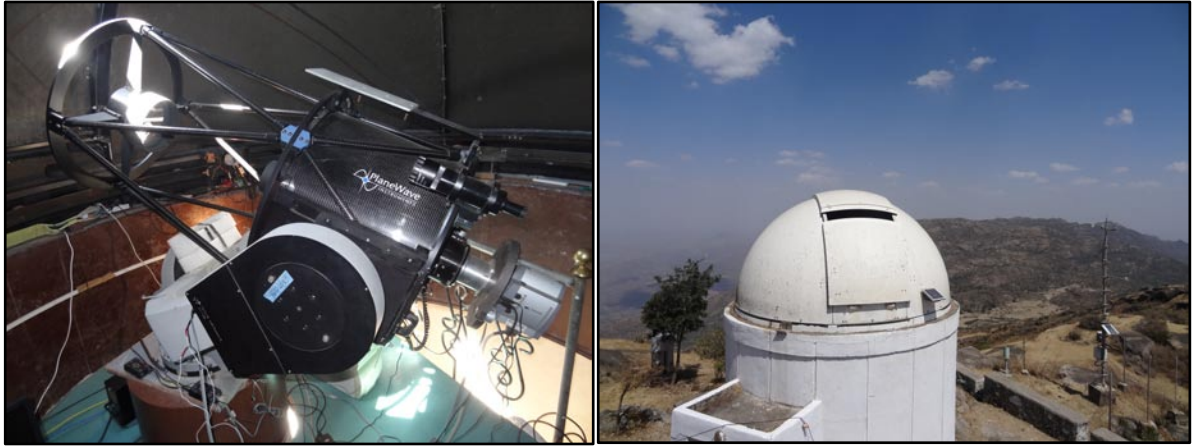
Figure 2.2 50 cm CDK reflector telescope and the dome.

Table 2.1 Johnson UBVRI band pass filters and their ranges.

Filter	Region in EM spectrum	Wavelength Range (nm)	Central wavelength (nm)
U	Ultraviolet	320 – 400	365.6
B	Blue	400 – 500	435.3
V	Visible	500 – 700	547.7
R	Red	550 – 800	634.9
I	Infrared	700 – 900	879.7

2.2 Photometry at Mout Abu

The photometric observations of SZ Lyn, summarized in Table 2.2, were carried out at Mount Abu observatory from 2013 to 2016 during several visits. An extensive observation was done using the 0.5 m CDK telescope to investigate SZ Lyn in UBVR bands with a FOV 13×13 arc minutes. The exposures were very short (typically < 5 seconds) since the CCD is electron multiplying CCD which saturates quickly for the high visual magnitude of 9.1 of SZ Lyn. This short exposure observation is advantages to obtain very high temporal resolution light curves particularly when looking for very high frequencies in the light curve. The exposure was scripted for the consecutive UBVRI loop until terminated. The 0.5 m CDK telescope is fully automated and can be controlled through the network facilitating observations are relatively easy which enabled vast amount of data collection of SZ Lyn. The

23

observations are listed in Table 2.2. The field of SZ Lyn with the two comparison stars, TYC 2979-1329 of m_v = 10.5 and TYC 2979-1343 of m_v = 10.8 are shown in Fig. 2.3.

After removing faulty frames, 4328 frames in B, 4569 frames in V and 6836 frames in R were acquired. The raw frames of SZ Lyn were initially corrected for the bias and flat fielding using basic Image Reduction and Analysis Facility (IRAF) routines. The offsets of the image frames were corrected by *imcentroid* and *imshift* tools in IRAF. This brought all fames to a common center of the accuracy of 0.54 pixels in X direction and 0.17 pixels in Y direction.

Table 2.2 The details of photometric observation of SZ Lyn at Mount Abu observatory. The exposure time (exp.) is in seconds and the coverage (cov.) is in hours. The coverage includes all raw data.

Band	B		V		R	
Date of Observation	exp. (s)	cov. (hr)	exp. (s)	cov. (hr)	exp. (s)	cov. (hr)
10 Dec. 2013	03	3.10	03	3.75	03	3.92
13 Dec. 2013	02	2.12	02	2.50	02	4.33
06 Jan. 2014	05	6.50	02	6.47	02	6.63
26 Jan. 2014	10	3.80	03	3.78	02	3.80
28 Jan. 2014	03	6.03	02	5.91	02	5.95
04 Feb. 2014	02	6.48	02	6.47	02	6.50
11 Nov. 2106	03	3.17	02	3.17	02	3.04
Total		31.20		32.05		34.17
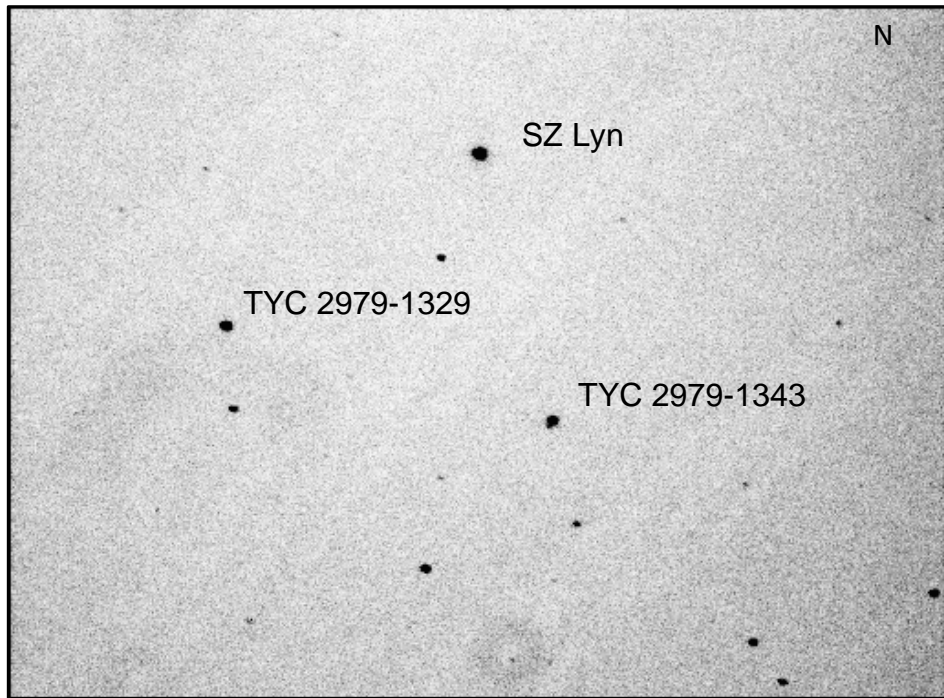
Figure 2.3 Inverted field of SZ Lyn taken by 0.5 m telescope at Mount Abu. 13×13 arc minute field of view is trimmed vertically to remove discontinuities. 10 frames of 2 seconds exposure in V band were averaged to produce this plate.

Measurements of the instrumental magnitudes of SZ Lyn and comparison stars were carried out by defining a circular aperture to extract the flux. Several aspects such as the brightness of the star, the circular symmetry, the sky background and the convolution of fluxes from the objects in the vicinity were considered in the determination of an optimum aperture to extract the instrumental magnitudes (Massey and Davis, 1992). The *phot* algorithm in IRAF is used to measure the instrumental magnitudes. The crucial parameters in the aperture selection are shown in Figure 2.4. The details routines of IRAF photometry are included in Appendix C.
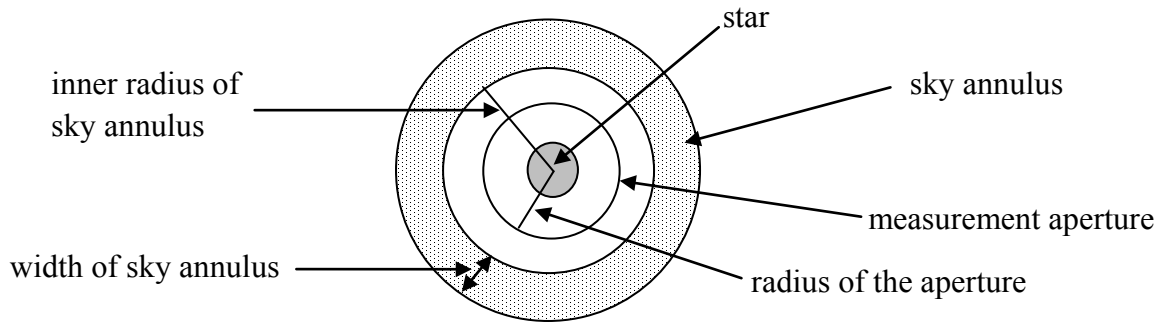
Figure 2.4 The definitions of aperture parameters
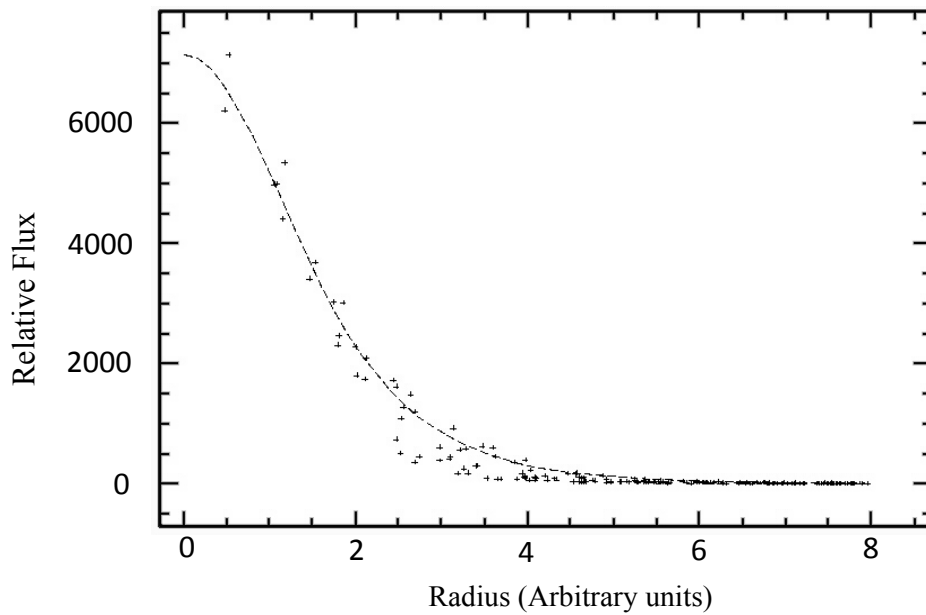
Figure 2.5 The radial profile of SZ Lyn obtained by 'imexamine' task in IRAF. The outputs of this task, FWHM of the Gaussian profile, ellipticity, peak value and the position angle were used to define the aperture of magnitude extraction.

These parameters were decided by observing the radial profile of SZ Lyn shown in Figure 2.5. The radial profiles of SZ Lyn were obtained covering the start, middle and end of the observation to eliminate variations in the profile and hence to represent an averaged single aperture to extract instrumental magnitudes from all the frames. The aperture is usually set to 3 or 4 times the FWHM to include all the light from the star within the aperture and at the same time make sure not to include too much of background to the aperture (Massey and Davis, 1992). In addition to the aperture radius, several parameters in Figure 2.4 have been defined in magnitude extraction. To model the value of the sky, the size and the location of the annulus have to be defined. In that case the sky was defined 5 pixels from the aperture and the width of the sky annulus was set to 5 pixels in the case of bright stars in the field. Finally the instrumental magnitudes were extracted running aperture photometry package called *phot*. All IRAF routines were included in Appendix C.

The extracted instrumental magnitudes were differentiated using the comparison stars to eliminate the atmospheric extinctions and sky transparency variations. A Part of differential light curve of SZ Lyn in BVR is shown in the Figure 2.6. The observation gaps were eliminated by converting time Julian Date (JD) into phase using equation 2.1 assuming the main pulsation period P = 0.1205349 days (Gazeas et al., 2004) and considering T_0 as 2456664.26171300 JD where a maxima occurs on the 6th January 2016.

$$T = T_0 + PE \qquad\qquad 2.1$$

where T is the time of any observation point and E is the cycle or phase.
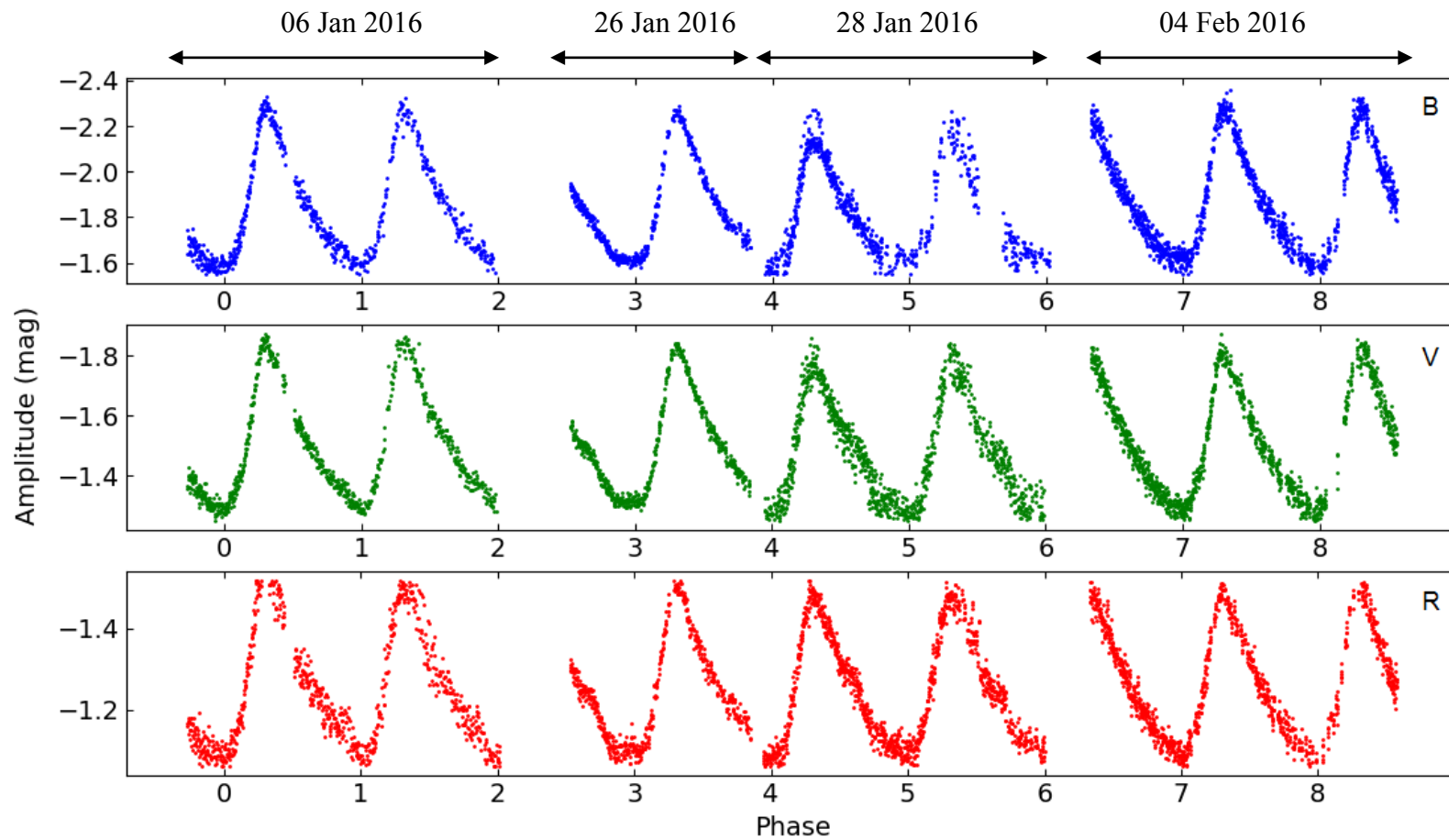
Figure 2.6 BVR light curves of SZ Lyn observed at Mount Abu observatory. The time in JD is converted to phase using the main pulsation period of 0.1205349 days. The observation dates are also indicated above the light curves. The observation gaps in time were eliminated by rearranging as a function of phase.

2.3 Spectroscopy at Mount Abu

The spectroscopic observations of SZ Lyn were carried out during October - December 2016 using Shelyak LISA visual slit spectrograph attached to the 50 cm CDK (see Figure 2.7). The spectra were obtained covering the entire visible band of 400 – 700 nm with a low resolving power R = 1000. Total 578 low resolution spectra of SZ Lyn were taken in five nights covering the entire pulsation period of SZ Lyn. The Ar-Ne calibration lamp was used for the wavelength calibration and inbuilt incandescent light in spectrograph was used for flat fielding. The observation summary is given in Table 2.3. The basic data reduction steps of spectroscopic data were performed using standard IRAF routines. Bias and flat field corrected 1-D spectra produced by apall task were calibrated using Ar-Ne emission spectrum and normalized to unity by continuum task. All the IRAF routines of spectroscopic data reduction are included in Appendix C. The low resolution spectrum of SZ Lyn is shown in Figure 2.8.

Table 2.3 Spectroscopic observation at Mount Abu observatory carried out during the period of October – December 2016.

Object	17 Oct	18 Oct	08 Dec	10 Dec	11 Dec	12 Dec
			Number of spectra			
SZ Lyn	17		98	131	113	219
CC And		32		206	207	242
HD 199908		23				
HD 223651	40					

In addition, the SZ Lyn was observed by LAMOST program and data were released as a part of Data Release 3 (DR3). The low resolution spectrum of R = 1800 of resolving power in the spectral range of 370 nm ∼ 700 nm clearly shows prominent hydrogen absorption lines and some metallic lines in SZ Lyn. Detail description of LAMOST is given by Zhao et al., (2012), Luo et al., (2015). The comparison of the LAMOST and Mount Abu observation of SZ Lyn is shown in Figure 2.8.
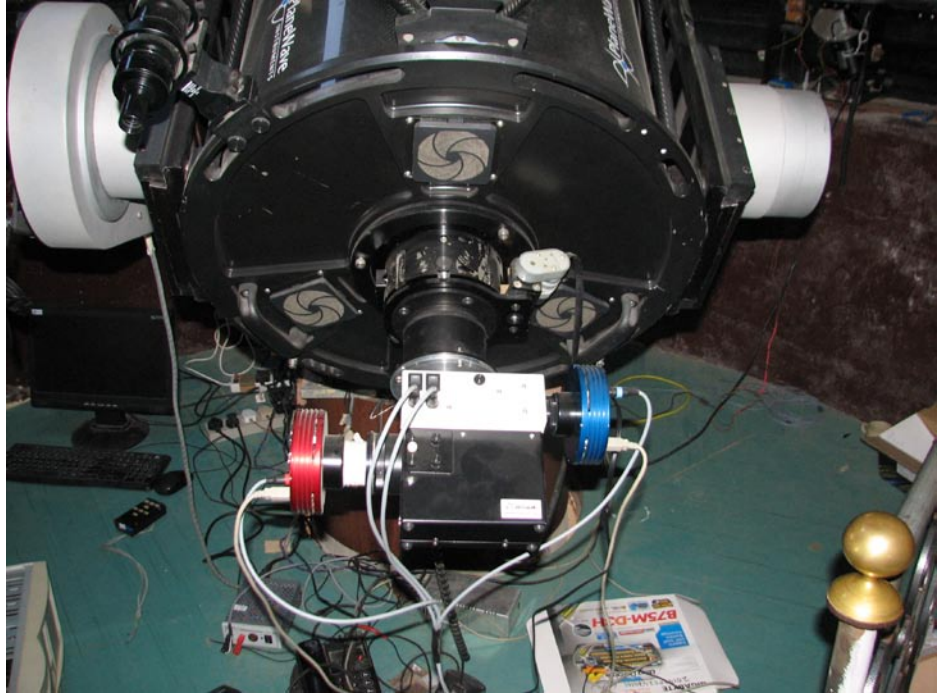
Figure 2.7 LISA spectrograph is attached to 50 cm CDK reflector
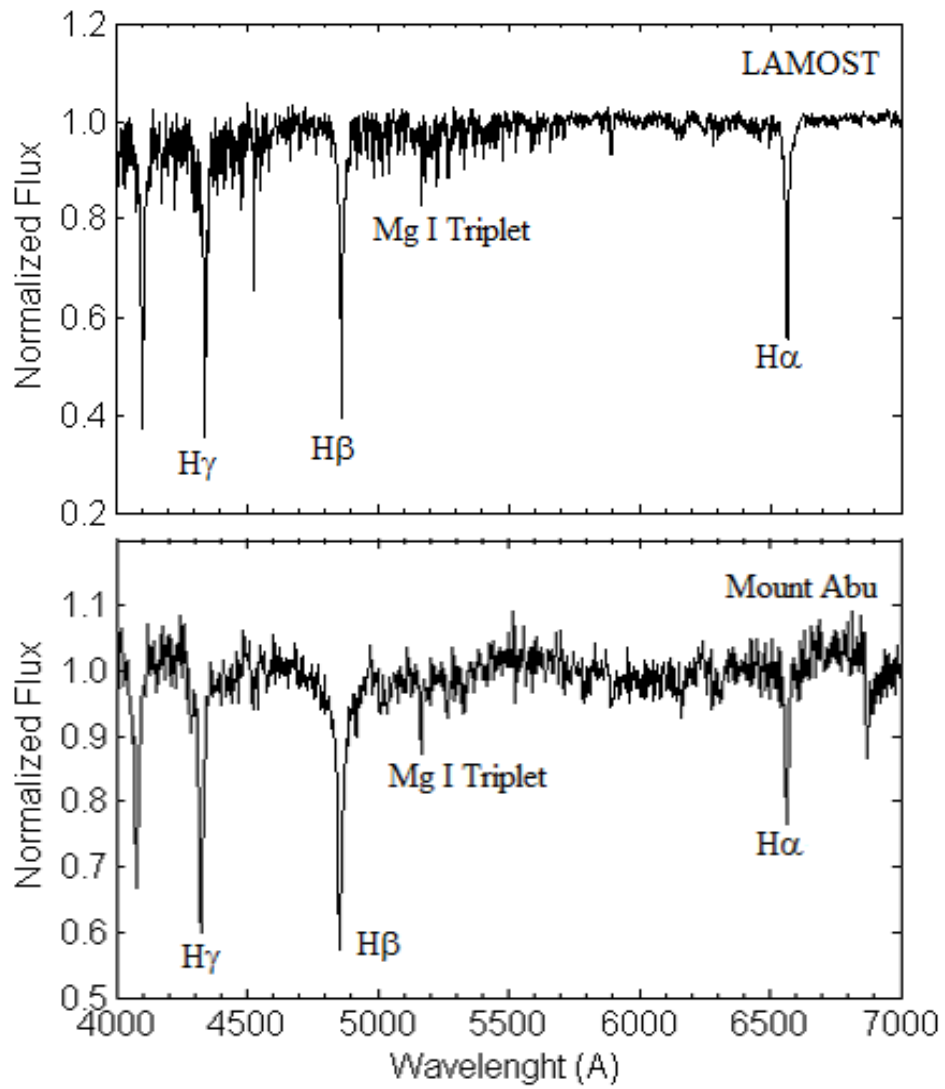
Figure 2.8 Spectroscopic observations SZ Lyn at Mount Abu observatory and LAMOST.

2.4 Fairborn Observatory

The single-site, ground-based observation of a time series is highly affected by the one day frequency aliasing. The frequency aliasing makes more complicated the distinguishing of stellar oscillations from the crowded frequency spectra. Therefore, to avoid the one day frequency aliasing of the ground-based observations, multi-site observations are needed. The detailed description of frequency aliasing of the ground-based observation is mentioned in section 3.3.1. The SZ Lyn was observed by 0.80 m Automatic Photoelectric Telescopes (APT) at Fairborn Observatory, Mt. Hopkins in southern Arizona (31° 24′ 57″ N, 110° 43′ 50″ W).

Figure 2.9 Horseshoe equatorial mount design 0.8m Cassegrain telescope at the Fairborn Observatory. Image credited: Fairborn observatory.

Additional photometric measurements of SZ Lyn were acquired in April and May 2014. Differential time-series photoelectric data were collected through the Johnson UBV filters with the 0.8 m Automatic Photoelectric Telescope (APT) at Fairborn Observatory in Arizona (Strassmeier et al., 1997). Two comparison stars, HD 67808 and HD 66113, were used. Integration times were 2 x 20 s in each filter, with the exception of the U filter for SZ Lyn in which we integrated 2 x 30 s to collect enough

photons. The data were reduced following standard photoelectric photometry schemes. First, the measurements were corrected for coincidence losses. Then, sky background was subtracted within each target/local comparison star group. Standard extinction coefficients were employed; small errors in their assumption would be compensated when computing differential magnitudes. Obviously, the same extinction correction was applied to each star. Some bad measurements due to partly poor telescope tracking had to be eliminated. Finally, differential magnitudes were computed by interpolation, and the timings were converted to Heliocentric Julian Date. During the reductions it turned out that HD 66113 could be a low-amplitude Delta Scuti star (f = 12.573 d^{-1}, A_V = 2:1 mmag), hence it was rejected from the computation of the differential light curves of the target SZ Lyn itself. We obtained a total of 701/688/672 good measurements for the U, B, and V filters, respectively, with an estimated accuracy of 4.5/3.5/3.5 mmag per point. The time span of the combined data set is 35.05 d, with data collected on 24 nights. The observation summary is in Table 2.4. A part of a light curve of SZ Lyn in UBV bands is shown in Figure 2.10.

Table 2.4 The observation summary of SZ Lyn at Fairborn observatory. The period of observation is 2457480.634 − 2457515.688 JD with the gaps and number of 24 effective nights.

Band	Exposure (s)	Number of frames	Effective hours
U	60	701	50.1
B	40	688	51.4
V	40	672	52.5
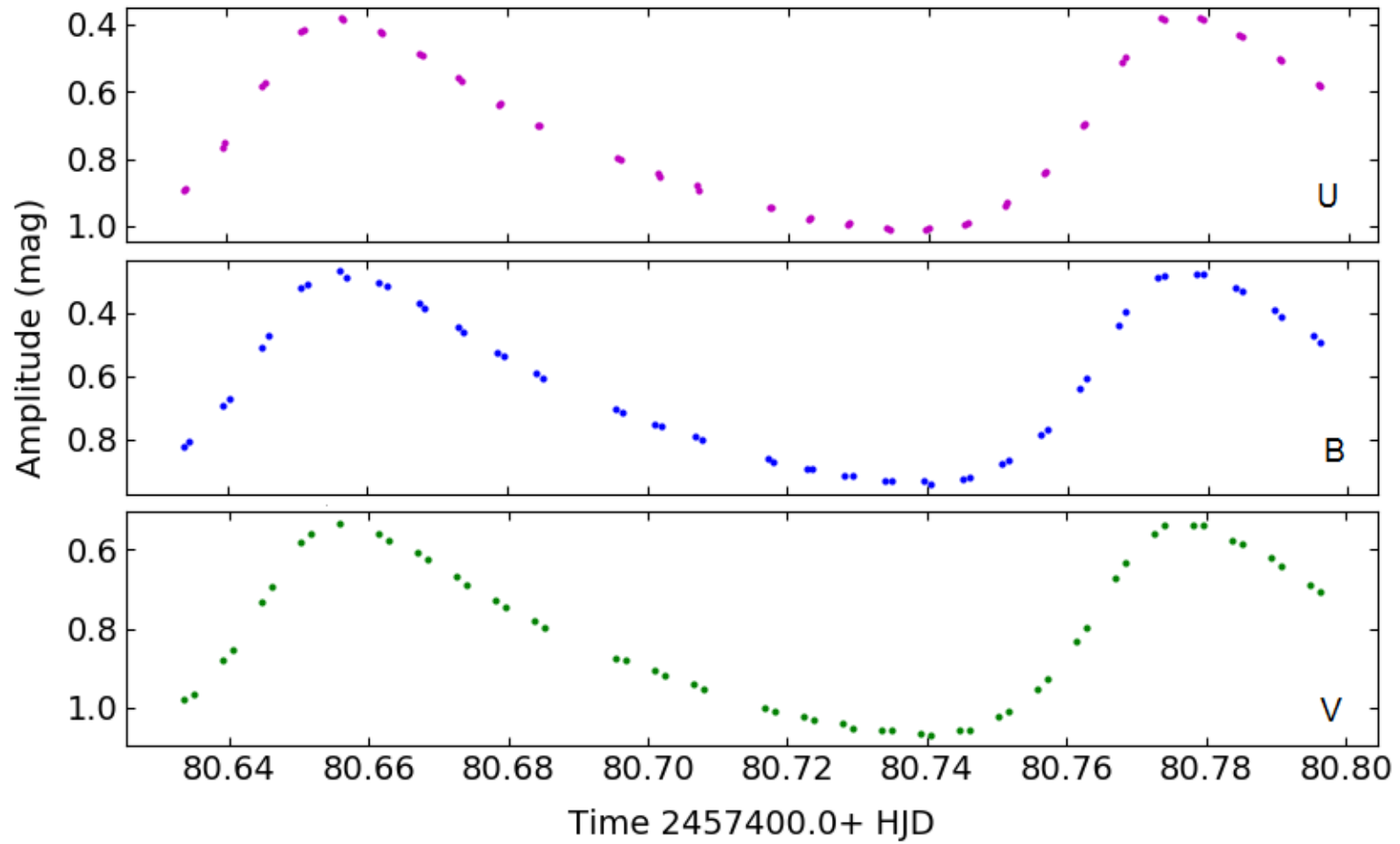
Figure 2.10 A part of UBV light curves of SZ Lyn observed at APT telescope at Fairborn observatory. The time is truncated Heliocentric Julian Date (HJD) and amplitude is differential magnitude.

2.5 Wide Angle Search for Planets (WASP)

The Wide Angle Search for Planets (WASP) is a fully robotic, ultra-wide angle survey for planetary transits located at La Palma (28° 45′ 49″ N, 17° 53′ 41″ W). It consists of 5 Apogee 10, 14-bit 2kx2k CCD cameras with Canon 200mm f/1.8 lens (See Fig. 2.11). This combination gives each camera a $9.5° \times 9.5°$ field of view while a pixel size of 13.5 μm means that the plate scale is expected to be 16.7 arcsec/pixel. The cameras have an operating temperature of −60 °C maintained by 3-stage Peltier cooling mechanisms and the readout time is 4 s. The Torus fork mounted enclosure is fully automated and linked to a built-in weather station (Street et al., 2002). WASP program also observed SZ Lyn in its own wide pass band of 400 – 750 nm (Butters et al.2010). Two exposures of each field with 30 seconds and each field were sampled every 9-12 minutes. The flux of total 2894 data points, covering 216 hours of observation during the period of 2454190.366 – 2454575.408 JD, were converted to apparent magnitudes by the WASP using its automated pipeline.

Figure. 2.11 SuperWASP observatory system with 5 cameras located at La Palma, Spain. Image credited: SuperWASP consortium.

2.6 Kepler observations of Delta Scuti star

Kepler space telescope was launched in 2009 to search for Earth-like planets. The period of Earth trailing orbit of the satellite is 372.5 days. The observations were focused in 115 square degrees field of view in the constellation of Cygnus and Lyra (Garcia et al., 2011). The stars were observed in Kepler magnitude (K_p) in the wavelength range of 430-890 nm. The K_p is defined as AB magnitudes, where AB = -2.5 log f_v − 48.60 (Oke, 1974), derived from each target's calibrated g, r, i magnitudes. u, g, r, i and z are photometric system used in Sloan Digital Sky Survey (Smith et al., 2002). Details of the K_p magnitude are available in Brown et al., (2011). Kepler observations are made in two different operating modes: Long-Cadence (LC) targets are sampled every 29.5 minutes (Nyquist frequency of 283.45 µHz) and Short-Cadence (SC) of 58.5 seconds of exposure (Nyquist frequency of ~8.5 mHz) (Garcia, et al., 2011, Gilliland et al., 2010). The analysis of SC light curves is resulted in the high resolution power spectra which can resolve frequencies up to 100 cycles per day (1.16 µHz). The corrected flux from the Kepler Asteroseismic Science Operations Center (KASOC) were obtained and performed further corrections of eliminating photometric jumps and outliers and linear trends for every quarter in SC data. A part of the light curve of KIC9700322 covering quarters 11 and 12 is shown in Figure 2.13. The time stamp of the light curves is in Barycentric Julian Date (BJD). From quarter to quarter of Kepler's observation, the mean flux levels of stars were considerably changed as shown in the top panel of Figure 2.13. To reorient spacecraft solar arrays, the Kepler satellite performed quarterly rolls (every 93 days) resulting in quarterly discontinuities in the mean flux levels of observed stars; specifically, the roll displaces a star between the 42 CCD modules which comprises the field-of-view with the modules having different characteristics (Garcia, et al., 2011). Furthermore, the changes in the average flux also occur within the quarter. To remove inter-and intra-quarter offsets, the medians of the two quarters were obtained by fitting linear polynomials and then quarter 12 was shifted by the difference of two medians (middle panel of Figure 2.13). The normalized two quarters were again approximated by third order polynomial for the conversion of parts-per-million (ppm) as shown in the middle panel of the Figure 2.13. Using the polynomial, the Kepler flux ($F_{Kp}(t)$) was reduced to a fractional quantity parts-per-million (ppm), with respect to the broad, underlying baseline characterized by a polynomial f(t), using the equation 2.2.

$$F_{ppm}(t) = 10^6 \left(\frac{F_{kp}(t)}{f(t)} - 1 \right)$$ 2.2

We tested polynomials with different orders that represented the baseline of the shifted quarters. We found third or fourth order polynomials sufficiently fit the overall baseline and provide a better fit than a linear baseline. A part of a light curve after the conversion to ppm is shown in the bottom panel of Figure 2.13. Data for all Kepler targets used in this thesis were converted to ppm using this method. This conversion process of flux improves the S/N ratio of the power spectrum and hence possible to determine the weak frequency signals. The corrected fluxes of Delta Scuti stars are available in Kepler Asteroseismic Science Operation Center (KASOC). All the Kepler targets used in this thesis are included in Table 2.5

.
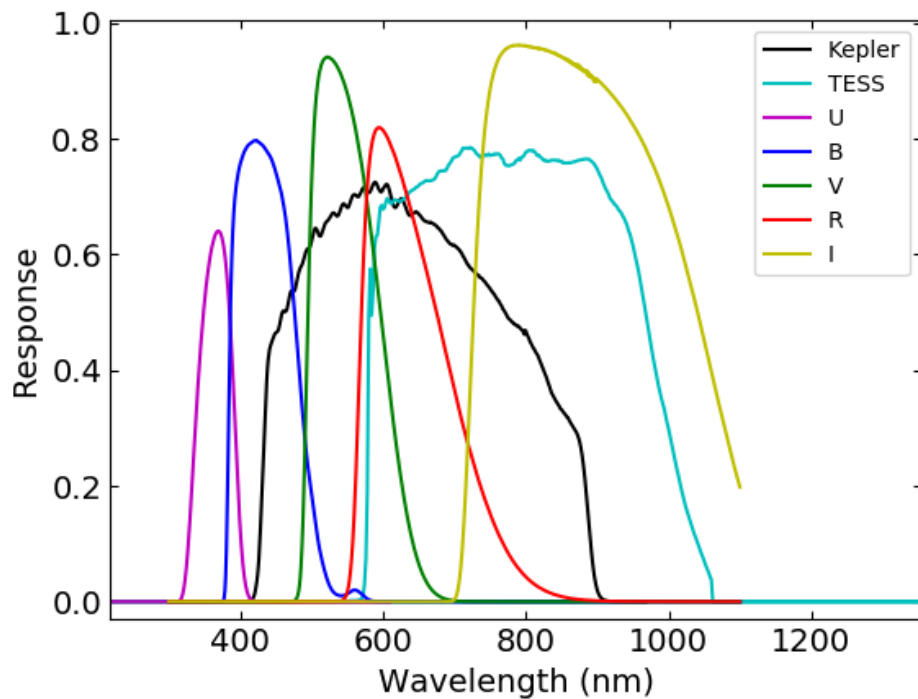
Figure 2.12 Spectral response of Bessel UBVRI photometric system and two space based telescopes, Kepler and TESS.
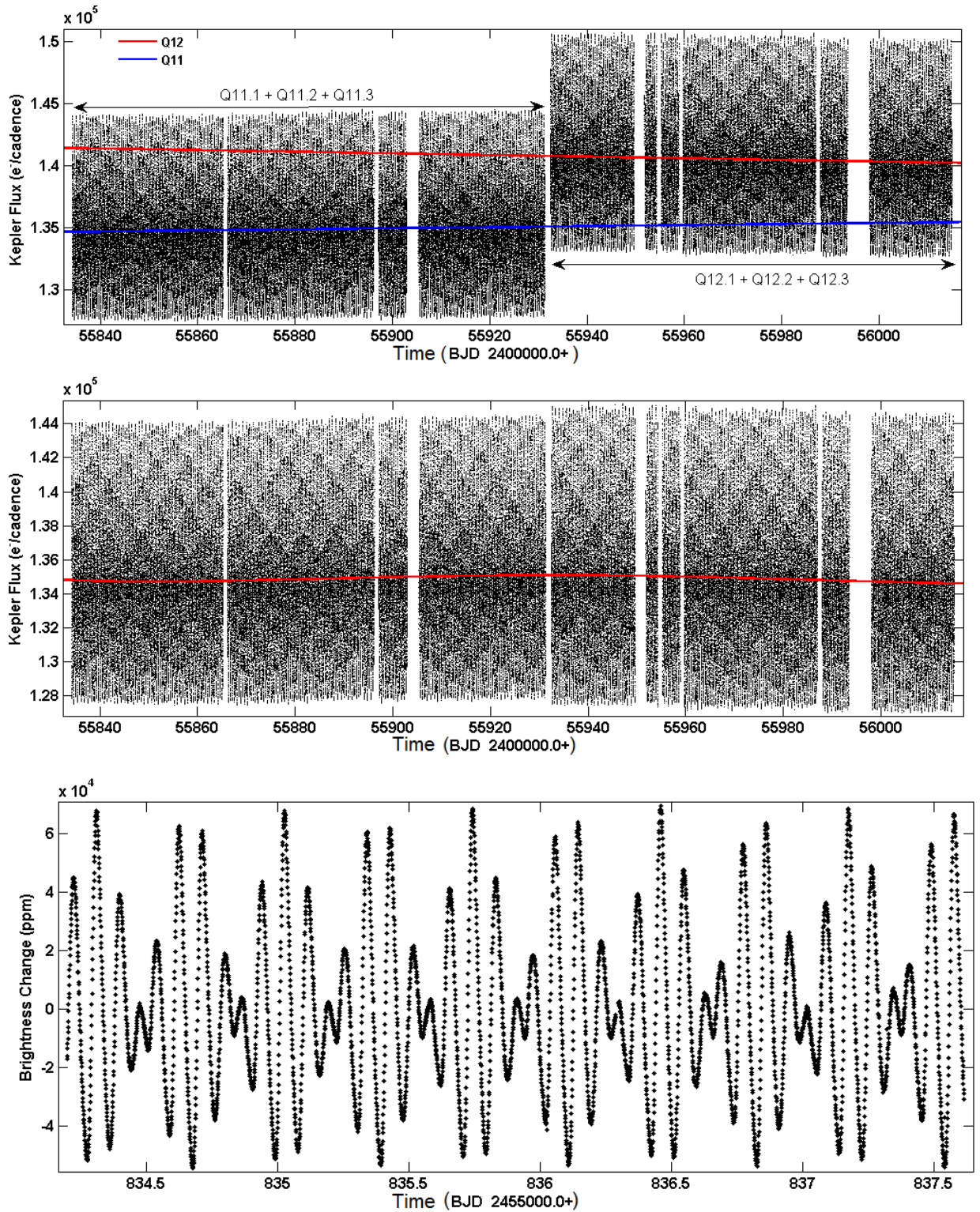
Figure 2.13 Upper panel shows the discontinuity of quarter 11 and quarter 12 of Kepler light curve of KIC 9700322. The middle panel is the shifted light curve of two quarters. The red line is the baseline polynomial, f(t), given in equation 2.2. A part of the light curve converted to ppm is shown in the bottom panel.

Table 2.5 Summary of Kepler observations of δ Scuti stars. K_p is the Kepler magnitude of the star. All light curves are short cadence (SC). The observation span is the start and end in BJD irrespective of the observation gaps.

Star	R.A.	Dec.	K_p	Kepler Quarters	Data points	Observation span (BJD) 2400000.0+
KIC 4077032	19:45:03.17	39:11:26.0	9.693	Q2.1	41934	55002 – 55033 (31 days)
KIC 8623953	19:25:59.76	44:44:45.3	9.428	Q10.1 Q10.2 Q10.3	134730 46170 44340	55739 – 55833 (94 days)
KIC 9700322	$19^h\,07^m\,50.7^s$	46° 29' 12''	12.685	Q11.1 Q11.2 Q11.3 Q12.1 Q12.2 Q12.3	45184 43543 46311 34037 39984 32946	55834 – 56204 (370 days)
KIC 9845907	$19^h\,49^m\,30.4^s$	46° 40' 02''	11.640	Q8.1 Q8.2 Q8.3 Q9.1 Q9.2 Q9.3	45184 38648 29390 53282 41711 45616	55568 – 55739 (171 days)
KIC 1162150	$19^h24^m53.76^s$	36°53'14''	11.240	Q4.3	42458	55246 – 55275 (29 days)
KIC 11754974	$19^h\,08^m\,15.9^s$	49° 57' 15''	12.678	Q6.1 Q6.2 Q6.3 Q7.1	39630 45255 43996 44036	55372 - 55493 (121 days)

2.7 TESS observation of SZ Lyn

Transiting Exoplanet Survey Satellite (TESS) is originally designed to discover small transiting exoplanets orbiting nearby bright stars (Ricker et al., 2014). One major consequence of the TESS survey is the enormous amount of time series data collected at high cadence of 2 minutes. The TESS is equipped with four 10 cm telescopes, each connected to four CCD of field of view of 24 deg^2 thus four CCDs together give a coverage of 96°×24° (Oelkers and Stassun, 2018). The SZ Lyn was observed by TESS in sector 20, ID number TIC 192939152, from 24th December 2019 to 19th January 2020 in 120 seconds of cadence. The light curves were generalized using simple aperture photometry and corrected by pre-search data conditioning (PDC). The PDC pipeline module uses single value decomposition to identify time-corrected instrumental signatures such as space craft pointing jitter, long-term pointing drifts due to differential velocity aberration and other stochastic errors (Jenkins et al., 2016, Balona et al., 2019). The corrected fluxes of SZ Lyn taken from Tess Asteroseismic Science Operations Center (TASOC) were re-calibrated as the fractional deviation of each flux, F_i, from its mean, $\langle F \rangle$, and then converted to a respective magnitude deviation, Δm_i. For all N data points, at corresponding time t_i, the i-th flux deviation is defined by;

$$\Delta m_i = -2.5 \, log_{10} \left(\frac{F_i}{<F>} \right) \qquad\qquad 2.3$$

where Δm_i is the deviation calculated in magnitude.

TESS has covered SZ Lyn in total 25 full days with 16550 data points resulting effective hours of observation 631.8 in its own waveband of 600 - 1000 nm. The light curve of corrected flux and converted to magnitude deviation are shown in Figure 2.14.

The ground based and space based observations of SZ Lyn and five Kepler targets mentioned in Table 2.4 were subjected to frequency analysis in Chapter 3 and Chapter 4.
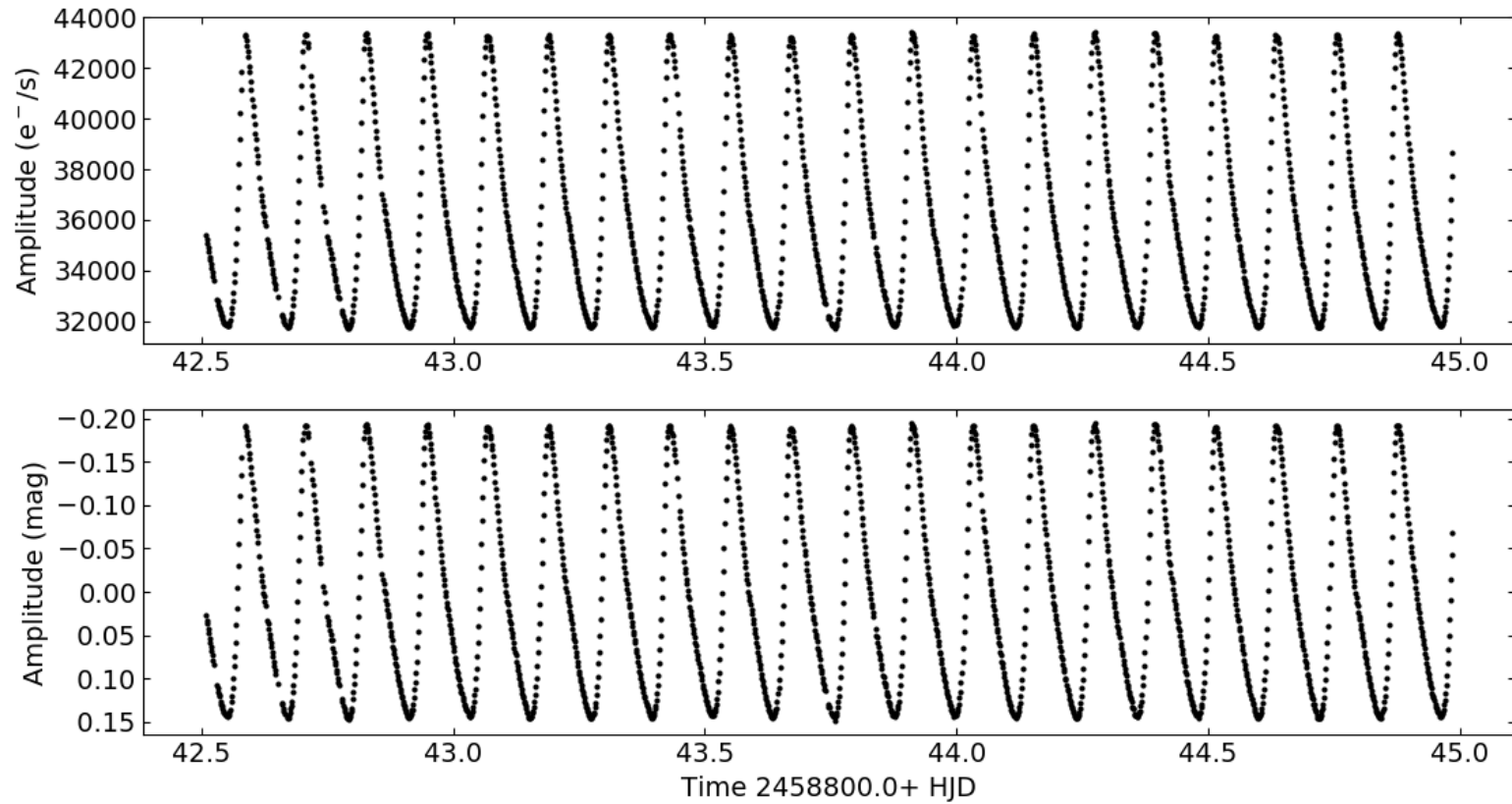
Figure 2.14 A part of light curve of SZ Lyn observed by TESS. The upper panel is in corrected flux and the lower panel is in magnitude scale which is converted to magnitude deviation using equation 2.3.

Chapter 3

Delta Scuti star SZ Lynx

3.1 Introductory remarks

Delta Scuti stars are located in the transition region of the classical instability strip and the main sequence on the Hertzsprung-Russel (HR) diagram (see Figure 1.1). These stars are in the late stages of their core hydrogen burning phase and the advance of the shell hydrogen burning transforms the core to a convective core. This transition produces a complex interior that can only detect by means of asteroseismology. Delta Scuti stars show radial and non-radial modes in their light curves. These radial and non-radial modes are used to determine their stellar properties. SZ Lyncis, HD 67390, AAVSO 0802+44, TIC 192939152 of RA = 08 h 09 m 35.8 s and DEC = +44° 28′ 17.6″ is a high amplitude Delta Scuti type binary star discovered by Hoffmeister (1949). SZ Lyn is a short period pulsator with a variation of visual magnitude m_v = 9.08-9.72 and a pulsation period of 0.1205379 days (2.89 hours). The orbital period of the binary system is 1173.5 days (Soliman et al., 1986). The pulsating star is the brighter component of the binary system while the faint component cannot observe in spectroscopy. SZ Lyn is characterized as a single-line spectroscopic binary (Gazeas et al., 2004). The ephemeris of the fundamental pulsation period was determined by Binnendijk (1968) and was later redefined by Gazeas et al., (2004). The star has been discussed several times in the literature for orbital and pulsation parameters. Van Genderen (1967) reported that the linear ephemeris does not accurately predict the time of pulsation maximum. Barnes III & Moffett (1975) suggested that the very long period orbital motion of SZ Lyn affected the linear ephemeris due to the light-travel time across the orbit. Using photometric and spectroscopic data, Moffett et al. (1988) introduced non-linear ephemeris for the time of light maxims and determined the best values for the pulsation and orbital parameters. A similar analysis made by Paparo et al., (1988) and Li & Qian (2013). Observation minus Calculation (O − C) analysis has the periodic variations and hence the main pulsation period changes by $(2.25 \pm 0.42) \times 10^{-12}$ day per cycle (Paparo et al., 1988). This value was later redefined to $(2.90 \pm 0.22) \pm 10^{-12}$ day per cycle by Gazeas et al., (2004). Apart from the orbital analysis, the physical parameters of SZ Lyn have been determined by several authors. SZ Lyn is nearly solar abundance (Alania, 1972;

Langford, 1976) and mean temperature of 7540K, log (g) of 3.88 (Langford, 1976). The BVJHK light curves were indicative of a radius of 2.76 $R_\odot$ and mass of 1.57 $M_\odot$ (Fernley et al., 1984). Bardin & Imbert (1981) determined the stellar atmospheric displacement as 0.115 $R_\odot$ assuming the radius to be 2.8 $R_\odot$ using the high time resolution radial velocity curves. Further, Bardin & Imbert (1981) determined the radial velocity of SZ Lyn as 30 km/s. The Large Sky Area Multi-Object Fiber Spectroscopic Telescope (LAMOST) has observed SZ Lyn in low resolution spectroscopic mode and determined T_{eff} = 7235 K, log (g) = 3.94. The GAIA determined the parallax 2.49±0.07 milliarcseconds and T_{eff} = 7799 K which is comparatively high relative to the other references (Gaia Collaborator et al., 2016, 2018; Luri et al., 2018). Although the star has been extensively analyzed in its binary nature fewer investigations were reported in its intrinsic variability. Fundamental period of 0.1205379 days with two harmonics was found by Gazeas et al., (2004). The stellar parameters of SZ Lyn are summarized in Table 3.1.

Table 3.1 Physical parameters of SZ Lyn

Parameter	Value	Reference
T_{eff} (K)	7540	Langford (1976)
	7465	McNamara (1997)
	7235	LAMOST
	7799	Gaia
log(g)	3.88	Langford (1976)
	3.94	LAMOST
Mass ($M_\odot$)	$1.57^{+0.17}_{-0.66}$	Fernley et al. (1984)
Radius ($R_\odot$)	2.76	Fernley et al. (1984)
	2.80	Bardin & Imbert (1981)
Parallax (mas)	2.49±0.07	Gaia

3.2 The orbital parameters of SZ Lyn

The pulsation stars are sometimes binary companions. The SZ Lyn system is a binary that has a very long period of more than 3 years. The orbital parameters of the SZ Lyn system can be determined using spectroscopic observations. Due to the 3 years long orbital period, it is difficult to cover the entire phase in spectroscopy. Therefore, no spectroscopic observations are available to determine the orbital parameters of binary.

However, the photometric data obtained by different observers with uneven time gaps can be used to investigate the orbital parameters. The orbital parameters of a binary system (see Figure 3.1) can be determined by spectroscopy if it were a double line or photometry if it were a transit system. SZ Lyn is neither a double nor a transit system. Instead, the pulsation properties of SZ Lyn can be used to generate Observation minus Calculation (O − C) diagram. Van Genderen (1967), Barnes and Moffett (1975), Paparo et al., (1988), Li & Qian (2013) used O − C variations to determine orbital parameters of SZ Lyn. The linear ephemeris of the time at maximum brightness for the pulsating stars is given as:

$$T_{max} = T_o + PE \qquad\qquad 3.1$$

where E denotes cycle number, P is the pulsation period, T_o is the initial epoch of maximum and T_{max} is the time at maximum brightness of the observation.

The linear equation in 3.1 predicts the times of light maxima known as calculated light maxima here after denoted as 'C'. The observed times of light maxima were taken by the light curve of SZ Lyn, denoted as 'O'. The assumption of constant pulsation period and linear ephemeris results, the O − C, the difference of observed and calculated to be zero. The O − C diagram of SZ Lyn was previously studied by several authors, Moffett et al., (1988), Paparo et al., (1988) and showed non-linear relation. The non-linearity of O − C diagram can be explained by periodic variations of the main pulsation period and light-travel time across the binary orbit (Irwin, 1952). The non-linear ephemeris is given by;

$$T_{max} = T_o + PE + \kappa + \tau \qquad\qquad 3.2$$

$$\kappa = \frac{\beta}{2}E^2 \qquad\qquad 3.3$$

$$\tau = \frac{a \sin i}{c}\left[\sqrt{1 - e^2}\, \sin E^* \cos \omega + \cos E^* \sin \omega - e \sin \omega \right] \qquad\qquad 3.4$$

The equations 3.3 and 3.4 are the periodic variation and light travel time effect of the binary orbit respectively. β - the secular change in the pulsation period, $a \sin(i)$ - the projected semi-major axis to the line of sight, e - the eccentricity, E^* - the eccentric anomaly, ω - the longitude of the periastron passage and c - the speed of light. The combination of the intrinsic pulsation and binary orbit produces a very complex $O - C$ diagram for SZ Lyn. A comprehensive $O - C$ analysis provides details of the orbital parameters and the pulsation properties. Therefore, all the observations have been used for the determination of stellar parameters of SZ Lyn.

The times of maximum magnitude of the observed light curve were obtained by fitting a smoothed spline function to the data as shown in Figure 3.2. The maximum magnitude was obtained by the zero crossing of the derivatives as shown in the bottom panel of Figure 3.2. The entire observation of Mount Abu light curve provides 20 times of light maxima. In addition, the WASP observation of SZ Lyn in V band includes 32 light maxima, 162 maxima from AAVSO and 164 from all the previous observations brought together for a total of 379 times of light maxima for O-C analysis. Therefore, the maximum number of data points is included in this analysis. The complete set of $O - C$ data is included in Appendix B.

True

Direction of motion

Periastron

Line of nodes

Descending node

ω

East

i

b

a

Ascending node

Apparent

North

E*

v

a

True ellipse

Auxiliary circle
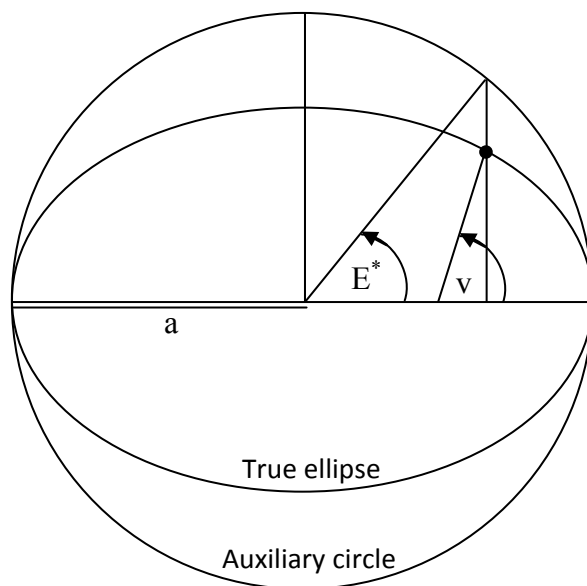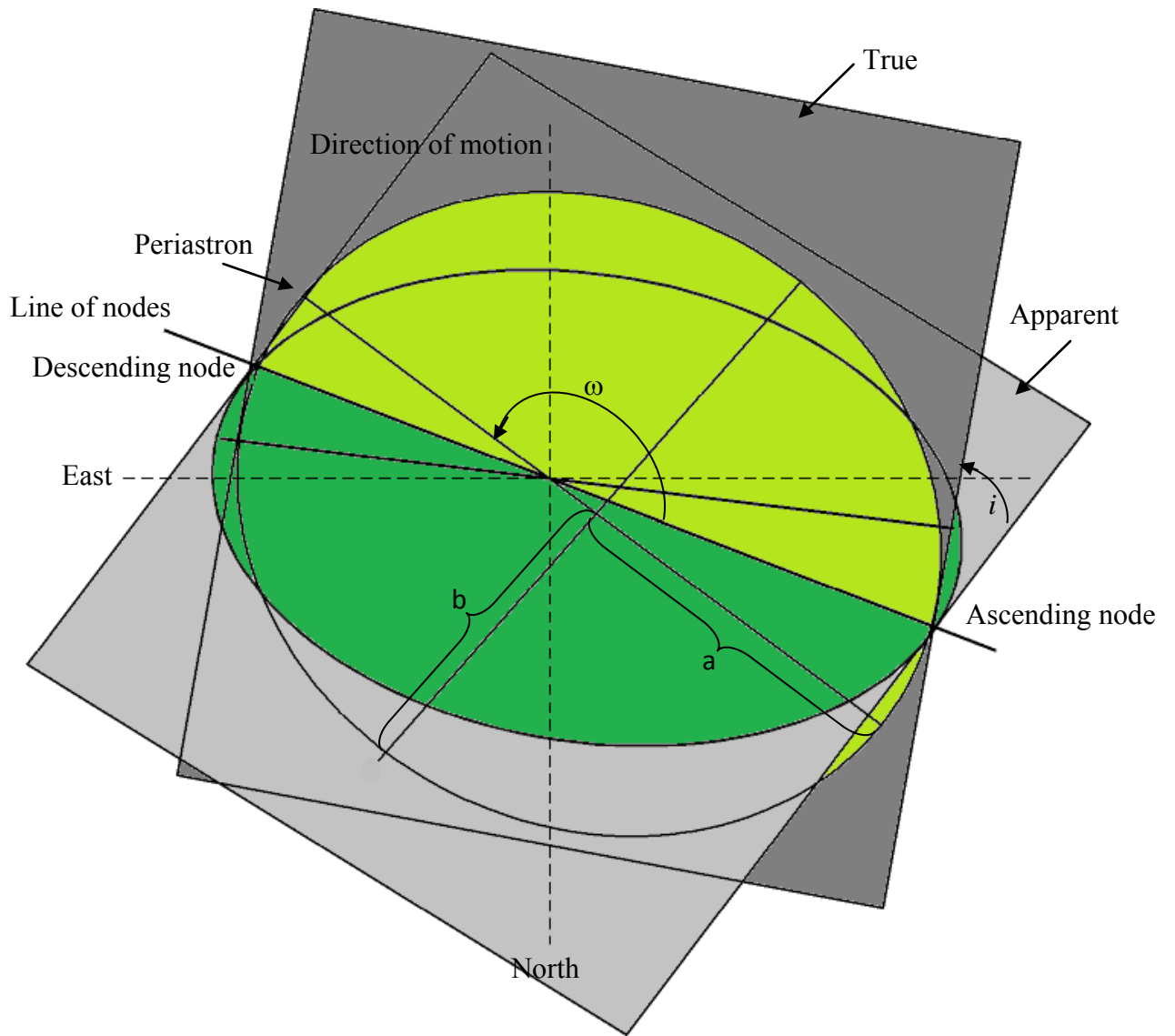
Figure 3.1 Orbital parameters of a binary star.
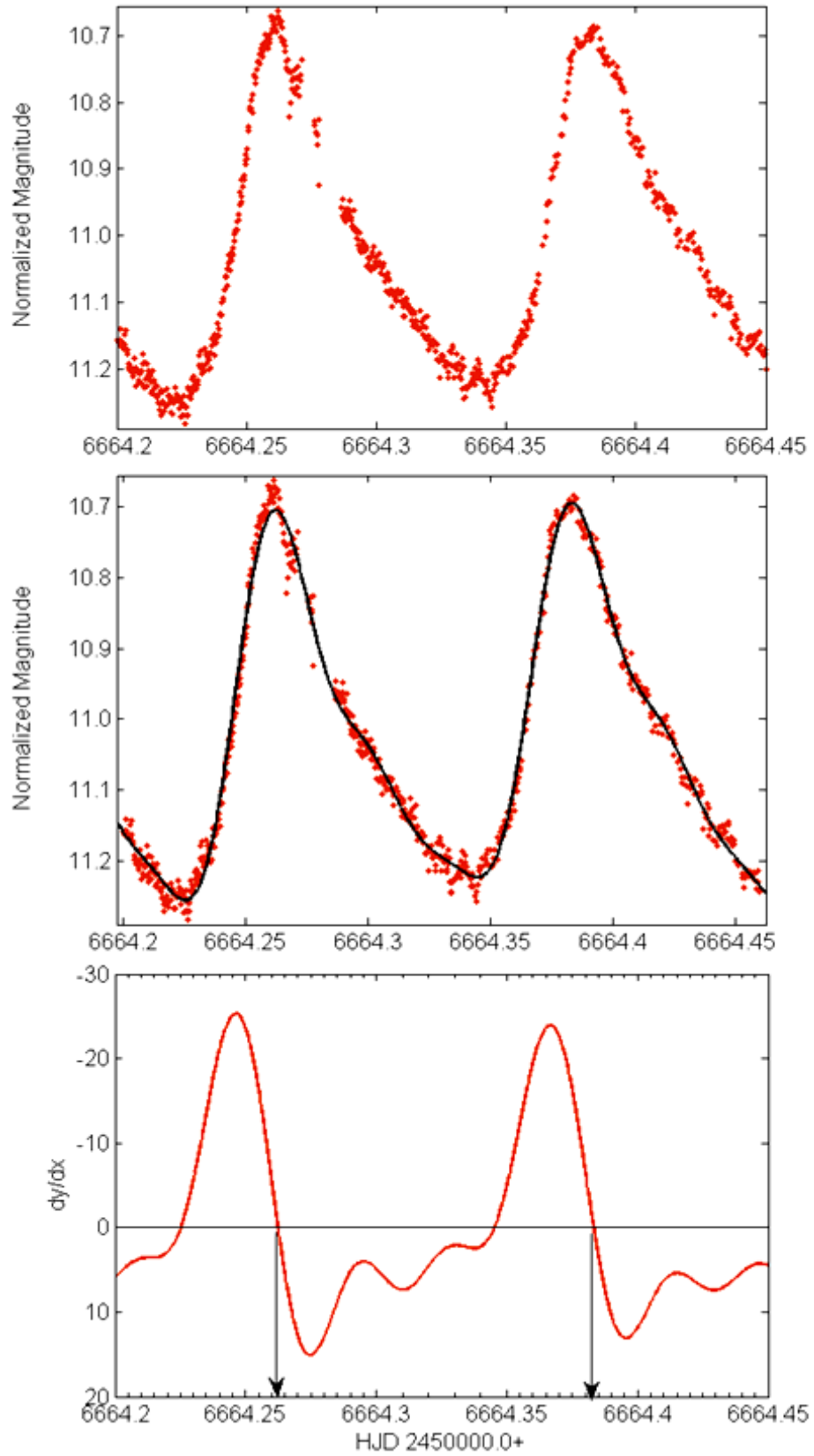
Figure 3.2 Top panel: Part of V band light curve of SZ Lyn. Middle panel: Smooth spline function fitted to the light curve. Bottom panel: The first derivative of the spline function with the determined times of light maxima (arrow marks).

47

3.2.1 O – C analysis

The ephemeris given by Paparo et al., (1998) in equation 3.5 was used to calculate the calculated times of light maxima (C). The number of cycles, E, were taken from equation 3.5 for the observed times of light maxima (T_m) and assuming pulsation period 0.12053492 days. These calculated values were converted to integers to represent the cycle number. Thereafter calculated times of light maxima, T_{max} which is denoted by 'C' were taken from equation 3.5 by feeding the corresponding number of cycles which are calculated using the observed T_{max}.

$$T_{max}\ (HJD) =\ 2438124.39955 + 0.12053492E \qquad\qquad 3.5$$

Finally, the differences of observed and calculated times of light maxima were calculated and denoted as O – C. The O – C value against the cycle number E is shown in Figure 3.3.
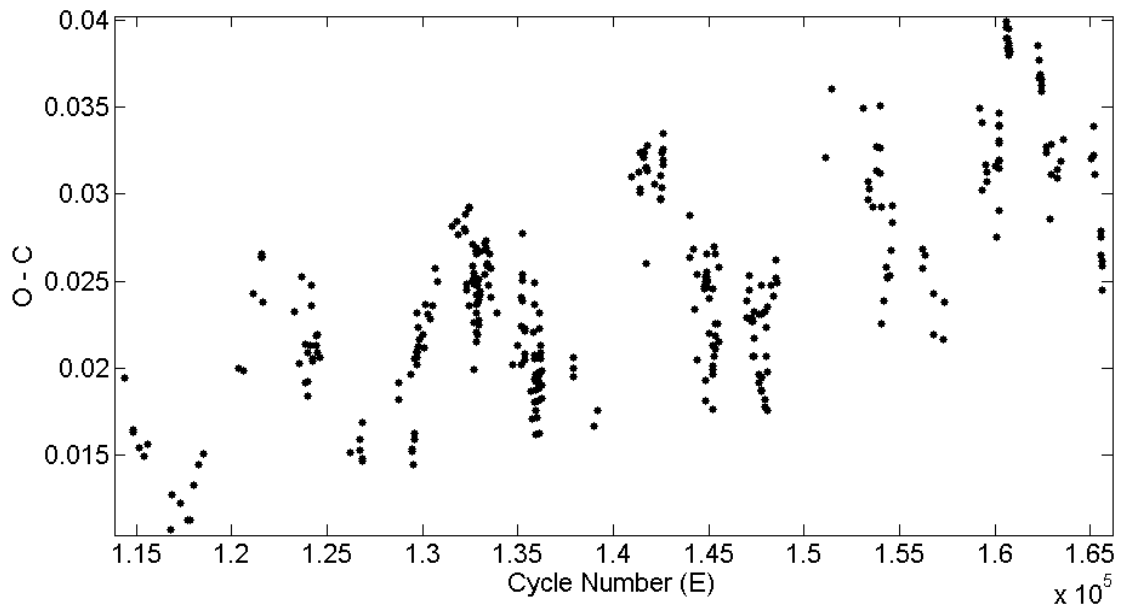
Figure 3.3 Difference of times of observed and calculated light maxima. (O – C) diagram of SZ Lyn

The O − C in Figure 3.3 is non linear distribution with an overall increase in O − C on top of a local variation. The non linear behavior implied that there is a countable effect of light travel time in the binary orbit of SZ Lyn (Irwin, 1952) as well as change in pulsation period. The overall increase is due to the change in pulsation period which is given by quadratic equation in 3.3. The local variation is a sinusoidal function which is given by the light travel time effect of the binary orbit in equation 3.4. The combination of these two effects with the ephemeris is represented in equation 3.2. Therefore the equation 3.2 provides the orbital parameters through non linear least square fitting to the O − C variation.

3.2.2 Non – linear curve fitting

The O − C diagram clearly shows that the O − C variation is not constant and it is non-linear. Therefore, ephemeris in equation 3.1 is inadequate to explain the variation of O − C. The terms in equation 3.3 and 3.4 are additionally needed to explain the variation of O − C. The exponential term (κ) in equation 3.3 explains the overall increase of the O − C variation and the light travel time effect (τ) along the binary orbit in equation 3.4 results in the sinusoidal variation. In order to fit the difference of observed and calculated times of light maxima, the equation of O − C should include the correction values of T_o and P denoted by δT_o and δP respectively. Therefore, O − C equation should be;

$$O - C = \delta T_0 + \delta PE + \kappa + \tau \qquad 3.6$$

The light time travel effect of equation 3.4 is a function of eccentric anomaly (E*) which is shown graphically in Figure 3.1. The eccentric anomaly should be converted to the common independent variable of cycle number (E) in equation 3.6. Therefore the equation 3.2 was transformed to the independent variable (E) using equations 3.7 and 3.8.

$$M = E^* - e \sin(E^*) \qquad 3.7$$

$$M = \frac{2\pi}{P_{orbital}} (T_{max} - T) \qquad 3.8$$

Where M is mean anomaly, $P_{orbital}$ is the orbital period of SZ Lyn, and T is the time of passage through the periastron where E* is zero. Equation 3.7 is known as Kepler equation and must be solved iteratively. In this iterative process, for the limit of zero eccentricity, e becomes zero and the equation simplifies to M = E*. The recursive expression is iterated to the third order approximation to fit the observation and obtained the minimum root mean square error as shown in Figure 3.4.

The parameters determined by Li Lin-Jia et al., (2013) given in Table 3.2 with the ephemeris given in equation 3.5 were used for initial calculations and estimations of δT_o and δP.

Table 3.2 Initial parameters of SZ Lyn used for optimization.

Parameter	Value
To (HJD)	2438124.39849
P (days)	0.120534908
β (days/cycle)	2.73×10^{-12}
a sin (i) (au)	1.002
e	0.17
ω (degrees)	117.6
P_{orbit} (days)	1182
T (days)	2445786.4

The optimization tool, lsqcurvefit, in MATLAB with two algorithms, 'trust-region-reflective' and 'Levenberg-Marquardt', was used iteratively to converge the solution. Equation 3.6 was fitted to the data points in the least square sense as shown in Figure 3.4 using lsqcurvefit solver. Two different optimization techniques given in Table 3.3 determine the orbital parameters.

The values of δT_o, δP, P and T were fixed as 0.001, 2×10^{-9}, 0.12053491 and 2454786.4 respectively. $a$sin (i), eccentricity (e), longitude of the periastron passage (ω), orbital period ($P_{orbital}$) and secular change (β) were considered as coefficients in the non-linear equation. In the lsqcurvefit approach, the initial values for those coefficients were assigned and the solution was converged to the minimum value of χ^2, 0.0022, in both algorithms mentioned in Table 3.3. Figure 3.4 shows the

approximation of the equation 3.6 to the observations. The least square minimization of orbital and pulsation parameters are given in Table 3.4.

Table 3.3 Optimization parameters of *lsqcurvefit*

Algorithm	Trust-region-reflective	Levenberg-Marquardt
MaxIter	5000	5000
TolFun	4×10^{-18}	4×10^{-18}
TolX	1×10^{-17}	1×10^{-17}
MaxFunEvals	5000	5000

Table 3.4 Refined orbital and pulsation parameters of SZ Lyn

Parameter	Trust-Region	Levenberg- Marquardt
Status of Convergence	Local minima possible	Local minima found
χ^2	0.0022	0.0022
a sin(i) (km)	$(1.4\pm0.1)\times10^8$	$(1.4\pm0.1)\times10^8$
e	0.17 ± 0.05	0.18 ± 0.07
ω (degrees)	106 ± 11	106 ± 5
β (days/cycle)	$(2.4\pm0.4)\times10^{-12}$	$(2.2\pm0.2)\times10^{-12}$
P_{orbit}(days)	1186 ± 15	1187 ± 15

The least square fitting of the Levenberg-Marquardt (L-M) algorithm is more successful over the Trust-Region algorithm since the L-M reached the local minima. Therefore, the orbital and pulsation parameters found using L-M algorithm is more appropriate to represent SZ Lyn.

The errors of the coefficient were estimated by the *nlparci* function in MATLAB. The parameters, residual, lambda, and Jacobian (J) produced by *lsqcurvefit* function were fed into the *nlparci* function to get the 95% confidence intervals of the coefficients, which are given as the *ci* matrix.
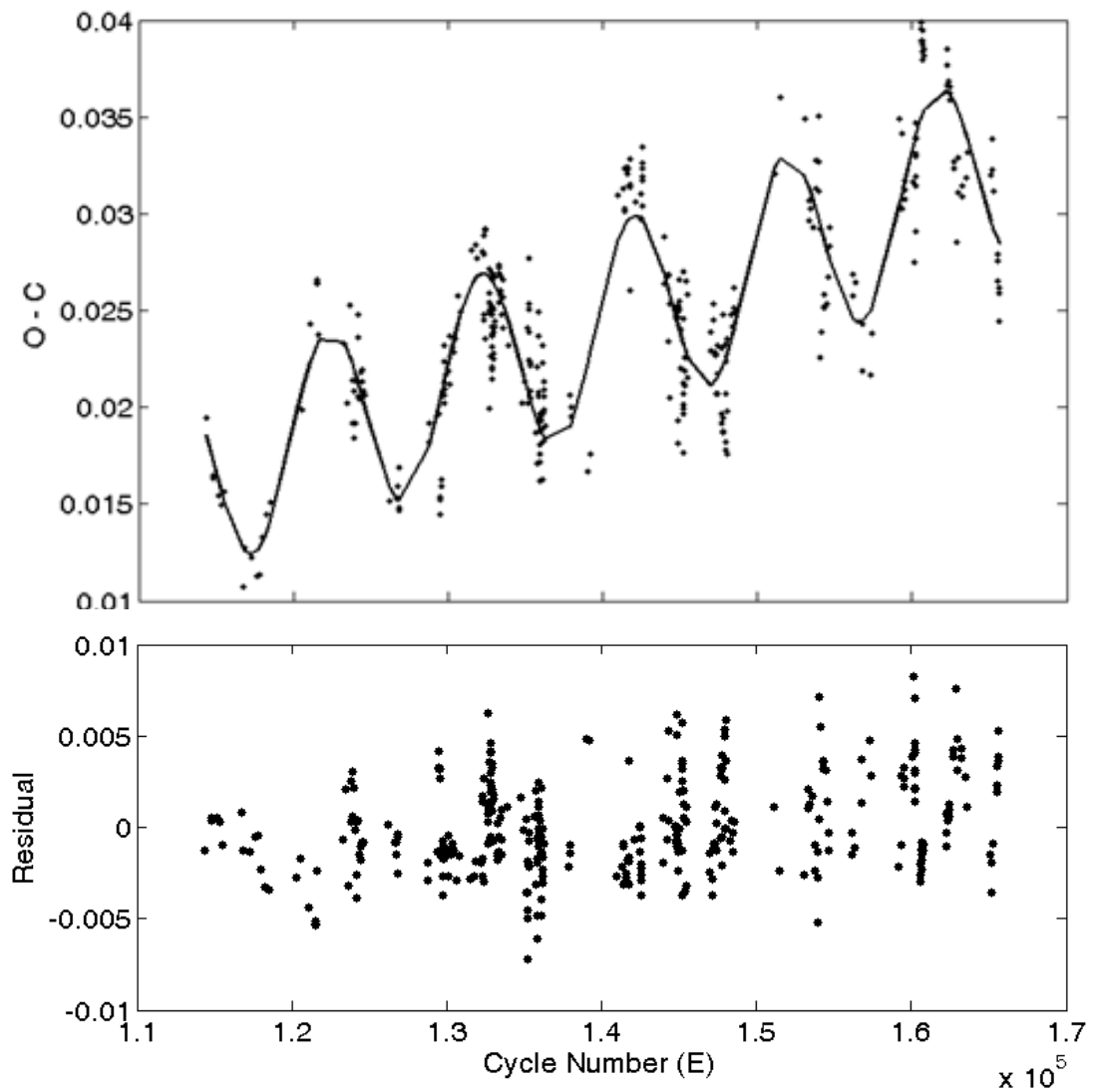
Figure 3.4 Upper: The least square fitting of equation 3.6 to the O − C. The continuous line is the best fit showing the secular change of the pulsation and the light travel time effect of the binary system. Lower: Residuals of the fitting and O − C.

3.3 Pulsation analysis of SZ Lyn

The pulsation analysis of any star highly depends on the detection of frequencies in their power spectra. Light curve analysis has been used and continues to excavate many more frequencies hidden among the significant modes and artifacts. Due to the observation limitations of non-availability of long time base observations and multisite observation, the frequency detection has limitations due to low S/N ratio and severely affected by frequency artifacts such as daily aliasing in the frequency spectra. To overcome these observational limitations, the Delta Scuti Network (DSN) was found in 1983 by Michel Breger. This is a collaboration of astronomers from all around the globe who observe and study short period variable stars. The collaboration produced successful results on few Delta Scuti stars, FG Vir (Breger, et al., 2005), 44 Tau (Breger, M. and Lenz, P., 2008) and 4 CVn (Breger and F. Hiesberger, 1999).

Past investigations of the pulsation stars were limited so that the SZ Lyn was also identified as a pure radial pulsator through observations with a fundamental pulsation frequency of 8.296 cycles per day (d^{-1}) and its few harmonics (Gazeas et al., 2004). Generally, the Delta Scuti stars show radial and non-radial pulsations in p-modes (Breger & Montgomery, 2001). These non-radial pulsations are mostly overwhelmed by the high amplitude radial nodes and identify as low amplitude, sometimes as very weak signals undetectable unless long time-based continuous observations are carried out. Therefore, for ground-based observations, multi-site campaigns are necessary with a coordinated observation. In this thesis, the data of SZ Lyn were collected from three ground-based observations and subjected to pulsation analysis. Fortunately, to fill up the gaps of ground-based analysis, the space mission, Transient Exoplanet Survey Satellite (TESS) also observed SZ Lyn recently and provided high-quality continuous data set which is necessary for asteroseismology. The technical information and data of these space and ground-based observatories are included in Chapter 2 under instruments and observations. A comprehensive log of space and ground-based observation of SZ Lyn is given in Table 3.5. The corrected and validated ground and space-based data discussed in Chapter 2 were comprehensively analyzed for the pulsation frequencies in this section.

Table 3.5 Summary of ground and space based observation of SZ Lyn. The TESS data is Barycentric Julian Date (BJD). Note the difference of duty cycle in ground based data and space based data of TESS. The columns of observation and effective nights are not parallel with other lines.

Observatory	Observation date HJD (2450000.0+)	Effective nights	Band	Effective hours	Number of data points
Mount Abu	6639.104	7	B	29.2	4328
(India)	6640.152		V	28.9	4569
	6664.134		R	55.3	6836
	6684.118				
	6686.172				
	6693.097				
	7705.135				
APT	7480.634 - 7515.688	24	U	50.1	701
(USA)			B	51.4	688
			V	52.5	672
WASP	4190.366 – 4575.408	39	400 – 750 nm	216.0	2894
(UK)					
TESS	8842.503 – 8868.827	25 (days)	600 – 1000 nm	631.8	16550

3.3.1 Frequency Analysis

The whole concept of asteroseismology depends on the frequency spectra of pulsating stars. Most of the pulsating stars oscillate simultaneously in the fundamental and first overtone radial modes. For the Cepheids, the ratio of the first overtone period to the fundamental period (P_1/P_0) is 0.71; for the Delta Scuti stars, 0.77 (Aerts et al., 2010) and the RR Lyrae it is 0.75 (Molnar et al., 2012). These period ratios drastically differ with an organ pipe of 0.33 and a taut string of 0.5. This profound difference is the beginning of asteroseismology, looking at the interior of stars by analyzing frequencies. The larger ratios in the Cepheids and Delta Scuti stars are a direct consequence of the sound speed gradient within them. These variations of the sound speed are produced by temperature, pressure, chemical composition gradients. The aim of asteroseismology is, for any star, to detect enough frequencies over the ranges *n*, *l* and *m*. Hence, the interior sound speed may be mapped with a high precision to determine interior and exterior properties of the star. A step along the way is to resolve sufficient frequencies in a star, and identify the modes associated with them unambiguously.

Accurate filtering of the stellar frequencies in the crowded frequency spectrum is time consuming and needs to handle carefully to determine the stellar parameters. Therefore, a detailed explanation of frequency analysis discussed, covering different techniques and all aspects of available tools in time series analysis. The statistical time series analysis is well established and used successfully (Bloomfield, 2004; Kendall & Ord, 1990), but in the case of data analysis in pulsating stars, this is rather complex because of the observation gaps. The observers from the ground affect the daily motion of the Sun, monthly motion of the moon and annular motion of the Earth, etc. These gapped data create frequency aliasing and rising hundreds of unwanted signals in the time series data set when subjected to the frequency analysis. The other limitation of the perfect determination of a set of stellar frequencies is the short observation span in one site. The limited telescope time allocations and unfavorable weather conditions for photometry make the observation span shorter and hence, result in weak power spectra. The SZ Lyn was observed from both ground and space, so that the similarities and differences of the analysis are included in detail under this section.

3.3.2 Discrete Fourier Transformation

The astronomical time series are obviously finite and discrete. Therefore, it is a common practice of extracting frequencies using Discrete Fourier Transform (DFT). However there are limitations and by-products of this process which should be clearly understood when dealing with the frequencies. The real data sets have finite number of data points and the DFT of a time series x(t) can be represented by;

$$F_N(v) = \sum_{i=1}^{N} x(t_i) \exp(2\pi i v t_i) \qquad 3.9$$

where N is the number of data points.

Depending on the number of data points (N) and the available gaps in the time series x(t), the conversion to the frequency domain can be expressed in the Figure 3.5 and Figure 3.6 (Aerts, 2010).Simply, the Fourier transformation implies that the time series, x(t), is represented by alternate sine and cosine functions by breaking the waveform into an alternate representation, characterized by sine and cosines. The Fourier transform shows that any waveform can be re-written as the sum of sinusoidal functions. Therefore, time series in the equation 3.9 can be re-written in the form of;

$$x(t) = A\cos[2\pi(v_1 t + \varphi_1)] \qquad 3.10$$

for which we have observations from $t = 0$ until $t = T$. In that case, the continuous Fourier transform is

$$F(v) = \int_0^T x(t) \exp(2\pi i v t)\, dt \qquad 3.11$$

The function of $|F(v)|$ versus frequency (v) is the periodogram and the shape of the periodogram is represented by;

$$\mathrm{sinc}(x)^2 = \left(\frac{\sin x}{x}\right)^2 \qquad 3.12$$

When T >> $1/v_1$ the, frequencies are well resolved and the width of the sinc(x) function is roughly 1/T. This is sometimes termed the Rayleigh criterion (Aerts, 2010). This means if the observation time is less the width of the frequency peaks of the periodogram is broad and the resolution is reduced.
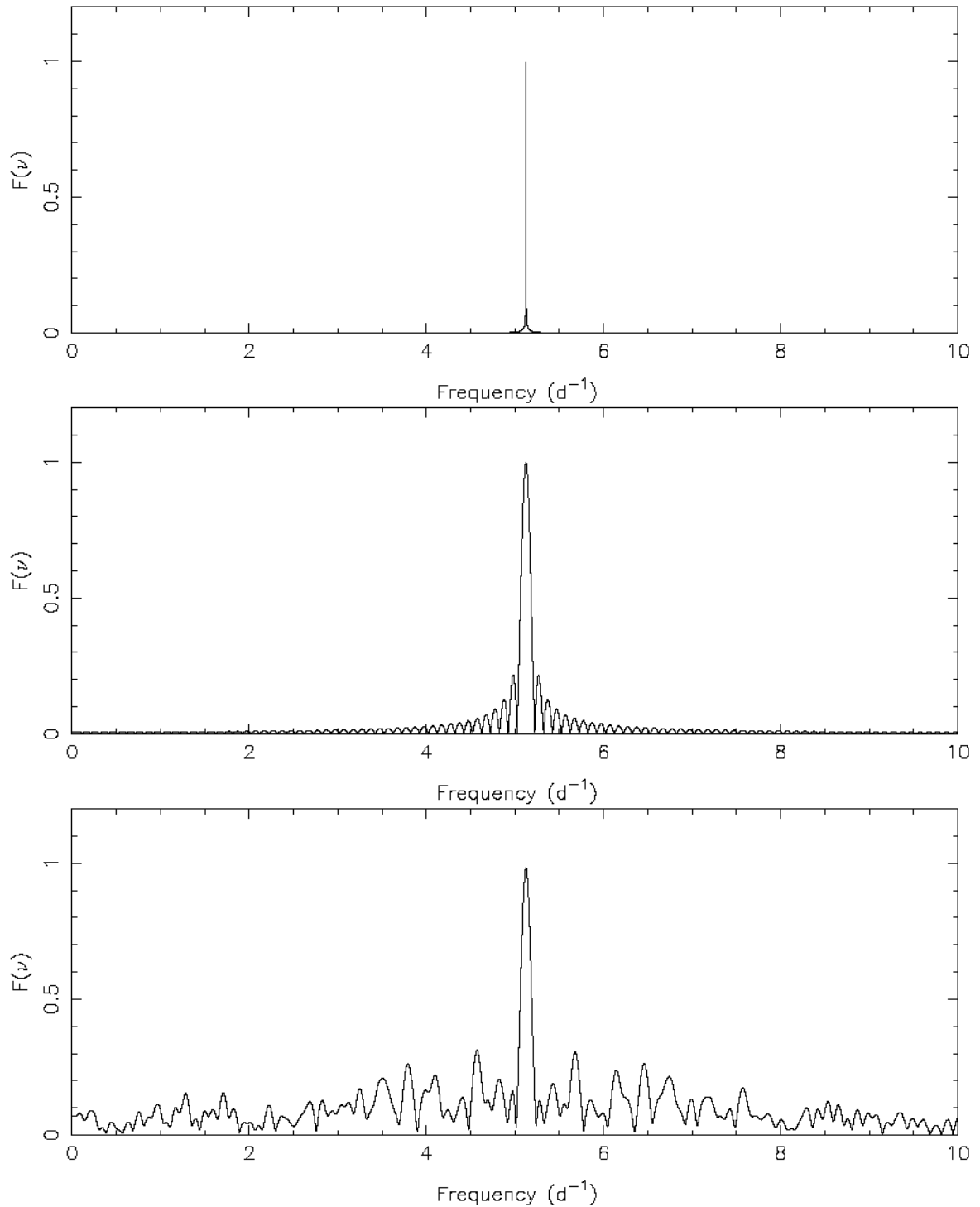
Figure 3.5 Fourier transforms of an almost infinite noiseless time series with 1000000 points spread over 1000 d for a harmonic signal with frequency $v = 5.123456789$ d^{-1} (top), of a noiseless time series with ten thousand points and a finite time span of 10 d (middle) and of a gapped finite noiseless time series with 4472 points and a time span of 10 d (bottom). The image is adopted from Aerts et al., 2010 and reproduced with the permission of Springer.
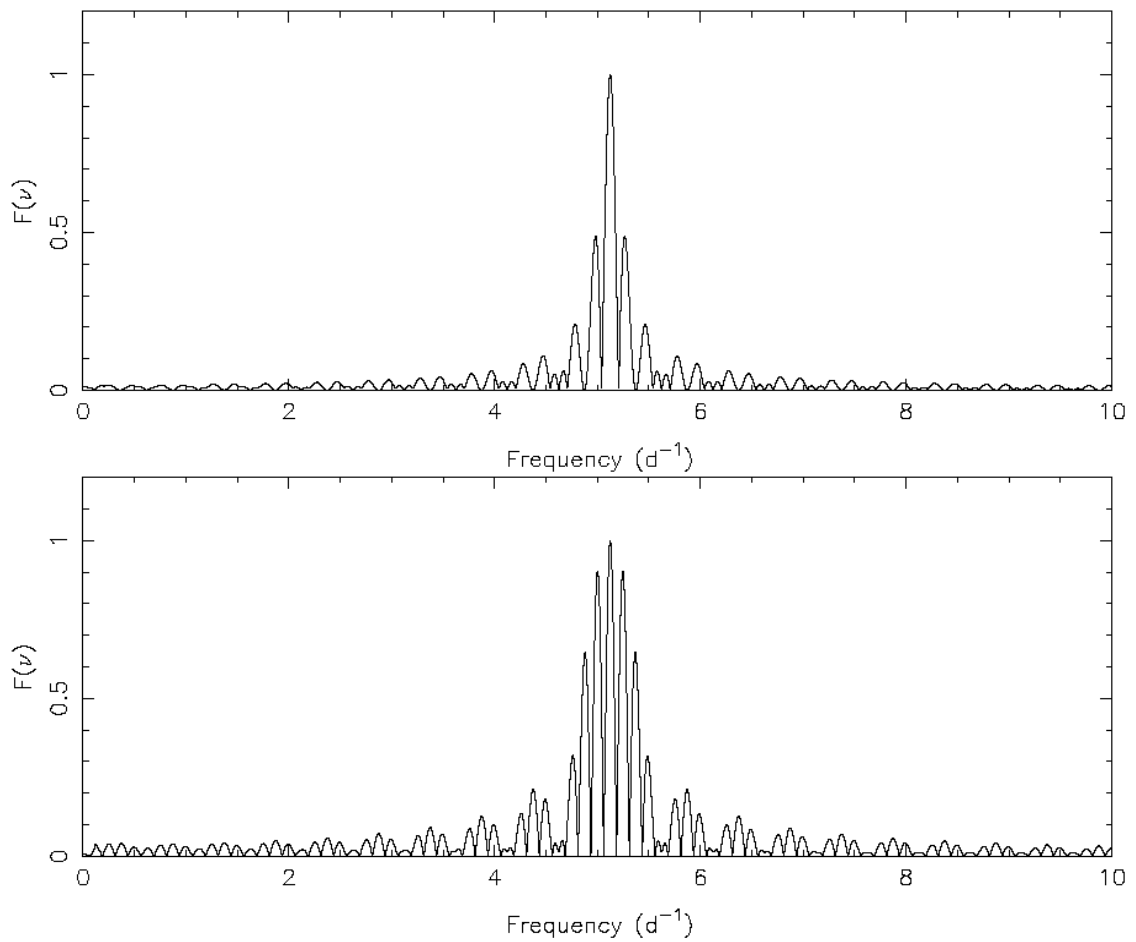
Figure 3.6 Fourier transforms of a noiseless time series of a sine function with frequency 5.123456789 d^{-1} generated for a finite time span of 10 d and containing one large gap from day 4 until day 6 (top) and from day 2 until day 8 (bottom). The image is adopted from Aerts et al., 2010 and reproduced with the permission of Springer.

The dependency of the width of the sinc(x) function on observation span (T) is remarkable in long based continuous observation of TESS data and short period gapped ground based data of SZ Lyn. The Mount Abu data of SZ Lyn is neither long period nor continuous (Table 3.5). Therefore, the resolution of power spectra is limited by the Rayleigh criterion and frequency determination has limitations. On the other hand, the TESS data was continuous and long based which would be able to resolve the frequencies in the power spectra much better than the ground based data. The results were clearly seen in the frequency table (Table 3.7) of SZ Lyn. The difference of this broadening and complexity due to side lobes at a frequency peak of 8.296 d^{-1} (96 μHz) for ground based data (Mount Abu, APT and WASP) and spaced based data (TESS) shown in Figure 3.7.
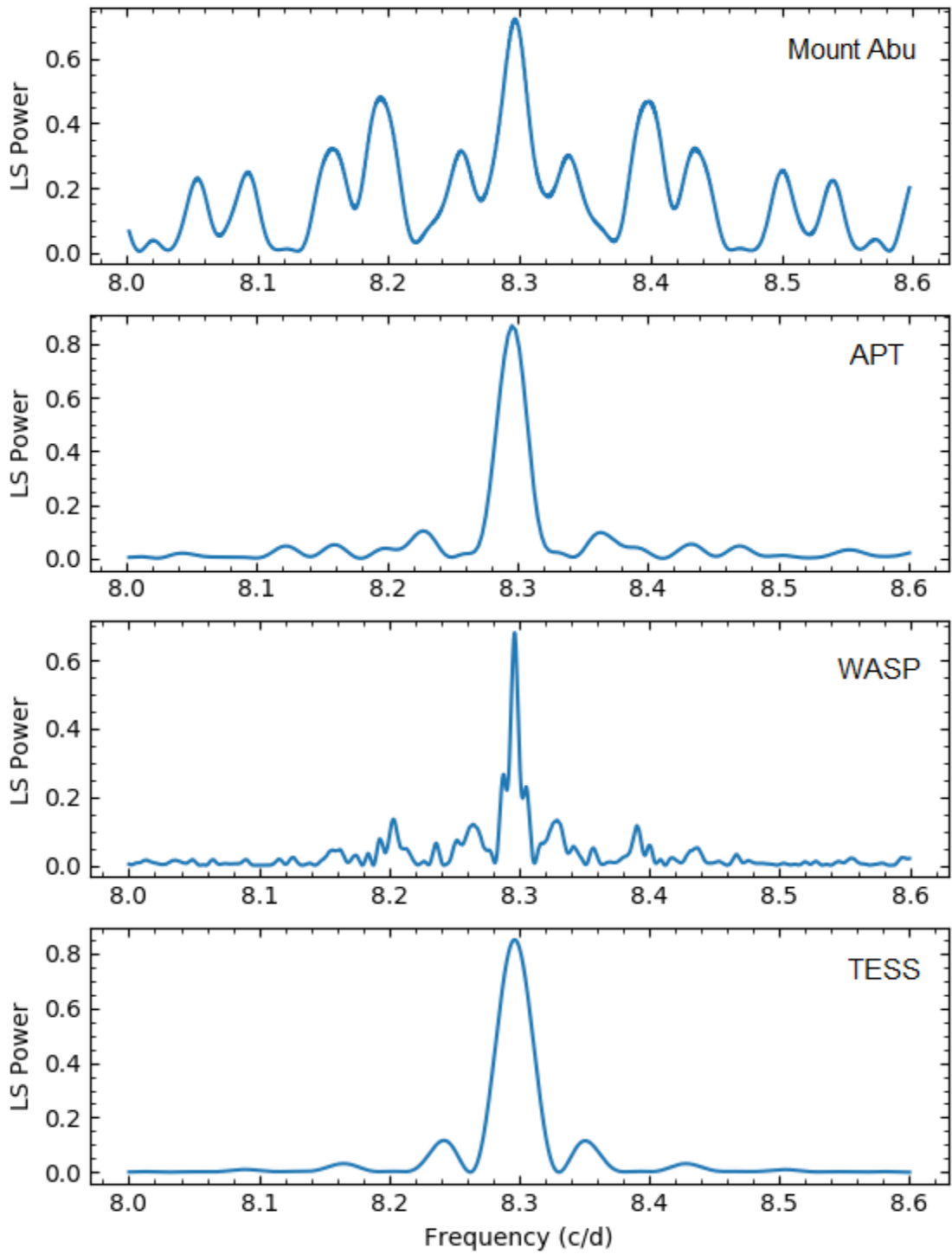
Figure 3.7 The Fourier spectra at the highest frequency of 8.296 d^{-1} (96 µHz) of SZ Lyn. The appearance of side lobes due to the noise and discontinuity of ground based data of Mount Abu, APT and WASP is a drastic difference compared to the smooth profile of TESS data.

3.3.3 Aliasing

The distribution of equally spaced peaks around both sides of a maximum in the periodogram is common in the ground-based time series analysis under DFT. The amplitude of these peaks decreases from the central frequency. This distribution in the power spectra makes it more complicated to distinguish actual stellar frequencies from these artifacts. The arising of these interferences in the power spectra was identified as frequency aliasing which does not correspond to actual frequencies. These maxima, due to noise and time gaps in observations, introduce spurious frequencies in the periodogram. This phenomenon is called aliasing (Aerts et al., 2010).

The difference periodic sources can produce the frequency aliasing. The simulations show certain periodicities in the observation times, such as $\Delta T = 1$ sidereal day, 1 sidereal year, etc., give rise the aliasing frequencies. They identified as one-day aliases, or the daily sidelobes, occurring with intervals of ± 1 d, ± 2 d, ± 3 d and so on when the frequency is expressed in d^{-1}. In ground-based observations, it is obvious that observations have one day gap even a few days of continuous observation. Therefore, light curves of ground-based time series are inherent with gaps of one day. These aliasing are unavoidable spurious frequencies in the Fourier analysis. The effect of this daily aliasing of ± 1 d, ± 2d, ± 3 d around a stellar frequency is clearly seen in the power spectra of SZ Lyn, shown in Figure 3.8.

The data taken from space missions also have some periodic effects such as roll-off to rearrange solar panels, attitude tweaks (García et al., 2011). The periods of these effects are very much higher, usually more than few days so that the frequencies are much smaller than the oscillations of Delta Scuti stars. Therefore, the effect of these aliasing is out of the range of Delta Scuti stars. This was confirmed by no aliasing effect in TESS power spectra of SZ Lyn shown in Figure 3.8.
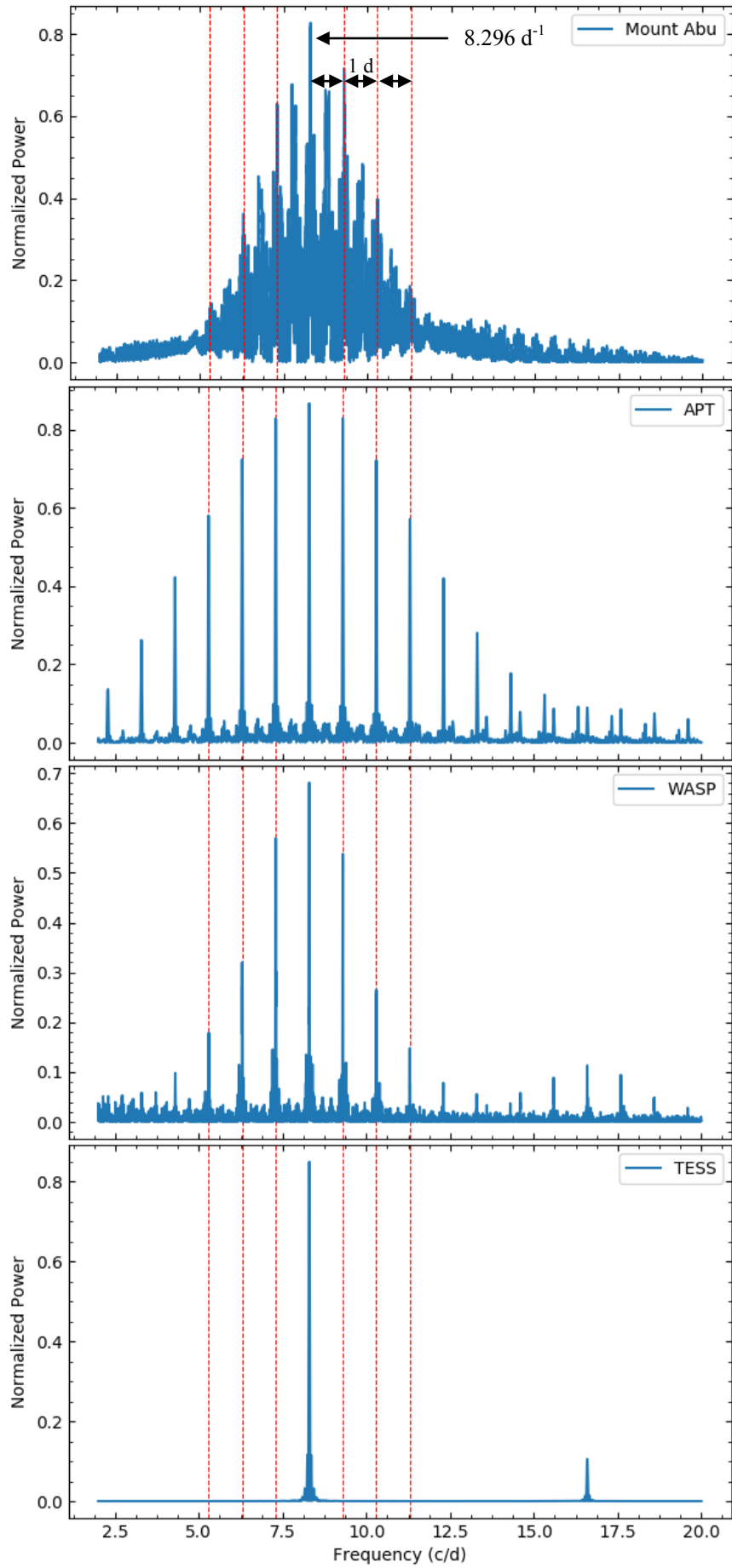
Figure 3.8 Aliasing effect of ground based data. The upper three panels of ground based data show the heavy ±1 d, ±2d, ±3 d and so on of daily aliasing effect around the peak of 8.296 d^{-1}.

62

3.3.4 Nyquist frequency (f$_{Nq}$)

The frequency aliasing is a challenge in asteroseismology because asteroseismology entirely depends on the discovery of true stellar oscillations. The aliasing effect can minimize through a good sampling in Fourier analysis. The procedure is stated simply as follows:

The sampling frequency should be at least twice the highest frequency contained in the signal. $f_s > 2f_m$ where f_s is the sampling frequency and f_m is the highest frequency in the signal. Therefore, the highest frequency of a signal should be derived. The highest useful frequency to search in any given time series is the so-called Nyquist frequency (f$_{Nq}$).

$$f_{Nq} = \frac{1}{2\Delta t}$$

3.13

where Δt is the sampling step in the even spaced data.

The Nyquist frequency is commonly used as an upper limit in frequency when calculating the amplitude spectrum of a discrete data set. The calculation of f$_{Nq}$ for spaced-based observation is easy because of the even spaced data with constant cadence. But, for ground-based observation, this is complex because of observational disturbances due to various atmospheric effects and daily observation gaps. Table 3.6 includes the Nyquist frequencies of the space and ground-based observations used in this analysis.

Table 3.6 The Nyquist frequencies of space based and ground based observations.

Observation	f$_{Nq}$ (d^{-1})
Kepler	
Short Cadence (SC)	723
Longer Cadence (LC)	24
TESS	360
Mount Abu	8640
APT	1080
WASP	1440

Theoretically, the Nyquist frequency is the highest frequency obtained from the Fourier spectrum. The signal-to-noise (S/N) ratio of the frequency spectrum is also a limiting condition which occurs well before reaching the highest frequency by the Nyquist principle. Due to this condition, the frequency searching limit of the frequency spectrum is practically kept well below the Nyquist frequency. The peaks were filtered out from the noise using significant criteria depending on the data set. The S/N level is computed as the average amplitude in a well sampled periodogram of the final residuals and for an appropriate interval in the frequency region where the desired frequency is situated. This level is denoted as σ_{res}. The cut-off is defined as $4\sigma_{res}$ (Breger et al., 1993). This criterion was supported from simulations based on data assembled with the Hubble Space Telescope Fine Guide Sensors and assuming photon-dominated white noise by Kuschnig et al., (1997). For low amplitude stellar peaks present in the amplitude spectrum that can easily distinguishable from noise the detection threshold level is possible to set greater than $4\sigma_{res}$ appropriately. In some cases, the threshold level brings down to a value of $3.5\sigma_{res}$ depending on the presence of very weak peaks of g-mode pulsations. The rotational splitting of the azimuthal modes (m) is also very weakly detected in amplitude spectra so that the reference level should bring down less than $4\sigma_{res}$. The $4\sigma_{res}$ threshold levels of the power spectrum of TESS and Mount Abu show in Figure 3.9.
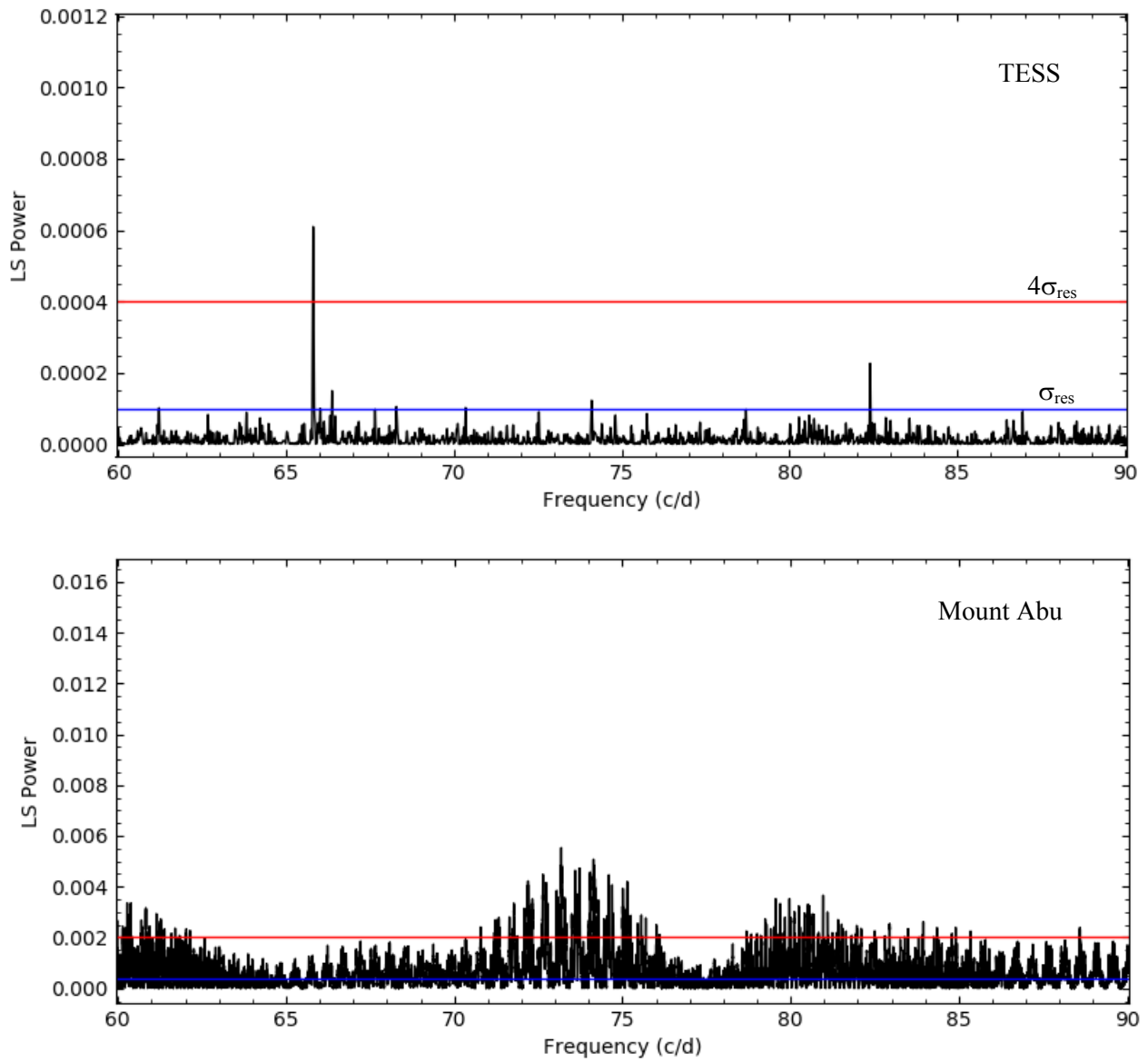
Figure 3.9 The significant level of power spectra of SZ Lyn. The blue line is the noise level (σ_{res}) and the red line is the cut-off level of $4\sigma_{res}$. Note that the cut-off level of space based data is less than the ground based data.

3.3.5 Lomb-Scargle Periodogram

The time series in astronomy is heavily disturbed by observation gaps. The Lomb-Scargle (LS) periodogram is a standard tool in the frequency analysis of unequally spaced data equivalent to least-squares fitting of sine waves. The fitting is a sine waves of the form y = acos(ωt) + bsin(ωt) (Zechmeister and Kürster, 2009). A detailed description of the theoretical background of the periodogram was given by Barning (1963), and also Lomb (1976) and Scargle (1982). While standard fitting procedures require the solution of a set of linear equations for each sampled frequency, the Lomb-Scargle method provides an analytic solution and It is, therefore, both convenient to use and efficient. (Zechmeister and Kürster, 2009). Perform an LS search using VARTOOLS (Hartman and Bakos, 2016) for the light curves for periodic sinusoidal signals and calculate the normalized power, false alarm probability and S/N ratio for each peak. The frequency searching range can be defined by setting the starting frequency, $f_{min} = 1/p_{max}$ and ending frequency, $f_{max} = 1/p_{min}$, with a uniform frequency step-size of $\Delta f = x/T$, where T is the time-span of the observations and x is the free parameter to define the desired sampling rate. The x parameter is useful when we have different data sources with different observation spans of T and need analyze with the same frequency sampling. Under sampling may lose the higher frequencies in the light curve and over sampling would be produced complicated side lobes as shown in Figure 3.6. In addition, over sampling takes more processing time and also very large data files. Therefore, it is an excellent exercise to learn how to optimize the correct sampling rate in the frequency analysis. The output of LS finds the highest amplitude peaks in consecutive order along with log (FAP) (the logarithm of the formal false alarm probability) and the spectroscopic signal to noise ratio (S/N) of each peak. An example of an input command line and its output are given in Appendix C.

The pre-whiten process is essential in this analysis. In principle, the dominant radial mode has the highest amplitude and with this, the minor modes are impossibly seen in the frequency spectra. This influence of dominant mode can be eliminated by applying the pre-whitening process in LS. In this process, the detected highest amplitude signal is removed from the light curve and recomputed for the subsequent frequency. The process is repeated until the specified number of peaks detected. If

whiten were applied, then the signal-to-noise ratio is computed on the whitened periodogram. The output spectrum contains the number of peaks detected successively in the whitened periodograms. The Appendix C encloses the command line inputs and the output files of the pre-whitened periodogram computed in this analysis.

The reduced light curves in Chapter 2 were subjected to LS and DFT using VARTOOLS (Hartman and Bakos, 2016) and PERIOD04 (Lenz and Breger, 2005), respectively. Due to the observation constraints, different instrumental characteristics and different observational parameters at three ground observations of Mount Abu, APT and WASP, the light curves could not be combined to a common light curve and hence, they were all analyzed separately. The LS periodograms produced by VARTOOLS do not give the phase information of the detected frequencies and error information is also not available. Nevertheless, the LS periodograms are normalized to unity (Zechmeister and Kürster, 2009) so that comparison of amplitudes of detected frequencies is easy for three ground-based observations and TESS. On the other hand, DFT of light curves using PERIOD04 provides the phase of frequencies and error estimation of all parameters of frequency, amplitude and phase. Therefore, the LS periodograms and DFT were used in this analysis whenever appropriate.

The uncertainty of the parameters can be determined in several ways depending upon the method used in frequency determination. Generally, the photometric observations provide error estimation of magnitude or flux but not in time strings. Therefore, the uncertainty of frequency, amplitude and phase cannot be easily transformed through the process of DFT or LS. The uncertainty of the parameters can be obtained by error matrix of a least-square calculation, Monte Carlo simulation or using analytically derived formulae. From these three methods, Monte Carlo simulation is widely used in this analysis. The uncertainties of Monte Carlo simulation are reliable compared to other methods as, in principle, it repeats an experiment, in this case, the optimization routine, on almost identical samples. The Monte Carlo simulation in Period04 generates a set of time strings. Each data set has times of the data points which are the same as for the original time strings. The magnitudes of the data points are the magnitude predicted by the last fit plus Gaussian noise. For each data set, a least-square calculation is done and based on the distribution of the fit parameters the

program calculates the uncertainties of the parameters. The higher number of iterations is needed to obtain reliable results. Throughout this analysis, 100 iterations were used (Lenz and Breger, 2005).

3.4 Pulsation frequencies of SZ Lyn

The lowest frequency of a searching range is usually set as zero and the upper limit of the range is theoretically equal to the Nyquist frequency. For the observations of SZ Lyn in ground and space, the Nyquist frequencies are listed in Table 3.6. In principle, the frequency 360 d^{-1} for the TESS is the upper limit of frequency search but practically, the Delta Scuti stars show very high frequencies in their frequency spectra (Breger & Montgmery, 2000). In addition, the S/N ratio drops very much due to the gaps of ground-based data in higher frequencies so that the upper limit of the frequency range is ideally very much below the Nyquist frequency. Hence the frequency range of SZ Lyn was set to 0 to 120 d^{-1} throughout this analysis. Figure 3.10 shows a part of four data sources in the left panel and the corresponding power spectra of the data. The power spectra of three ground-based data are heavily affected by ±1 d aliasing around the central peak of 8.296 d^{-1}, whiles the TESS, is a clear single peak without side lobes. Figure 3.10 shows the significance of the effect of high quality continuous data on frequency analysis. Due to the very high amplitude dominant mode the low amplitude modes are not able to be discovered. The application of pre-whitening, removing the dominant component from the light curve and search frequencies again in the residuals is a common practice to discover the minor oscillations. Therefore, pre-whitening enables to detect the prominent frequencies along with other weak modes in the ground based data. The frequencies determine in common for three data sources, TESS, Mount Abu and APT, were shown in Figure 3.11. The frequencies determined using TESS data are shown in Figure 3.12. The detected frequencies of four data sources were tabulated in Table 3.7.
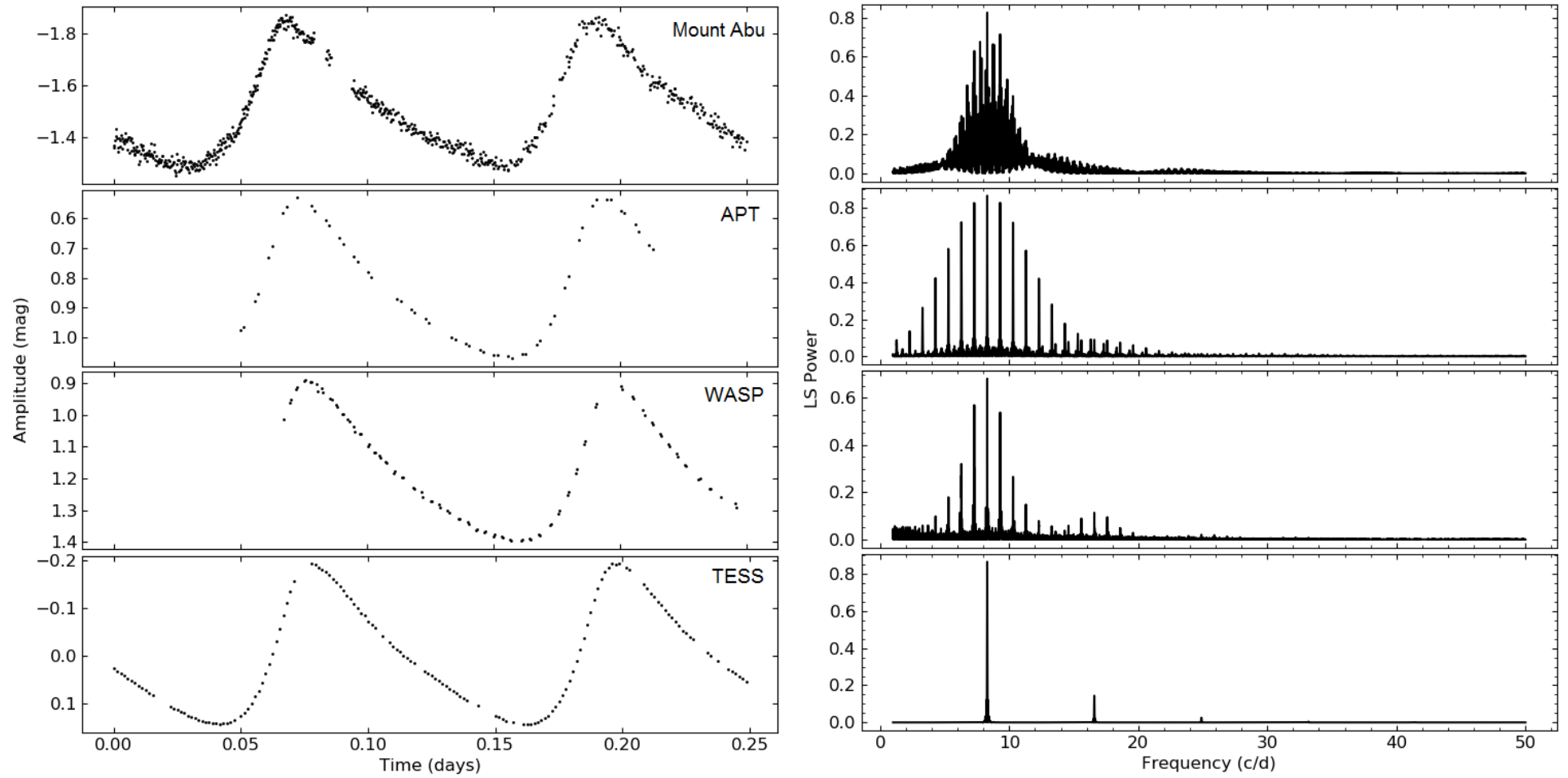
Figure 3.10 Four rows in the left panel show a part of light curves of SZ Lyn of four data sources. The light curves of four sources were brought to a common period of 0.25 days with the available observation phases. Due to the unavailability of common observation phases APT and WASP could not bring to common zero. The right panel shows the corresponding LS power spectra of four data sources in the frequency range of $2 - 50$ d^{-1}. Note that the daily aliasing of ± 1 d distribution around the frequency 8.296 d^{-1} is prominent in ground based observation. The power spectra are not whitening so that other peaks are not notably appeared.
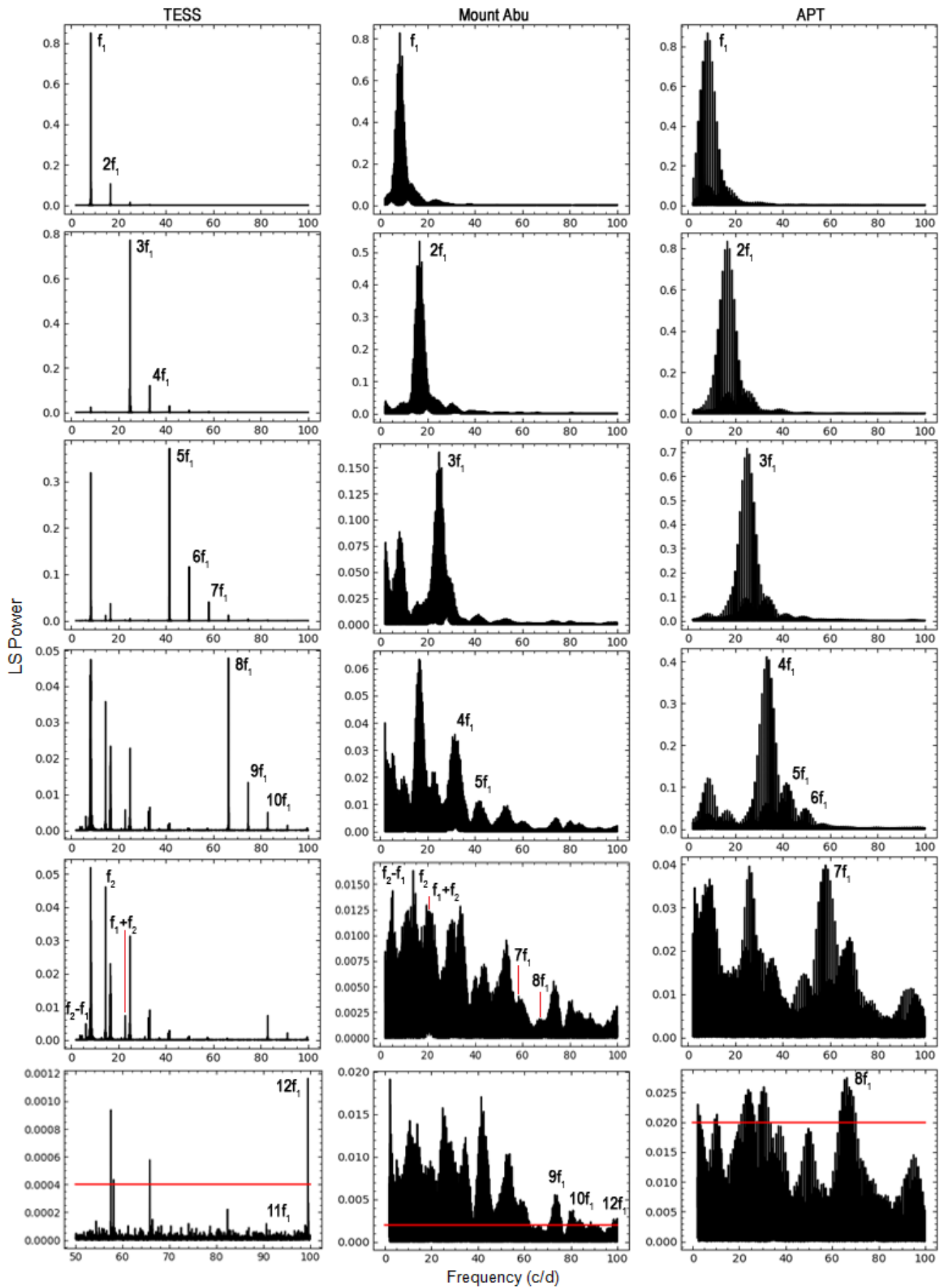
Figure 3.11 The pre-whiten power spectra of SZ Lyn observed in three data sources, TESS, Mount Abu and APT. The WASP is omitted here as it detected only four frequencies. The red line in the last row is the significance level of each data source.

70
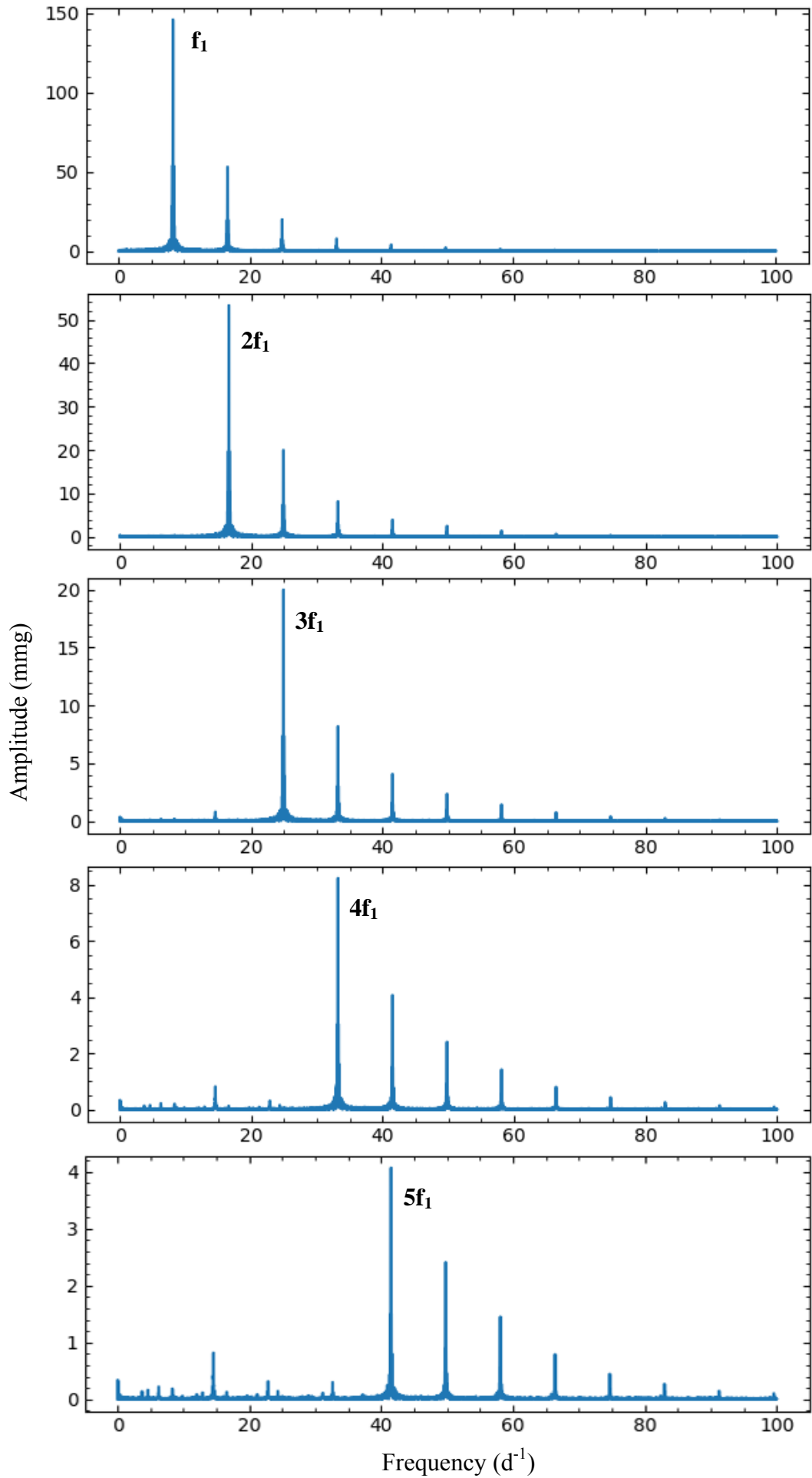
Figure 3.12 Pre-whiten frequency spectra of SZ Lyn using TESS data
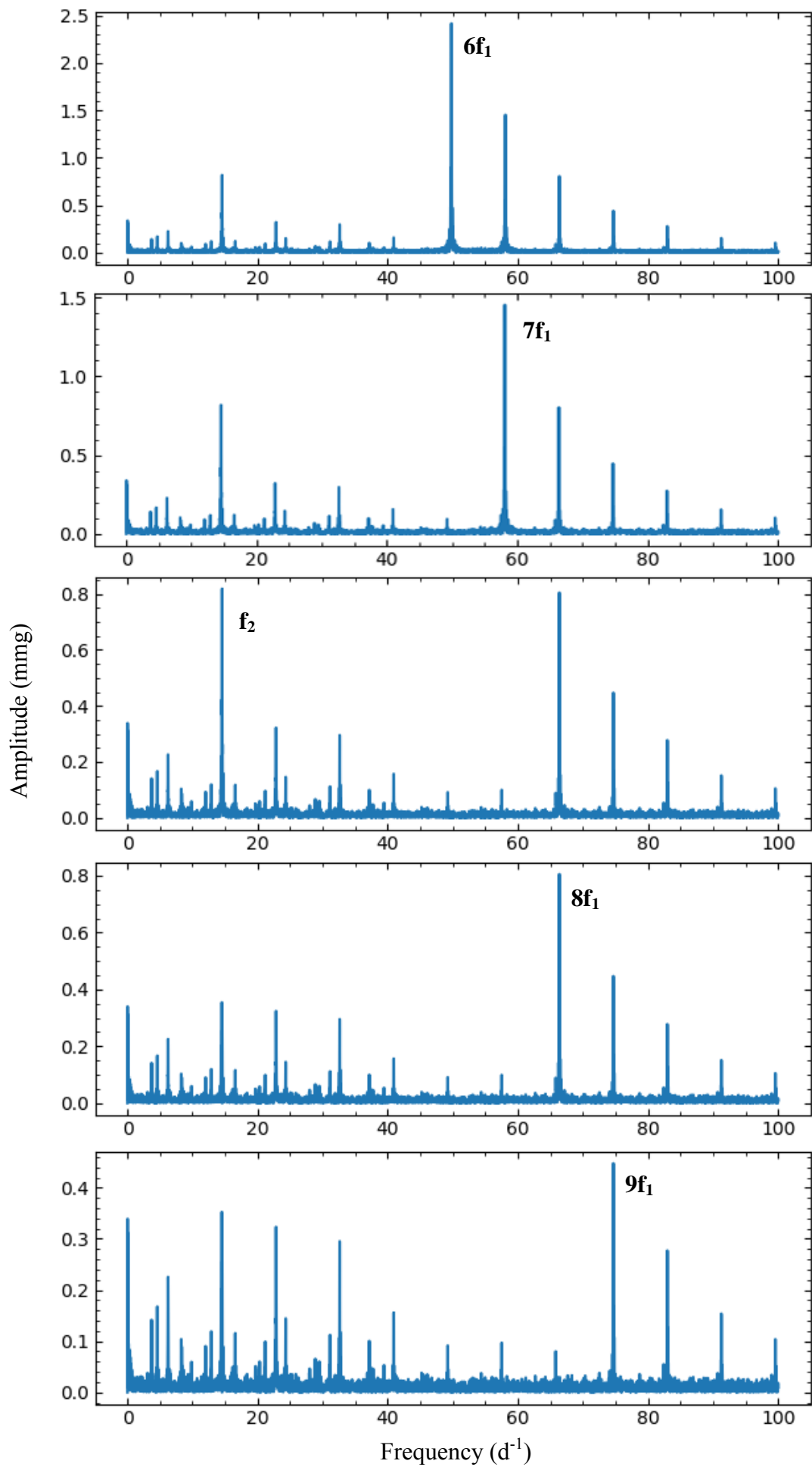
Figure 3.12 Continued.
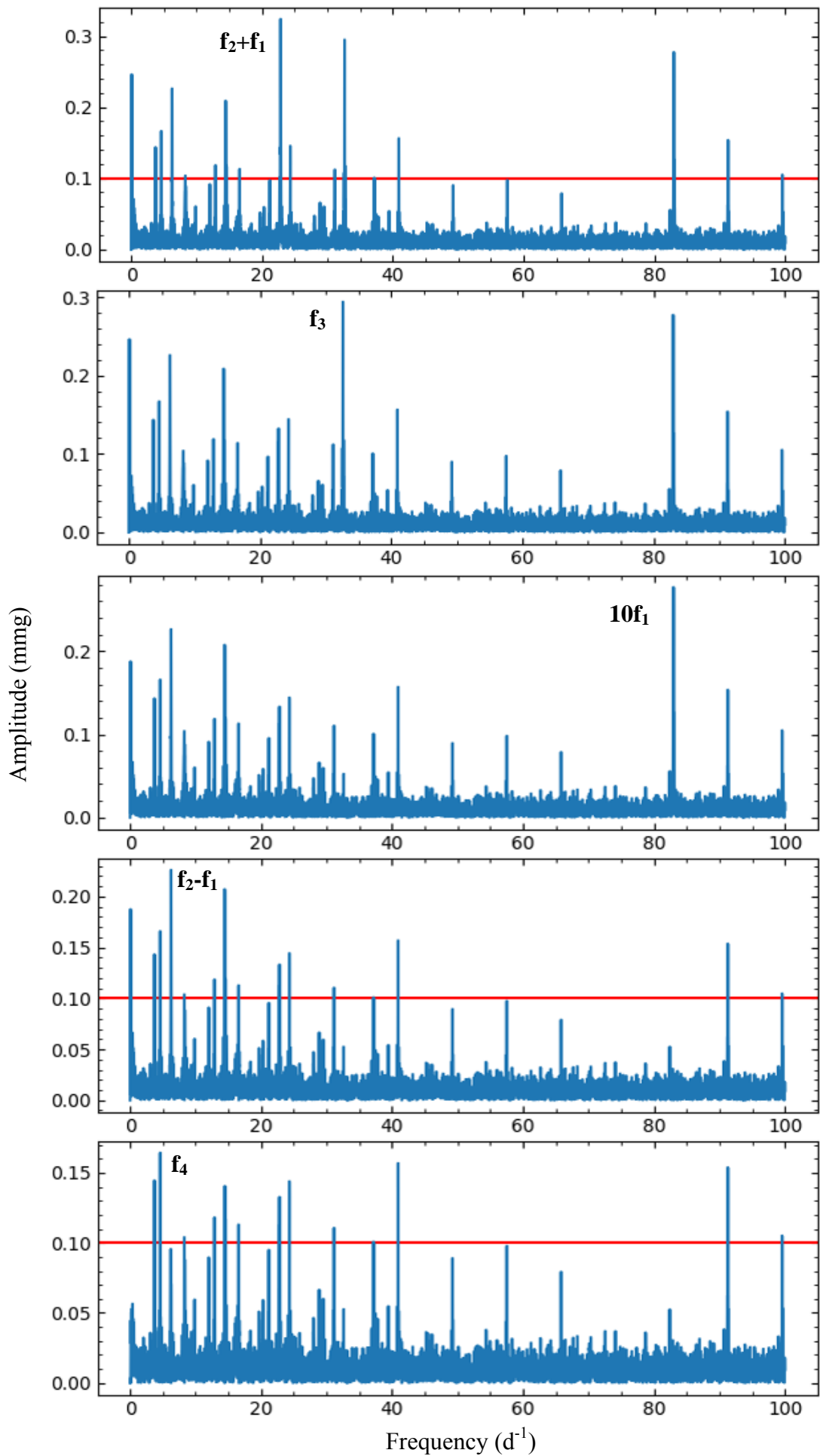
Figure 3.12 Continued. The red line is the $4\sigma = 0.1$ significant level of frequency detection.

73

Figure 3.12 Continued.

74
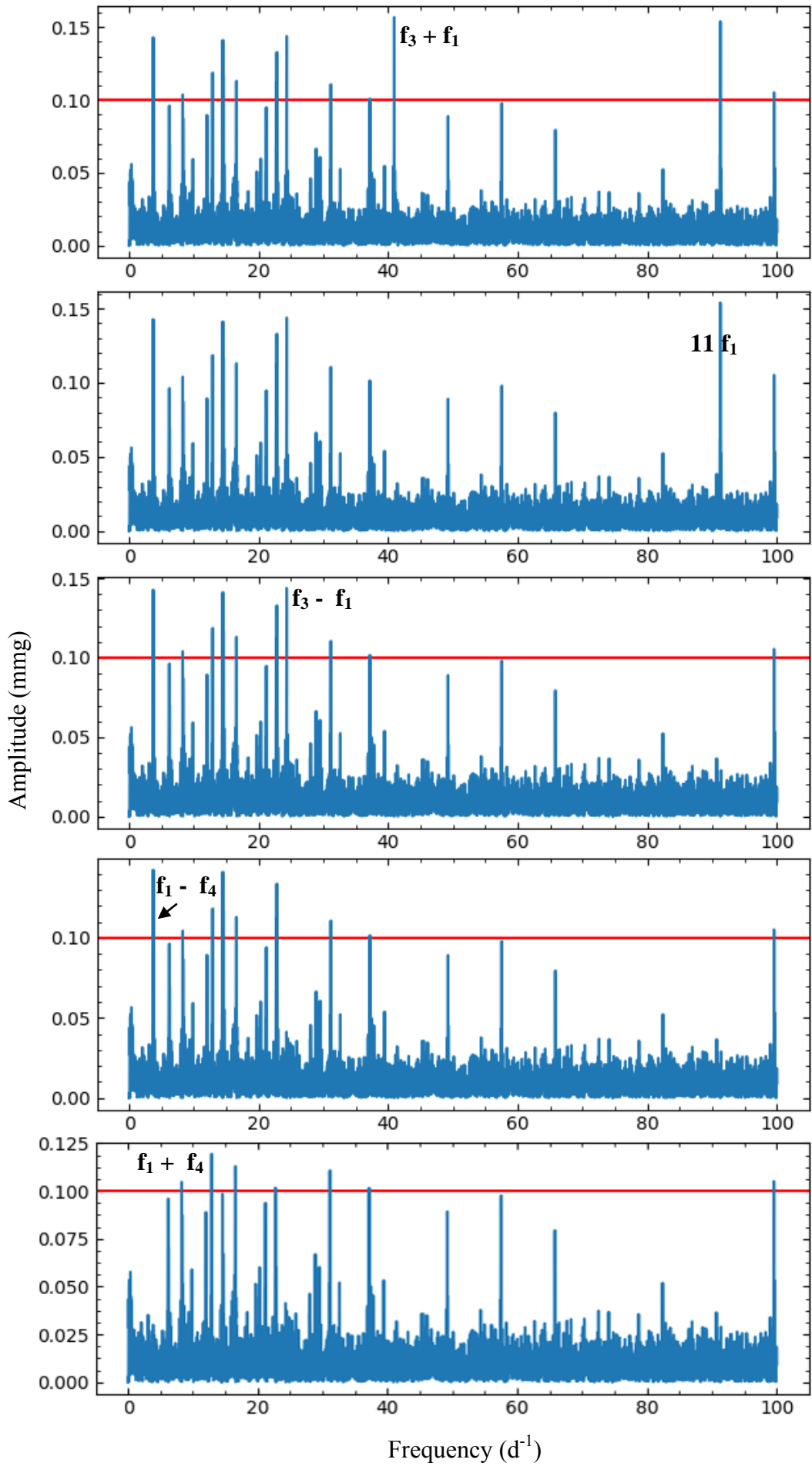
Table 3.7 Frequencies and amplitudes of SZ Lyn. V band data are only shown for Mount Abu and APT. The amplitude is in milli-magnitude. The errors of the amplitudes were obtained by Monte Carlo simulation using Period04. The 4σ threshold limit for TESS is 0.08 which indicates by short horizontal line. The frequencies of V band are shown for Mount Abu and APT.

	TESS			Mount Abu		APT		WASP	
ID	Frequency (d^{-1})	Frequency (μHz)	Amplitude (mmg)	Frequency (d^{-1})	Amplitude (mmg)	Frequency (d^{-1})	Amplitude (mmg)	Frequency (d^{-1})	Amplitude (mmg)
f_1	8.296	96.018	145.850±0.02	8.296	229.0±3.0	8.296	232.0±3.0	8.296	224.0±3.0
$2f_1$	16.592	192.036	53.320±0.01	16.590	76.0±3.0	16.592	82.0±3.0	16.593	76.0±3.0
$3f_1$	24.889	288.065	20.020±0.01	24.890	32.0±1.0	24.889	31.0±1.0	24.890	24.0±1.0
$4f_1$	33.186	384.095	8.220±0.01	33.186	11.0±1.0	33.185	13.0±1.0	33.185	15.0±1.0
$5f_1$	41.482	480.113	4.080±0.01	41.483	9.0±1.0	41.481	6.0±1.0	41.567	7.0±1.0
$6f_1$	49.779	576.142	2.420±0.01	49.849	3.0±1.0	49.777	4.0±1.0		
$7f_1$	58.075	672.160	1.460±0.01	58.065	7.0±1.0	58.157	3.0±1.0		
$8f_1$	66.372	768.190	0.800±0.01	66.365	4.0±1.0	66.339	3.0±1.0		
f_2	14.535	168.228	0.800±0.01	14.221	6.0±1.0				
$9f_1$	74.668	864.207	0.470±0.01	73.120	3.0±1.0				
$f_2 + f_1$	22.830	264.234	0.309±0.008						
f_3	32.620	377.544	0.293±0.008						
$10f_1$	82.965	960.237	0.277±0.008						
$f_2 - f_1$	6.237	72.187	0.223±0.010						
f_4	4.584	53.055	0.164±0.007						
$f_3 + f_1$	40.888	473.238	0.157±0.010						
$11f_1$	91.261	1056.255	0.154±0.009						
$f_3 - f_1$	24.308	281.341	0.144±0.007						
$f_1 - f_4$	3.703	42.858	0.143±0.009						
$f_1 + f_4$	12.880	149.073	0.120±0.006						
$12f_1$	99.564	1152.354	0.105±0.008						
$13f_1$	107.824	1247.955	0.068						
$14f_1$	116.104	1343.788	0.042						

3.4.1 Radial modes of SZ Lyn

The Delta Scuti stars pulsate simultaneously in fundamental radial mode with the first overtone radial mode (Aerts et al., 2010). This fundamental radial mode is prominent and sometimes claims superiority so that the other modes may not be clearly seen in power spectra with this dominant mode. SZ Lyn is a good example of such a pulsator. The radial modes can be identified as $l = 0$ (See Section 1.2.2) and $n = 0$ for the fundamental and n = 1, 2, 3… for the overtones respectively. However, SZ Lyn was identified with a prominent radial mode at the frequency $f_1 = 8.296$ d^{-1} in literature and here in Table 3.7, it was reconfirmed as f_1. The confirmation of this fundamental radial mode was made by simply looking at the highest amplitude of the frequency spectra. The Astroseismic approach has not been used to confirm to the fundamental mode of SZ Lyn until then. Here, the frequency f_1 was subjected to asteroseismic technique and hence proved that f_1 belongs to $l = 0$ mode. In order to confirm that f_1 is a radial mode, several techniques can be used. Among them, the amplitude ratio and phase differences are widely used with the availability of UBVRI photometry data (Balona and Evers, 1999; Garrido et al., 1990). The accuracy of this technique is depending on the availability of high quality continuous UBVRI light curves of the star. For SZ Lyn, the observation of BVR bands at Mount Abu observatory and UBV bands at APT were used for the analysis. The amplitudes of the frequency f_1 obtained for UBV bands for the observational data is shown in Figure 3.13 and the amplitudes and phases were tabulated in Table 3.8. In Figure 3.13, it is clear that the amplitudes of the frequency f_1 in UBV bands are different and the highest amplitude is in B band. Therefore, B band was considered as the reference to compare the amplitude ratios of A_U/A_B, A_B/A_B, A_V/A_B and A_R/A_B where A_U, A_B, A_V and A_R are the amplitudes of U, B, V and R bands respectively. The calculated amplitude ratios and phase differences were shown in Table 3.8. These observational amplitude ratios were used in Chapter 4 to identify the spherical degree l of the frequency f_1.

Table 3.8. Observed amplitudes (A in magnitude) and phases (φ in radians) for the main frequency f_1=8.296 d^{-1} obtained from PERIOD04. Only f_1 is included in the table as this is the only independent frequency available in multi-band photometry of ground based data. The observed amplitude ratios in the middle row were used in Chapter 4. The last row is phase difference in degrees. The phase zero is at 2457480.63391813 HJD.

	U	B	V	R
A	0.275±0.003	0.290±0.004	0.229±0.003	0.171±0.002
φ	0.834±0.003	0.805±0.003	0.803±0.003	
	A_U/A_B	A_B/A_B	A_V/A_B	A_R/A_B
	0.95±0.02	1.00	0.79±0.02	0.59±0.02
	$\varphi_U - \varphi_B$	$\varphi_U - \varphi_V$		
	1.7±0.2	1.8±0.2		
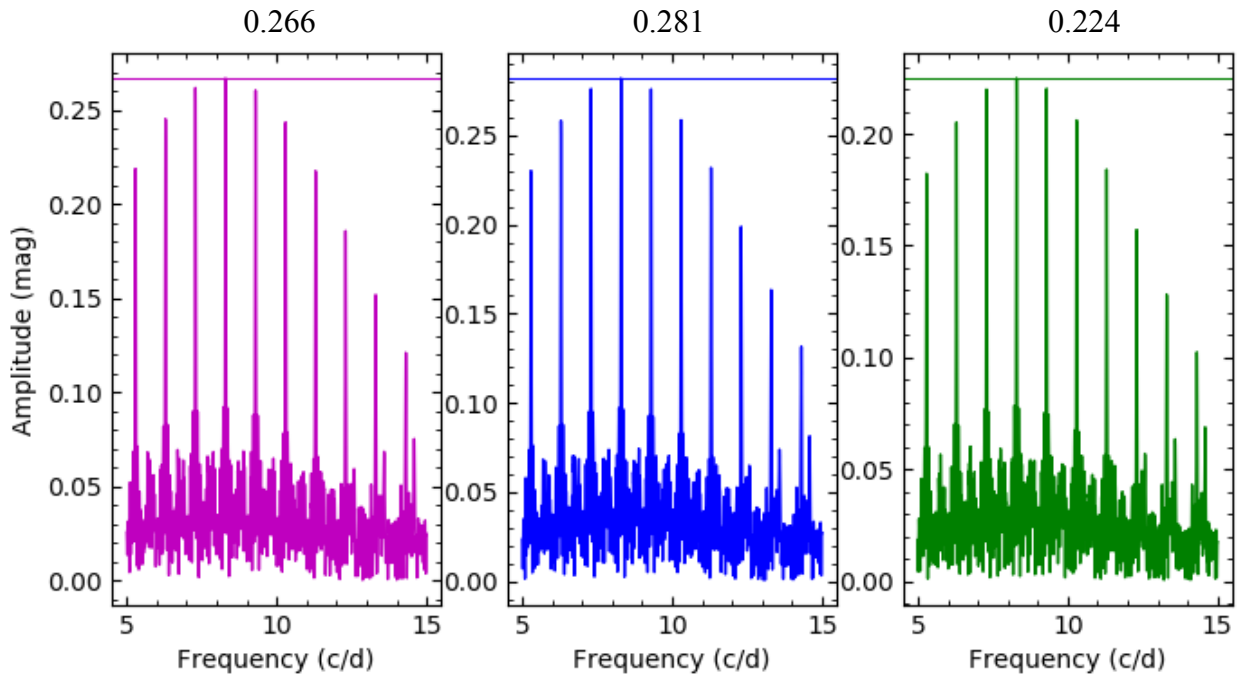
Figure 3.13 Observational amplitudes in magnitude scale for the main frequency (f_1) 8.296 d^{-1} for UBV bands. The colors magenta, blue and green represent the U, B and V bands respectively. The horizontal line and the value on top of each plot show the amplitude of the frequency 8.296 d^{-1}. The equidistance spectral lines of ±1 d^{-1} on both sides of f_1 are the daily aliasing which is highly affected the amplitude spectra.

3.4.2 Harmonics

The frequency $f_1 = 8.296$ d^{-1} (0.12054 days) is the dominant mode of oscillation in SZ Lyn. This frequency was previously observed by Gazeas, et al., (2004); Moffett et al., (1988) and Papar´o (1988). These previous observations were basically focused on the orbital parameters of the binary. As a result, the frequency f_1 found to have undergone a frequency change over the pulsation cycles. This secular change in the pulsation period is in the order of 10^{-12} day per cycle so that even for observation of SZ Lyn in year 2020 from 2004 has encountered roughly 46720 cycles and the change in the period is 10^{-8} days. Therefore, the new observation of f_1 does not make a considerable change in the frequency of both ground and space-based data. The SZ Lyn is identified as High Amplitude Delta Scuti Star (HADS) with this main pulsation frequency (f_1) as the fundamental radial mode. Apart from that, Gazeas, et al., (2004) concluded the availability of two harmonics of the fundamental identified as $2f_1$ and $3f_1$ in Table 3.7. In past literature, these are the only frequencies found in SZ Lyn. In this analysis of space and ground-based photometry, 11 more harmonics of the fundamental were identified and the first 8 of them were clearly seen in Mount Abu and 7 of them in APT and 4 in WASP ground observations. These harmonics are generated by the non-sinusoidal components of the light curve.

This effect can be clearly seen in Figure 3.14 when the light curve is fitted with the set of Fourier components. SZ Lyn has a rapid rise and a more gradual decrease light curve and in the phase of gradual decrease, it shows disturbances in the light curve so that these local peaks are represented by harmonic frequencies of the main oscillation frequency. These harmonics are integer multiples of main oscillation given by $2f_1$, $3f_1$, $4f_1$ etc. in Table 3.7. These harmonics are common in Delta Scuti stars (Breger et al., 2010; Breger et al., 1999; Murphy et al., 2013; Papics et al., 2012). These harmonics are not independent oscillation modes present in the star and the presence of more harmonics in the frequency spectrum makes it more difficult to find out the other independent modes available. Therefore, the fundamental mode and at least few higher amplitude harmonics should be removed before searching the rest of the frequencies. The removal of harmonics of SZ Lyn was performed by applying the *'killharm'* routine using VARTOOLS. In this process, the LS routine was initially applied and the most prominent frequency in the light curve was determined. Subsequently, the predicted harmonics were generated by this prominent frequency

using Fourier analysis. The input and output parameters of '*killharm*' routine are given in Appendex A. The upper panel of Figure 3.15 shows the light curve of SZ Lyn observed at APT. The fundamental frequency, f_1, 8.296 d^{-1} and its first there harmonics, $2f_1$, $3f_1$ and $4f_1$ were fitted with Fourier components and then subtracted the fundamental and three harmonics were subtracted from the light curve to obtain the residual light curve shown in the bottom panel of Figure 3.15. Note that the magnitude of the residual light curve is less than the original light curve. The remaining frequencies in the light curve can be obtained by applying LS or DFT to the residual light curve. The rest of the harmonics of $5f_1$ to $9f_1$ were recovered in Mount Abu data using the residual light curve.
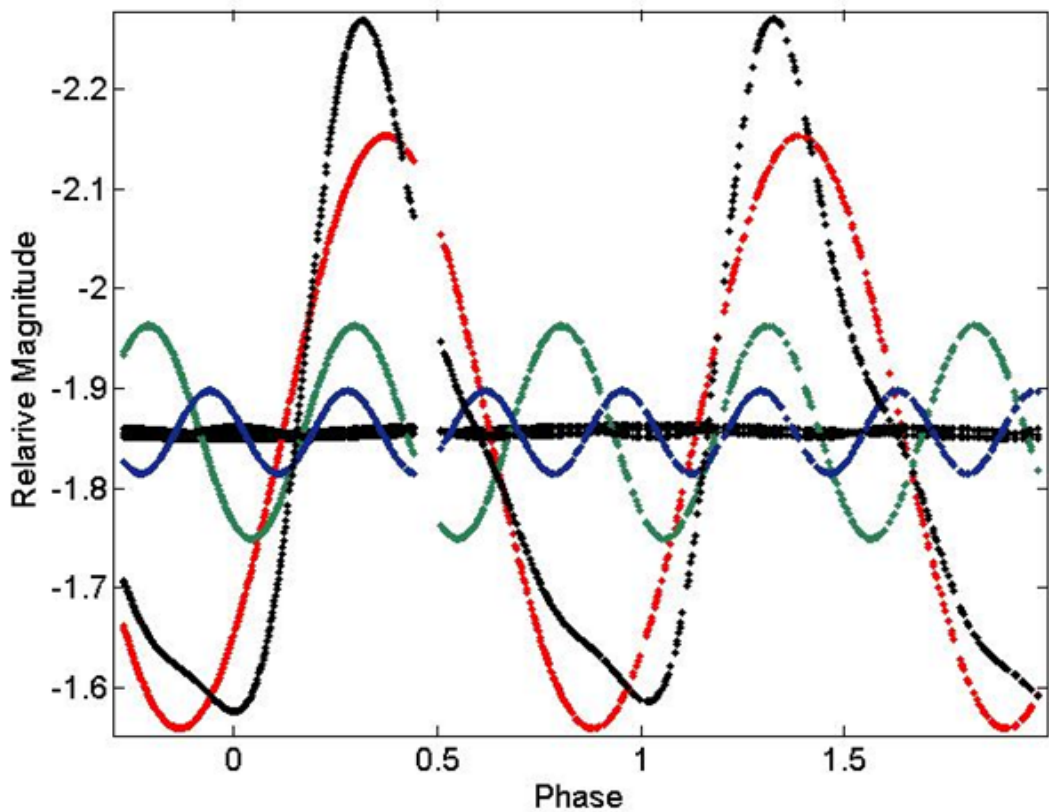
Figure 3.14 Fourier representation of light curve of SZ Lyn. The black dots represent observed light curve of SZ Lyn at Mount Abu. The red dots represent the dominant frequency while green and blue dots are harmonics fitted to represent non-sinusoidal nature of the light curve. The remaining black dots are harmonics of negligibly small in amplitude.
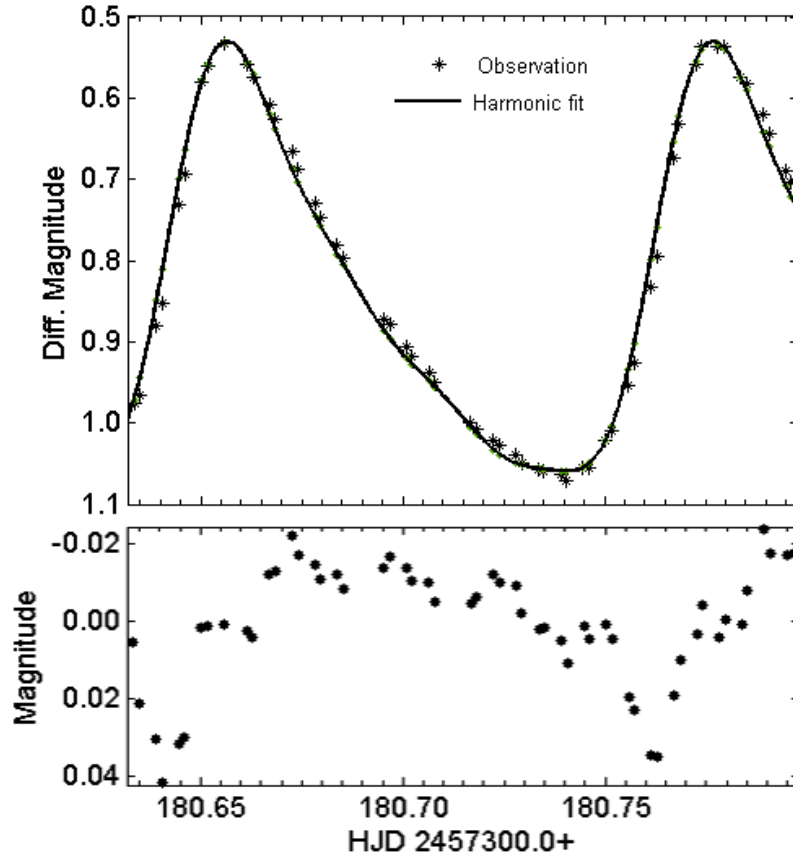
Figure 3.15 Upper panel: The continuous line is function of the frequency f_1 and its first three harmonics fitted to the original light curve of APT data. The data points are the observations. Lower panel: The residual light curve after removing the main frequency, f_1 and three of its harmonics.

3.4.3 Non radial p-modes and g-modes

Generally, the pulsation stars have more than one independent oscillation modes. These independent modes can be radial or non-radial. Apart from the fundamental radial mode, the presence of overtones of the radial fundamental is referred to as double-mode oscillations (Christensen-Dalsgaard, 1976). Most importantly, the frequencies f_2 (14.535 d^{-1}), f_3 (32.620 d^{-1}) and f_4 (4.584 d^{-1}) in Table 3.7, none of them harmonics of f_1, are new for SZ Lyn. These three frequencies do not influence radial fundamental and hence can be independent modes. Therefore, f_2, f_3 and f_4 are initially considered as non radial modes and further examined.

These overtones are parts of radial oscillations and could be identified by period ratios. Therefore, the period ratio method was applied to frequencies f_2 and f_3 to check whether they have any signs of overtones of the fundamental mode. The ratios of the first overtone to the fundamental and second overtone to the fundamental are well defined ranges given as 0.772 - 0.776 (Suarez et al., 2006) and as 0.611 - 0.632 (Stellingwerf, 1979), respectively. Given that 8.296 d^{-1} is the fundamental radial mode, the possible first and second overtones were estimated as 10.746 d^{-1} and 13.578 d^{-1}, respectively. However, these frequencies are not available in frequency spectra of SZ Lyn and frequency f_2, 14.535 d^{-1} rather deviates from the predicted second overtone of 13.578 d^{-1}. The analysis supports that the frequency f_2 is not an overtone and can be concluded as non-radial mode.

In addition, the occurrence of frequency combinations is more common in Delta Scuti stars whenever independent modes are available (Murphy et al., 2013; Breger et al., 2011). The presence of two independent frequencies, v_1 and v_2, produces linear combinations $mv_1 \pm nv_2$ where m and n are integers. These combinations result in more complex frequency spectrum and detection of additional basic frequencies is difficult since these might easily be confused with the combination frequencies. However, on the other hand, a frequency can be determined as independent mode if it combines with the most prominent frequency and shows combinations in the frequency spectrum. Delta Scuti stars shows very complex linear combinations particularly when there are more independent oscillation modes present (Breger 2010, Paparo et al., 2018). SZ Lyn has few linear combinations as mentioned in Table 3.7. In fact, these combinations are produced by frequencies f_2, f_3 and f_4 with the fundamental frequency f_1. The frequencies f_2, f_3 and f_4 and their linear combinations with f_1 are shown in Figure 3.16.
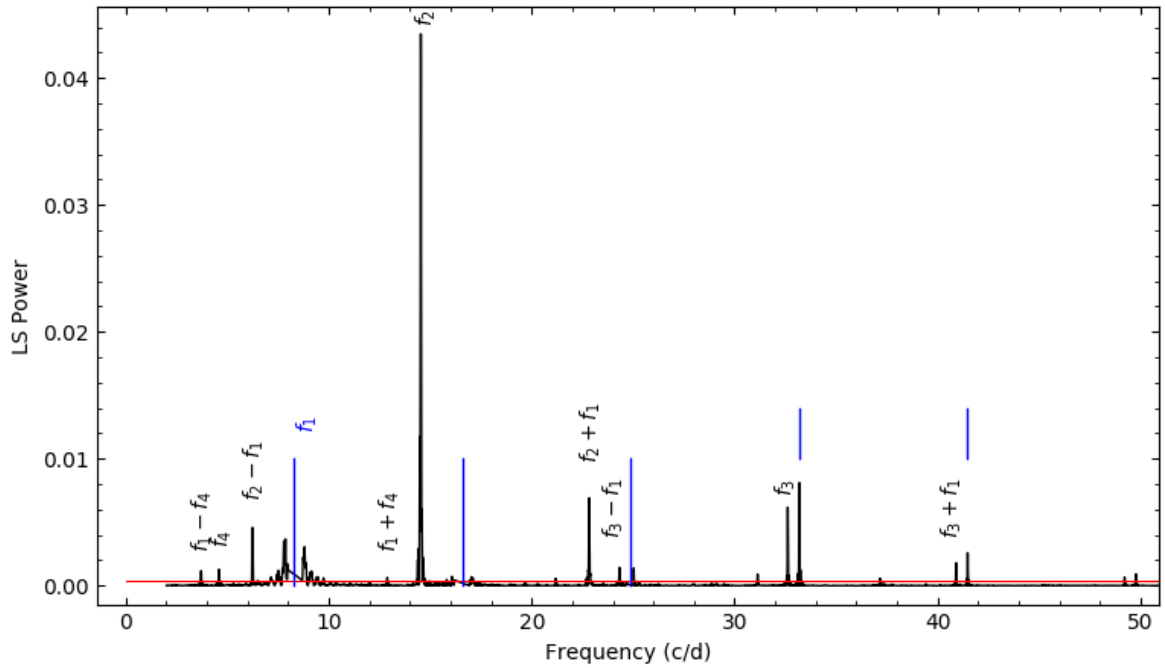
Figure 3.16 Independent frequencies and their combinations of SZ Lyn. The vertical blue lines show the frequencies of the whiten f_1 and four of its harmonics. The horizontal red line indicates the 4σ significant level. The power spectrum is obtained using TESS data.

This is strong evidence that f_2, f_3 and f_4 are independent non radial modes of SZ Lyn. In 2004 Gazeas et al., concluded that SZ Lyn has only radial pulsations with two harmonics but actually SZ Lyn has both radial and non-radial pulsations according to present analysis. Out of these three frequencies, f_2 and f_3 are in the range of higher frequency (6 - 30 d^{-1}) in general considered as p – modes. The amplitude spectrum of Delta Scuti stars, KIC 11145123 shown in their Figure 3.17 (Kurtz et al., 2014), KIC 9700322 (Breger et al., 2011) and KIC 11754974 (Murphy et al., 2013) are also provide evidences of having p – mode pulsations in the range of 6 - 50 d^{-1}.

The frequency f_4 is located in the low frequency range (0 - 6 d^{-1}) less than the assumed fundamental radial mode of f_1. Kurtz et al., (2014), Aerts et al., (2010) and Breger et al., (1999) strongly state that gravity modes (g-modes) are located in the range 0 - 5 d^{-1}. Therefore, the frequency f_4 could be a medium order gravity mode. Based on the observations of Kurtz et al., (2015), Kurtz et al., (2014), f_4 could be a

82

combination of higher order p-modes or very low order g-modes. The frequency spectrum of SZ Lyn does not consist of frequencies in the higher region except the harmonics of the highest amplitude of 8.296 d^{-1}. Therefore, the possibility of f_4 being a combination is very low. Furthermore, Kurtz et al., (2014) shows that the availability of combinations $\nu_1 \pm \nu_g$ with ν_1 and ν_g being the frequencies of the highest amplitude singlet p-mode and a g-mode respectively. These combinations of frequencies produced by fundamental radial p-mode and a g-mode can be naturally explained by non-linear effects that occur when the p-mode and the g-modes are excited simultaneously. The fact that the g-mode frequency distributions are precisely re-produced in both sides of fundamental p-mode is fully consistent with the observation of having the combinations of f_1+f_4 (12.880 d^{-1}) and f_1-f_4 (3.703 d^{-1}) in Figure 3.16. The availability of these combinations in SZ Lyn supports the idea that f_4 is a gravity mode excitation and indicates that both p-modes and g-modes are present in SZ Lyn.
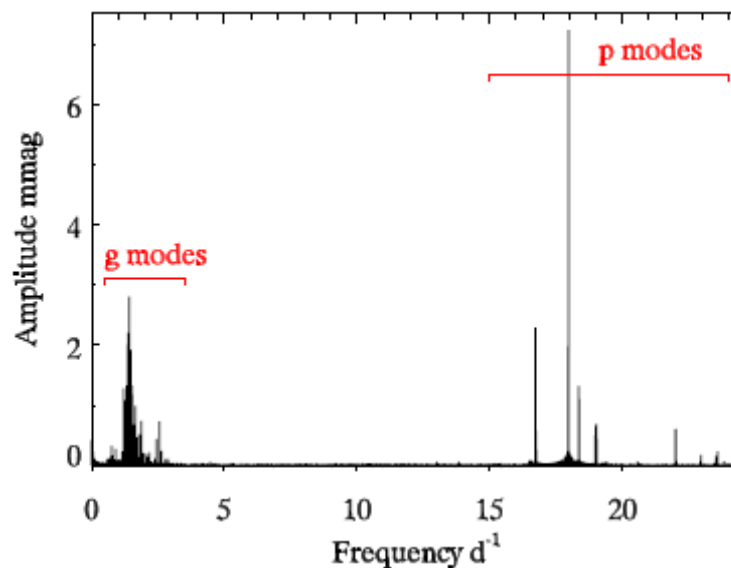
Figure 3.17. The amplitude spectrum for the Q0–Q16 *Kepler* LC data up to the Nyquist frequency for KIC 11145123, showing the presence of both g-modes and p-modes that are clearly separated. Image is adopted from Kurtz et al., 2014.

Chapter 4

Mode Identification

4.1 Introductory remarks

The spherical degree, *l,* and azimuthal order, *m*, of the stellar oscillation can be determined using several methods in photometry. If the data source is single band like Kepler or TESS, the rotational splitting, frequency spacing and echelle diagrams (Aerts, 2020) are the standard techniques that use to determine the spherical degree *l* and azimuthal order *m*. There are plenty of investigations found in the literature where these methods are extensively used. Kern et al., (2018), Tian et al., (2014) used single band Kepler data to determine the spherical degree *l* using period spacing and rotational splitting. Due to the availability of high quality continuous space-based data such as Kepler and TESS, recent studies in asteroseismology are focused on mainly frequency splitting and frequency spacing methods to determine the *l* and *m*.

In multi-band photometry, with the availability of UBVRI bands, the amplitude ratios and phase difference of the bands can be used in addition to the above mentioned methods to determine spherical degree *l* (Garrido, 2000, Balona & Evers, 1999, Breger et al., 1998). However, multi-band observations are mostly carried out from ground-based facilities. From a single site, the continuity and consistency of the data set are difficult to achieve. Hence the analysis would be much more complex and may not detect the fine structures such as rotational splitting and frequency spacing. Before the space-based Kepler mission was commissioned, the researchers depended on ground-based data and the amplitude ratio and phase difference were widely used techniques. In addition, the amplitude ratio method depends on stellar models; hence profound computations were involved in the analysis. With the availability of light curves in UBVR bands of SZ Lyn, the frequency analysis was performed separately for UBVR. Hence, amplitude ratio method could be performed to determine spherical degree *l* of the detected frequencies. In the amplitude ratio method, the observed amplitudes tabulated in Table 3.8 should be compared with the theoretical amplitudes computed using stellar models. A comprehensive description of computations of synthetic amplitudes is included in this section.

4.2 Theoretical amplitudes

The amplitudes due to stellar oscillations can be theoretically computed for the different models with a set of stellar parameters. The complex radial and non-radial oscillations were comprehensively studied and developed theoretically, considering all the input parameters in stellar magnitude variations. The magnitude of a star changes basically with temperature and gravity. When the star pulsates, i.e., swelling and contracting, the temperature and radius of the star vary in different phases. This variation of apparent magnitude with effective temperature and other parameters for δ Cephei is shown in Figure 4.1.

4.2.1 Flux variations due to temperature and gravity

The spherical degree l can be determined using the amplitude ratios and phase differences in multi-band observations (e.g., Balona & Evers 1999; Aerts et al., 2010). The process is model-dependent because the amplitude and phase variations depend on the spherical harmonic degree l (Balona & Evers 1999), and higher extent on the effective temperatures and gravities of the models as shown in Dupret et al., (2003). In general, flux changes in pulsating stars originate from the temperature and gravity variations as a function of radius (Garrido et al., 1990). The mode identification needs a sequence of theoretical modeling of different combinations of parameters of the star. The theoretical aspects of flux variations of the model star were discussed in detail with the consideration of non-adiabatic parameters and limb darkening effect by Watson (1988) and Heynderickx (1994).
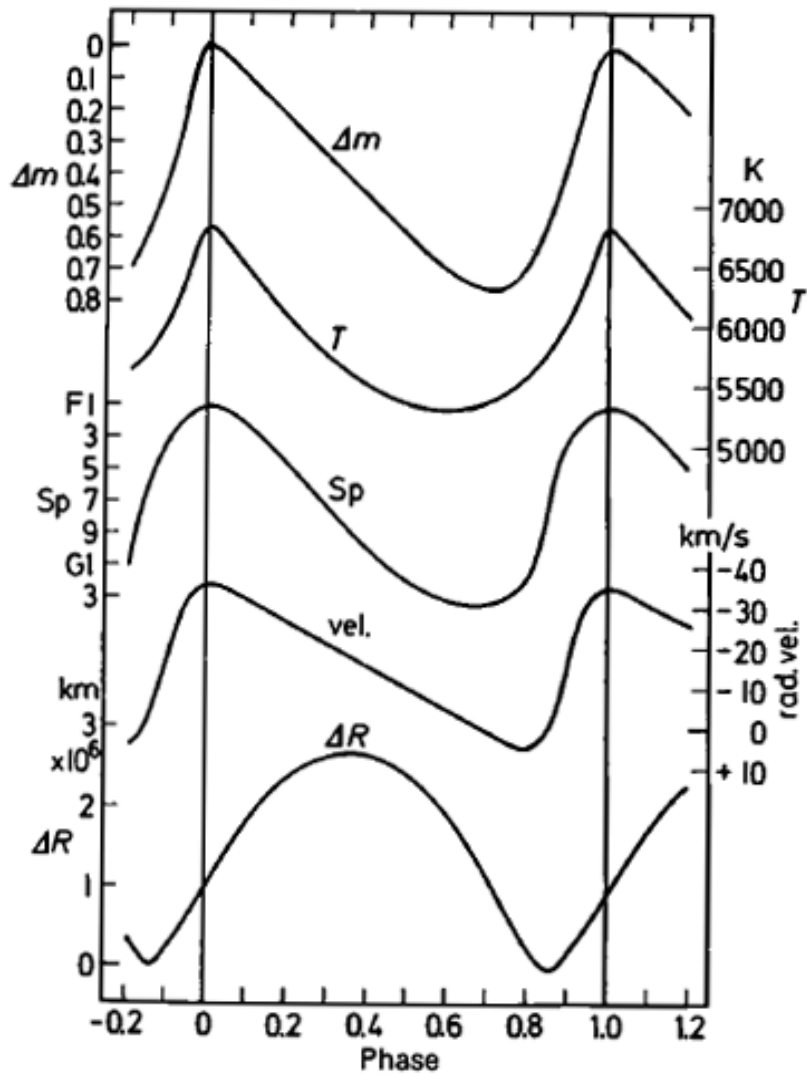
Figure 4.1. The observed variation of the apparent visual magnitude, the effective temperature, the spectral types and the radial velocities for δ Cephei are shown as a function of phase. At the bottom of the changes in radius are shown as obtained by integrating over the pulsation velocities. The radius is nearly the same for maximum and minimum brightness. Adopted from Becker, 1950.

The single-layer approximation assumes that a stellar sphere consists of one plane-parallel layer whose temperature is equal to the effective temperature of the star. Moreover, it is assumed that the outward flux does not depend on the optical depth in the atmosphere. Under these assumptions, the monochromatic flux (F) variation in the local atmosphere is given by;

$$F_{\lambda,0} + \delta F_\lambda(\theta, \phi, t) = F_\lambda[T_{eff,0} + \delta T_{eff}(\theta, \phi, t), g_0 + \delta g_e(\theta, \phi, t)] \qquad 4.1$$

where θ and ϕ are colatitude and longitude respectively. δT_{eff} and δg_e are Lagrangian perturbations of effective temperature and gravity respectively.

In linear approximation this can be written as

$$\frac{\delta F_\lambda}{F_{\lambda,0}} = \left(\frac{\partial lnF_\lambda}{\partial lnT_{eff}}\right)\frac{\delta T_{eff}}{T_{eff,0}} + \left(\frac{\partial lnF_\lambda}{\partial lng_e}\right)\frac{\delta g_e}{g_0} \qquad 4.2$$

$$= \alpha_{T,\lambda}\frac{\delta T_{eff}}{T_{eff,0}} + \alpha_{g,\lambda}\frac{\delta g_e}{g_0} \qquad 4.3$$

where $\qquad \alpha_{T,\lambda} = \dfrac{\partial ln F_\lambda}{\partial ln T_{eff}}, \qquad \alpha_{g,\lambda} = \dfrac{\partial ln F_\lambda}{\partial ln g_e}$

Here $\alpha_{T,\lambda}$ is rate of change in flux with temperature for a constant gravity and $\alpha_{g,\lambda}$ is rate of change in flux with gravity for a given temperature. In addition, the temperature and gravity perturbations can be given in terms of radial displacement of the pulsating star. In principle, the temperature perturbation $\dfrac{\delta T_{eff}}{T_{eff,0}}$ can be any value of phase with the radial displacement S_r given in equation 1.9. Therefore, the expression can be defined as;

$$\frac{\delta T_{eff}}{T_{eff,0}}(R, \theta, \phi) = f_T \frac{S_r(R)}{R}\exp(-i\psi_T) \qquad 4.4$$

The gravitational perturbation $\frac{\delta g_e}{g_0}$, is anti-phase with the radial displacement R.

Therefore it can be given by

$$\frac{\delta g_e}{g_0}(R,\theta,\phi) = -f_g \frac{S_r(R)}{R}$$
4.5

The equations, 4.4 and 4.5 introduce set of coefficients, f_T, f_g and ψ_T known as non-adiabatic observables (Aerts et al., 2010) and the coefficient ψ_T is known as phase lag between the temperature and radial displacement of the star. This phase difference is further explained in Figure 4.1. f_T and f_g are the amplitudes of $\frac{\delta T_{eff}}{T_{eff,0}}$ and $\frac{\delta g_e}{g_0}$ corresponding to the normalized displacements at the photosphere respectively. The derivations of the above equations can be found in Watson (1988), Heynderickx et al., (1994), Dupert (2001), Daszy´nska-Daszkiewicz et al., (2002), all of which follow the original work by Dziembowski (1977).

4.2.2 Limb darkening effect

The solar disk is not equally bright all over, but it is darkened towards the limb. This unevenness of brightness from the center of the disk towards the limb is known as limb darkening. This effect occurs due to very important thermodynamic fact - heat transfer. In order to improve accuracy of the theoretical amplitudes the limb darkening effect should be included in the computation. The effect is more pronounced at the blue end of the spectrum and less pronounced at the red. A reasonably good empirical representation of the limb darkening is given by an equation for the specific intensity;

$$I(r) = I(0)\left[1 - u\left(1 - \sqrt{\frac{R^2 - r^2}{R^2}}\right)\right]$$
4.6

where I(0) is the specific intensity at the center of the disk, R is the radius of the star and u is the limb darkening coefficient (LDC).
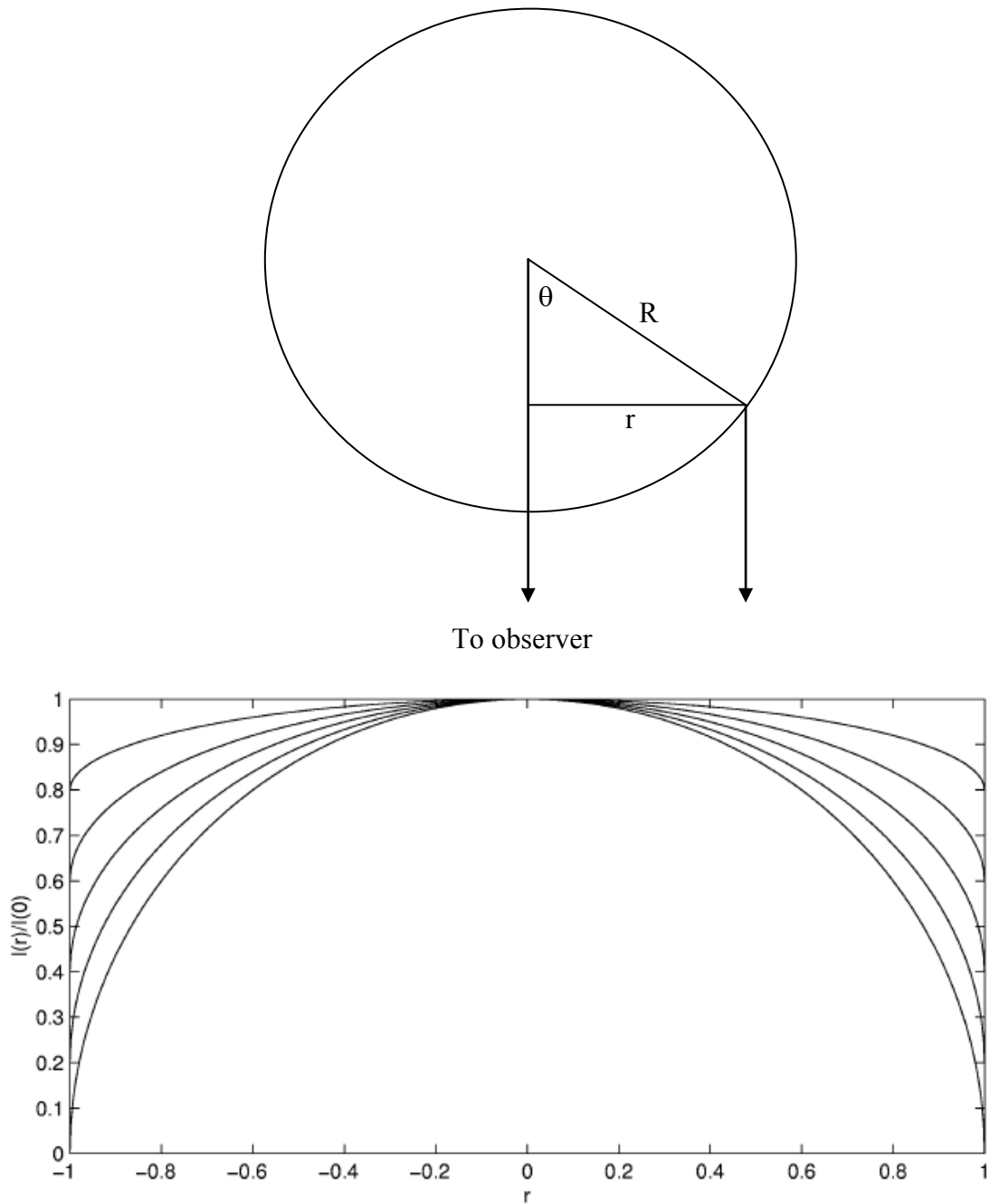
Figure 4.2 Above: Geometrical orientation of the limb darkening effect from the center to the limb with respect to an observer. Below: equation 4.6 for six limb darkening coefficients, from the lowest curve upwards, u=1.0, 0.8, 0.6, 0.4, 0.2 and 0.0. The curve for the last of these (no limb darkening) is formed from three of the boundary lines. The curve u=1 is a circle. The radius of the disk is taken to be 1, r = 0 is the center of the disk and r = ±1 is the limb.

The limb darkening coefficient u is usually written in terms of θ or $\mu = \cos\theta$. Then the equation 4.6 can be re-written as

$$I(\theta) = I(0)[1 - u(1 - \cos\theta)] = I(0)[1 - u(1 - \mu)] \qquad 4.7$$

Similar to the flux variation due to the temperature and gravity, the limb darkening is also subjected to the variation on temperature and gravity and expressed as follows using limb darkening integral in equation 4.8.

$$b_{l,\lambda} = \int_0^1 \mu h_\lambda(\mu) P_l \, d\mu \qquad 4.8$$

here h_λ limb darkening law defined in Eq. 4.7 and P_l represents Legendre polynomials which depend on the spherical degree l.

Hence it is possible to define the limb darkening derivatives, which are the variation of limb darkening with temperature and gravity as follows.

$$\beta_{T,\lambda} = \frac{\partial \ln b_{l,\lambda}}{\partial \ln T_{eff}} \, , \qquad\qquad \beta_{g,\lambda} = \frac{\partial \ln b_{l,\lambda}}{\partial \ln g} \qquad 4.9$$

Finally, the observed variation of the monochromatic visual magnitude at wavelength λ can be written as (Aerts et al., 2010)

$$\delta m_\lambda = -\frac{2.5}{ln10} \sqrt{4\pi} \frac{S_r(R)}{R} c_{lm} P_l^m(\cos i) b_{l,\lambda}$$
$$\times \left[-(l-1)(l-2)\cos(\omega t) + f_T \cos(\omega t + \psi_T)(\alpha_{T,\lambda} + \beta_{T,\lambda}) \right.$$
$$\left. - f_g \cos(\omega t)(\alpha_{g,\lambda} + \beta_{g,\lambda}) \right] \qquad 4.10$$

where c_{lm} and $P_l^m(\cos i)$ are defined in equation 1.12.

Although the change in monochromatic visual magnitude is depending on several parameters in equation 4.10, it can be approximated while omitting the common factor $\frac{2.5}{\ln 10}\sqrt{4\pi}\frac{S_r(R)}{R}c_{lm}P_l^m(\cos i)$ and re-written in the following form for a filter band pass j

$$A_{j,th} = \frac{\int_{\lambda_{blue}}^{\lambda_{red}} |b_{l,\lambda}||T_1 + T_2 + T_3|\varphi_j(\lambda)d\lambda}{\int_{\lambda_{blue}}^{\lambda_{red}} \varphi_j(\lambda)d\lambda} \qquad 4.11$$

With
$$T_1 = (1 - l)(l + 2) \qquad\qquad 4.12$$
$$T_2 = f_T \exp(-i\psi_T)\left(\alpha_{T,\lambda} + \beta_{T,\lambda}\right) \qquad 4.13$$
$$T_3 = -f_g\left(\alpha_{g,\lambda} + \beta_{g,\lambda}\right) \qquad\qquad 4.14$$

The terms T_1, T_2 and T_3 represent the geometrical term, temperature dependent and gravity dependent terms of the oscillating star respectively. In order to determine the theoretical amplitude $A_{j,th}$ one must calculate all T terms i.e. all the α, β terms and f_T, f_g , ψ_T for all bands of UBVRI.

4.2.3 Non – adiabatic models

Although the amplitude ratio method is a relatively complicated procedure than the frequency spacing and rotational splitting methods, this method provides an opportunity to converge stellar parameters through set stellar models. Hence, this model dependent iterative procedure is converging stellar parameters of the star to the optimum solution while determining the degree l of the observed frequencies. The SZ Lyn has been observed and determined the stellar parameters by several observers which are listed in Table 3.1. The results of the comprehensive frequency analysis of this study are given in Table 3.7. The frequency list consists of newly discovered frequencies of SZ Lyn. The amplitudes and phases of these frequencies were further investigated with the stellar pulsation models.

The DSS are predominantly driven by the partial ionization zone of ionized helium. This layer is positioned near $\log (T_{eff}) \approx 4.6$ (Aerts et al., 2010), i.e., much further out where the non-adiabatic effects are more robust. Therefore, for DSS, non-adiabatic treatments are more appropriate for the analysis of DSS observations. However, the model driven mode identification has some major difficulties due to interdependencies of the primary parameters, f_T, f_g, ψ_T and flux and limb darkening derivatives of equations 4.12 to 4.14. The determination of flux and limb darkening derivatives will be explained in sections 4.2.4 and 4.2.5, respectively. The major complication is which set of values suitable for f_T, f_g, and ψ_T to represent the oscillations of DSS stars. Due to this difficulty, early analysis neglected some terms of the theoretical amplitude of equation 4.11. For ZZ Cet stars, Brassard et al., (1995) neglected T_1 and T_3. Heynderickx et al., (1994) set the above parameters as free parameters for the analysis of β Cep stars. Balona et al., (1997) use values of f_T and ψ_T from non-adiabatic pulsation calculations, thereby removing two free parameters. Dupret et al., (2001) introduced a non-adiabatic pulsation code resulting in the eigen values f_T, f_g, and ψ_T for the stellar models and oscillation frequencies and removed all three free parameters from the computations. In this analysis, the pulsation models were generated using state-of-art Time Dependent Convection (TDC) non-adiabatic computations (Dupret et al., 2001). The initial parameters of SZ Lyn, T_{eff} = 7540 K, $\log (g)$ = 3.88 (Langford 1976) and M = 1.57 $M_\odot$ (Fernley et al. 1984) were passed to the TDC non-adiabatic code[1] (Dupret et al., 2001) to generate the pulsation models which give frequencies close to the observed main frequency of 8.296 d^{-1}. The two resulting models that are close to our observational results are shown in Table 4.1. The output of the non-adiabatic code also provides the values f_T, f_g and phase angle ψ_T which are inputs of equations 4.13 and 4.14. The values f_T, f_g and ψ_T for the set of frequencies and different degree l were computed. The output models of TDC are included in Appendix A. The interpolation of the f_T, f_g and phase angle ψ_T with polynomials for different degree l give the desired values at the observed frequency 8.296 d^{-1} of SZ Lyn. The interpolation of three parameters for l = 0 for Model 1 and Model 2 is shown in Figure 4.3

---

[1] The results of the code is provided by M. A. Dupret through private communication

Table 4.1 Two pulsation stellar models generated by TDC non-adiabatic code for the observed frequency range of 8.296 d^{-1} of SZ Lyn. X is hydrogen mass fraction and Z is the heavy element mass fraction (chemical composition). α_{ML} is mixing length parameter of order unity, typically $0.5 > \alpha_{ML} > 3.0$.

Model 1		
$M/M_\odot = 2.00$	$T_{eff} = 7522$ K	$\log(L/L_\odot) = 1.425$
$\log(g) = 3.77$	$R/R_\odot = 3.00$	$age(yr) = 1.0 \times 10^9$
$X = 0.72$	$Z = 0.014$	$\alpha = 1.7$
Model 2		
$M/M_\odot = 1.90$	$T_{eff} = 7557$ K	$\log(L/L_\odot) = 1.322$
$\log(g) = 3.86$	$R/R_\odot = 2.68$	$age(yr) = 1.1 \times 10^9$
$X = 0.72$	$Z = 0.014$	$\alpha = 1.7$
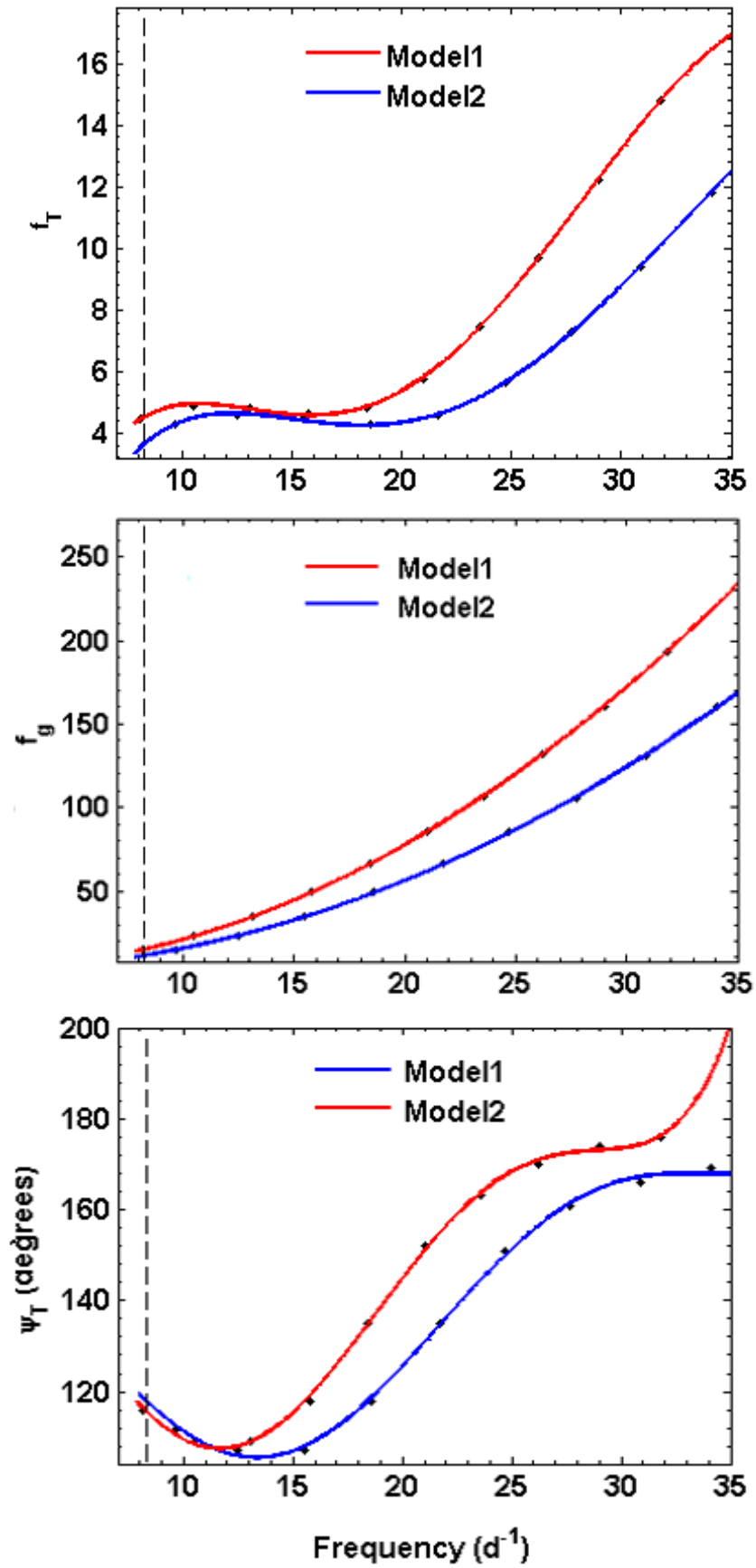
Figure 4.3 The results of non-adiabatic computations. The dots are the values of parameters and continuous lines are the polynomials fitted to the points. The dotted line is the frequency f_1=8.296 d^{-1} observed in SZ Lyn.

4.2.4 AlphaTg Code

The flux derivatives $\alpha_{T,\lambda}$, $\alpha_{g,\lambda}$ and limb darkening derivatives $\beta_{T,\lambda}$, $\beta_{g,\lambda}$ should be computed in order to find T_2 and T_3 in equation 4.13and 4.14, respectively. For the computations of flux derivatives in the observational error box of SZ Lyn, the grids of monochromatic model atmospheres ATLAS9[2] originally developed by Kurucz (1993) and later modified by Castelli (2004) were used. The flux models are available in the temperature steps of 250 K through the range of 3500 K to 50000 K and gravity steps of log (g) of 0.5 through the range of 0 to 5. These grids are available for different chemical abundance ratio (M/H) and typically 476 (Castelli and Kurucz, 2004) models are available for one M/H value. For a suitable chemical abundance ratio (M/H) of SZ Lyn, the temperature and gravity error box was decided according to the range of temperature and gravity of SZ Lyn as given in Table 3.1. Using the TDC non-adiabatic code, the SZ Lyn was approximated to two models called Model 1 and Model 2 given in the Table 4.1. Therefore the temperature and gravity error box of the grid is defined by centering the T_{eff} = 7500 K and log (g) = 4.0. Now the flux values should be obtained for the UBVR bands of models from T_{eff} = [6000 K − 9000 K] with steps of 250 K and log (g) = [0.0 − 5.0] with the steps of 0.5. Due this complexity of lookup tables in all UBVR bands and the calculations of flux derivatives $\alpha_{T,\lambda}$, $\alpha_{g,\lambda}$ using Kurucz grids, the AlphaTg code was developed. The interface of the code is shown in Figure 4.4. This code is given the name AlphaTg. It readout the model flux from the grid for the user define range of temperature and log (g) with a step size of 250 K and 0.5, respectively. The absolute flux ranging from 10 nm to 10000 nm is available in each model covering all pass bands of UBVRI (Johnson et al., 1966). Hence it is possible to integrate the separate pass bands UBVRI for flux using the equation 4.15. The wavelengths of the UBVRI pass bands and their central wavelengths are given in Table 2.1 and graphically displayed in Figure 2.12. Once the flux is determined for the user defined range of temperature and gravity, the data are fitted by a polynomial with the minimum root-mean-square (RMS). This distribution is then used to calculate the partial derivatives, $\alpha_{T,\lambda}$ and $\alpha_{g,\lambda}$ again by user define temperatures and gravity. $\alpha_{T,\lambda}$ and $\alpha_{g,\lambda}$ calculated within the observational error box of SZ Lyn using AlphaTg code are shown in Figure 4.5

---

[2] http://wwwuser.oats.inaf.it/castelli/grids.html

$$F_i = \int_{\lambda_{blue}}^{\lambda_{red}} F_\lambda \omega_i(\lambda) d\lambda \qquad\qquad 4.15$$

here $\omega_i(\lambda)$ is the transmission curve of the particular band i, which represents UBVRI.

According to the physical parameters mentioned in Table 3.1, the temperature T_{eff} and gravity log (g) of SZ Lyn are assumed to be 7500 K and 4.0 dex respectively. The error box was selected by centering of these two values in the Kurucz grid and determine the fluxes of the models across the point [7500 K, 4.0 dex] for temperatures from 6000 k to 9000 K keeping log (g) = 4.0 dex and for gravity from 1.5 to 5.0 keeping T_{eff} = 7500 K. The computations were done using AlphaTg code so that all the models included in the error box were processed and determined $\alpha_{T,\lambda}$ and $\alpha_{g,\lambda}$. The flux derivatives in the above temperature and gravity range for the UBVR bands are shown in Figure 4.5.
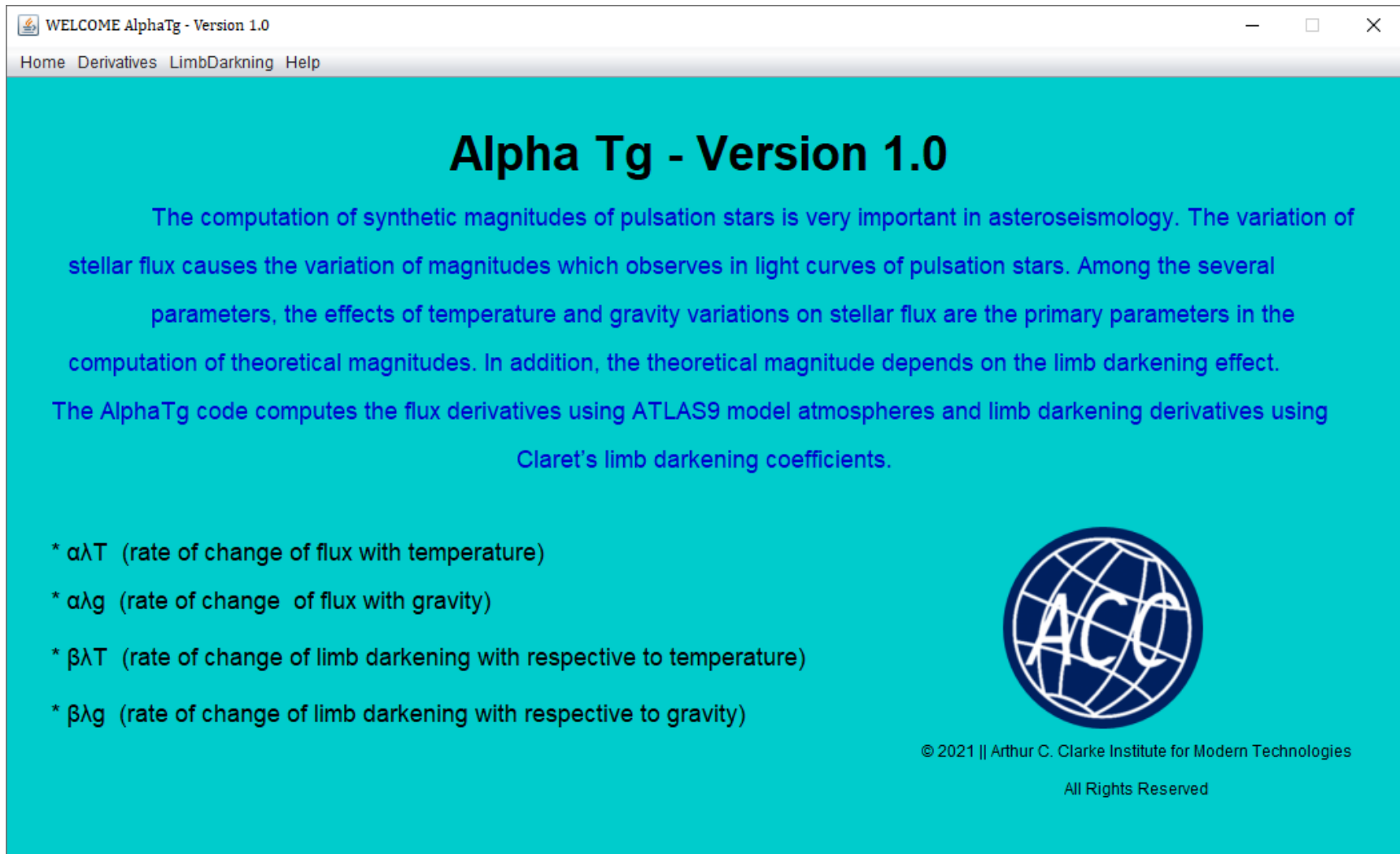
Figure 4.4 Interface of AlphaTg
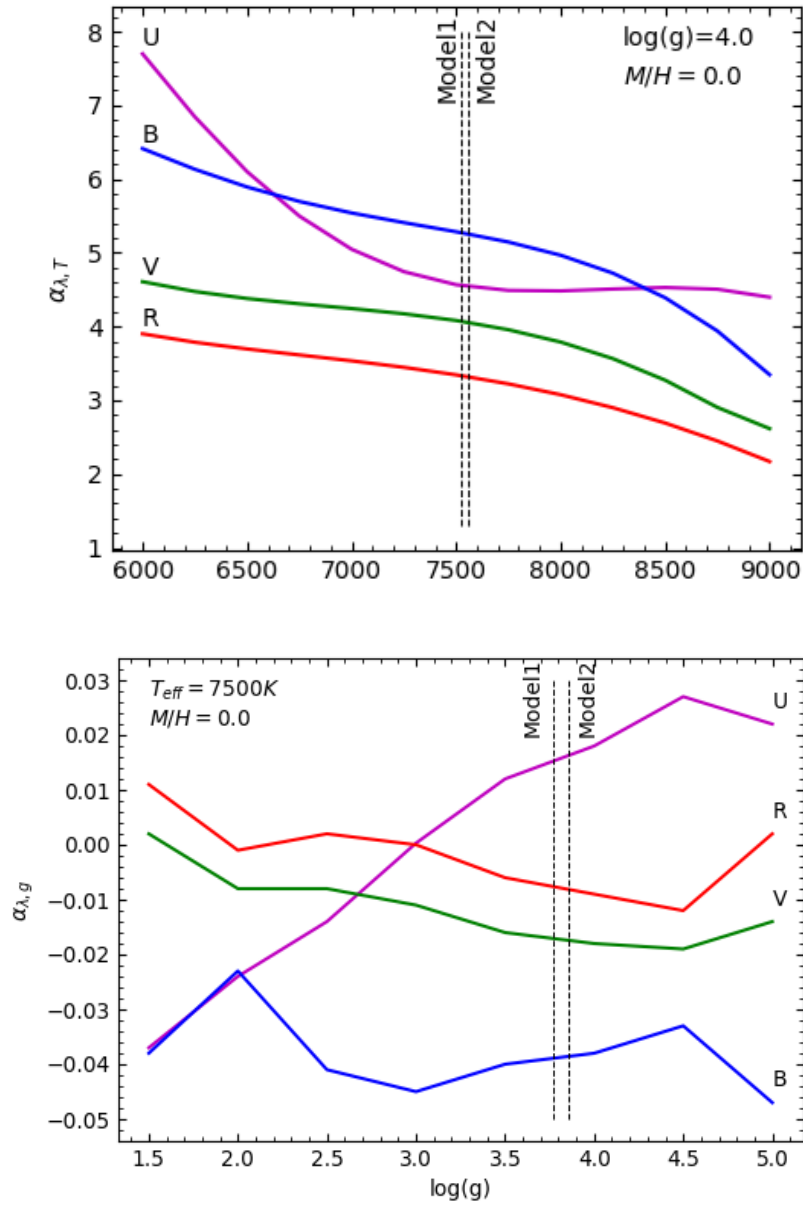
Figure 4.5 Above: The flux derivate $\alpha_{T,\lambda}$ for log (g) = 4.0 and chemical abundance (M/H) = 0.0. The temperature points of Model 1 and Model 2 in Table 4.1 are shown in vertical dashed lines. Below: The flux derivatives $\alpha_{g,\lambda}$ for T_{eff} = 7500 K and for the same chemical abundance (M/H) = 0.0. The two vertical dashed lines indicate the gravity points of Model 1 and Model 2. The colors, violet, blur, green and red represent UBVR bands respectively.

Next, the limb darkening derivatives $\beta_{T,\lambda}$, $\beta_{g,\lambda}$ should be determined. This computation is also included in the AlphaTg code. The limb darkening integral in Eq. 4.8 has spherical harmonic (l) dependency through the Legender polynomials. Since the frequencies of SZ Lyn are searching in the range of spherical harmonics of $l = 0$, 1, 2 and $m = 0$ case, the corresponding Legender polynomials taken for the computations are;

$$
\left.
\begin{aligned}
l = 0 \;\rightarrow P_0\,(\mu) &= \; 1 \\
l = 1 \;\rightarrow P_1(\mu) &= \; \mu \\
l = 2 \;\rightarrow P_2(\mu) &= \frac{1}{2}(3\mu^2 - 1)
\end{aligned}
\right\}
\qquad 4.16
$$

The linear limb darkening law was taken from Claret (2000) as;

$$
h_\lambda = 1 - u(1 - \mu) \qquad\qquad 4.17
$$

the limb darkening integral from Eq. 4.18 for $l = 2$ mode can be written with the replacement of Eq. 4.16 and Eq. 4.17 as;

$$
b_{l,\lambda} = \int_0^1 \mu[1 - u(1 - \mu)] \times \frac{1}{2}(3\mu^2 - 1)d\mu \qquad 4.18
$$

where, u stands for limb darkening coefficient (LDC) which is depending on stellar parameters such as temperature, gravity and metallicity as well as wavelength.

Similar to the Kurucz grids, Claret (2000) published a grid for the LDC which contains the computations for 19 metallicities ranging from 10^{-5} up to 10^{+1} solar abundances, with log (g) varying between 0.0 and 5.0 and effective temperatures between 2000 K − 50000 K. AlphaTg code is used to readout LCD's for the desired range of temperature and gravity and hence computed limb darkening derivatives. The AlphaTg code, under the limb darkening option, is looking up this grid and first compute the limb darkening integral for all UBVRI bands in the user defined temperature and gravity for $l = 0$, 1 and 2 options. Subsequently, the limb darkening integrals were fitted through a polynomial minimizing RMS and used to compute $\beta_{T,\lambda}$ and $\beta_{g,\lambda}$ for the user defined effective temperature and gravity. The limb

darkening derivatives computed using AlphaTg code in the range of temperature and gravity of SZ Lyn are shown in Figure 4.6.
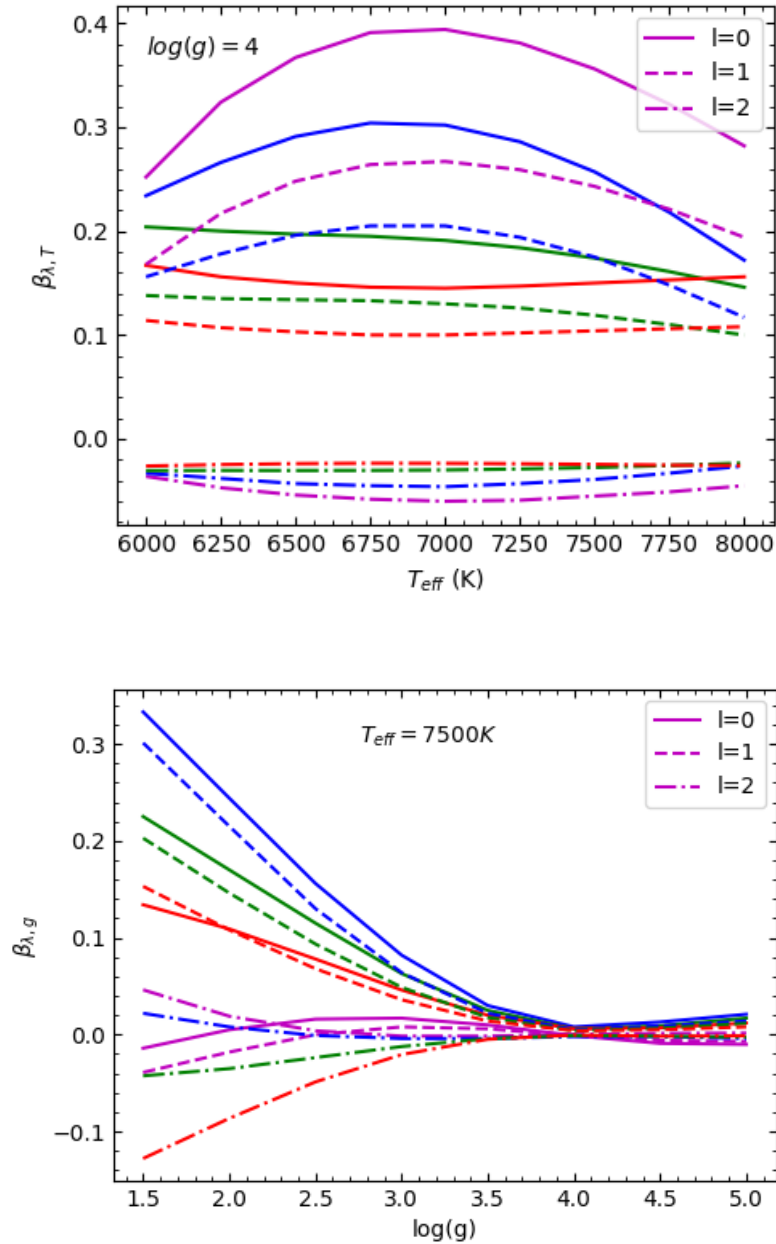
Figure 4.6 Above: Limb darkening derivatives with respective to the temperature for constant gravity of log (g) = 4.0 for all spherical degrees of l = 0, 1 and 2. Below: Limb darkening derivatives with respect to the gravity for constant T_{eff} = 7500 K for all l of 0, 1 and 2. The colors, violet, blue, green and red represent UBVR bands respectively.

4.2.5 Theoretical amplitudes of SZ Lyn

From the computations explained through sections 4.2.1, 4.2.2 and 4.2.3, all the parameters necessary to calculate the theoretical amplitudes in Eq. 4.11, for the pass bands UBVR are placed in Table 4.2. The theoretical amplitudes were calculated based on the parameters of two models mentioned in Table 4.1, for three different spherical degrees of $l = 0$, $l = 1$ and $l = 2$, for the observed frequency $f_1 = 8.296$ d^{-1}. These theoretical amplitudes represent the models for the observational amplitudes mentioned in Table 3.8 for the same frequency f_1. Therefore, the comparison can be performed to identify the spherical degree l of the frequency and subsequently used to narrow down the best fit model for SZ Lyn. Hence asteroseismology is used simultaneously to determine the oscillation modes n and l of the frequencies and secondly redefine the stellar parameters of SZ Lyn. The prime objective of the investigation is revisiting the stellar parameters of SZ Lyn using the asteroseismological approach. The comparison of theoretical and observational amplitude ratios are graphically shown in Figure 4.7. The results of the amplitude ratios clearly specifies that the frequency f_1 is close to $l = 0$ mode for both models. Therefore it can be concluded that f_1 is the radial fundamental mode of $n = 1$ and $l = 0$.

The parameters of two TDC non-adiabatic models in Table 4.1 are very close to each other (difference of $T_{eff} \approx 35$ K) and non-adiabatic parameters in Figure 4.3) so that the theoretical amplitudes of two models are very close to each other in Fig 4.7. Though it is clear that the frequency f_1 is close to $l = 0$, the appropriateness of Model 1 and Model 2 is visual impractical to determine. Therefore χ^2 minimization given in equation 4.19 (Daszy´nska-Daszkiewicz & Walczak 2009) was computed for the two models with the observation.

$$\chi^2(l) = \sum_{j=1}^{filters} \left(\frac{\frac{A_{j,th}}{A_{ref,th}} - \frac{A_{j,obs}}{A_{ref,obs}}}{\sigma_{j,obs}} \right)^2$$ 4.19

where 'filters' represent U, B, V and R bands and $\sigma_{j,obs}$ given in equation 4.20 is the properly propagated standard error of the observed amplitude ratio for filter j and the reference filter.

$$\sigma_{j,obs} = \frac{A_{j,obs}}{A_{ref,obs}} \sqrt{\left(\frac{SA_{j,obs}}{A_{j,obs}}\right)^2 + \left(\frac{SA_{ref,obs}}{A_{ref,}}\right)^2}$$ 4.20

Where $SA_{j,obs}$ is the standard error of the observed amplitude in filter j.

The calculated χ^2 values for the Model 1 and Model 2 are given in Table 4.3. The graphical presentation of χ^2 against the spherical degree l for the two models is shown in Figure 4.8.

Table 4.2 Theoretical amplitude ratios of SZ Lyn for Model 1 and Model 2. Non − adiabatic parameters and all the T terms and the corresponding amplitudes $A_{j,th}$ for pass bands of UBVR are mentioned under each column for three spherical degrees, $l = 0$, $l = 1$ and $l = 2$. The last three columns in each model are showing the amplitude ratios with respect to B band.

Model 1

l	T_1	f_T	f_g	Y_T	U			B			V			R			Amplitude Ratio			
					T_2	T_3	$A_{U,th}$	T_2	T_3	$A_{B,th}$	T_2	T_3	$A_{V,th}$	T_2	T_3	$A_{R,th}$	U/B	B/B	V/B	R/B
0	2	4.505	14.917	115.466	-9.507	-0.288	3.173	-10.704	0.352	3.274	-8.221	0.090	2.510	-6.749	-0.030	2.012	0.969	1.000	0.767	0.614
1	0	4.501	15.007	115.370	-9.249	-0.275	2.731	-10.501	0.429	2.840	-8.080	0.150	2.284	-6.630	0.015	1.945	0.962	1.000	0.804	0.685
2	-4	4.469	14.985	116.047	-8.831	-0.223	1.692	-10.269	0.608	1.783	-7.938	0.300	1.501	-6.470	0.150	1.333	0.949	1.000	0.842	0.748

Model 2

l	T_1	f_T	f_g	Y_T	U			B			V			R			Amplitude Ratio			
					T_2	T_3	$A_{U,th}$	T_2	T_3	$A_{B,th}$	T_2	T_3	$A_{V,th}$	T_2	T_3	$A_{R,th}$	U/B	B/B	V/B	R/B
0	2	4.287	11.929	117.837	-9.787	-0.218	3.263	-11.016	0.322	3.452	-8.464	0.107	2.602	-6.942	0.000	2.081	0.945	1.000	0.754	0.603
1	0	3.922	11.332	118.107	-8.828	-0.207	2.594	-10.020	0.351	2.727	-7.712	0.136	2.182	-6.323	0.023	1.852	0.951	1.000	0.800	0.679
2	-4	3.882	11.358	119.088	-8.466	-0.185	1.640	-9.844	0.466	1.746	-7.606	0.227	1.477	-6.215	0.102	1.307	0.939	1.000	0.846	0.748
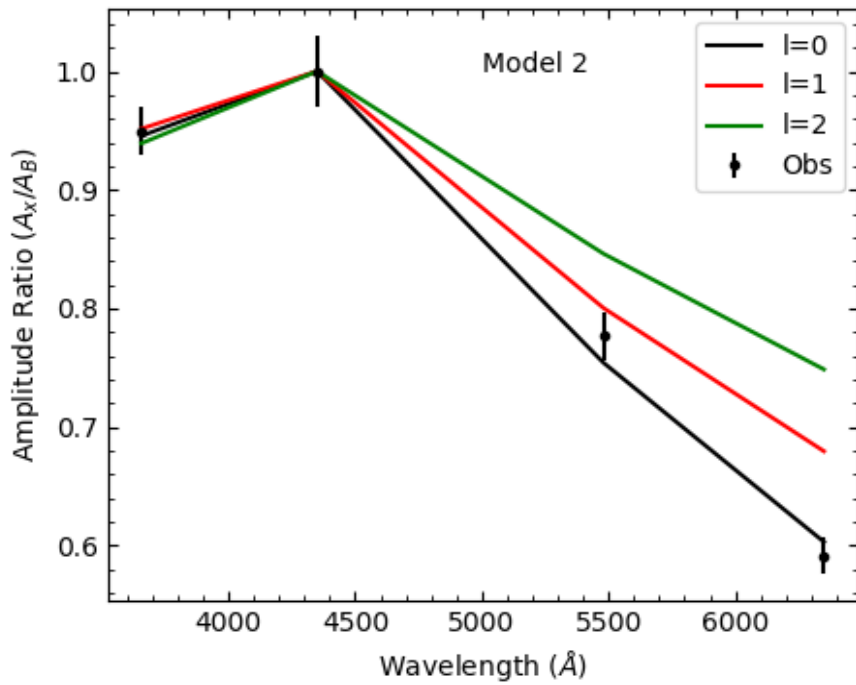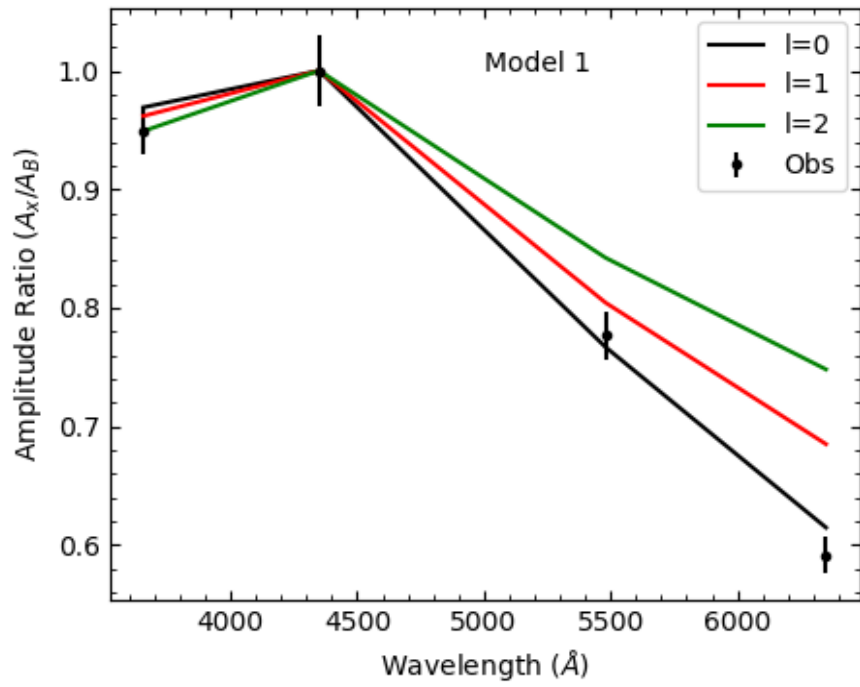
Figure 4.7 The observational and theoretical amplitude ratios for the frequency f_1=8.296 d^{-1}. The points with error bars are the observations and continuous lines are the theoretical amplitude ratios for l = 0, 1 and 2.

Table 4.3 The standard error (σ) of the observed amplitudes in U, B, V and R filters and χ^2 values calculated using the amplitudes and σ using the equation 4.19 for l = 0, 1, 2 for Model 1 and Model 2.

Filter	$\sigma_{j,obs}$
U	0.01670
B	0.01953
V	0.01505
R	0.01069

Model 1			Model 2		
$\chi^2(l=0)$	$\chi^2(l=1)$	$\chi^2(l=2)$	$\chi^2(l=0)$	$\chi^2(l=1)$	$\chi^2(l=2)$
6.6565	80.8478	234.47	3.56677	70.7481	238.288
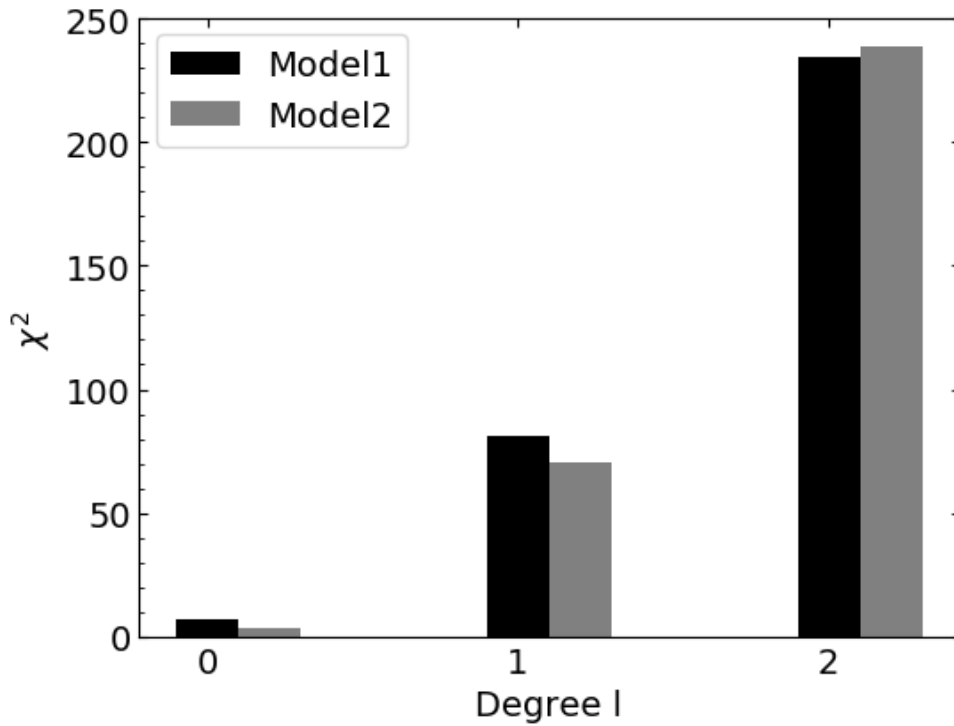
Figure 4.8 χ^2 minimization of frequency f_1 = 8.296 d^{-1}. The frequency f_1 is minimized to the spherical degree l = 0 mode and further from two models, Model 2 is more closed to the observations with the minimum χ^2 of two models at l = 0.

Chapter 5

Pulsation and evolutionary models

5.1 Introductory remarks

The ultimate objective of an astronomical analysis of a star is to determine the physical parameters up to maximum accuracy. The different techniques have been used to achieve this higher accuracy and from time to time, the stellar parameters are being updated. With the discovery of asteroseismology (Christensen-Dalsgaard et al., 1996, Aerts et al., 2010), the state-of-art investigation of stellar interior, the method is being used to refine stellar parameters through the frequency analysis. The observations of pulsating stars should be compared through a set of pulsation models. The analysis described in Chapter 4 is an example of such an attempt. As a result of the mode identification in Chapter 4, the best theoretical model can also be determined for SZ Lyn. The updated stellar parameters of SZ Lyn are mentioned in Table 3.1. However, this approach is very complex due to the model dependencies on several input parameters. Therefore, the best model should be determined through an investigation of the behavior of the perturbed model on input parameters. In this way, a better understanding can be obtained about how the input parameters affect on the models and subsequently the behavior of the models upon uncertainties of the parameters. This approach is followed in almost all asteroseismology analysis and few good examples are given in Dupret et al. (2003); Dupret et al., (2005); Murphy et al., (2013); Kurtz et al., (2015).

In addition, different stellar oscillation codes produced relating to new concepts and new databases should be considered for a robust analysis for selecting an appropriate model. The use of different codes, thereby producing different models to a single observation, would be an ideal to eliminate the effect of model dependencies. Considering this aspect of model convergence to SZ Lyn, different models produced by different codes are discussed in this Chapter.

5.2 HELAS pulsation models.

European Helio and Asteroseismology Network (HELAS) program developed a platform for asteroseismology providing various codes of modeling the stellar pulsations. The computations were performed using Warsaw-New Jersey evolutionary code of Paczyński (Dziembowski and Pamyatnykh, 1993) and linear non adiabatic pulsation code of Dziembowski (1977). Details of the codes are available in Pamyatnykh (1999). The pulsation models were searched in line with the observed frequencies of SZ Lyn listed in Table 3.7.

The pulsation models of radial and non radial were searched in linear non-adiabatic code Dziembowski (1977) through a mass range $1.7\ M_\odot < M < 2.2\ M_\odot$ and chemical compositions Z = 0.015 and Z = 0.02. OPAL opacities (Iglesias and Rogers, 1996) and AGSS09 chemical composition (Asplund, 2009) were used in the computations. The models with frequencies of $l = 0$, $l = 1$ and $l = 2$ modes which are close to the observed frequency of $f_1 = 8.296\ d^{-1}$ were shown in the Figure 5.1
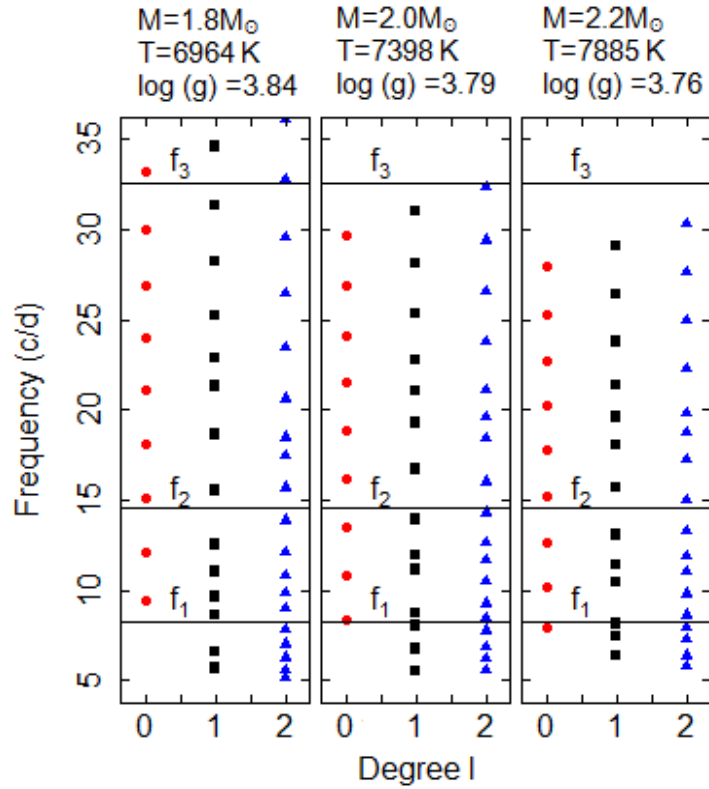
Figure 5.1 HELAS pulsations models for three masses and spherical degree $l = 0$, 1 and 2. The color dots, squares and triangles indicate the frequencies available in the models. The horizontal lines of f_1, f_2 and f_3 are the indications of observed frequencies of SZ Lyn. The errors of the observed frequencies are too small to indicate.

The Figure 5.1 indicates the model frequencies of spherical degree $l = 0$, $l = 1$ and $l = 2$. The model of mass $M = 2.0 M_\odot$ has the closest frequency at $l = 0$ mode with the observed frequency $f_1 = 8.296$ d^{-1}. This is good agreement with the results obtained in mode identification. In mode identification, the TDC non-adiabatic Model 2 with frequency close to f_1 was approximated to $l = 0$ using amplitude ratio method. Furthermore, the HELAS $M = 2.0 M_\odot$ model in Figure 5.1 indicates the presence of two frequencies of $l = 2$ mode close to the observed frequencies f_2 and f_3. This result supports that the frequencies f_2 and f_3 are non-radial and conformed SZ Lyn has both radial and non-radial pulsations. The models used are not only to determine the modes

of frequencies but also provide some idea of the stellar parameters of SZ Lyn. The appropriate HELAS stellar models with close frequencies with the observed fundamental radial mode of $f_l = 8.296$ d^{-1} are tabulated in Table 5.1.

Table 5.1 The HELAS pulsation models of radial fundamental mode of oscillation around the observed fundamental radial mode of $f_l = 8.296$ d^{-1}. Z is the chemical composition and α_{MLT} is the mixing length parameter. The frequency generated by the model is in the last column. The model with * marks are close to the Model 1 and Model 2 of TDC non adiabatic pulsation model which discussed in section 4.

Model	Mass (M$_\odot$)	T$_{eff}$ (K)	Log (g)	Log (L/L$_\odot$)	Z	α_{MLT}	Freq. (d^{-1})
H1	1.7	6613	3.763	1.139	0.02	1.0	8.298
H2	1.8	6912	3.768	1.235	0.02	1.0	8.285
H3	1.9	7205	3.772	1.326	0.02	1.0	8.250
H4	2.0	7518	3.782	1.413	0.02	1.0	8.299*
H5	2.2	8110	3.791	1.577	0.02	1.0	8.249
H6	1.7	6933	3.756	1.227	0.015	0.5	8.255
H7	1.8	7247	3.761	1.324	0.015	0.5	8.230
H8	1.9	7574	3.771	1.414	0.015	0.5	8.269*
H9	2.0	7892	3.778	1.501	0.015	0.5	8.274
H10	2.2	8511	3.789	1.663	0.015	0.5	8.244

The fundamental radial modes of the models in Table 5.1 are very close to the observed fundamental radial mode of 8.296 d^{-1} of SZ Lyn. Since the frequency error of the observation is very much smaller than the separations of the model frequencies in Table 5.1, the determination of a closest model for the observation by looking at list is inappropriate. However, the models of H4 and H8 are consistent with the parameters of the two TDC models in Table 4.1. The HELAS models in Table 5.1 provide evidences that the solution is highly depending on the uncertainties of the parameters of the models. For example, the models H1, H4 and H8 with different sets of stellar parameters are approaching the same solution of the observed frequency of 8.296 d^{-1}. Therefore, the set of parameters courses the model should be subjected to robust analysis with appropriate caveats and uncertainties. In addition, inconsistencies

of α_{ML} with up-to-date value of α_{ML} between 1.8 to 2.0 for Delta Scuti stars (Bowman and Kurtz, 2018) also provide uncertainties to the models.

5.3 MESA Evolutionary models

The evolutionary status of SZ Lyn can be obtained by placing the pulsation models used in Section 4 and in Section 5.2. The state of art evolutionary sequences were generated by Modules for Experiments in Stellar Astrophysics (MESA) code introduced by Paxton et al., (2013), Paxton et al., (2015). The code is comprehensive stellar modeling code with the availability of binary and pulsation evolutions. The evolutionary sequences were computed using version 11701 of the MESA. Initially, the evolutionary tracks of mass ranging from 1.80 $M_\odot$ to 2.0 $M_\odot$ with the step size of 0.05 $M_\odot$ for the standard solar abundance Z=0.014 (Asplund et al., 2009) were computed to represent the SZ Lyn. All the sequences used OPAL opacities (Iglesias & Rogers, 1996) and single fixed value for the mixing length parameter (α_{MLT}) = 2.0. The full set of evolutionary sequences is shown in Figure 5.2. Due to the fact that the stellar evolution, especially the main sequence and post main sequence stages are very much sensitive to metallicity (Z) and overshooting parameter (f_{ov}), a set of models were generated for Z values of 0.01, 0.02 and f_{ov} of 0.00, 0.007 and 0.014 covering the mass range of 1.7 $M_\odot$ to 2.0 $M_\odot$ with a step size of 0.1 $M_\odot$. The sequences were shown in Figure 5.3.
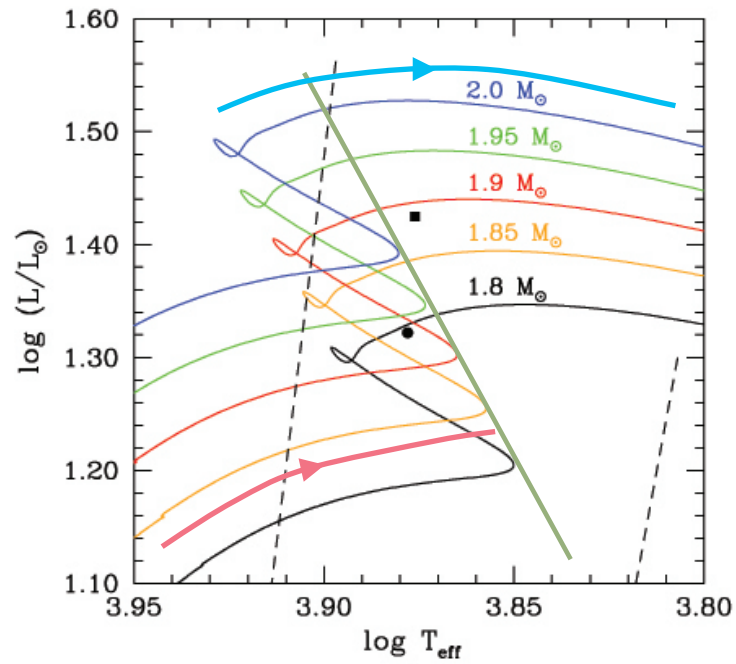
Figure 5.2 The evolutionary tracks of SZ Lyn for Main Sequence (MS) and post main sequence. Four models of different masses from 1.8 $M_\odot$ to 2.0 $M_\odot$ with the steps of 0.05 $M_\odot$ are included. The square and circle indicate the non adiabatic TDC Model 1 and Model 2 mentioned in Table 4.1 respectively. The two dashed lines indicate the instability strip. The purple line is the Termination Age Main Sequence (TAMS). The green arrow line shows the MS stage while red arrow line shows the part of post main sequence stage of the star.
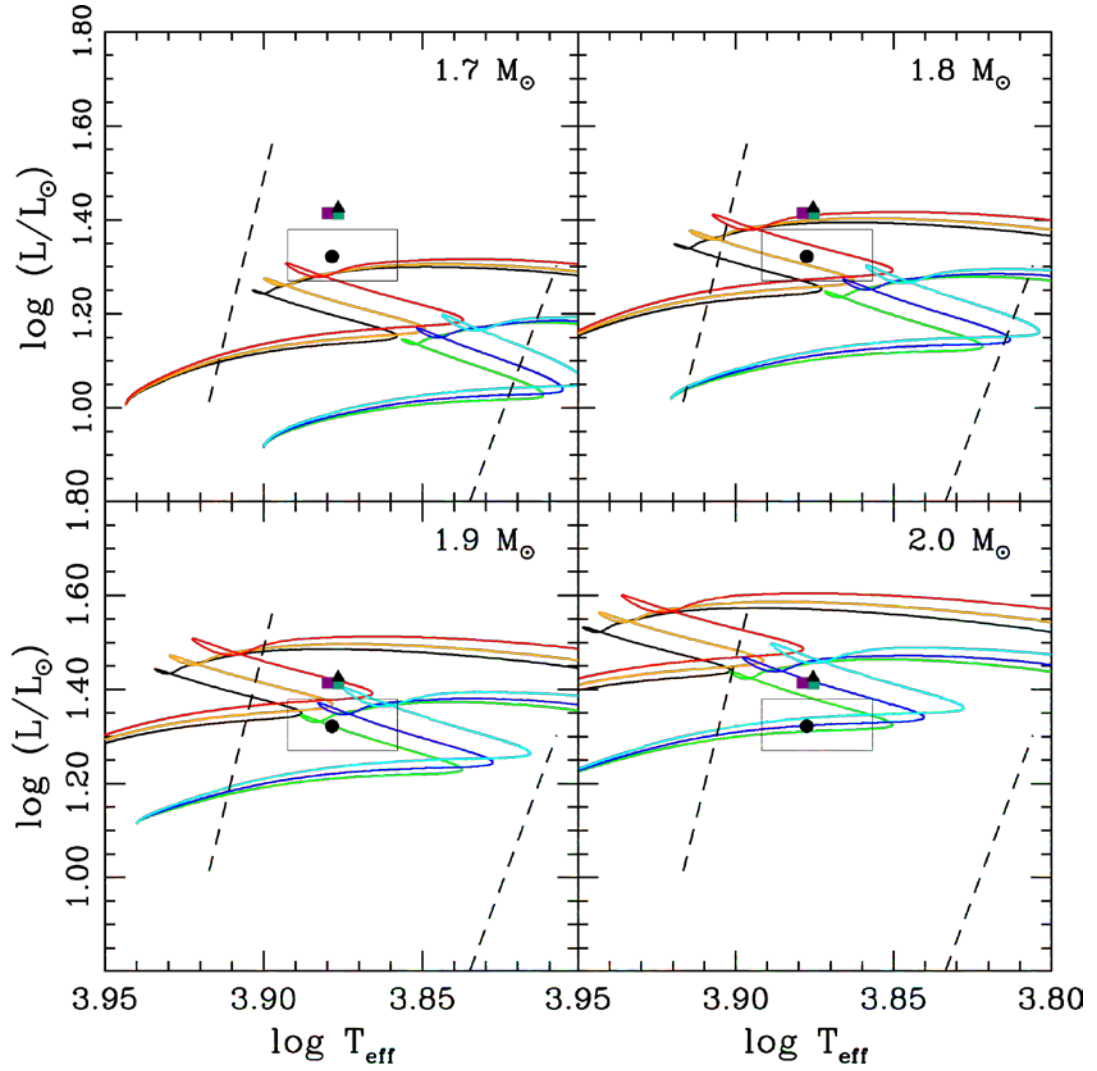
Figure 5.3. Main and post-main sequence evolutionary tracks of stars in the range 1.7 - 2.0 $M_\odot$ for the scaled AGSS09 chemical composition Z = 0.01 (upper set of tracks in each panel) and Z = 0.02 (lower set of tracks in each panel) for α_{MLT} = 2. Curves of green and black colours correspond to f_{ov} = 0.00, dark blue and orange to f_{ov} = 0.007, and light blue and red to f_{ov} = 0.014. The black triangle and dot represent TDC Model 1 and Model 2, respectively (Table 4.1). The purple and green squares represent two asterisk models from Table 5.1. The rectangle shows observation error box. Instability strip is shown in dashed lines.

The placement of two models of masses, 1.9 $M_\odot$ (Model 2) and 2.0 $M_\odot$ (Model 1), in Figure 5.2 and Figure 5.3 give a better understanding of the evolutionary status of the SZ Lyn. In addition, two HELAS pulsation models close to the observed frequency of $f_1 = 8.296$ d^{-1} were also placed in Figure 5.3. By reference to the placements in Figure 5.2 several possibilities can occur. The TDC model (Model 2) of mass 1.9 $M_\odot$ can be either post main sequence of 1.8 $M_\odot$ or 1.9 $M_\odot$ Hertzsprung gap phase of evolutionary models. On the other hand, the TDC model (Model 2) of mass 2.0$M_\odot$ is very much close to the post main sequence of 1.9 $M_\odot$ evolutionary model. The dependency of metallicity on luminosity is significant as shown in Figure 5.3. Therefore the placements of both TDC and HELAS models in Figure 5.3 provide a better approximation of metallicity of SZ Lyn. According to the MESA models of 1.9 $M_\odot$ and Z = 0.02, the TDC Model 2 of mass 1.9 $M_\odot$ is in the Hertzsprung gap phase while MESA models of 2.0 $M_\odot$ and Z = 0.02, the TDC Model 2 of mass 1.9 $M_\odot$ is in the phase of the main sequence. In both cases, the TDC model of mass 1.9 $M_\odot$ is within the observational error box as well. It is obvious that inconsistencies are taking place when output of one model is compared with another model. Despite these inconsistencies, the physical parameters of SZ Lyn can be represented within ranges considering different models and finding out common factors. Since Model 2 of mass 1.9 $M_\odot$ is the more appropriate model for the observation, the evolutionary tracks indicate this model placed either post main sequence of 1.8 $M_\odot$ or 1.9 $M_\odot$ Hertzsprung gap of about 1000 years. Therefore, SZ Lyn should be either in post main sequence or the stage of Hertzsprung gap with the error of mass ±0.1 $M_\odot$. The set evolutionary tracks in Figure 5.2 and Figure 5.3 are also emphasized the conclusion made. The HELAS pulsations models also indicated that the models of masses 2.0 $M_\odot$ and 1.9 $M_\odot$ in Table 5.1 have the pulsation frequencies closed to the observed $f_1=8.296$ d^{-1}. The analysis was performed with three different codes namely, TDC

non-adiabatic code, HELAS non-adiabatic pulsation code and MESA evolutionary sequences. From the generated ample models, the best model for SZ Lyn was selected. In this process, although the inconsistencies were found from one code to another, due to the code limitations and outputs, a general model that represents SZ Lyn was made. Based on that, the mass of SZ Lyn is determined as $1.8 M_\odot \leq M \leq 2.0 M_\odot$. This estimation is much higher than the mass $1.57\ M_\odot$ of SZ Lyn determined by Fernley et al. (1984). The ideal set of other physical parameters of SZ Lyn is given in the Table 5.2.

5.4 Physical parameters of SZ Lyn

Since only one radial mode determined without any overtones, the period ratio method would not applicable to determine the average density of SZ Lyn. Nevertheless, we could estimate the average density of SZ Lyn using the pulsation constant (Q) using the relation in equation 5.1.

$$P = Q \left(\frac{\rho}{\rho_\odot} \right)^{-1/2} \qquad\qquad 5.1$$

above from adiabatic sound speed where P is the period of the fundamental oscillation in days and Q is the pulsation constant. The average density of the Sun is $\rho_\odot = 1.4103$ g cm^{-3} and our stellar pulsation models in Sec. 4 predicted the Q values of 0.035 for the Model 2 result in an average density of $\rho = 0.1189$ gcm^{-3}.

Furthermore, with the fundamental period of SZ Lyn, P = 0.1205299 d and for more narrow range of Q values $0.0327 \leq Q \leq 0.0332$ (Fitch, 1981), the average density is found to be $\rho = 0.1054 \pm 0.0016$ gcm^{-3} for the above range. Suarez et al., (2014) computed the mean densities of δ Scuti stars using their virtual observatory tool, TOUCAN, found that the fundamental frequency range of 95 -113 µHz (0.121832 - 0.102425 d) has relative densities ($\rho/\rho_\odot$) less than 0.11. Hence we can conclude that the density of $\rho = 0.1054 \pm 0.0016$ gcm^{-3} is an appropriate value for SZ Lyn as expected for an evolved star.

Table 5.2 Best fitting physical parameters of SZ Lyn

Physical parameter	Value
Mass ($M_\odot$)	$1.8 \leq M \leq 2.0$
Temperature (K)	$7500\ K \leq T_{eff} \leq 7800\ K$
Gravity, Log (g)	3.86
Radius ($R_\odot$)	2.68
Mean Density (g cm^{-3})	0.1054 ± 0.0016
Chemical composition	$0.14 \leq Z \leq 0.20$
Mixing length parameter	$1.7 \leq \alpha_{MLT} \leq 2.0$

Chapter 6

Spectroscopic observations of Delta Scuti stars

6. 1 Introductory remarks

The stellar oscillations vary the flux and hence the effect transfers to the photosphere to make Doppler displacements. The Doppler displacements lead to profile variations in the spectral lines. Therefore, spectroscopic observations can be used to identify oscillation signatures in pulsation stars. However, these non-radial velocity fields are very small, particularly for minor modes, the high resolving power (typically above 40,000) and high signal-to-noise ratio (above 200) are preferable (Aerts et al., 2010). Nevertheless, Viskum et al., (1998) used low resolution spectroscopy to identify dominant modes of FG Vir. Similar to the multi-color amplitude ratio method discussed in Chapter 4, the properties of the line profiles such as Equivalent Widths (EW), Full Width at Half Maxima (FWHM), asymmetry, etc. of spectral lines can be used to differentiate the oscillation modes. These properties are highly dependent on the spectral line chosen for the analysis. The availability of Balmer lines, Hα, Hβ and Hγ, is very prominent in all spectroscopic observations, but due to the very high broadening due to the Stark effect, the profile variations due to the oscillations may not be discovered. In fact, the metallic lines such as Fe, Mg, Si are preferable for mode identification due to the less natural broadening effects (Aerts and De Cat 2003, Aerts et al., 1999, Zema et al., 2006).

The computational codes for theoretical line profiles attempted by Aerts and Waelkens (1993), De Ridder et al., (2002), Zima (2008) are being used for mode identification. The azimuthal order m of an oscillation can be characterized by rotational splitting in the power spectra. Since most Delta Scuti stars are slow rotators, this feature is not prominent. Therefore, azimuthal order, m is very rarely identified using photometry. Comparatively, the high resolution spectroscopy is very useful to identify m. The computational models shown in Figure 6.1 indicate the variation of line profiles for combinations of l and m. However, the spectroscopic observations of Delta Scuti stars are still very limited compared to the photometric observations. Therefore, the pulsation analysis through spectroscopy is still somewhat new compared to photometry and more observations are essential to understand the behaviors of models. This chapter discussed, the low resolution (R=1000)

spectroscopic observations of SZ Lyn taken from Mount Abu observatory (see Table 2.3).
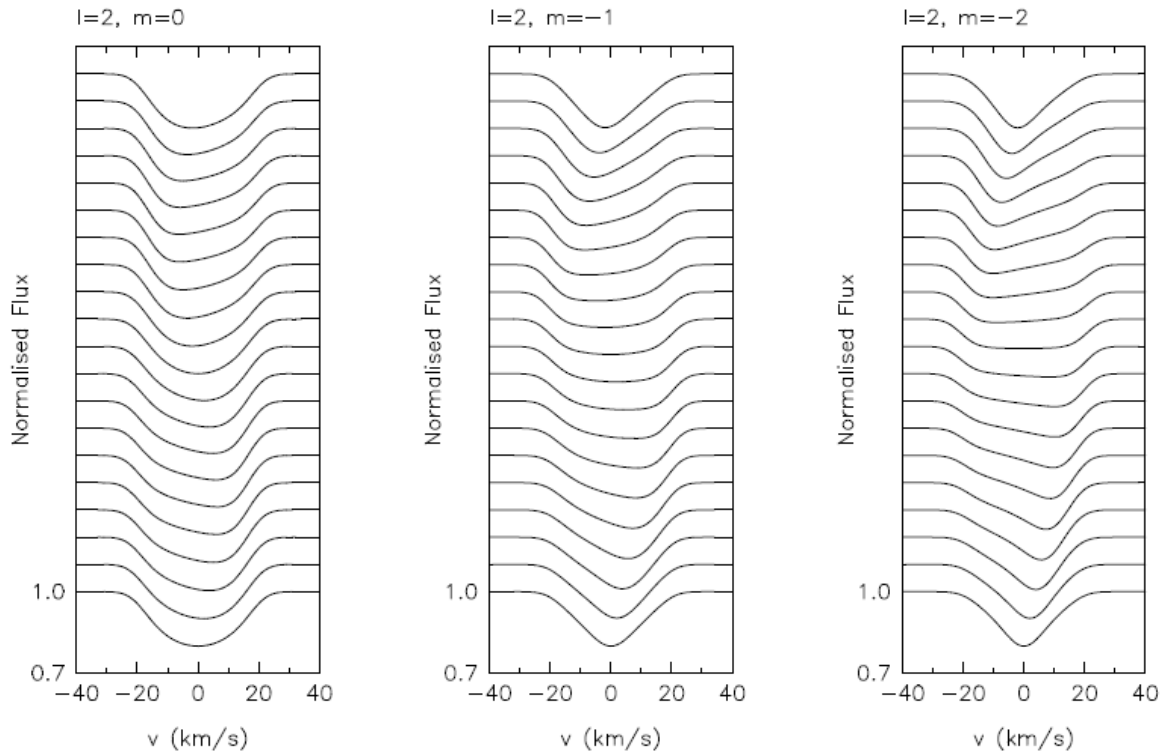
Figure 6.1 Theoretically determined line-profile variations calculated by means of the basic formalism described in the text considering an $l = 2$ mode and $m = 0$ (left panel), $m = -1$ (middle panel), and $m = -2$ (right panel) respectively. The other velocity parameters are: pulsation amplitude $v_p = 5$ km/s, projected rotational velocity $v \sin i = 30$ km/s, thermal velocity $v_{int} = 4$ km/s, and inclination $i = 55°$. The line-of-sight velocity is given on the x-axis while the normalized flux (unitless, with values between 0.7 and 1.0) is drawn on the y-axis. The profiles are stacked according to increasing oscillation phase, from 0.00 (lowest profile) to 0.95. (uppermost profile) in steps of 0.05. The figure and caption is taken from Aerts et al., (2010), their figure 6.12. The image is reproduced with the written permission of Springer.

6.2 Equivalent width of Balmer lines

The Balmer lines are very strong in A and F type stars. The SZ Lyn is A-F type star so that the very strong Balmer lines are present. The Normalized spectra covering the entire pulsation cycle were obtained to see the variations of Balmer lines over the pulsation cycle. The observations epoch of spectra were converted to phase using the T_o = 2456664.224734 HJD and the main pulsation period of 0.12054 days. The low resolution spectra over the entire pulsation phase are shown in Figure 6.2. Three Balmer lines, Hα (6563 Å), Hβ (4861 Å) and Hγ (4340 Å) were used for the analysis. In addition, few metallic lines were also detected and Mg I Triplet (5167.3 Å, 5172.7 Å and 5183.6 Å) is shown in inset of Figure 6.2.
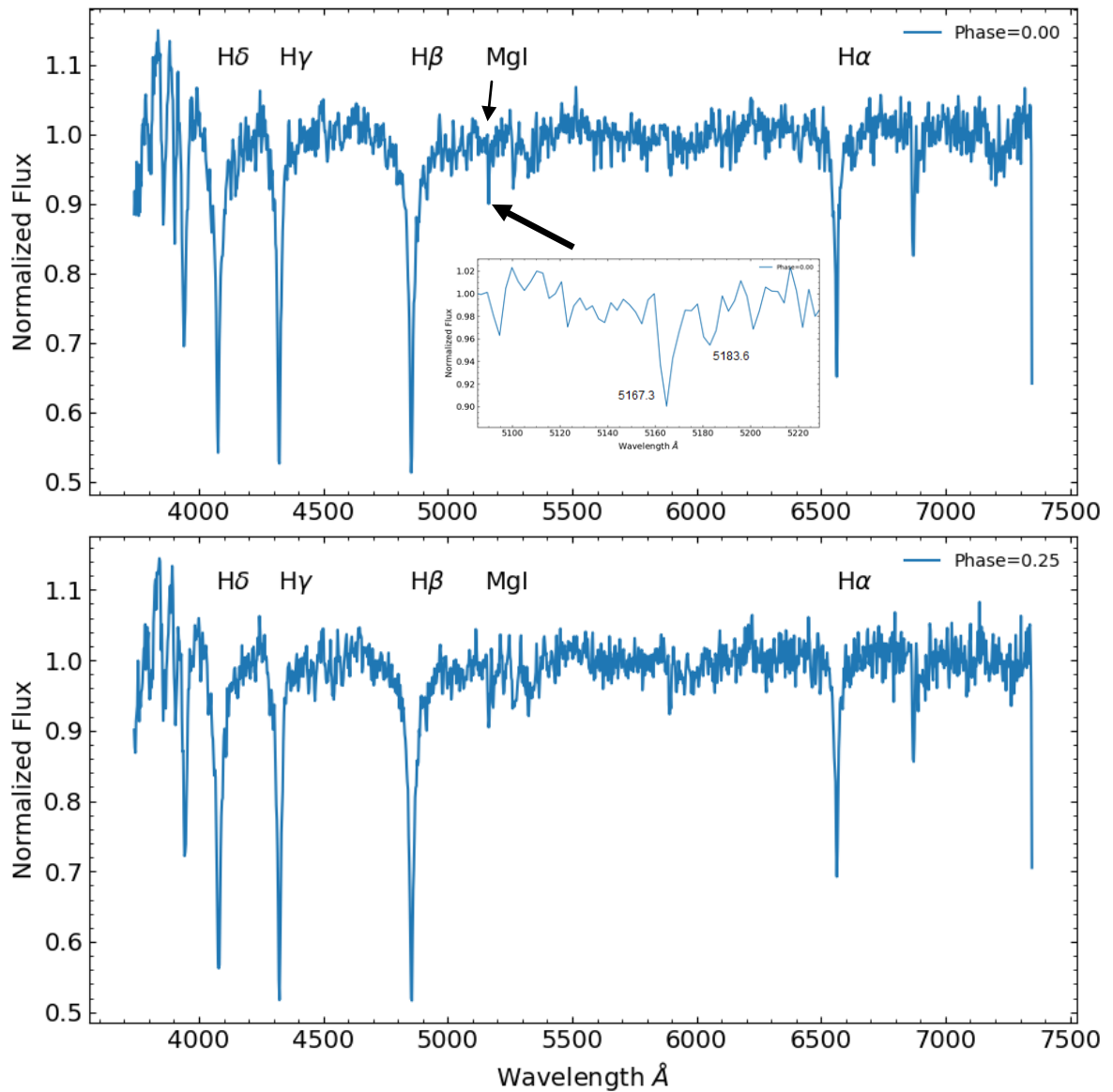
Figure 6.2. The low resolution absorption spectra of SZ Lyn for 0.0 and 0.25 phase. The phase is relative to the epoch T_0=2456664.224734 HJD and period of 0.12054 days (f_1=8.296 d^{-1}). The inset plot is the magnified Mg I (Triplet). The two lines 5167.3 Å and 5183.6 Å are well resolved while line 5172.7 Å is not resolved.
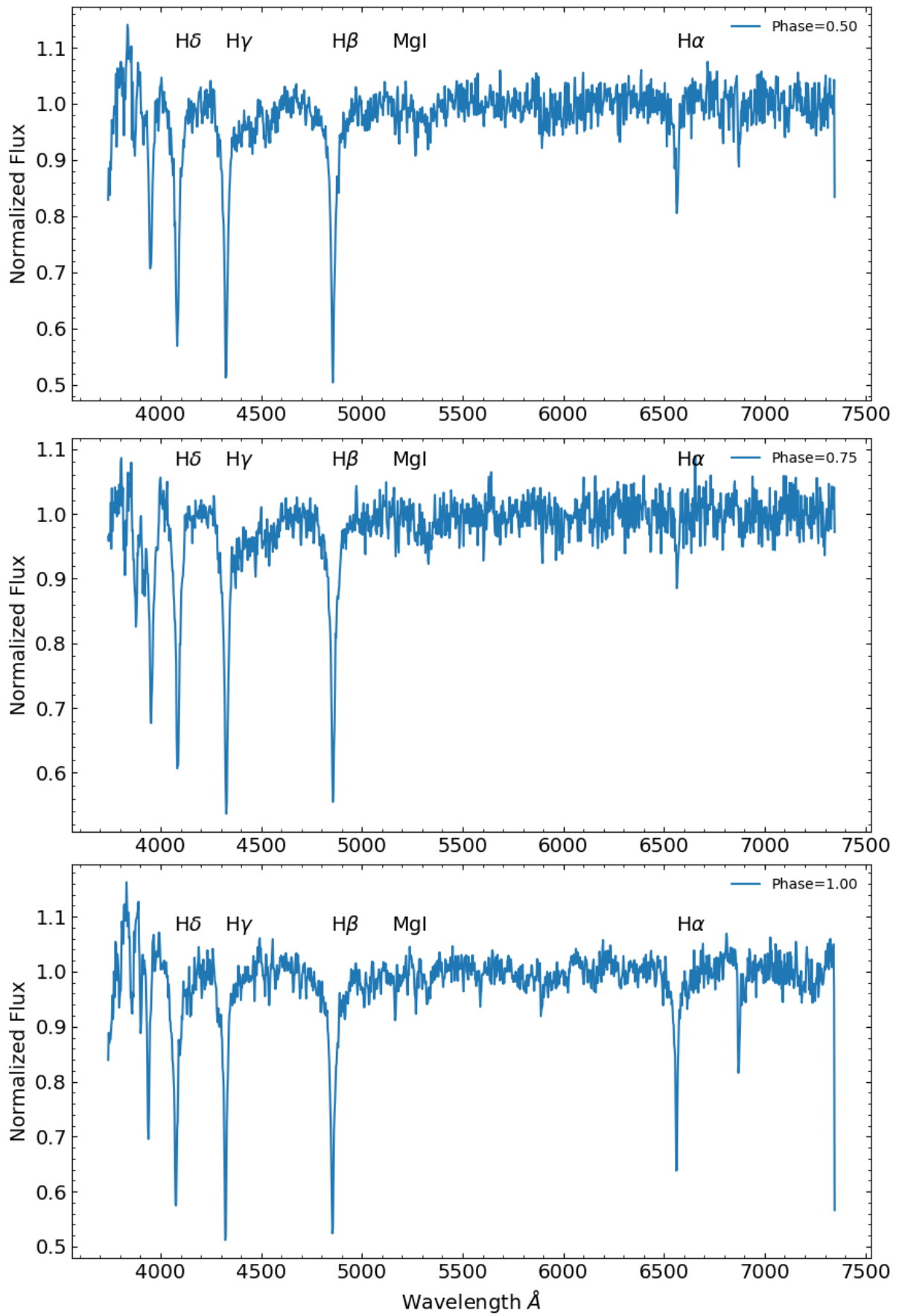
Figure 6.2 Continued. Low resolution spectra of SZ Lyn.

The EW and FWHM of Balmer lines were obtained using the IRAF '*splot*' routine. Both sides of the profile wings were considered in the calculation of the EW and the FWHM. The variation of the EW and FWHM over the primary pulsation cycle is given in Figure 6.3. The EW represents the energy emission from the star. The Figure 6.3 shows the EW's of higher wavelengths, particularly Hγ and Hβ, are higher concerning the rising phases (0.0 and 1.0) of the light cure. At the same phases the EW's of the low wavelength side, Hα, are minimized. This observation characterizes the variation of the spectral type of SZ Lyn from F to A type during the primary pulsation cycle. This spectral change is emphasized by the observations of Delta Scuti star in Figure 6.5. The amplitude ratios of the EW of Hα and Fe I line were used by Viskum et al., (1998) and amplitude ratios of photometry are replaced by amplitude ratios of the EW variations. Due to the low resolution spectroscopy of SZ Lyn, the metallic lines such as Fe and Mg are very weak and could not measure the EW's with higher accuracy. However, the asymmetric variation of radial expansion and contraction is clearly seen in the phase diagram Figure 6.3.

As shown in Figure 6.1, the investigation of individual line profile variations reveals the spherical degree *l* and azimuthal order *m* of non-radial oscillations. The high resolution spectra (R> 40,000) should be subjected to different techniques such as well known Cross-Correlation Function (CCF), Least-Square De-convolution (LSD), Pixel-by-Pixel method, etc. (more details Aerts et al., 2010) to determine *l* and *m*. Although the SZ Lyn was observed in low resolution (R≈1000) the profile of Hβ variation over the fundamental period of f_1=8.296 d^{-1} was investigated. The Hβ line profile over the entire pulsation is shown in Figure 6.4. The normalized spectra were shifted by 0.1 in y- axis for clarity. Due to the low resolution, the fine variation could not be seen in the profile. The observation line of Hβ is very much close to the theoretical line of Hβ (4861Å) and slightly less. This may be due to either the error of the wavelength calibration or the non-correction of the radial velocity of the binary orbit. The correction of radial velocity due to binary is impossible without the knowing the orbital phase of the binary. Due to the very large orbital period of binary (1173.5 days Soliman et al., 1986) and the single line spectroscopic binary nature of SZ Lyn there are no radial velocity data available for SZ Lyn. Therefore, the orbital phase could not be determined.
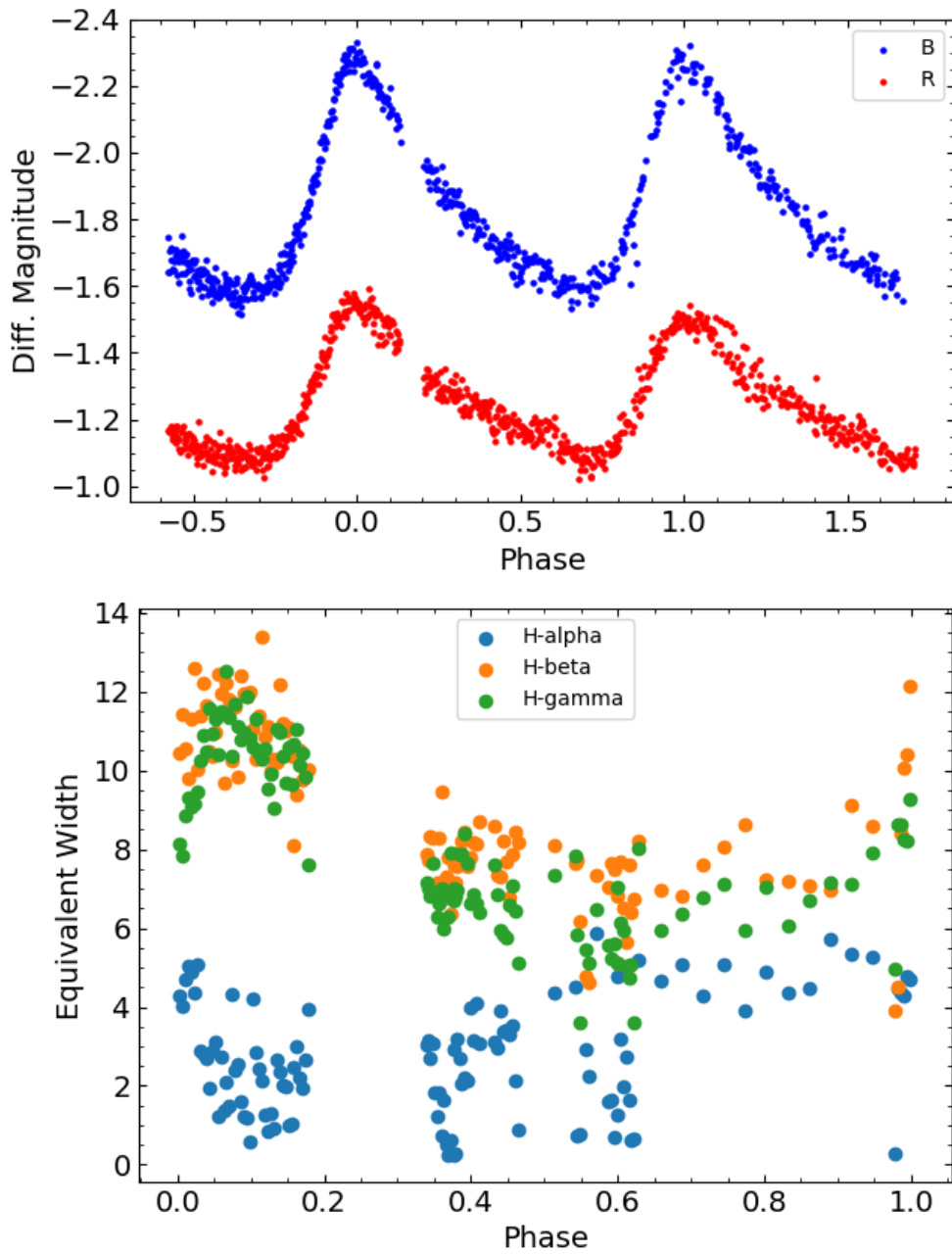
Figure 6.3. Above: The magnitude variation of SZ Lyn in B and R bands with the phase. Below: The variation of the equivalent width of the three Balmer lines, Hα, Hβ and Hγ with the phase of the fundamental frequency (f_1=8.296 d^{-1}) of SZ Lyn. The phase conversion is based on epoch T_0 = 2456664.224734 HJD and period = 0.12054 days (f_1=8.296 d^{-1}). There is an observation gap between 0.20 and 0.35.

6.3 Hβ line profiles of SZ Lyn

The Hβ line profiles of SZ Lyn in Figure 6.4 reveal Doppler shift due to pulsation. The phases of 0.003 and 0.999 which are closed to 0 and 1 phases where the magnitude of B and R maximum (See Figure 6.3) are shifted to the blue side of the spectra with respect to theoretical line Hβ of 4861 Å. The phases of 0 and 1 are the maximum magnitude and brightness and hence showing the radial expansion of the star towards the line-of-sight. The contracting phase of the star corresponds to 0.1 to 0.7 in phase diagram shows the decreasing brightness in Figure 6.3 and similarly the Hβ profiles in Figure 6.4 show the red shift of the spectral line especially at phases 0.103 and 0.631. In these phase the stellar photosphere contracts and therefore moves away radially from the line-of-sight. This observation explains the most prominent fundamental mode of radial pulsation in terms of spectroscopic profiles of SZ Lyn. The distribution of effective temperature (T_{eff}), spectral type, radial velocity and radius (ΔR) in terms of magnitude (Δm) for δ Cephei given in Figure 4.1 (Böhm-Vitense, 1992) also emphasized the similar results.

In addition to this, there is another variation at the phases 0.339 and 0.400. The spectral line has shifted towards the blue side again during these phases. The consequence of this may be due to another independent pulsation frequency which may be a radial overtone or this can be the immediate harmonic $f_2 = 16.592$ d^{-1} of the radial fundamental of $f_1 = 8.296$ d^{-1}. Although the resolution is low at least some of the pulsation characteristics have been discovered with this observation.
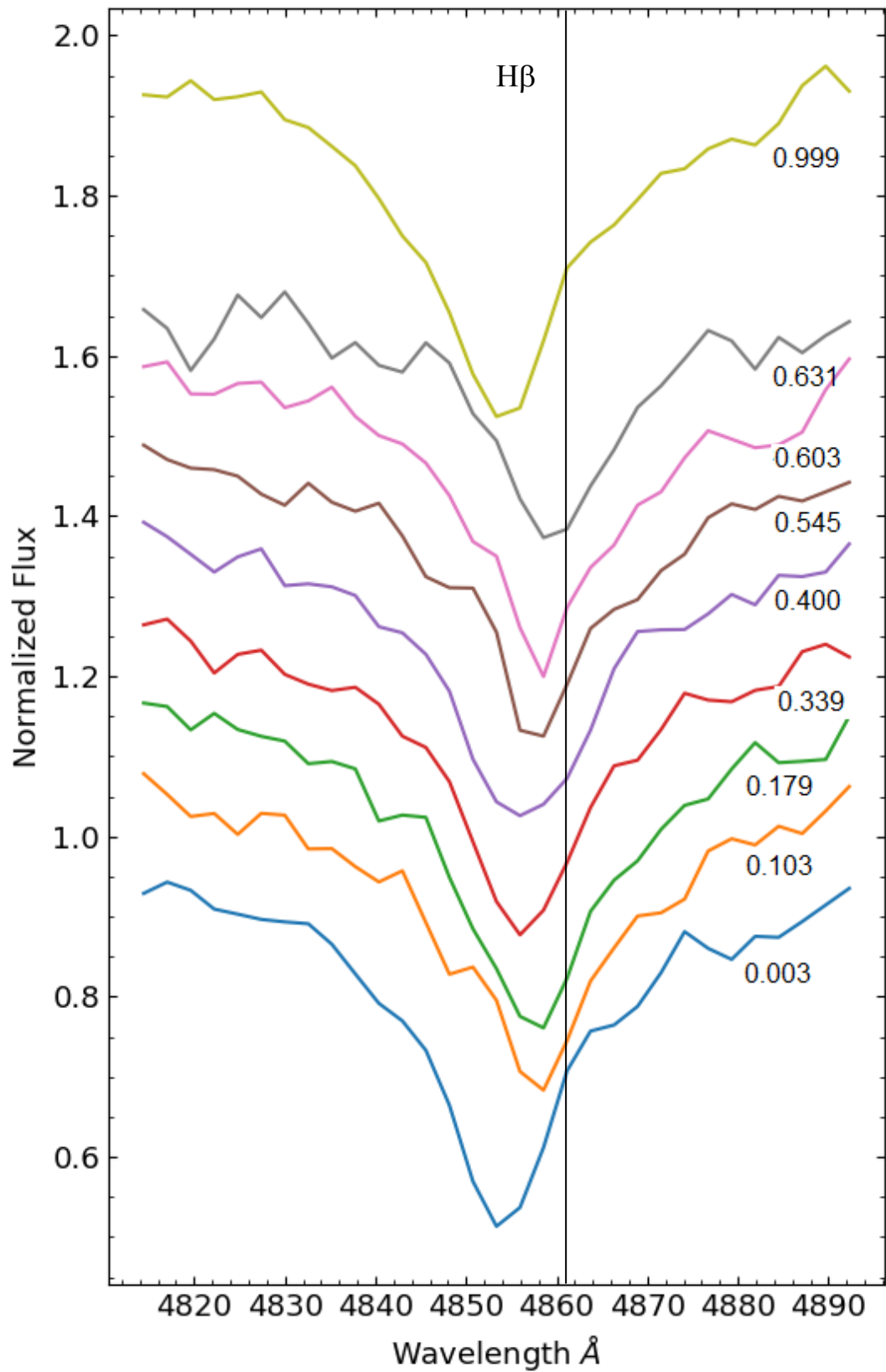
Figure 6.4. Line profile variation of Hβ (4861 Å) over the phase of fundamental frequency f_1=8.296 d^{-1}. The phase of each profile is shown in the right hand side. The vertical line is the theoretical value of Hβ (4861 Å). The normalized spectra were shifted by 0.1 in y axis consecutively for the clarity.

6.4 Theoretical line profile variations.

The pulsation velocity fields in the stellar surface depend on several unknown. Therefore, the mode identification using line profile variations is complicated compared to the mode identification using photometry. Osaki (1971) introduced a scheme on how to compute theoretical line-profile variations for non-radial oscillations. It is clear that the velocity field based on the non-radial oscillation theory contains many free parameters. To overcome the computational obstacle of line-profile fitting, and to make the identification more objective, a method called moment variations of the spectral lines was first introduced by Balona (1986) and further developed by Aerts et al., (1992), De Pauw et al., (1993), Aerts (1996), Cugier & Daszynska (2001) and Briquet & Aerts (2003). This method is appropriate to identify low-degree modes ($l \leq 4$) in slow rotators ($v \sin i \leq 50$ kms^{-1}) (Aerts et al., 2010).

The moment method is defined as the convolution of an intrinsic profile with the flux in the direction of the observer. The intrinsic profile is assumed to be Gaussian with a total pulsation and rotation velocity fields. The line profile can be reconstructed from the entire series of moments of order j. The first three moments, *i.e.*, those for $j = 1, 2, 3$ moments are connected to a specific property of the line profile:

i) the first moment is the *centroid* of the line profile in a reference frame with origin at the stellar centre (v)

ii) the second moment is a measure of the width of the line profile (v^2)

iii) the third moment is a measure of the skewness of the line profile (v^3)

In Figure 6.5 and Figure 6.6 show some observed profile variations and the three normalised moments of the Delta Scuti star (Aerts et al., 2010). The full lines in Figure 6.6 correspond to the result of a harmonics. The peak-to-peak value of the first moment causes by main oscillation of 7.098 d^{-1}.
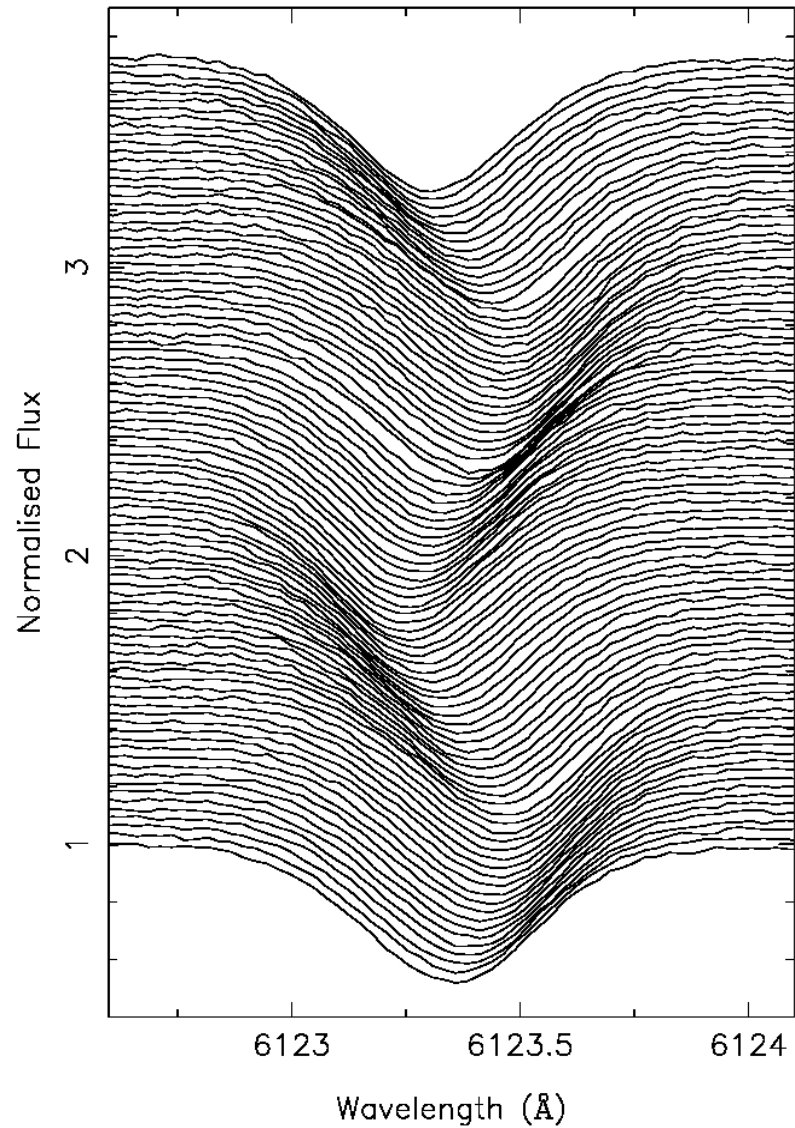
Figure 6.5 Observed line-profile variations of the δ Sct star ρPup obtained in 1995 with the Coud´e Auxiliary Telescope of the European Southern Observatory in Chile phased with the dominant frequency of 7.098 d^{-1}. Data taken from Mathias et al. (1997). The imaged is reproduced with a written permission of Springer.
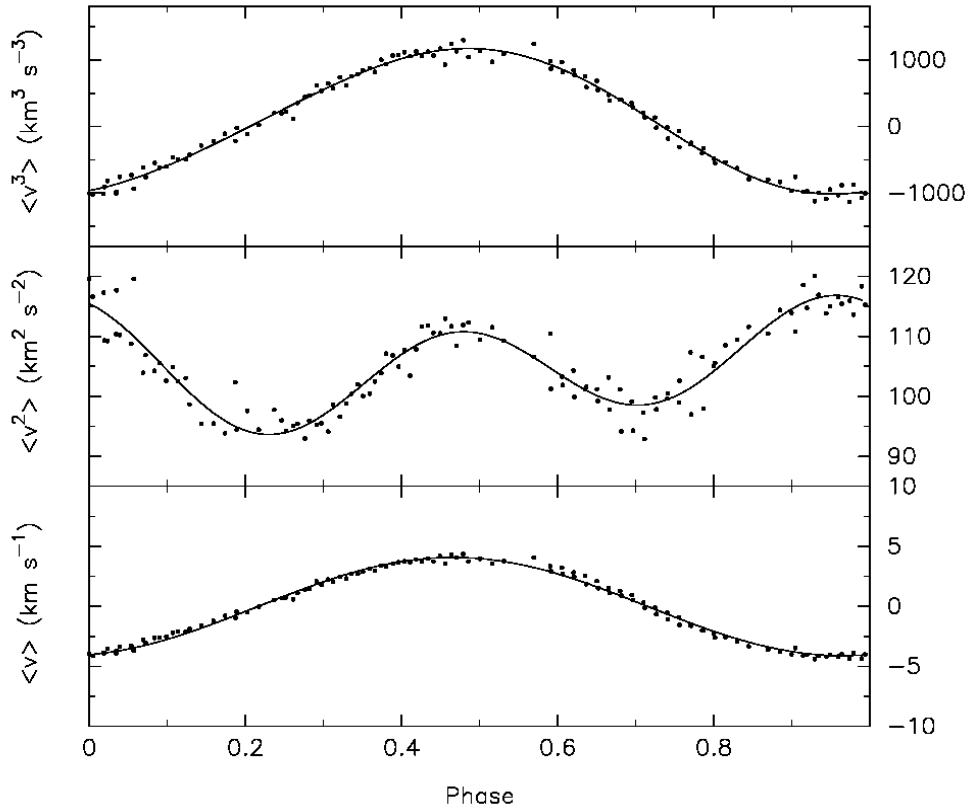
Figure 6.6. Phase diagrams of the normalized moments of the δ Sct star ρ Pup for the dominant frequency 7.098 d^{-1}. The dots are the observations and the lines are the result of harmonic analyses. Data taken from Mathias et al., (1997). The analysis shows that this mode is radial. Part of the scatter in the diagrams arises from the presence of other, weaker modes. Figure and caption are reproduced with a written permission of Springer.

For a linear oscillation, the first moment is expected to be a sinusoidal as seen in Figure 6.6. The second moment is a very good approximation for the azimuthal number m. When v^2 can be described by a single sine function it is possible to determine that $m = 0$. The middle panel of Figure 6.6 therefore implies that it is likely that $m = 0$ for the main mode of ρPuppis, although there is clearly a small sinusoidal contribution of v^2 is not fully symmetric. Any intermediate situation, i.e., a second moment in which both a term with frequency of the harmonics of ω and one with 2ω occur with equal amplitudes, points towards a tesseral mode.

The moment method should be used carefully with low resolution spectra. Since the low resolution spectra have only few data points to represent the line profile, here in SZ Lyn there are only 10 data points to represent the Mg I triplet, the flux values for moment calculation should be taken by interpolation of the 10 data points. When 10 data pints fit with a suitable function the original shape of the line profile may be modified. This may add some artificial variations to the overall profile and hence affected to the moment determination. Therefore, the low resolution spectra of SZ Lyn taken at Mount Abu observatory cannot be used for moment analysis. However the Figure 6.4 shows the line profile variations of Hβ of SZ Lyn.

Chapter 7

Kepler observations of Delta Scuti stars

7.1 Introductory remarks

The NASA Kepler mission was launched March 6, 2009, with a primary objective to use high precision long time-series photometry to search for exo-planets via planetary transits. This high precession photometry is being extensively used to study stellar variability as well. The K2 mission initiated in 2013 after the failure of the second of four reaction wheels that were used to point the spacecraft cameras continuously toward the same field of view in the Cygnus-Lyra. The spacecraft eventually exhausted its fuel and was retired on November 15, 2018 (Guzik et al., 2019). The initial four year lifetime of Kepler observed 200 000 stars with a precision of 1 part per million (ppm) (Bowman, 2017).

Kepler data can be obtained through the exo-planet archive at the NASA Exo-planet Science Institute and the Mikulski Archive for Space Telescopes (MAST) hosted by the Space Telescope Science Institute (STScI). There are three main data products, Full Frame Images (FFIs), Target Pixel Files (TPFs) and Light Curve Files. The light curves are corrected for outliers, discontinuities and other systematic effects. Therefore, light curves are easy to use for variability studies. To serve the data needs, Kepler Asteroseismic Science Operations Center (KASOC) is established at Aarhus University, Denmark. KASOC provides asteroseismological data from the NASA Kepler and K2 missions to astronomers who are members of the Kepler Asteroseismic Science Consortium (KASC). The KASOC archive classifies the pulsation stars into subcategories and Delta Scuti stars corrected by Working Group 4 (WG4). The light curves are available in both Long Cadence (LC) and Short Cadence (SC) exposures. This chapter includes the analysis of 6 Delta Scuti stars obtained through the KASOC data archive. The details of preliminary preparations of the data are included in section 2.4 in Chapter 2.

7.2 KIC 4077032

One minute exposure SC Kepler light curves of KIC 4077032 obtained through KASOC data archive were analyzed to determine the oscillation frequencies. The reduced light curve was subjected to frequency analysis using PERIOD04 (Breger and Lenz, 2005). A part of reduced light curve is shown in Figure 7.1. Eighteen dominant frequencies were found in KIC 4077032 and listed in Table 7.1. The errors of the frequency and amplitude were obtained by hundred iterations Monte Carlo Simulation in PERIOD04. The amplitude spectra of first nine frequencies are shown in Figure 7.2.
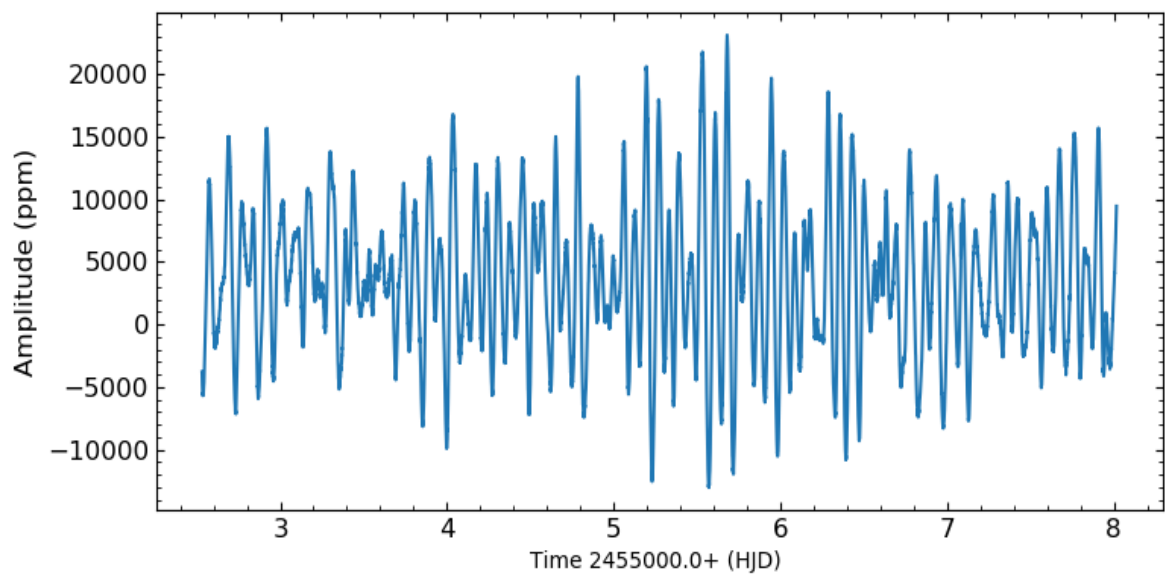
Figure 7.1. A part of light curve of KIC 4077032. The Kepler flux is converted to ppm. Note that beating effect of different modes causes the light cove more complex with variations.

KIC 4077032 was observed by LAMOST low resolution spectroscopic survey and determined the temperature (T_{eff}) and log (g) as 7270 K and 3.82 respectively. Data from the Kepler mission provides the same parameters as T_{eff} = 6789 K and log (g) = 4.05. In addition, parallax of 1.9789±0.0389 milliarcseconds observed by Gaia mission results in a distance of 505.33 pc. The apparent magnitude m_v = 9.71 with the distance scale gives the absolute magnitude (M_v) of KIC 4077032 as 1.19. This absolute magnitude was converted to bolometric magnitude (M_{bol}) using bolometric correction (BC) given in Cox (2015). This bolometric magnitude (M_{bol}) and other physical parameters of KIC 4077032 were substituted to the equation 7.1 to determine the pulsation constant Q for the frequencies listed in Table 7.1. The fundamental radial oscillations can be determined by the pulsation constant, Q (Balona et al., 2012, Breger and Bregman, 1975) given by equation 7.1. and hence the average density (ρ) of the star can be estimated using equation 7.2.

$$\log(Q) = \log(P) + \frac{1}{2}\log(g) + \frac{1}{10}M_{bol} + \log(T_{eff}) - 6.454 \qquad 7.1$$

$$P = Q\left(\frac{\rho}{\rho_\odot}\right)^{-\frac{1}{2}} \qquad 7.2$$

Table 7.1. The oscillation frequencies of KIC 4077032. The pulsation constant (Q) is given for the substantially different frequencies only.

	Frequency (d^{-1})	Amplitude (ppm)	Identification	Pulsation Constant (Q)
f_1	14.482±0.001	3831±280	Non radial	0.018
f_2	8.038±0.001	2997±231	Fundamental Radial	0.033
f_3	14.799±0.001	2986±344		
f_4	12.046±0.001	3020±595		0.022
f_5	12.152±0.002	1943±80		
f_6	9.640±0.001	1790±63		0.028
f_7	14.059±0.012	1660±93		
f_8	12.191±0.001	1704±69		
f_9	9.736±0.001	1448±72		
f_{10}	6.311±0.001	1357±110	f_1-f_2	
f_{11}	16.298±0.001	1067±62		
f_{12}	18.563±0.001	963±175		
f_{13}	12.334±0.001	947±58		
f_{14}	14.626±0.001	964±72		
f_{15}	6.936±0.011	917±66	f_3-f_2	
f_{16}	11.679±0.001	842±187		
f_{17}	22.125±0.011	822±160		
f_{18}	14.089±0.011	800±68		

The fundamental radial modes of Delta Scuti stars have a well defined range of $0.0327 \leq Q \leq 0.0332$ (Fitch, 1981). The Q values determined for the larger amplitude frequencies 14.482 d^{-1} and 8.038 d^{-1}. The Q value, 0.033, for the frequency 8.038 d^{-1} is well within the range of Q values for the fundamental radial nodes given by Fitch in 1981. Therefore, frequency 8.038 d^{-1} was concluded as the fundamental radial mode of KIC 4077032.

The set of frequencies consist of several non-radial oscillations. Rotational splitting of frequencies is used to detect these non-radial modes. m ≠ 0 in equation 1.9 and 1.12, the phase factor results traveling waves in both, direction of stellar rotation and against. These traveling waves represent $m > 0$, prograde modes and $m < 0$ retrograde modes. For a spherically symmetric star, the rotational multiplet is given by $2l+1$ such that dipole mode of $l = 1$ gives m = -1, 0 and +1 azimuthal orders. In a rotating star, the Coriolis force causes pulsational variations and because of this effect, the prograde modes traveling in the direction of rotation have frequencies slightly lower than the m = 0 central mode, and the retrograde modes going against the rotation have slightly higher frequencies, thus the degeneracy of the frequencies of the multiplet is lifted. This characteristic of frequency splitting can be seen in the amplitude spectra. The highest amplitude mode of f_1 = 14.482 d^{-1} has four frequencies, f_3, f_7, f_{14} and f_{18}, alongside it (See Figure 7.3). This multiplet was further analyzed considering rotational splitting. The first order approximation of rotational splitting was given by Ledoux (1951);

$$f_{nlm} = f_{nl0} + m(1 - C_{nl})\frac{\Omega}{2\pi}$$

7.3

Where f_{nlm} is the observed frequency and f_{nl0} is the unperturbed central frequency of the multiplet (m = 0) which is unaffected by the rotation. C_{nl} is Ledoux constant which has value of less than 1. Ω is the angular velocity of the star.

The stellar rotation period (P_{rot}) can be given by;

$$P_{rot} = \frac{1 - C_{n,l}}{f_{n,l,m} - f_{n,l,0}}$$
7.4

The offset of f_3 and f_7 from f_1, 0.317 d^{-1} and 0.423 d^{-1} respectively are different and the symmetry of rotational splitting was not observed. If the rotational axis is not perpendicular to the line of sight and has some inclination, this asymmetry can occur in the rotational splitting. The amount of splitting can be used to estimate the rotational period Ω of the star using equation 7.3. In 2015, spectroscopic observations of Niemczura et al., determined the projected rotational velocity v sin (i) for KIC 4077032 as 17 km/s. The v sin(i) and the Kepler data of radius R = 1.772 R$_\odot$ give the rotation period as 5.278 days and hence using equation 7.4, the predicted rotational splitting was estimated. The estimated rotational splitting of 0.189 d^{-1} is much less than the two measured values for f_3 and f_7, resulting that the two separations were not consistent enough to be rotational splitting. Therefore, the presence of the two peaks, f_3 and f_7, could not be confirmed as the rotational splitting. However, without uncertainties of the parameters of v sin (i) and radius (R), a firm conclusion cannot be made about the two very close peaks of f_3 and f_7 whether they are rotational splitting or not. The average density of KIC4077032 was estimated for the fundamental radial mode of f_2 = 8.038 d^{-1} using equation 7.2 as 0.07 ± 0.01 $\rho_\odot$.
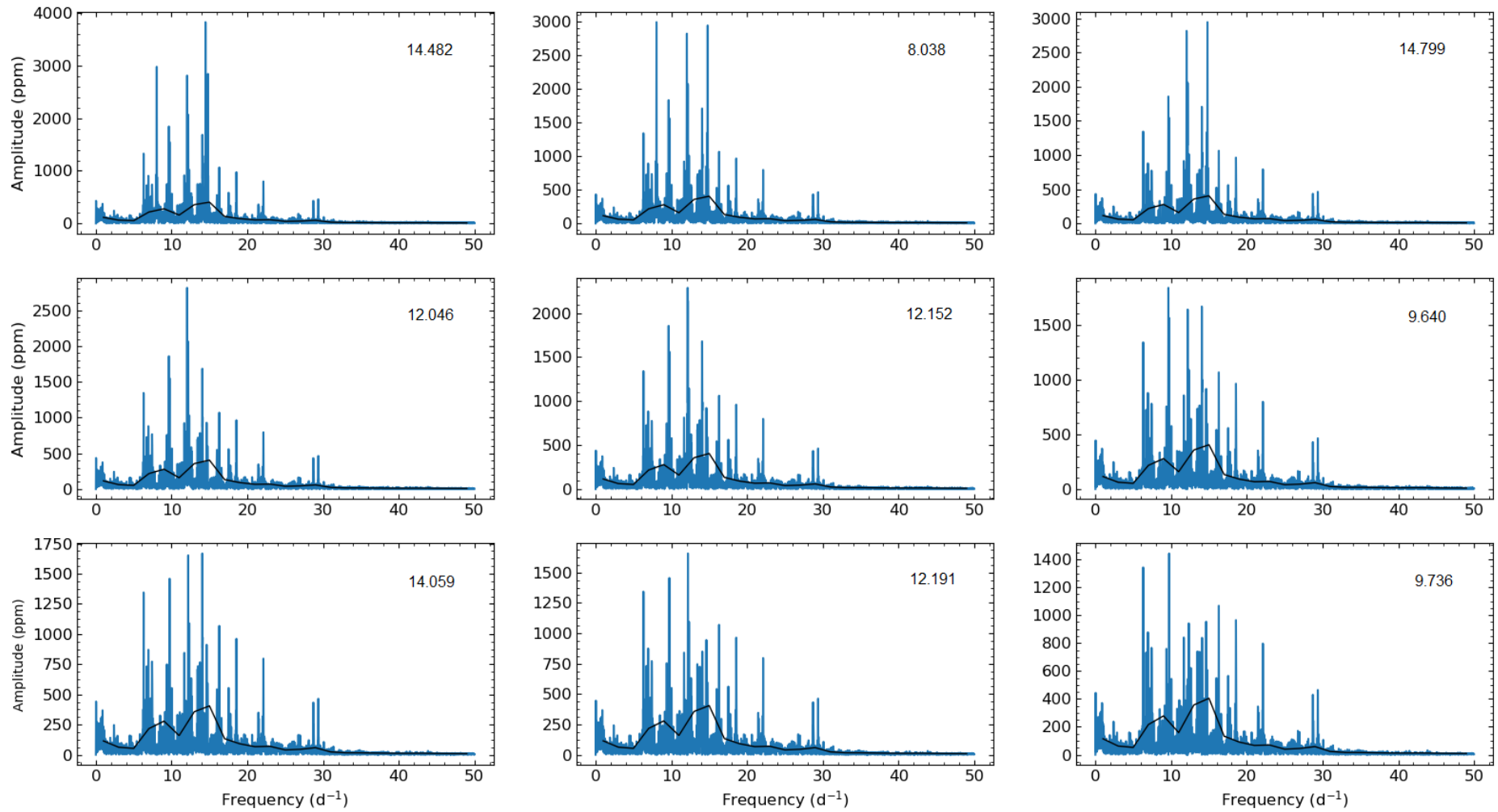
Figure 7.2. The amplitude spectra of first 9 frequencies of KIC 4077032 mentioned in Table 7.1. The Frequency in each panel is in d^{-1}. The each frequency is pre-whiten before determine the subsequent frequency. The black continuous line is the frequency dependent noise level determined by PERIOD04.
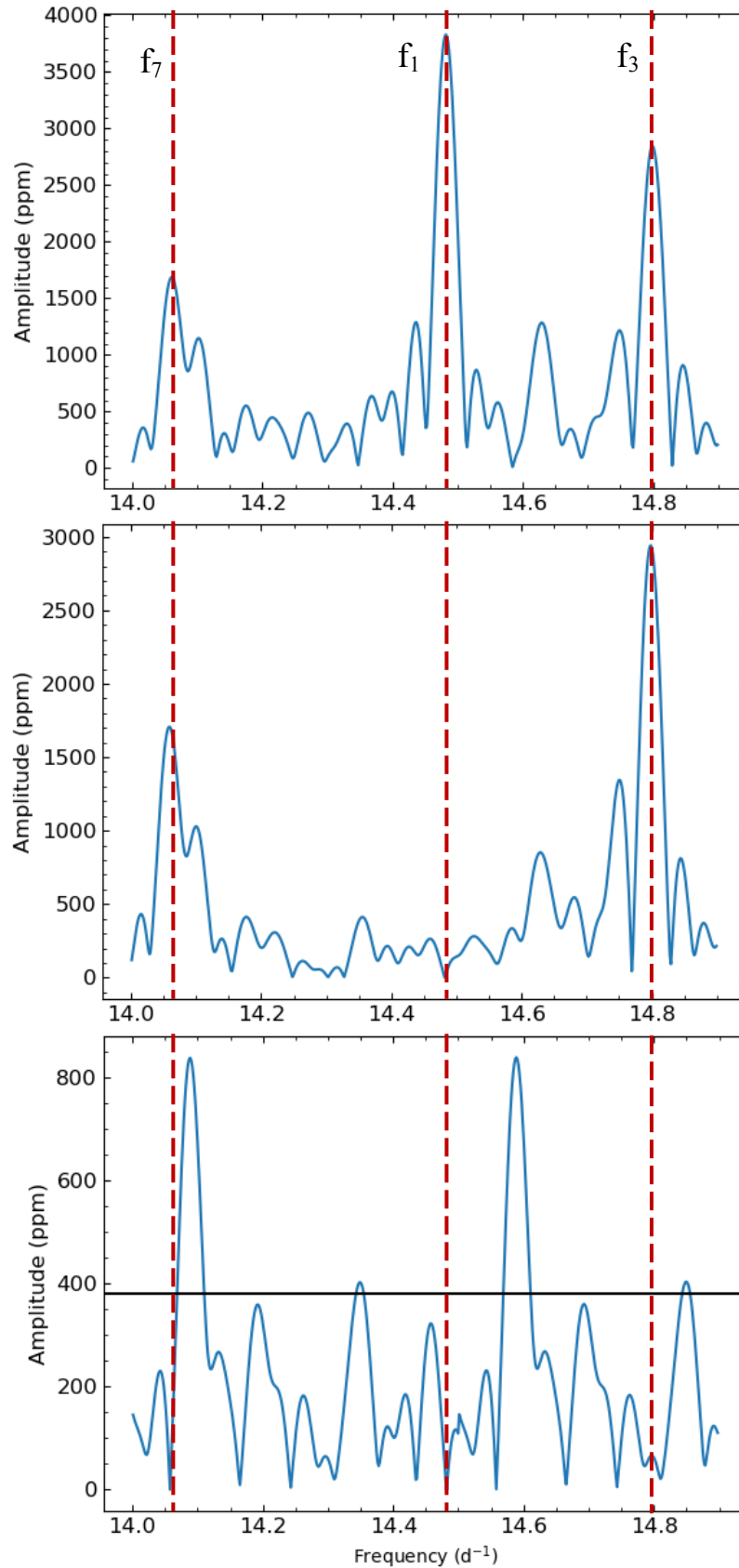
Figure 7.3. Multiplet of frequency f_1 in the KIC 4077032 system. Top panel shows the central frequency (f_1) and the components f_3 and f_7. The middle panel is the pre-whitened central unperturbed frequency. The bottom panel shows the pre-whitening of all thee frequencies and remaining residuals. The black horizontal line is the noise level of the amplitude. Note the low amplitude level of the bottom panel.

7.3 KIC 8623953

KIC 8623953 has a smooth light curve (see Figure 7.4) consists of relatively higher frequencies in its frequency spectrum. The parallax of the star measured by GAIA mission, 2.77 milliarcseconds results in the distance of 361 pc. Hence the bolometric magnitude estimates were substituted in equation 7.1 with the other stellar parameters to determine the pulsation constant Q for the frequencies in Table 7.2. Among the 10 dominant frequencies with relatively higher amplitudes, none of the frequencies is consistent with the range of Q value of fundamental radial mode. Nevertheless, the frequency, $f_{12} = 11.745$ d^{-1} with relatively low amplitude, results pulsation constant, Q of 0.0320 which is close to the range of fundamental radial mode. But this frequency is also claimed as a combination of f_5 and f_8, suspect that it would not be the fundamental radial mode. The pulsation constants of higher frequencies deviate from the standard range of fundamental radial mode ($0.0327 \leq Q \leq 0.0332$) so that in terms of pulsation constant, none of the higher amplitude frequencies belong to the fundamental radial mode. The presence of linear combinations of frequencies f_1, f_2, f_3, f_5 and f_6 in Table 7.2 hinted that they are independent modes. The frequency $f_1 = 27.257$ d^{-1} is the dominant mode with the amplitude 5 times higher than the next highest amplitude calming that f_1 is more compatible with the fundamental radial mode. The rest of the frequencies do not show any sign of rotational splitting or regular frequency spacing which makes it more difficult to determine the spherical degree l of these modes.
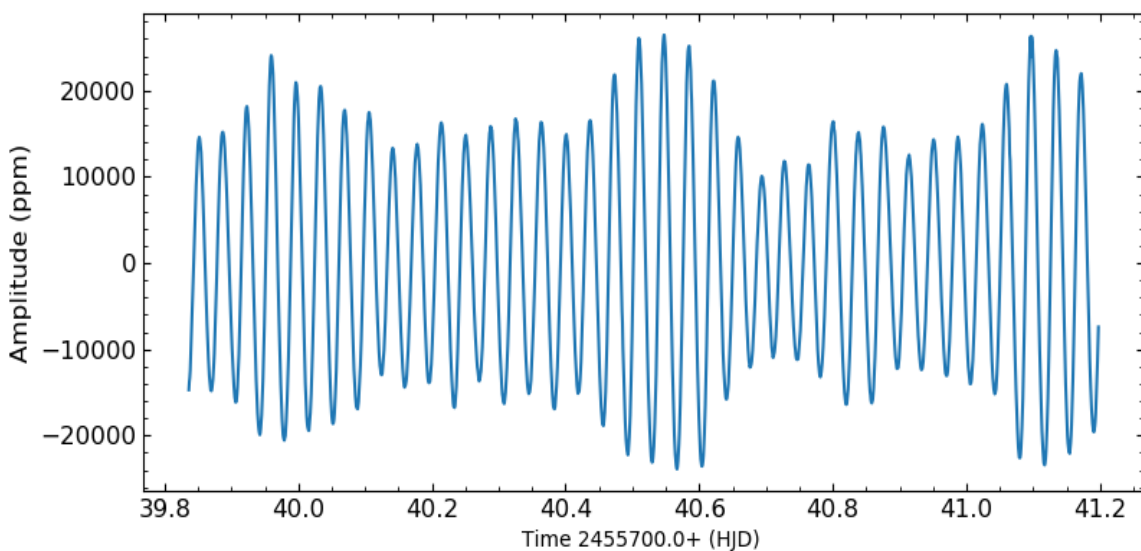
Figure 7.4. Part of light curve of KIC 8623953.
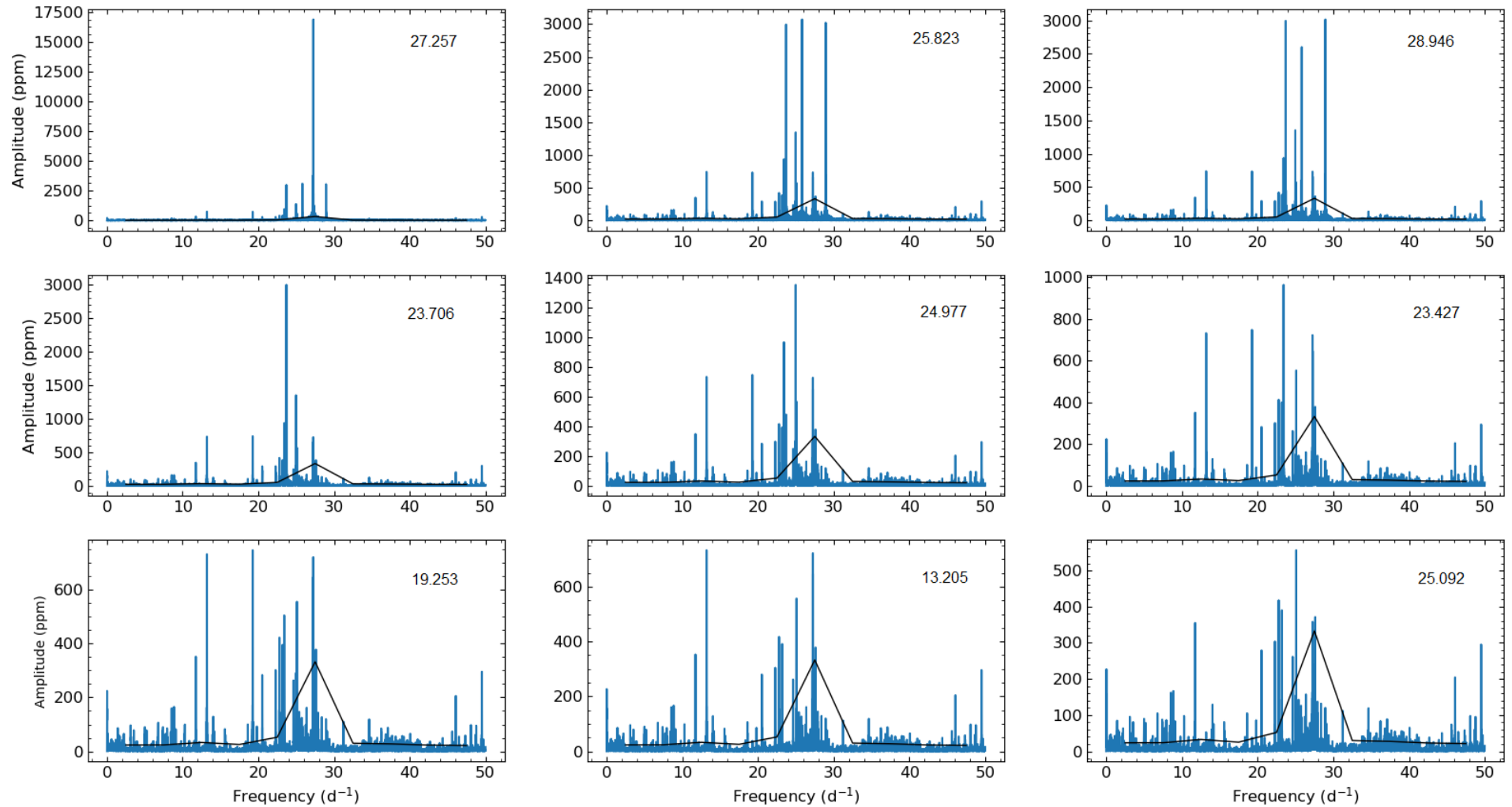
Figure 7.5. The amplitude spectra of first 9 frequencies of KIC 8623953. The frequency of the height amplitude is given in d^{-1}. Each frequency is pre-whiten before determine the subsequent frequency. The black continuous line is the frequency dependent noise level determined by PERIOD04.

Table 7.2. The oscillation frequencies of KIC 8623953. The possible linear combinations, harmonics and pulsation constants for the suspected fundamental radial modes are also included.

	Frequency (d^{-1})	Amplitude (ppm)	Linear combinations	Pulsation constant (Q)
f_1	27.257	38444±70	Fundamental radial	0.0105
f_2	28.948	8197±17		0.0090
f_3	25.820	7411±15		0.0111
f_4	23.705	7308±15		0.0120
f_5	24.977	2975±12		0.0112
f_6	23.426	2411±12		0.0122
f_7	19.252	1811±12		0.0148
f_8	13.207	1583±12		0.0216
f_9	25.091	1494±12		
f_{10}	54.514	1009±11	$2f_1$	
f_{11}	22.785	922±11		
f_{12}	11.745	778±11	f_5-f_8	0.0320
f_{13}	27.606	707±11		
f_{14}	49.528	702±11	f_3+f_6	
f_{15}	22.284	684±10		
f_{16}	23.194	587±11		
f_{17}	20.514	469±10		
f_{18}	53.077	434±10	f_1+f_3	
f_{19}	50.962	415±10	f_3+f_5	
f_{20}	56.205	378±10	f_1+f_2	

7.4 KIC 9700322

The complete data set of KIC 9700322 from quarter 11.1 (Q11.1) through quarter 12.3 (Q12.3) was obtained from the KASOC. Total data points of 242005 have covered 180 days irrespective of day and night. After normalization, the pulsation frequencies were determined by applying discrete Fourier transformation (DFT) using Period04 software. The oscillation frequencies searched in the range of 0 d^{-1} to 100 d^{-1} with a step size of 0.0008 d^{-1}. The dominant independent modes with their combinations and harmonics are shown in Figure 7.6. The complete frequency list is given in Table 7.3. This target was also observed and analyzed for frequencies by Breger et al., 2010. Both analyses derived the same set of prominent frequencies with $l = 2$ quintuplets. In addition, this analysis is conformed the fundamental frequency as 9.792 d^{-1} and first overtone as 12.569 d^{-1} using the period ratio method. Furthermore, using equation 7.2, the relative density of KIC 9700322 ($\frac{\rho}{\rho_\odot}$) was determined as 0.10 $\pm$ 0.04. The period ratio of P_2/P_1 of this star is 0.779 which is relatively high compared to the 0.687 (Böhm-Vitense, 1992) for a more realistic polytrope of $n = 3$, where n is the polytrope index. For higher n, higher mass concentration towards the center of a star which represents a real star. Therefore, the higher P_2/P_1 ratio of KIC 9700322 implies a higher central density concentration. In 2014 Suarez et al., showed the relation of large frequency separation and mean density of DSS. According to this prediction, the relative mean density of 0.10 $\pm$ 0.04 is compatible with the fundamental frequency of 9.792 d^{-1}. In general, the upper limit of the mass of DSS is 2.5 $M_\odot$ (Aerts et al., 2010). Therefore, the upper limit of the radius of KIC 9700322 can be estimated as 2.9 $\pm$ 0.3 $R_\odot$.

For the star KIC 9700322, the frequency splitting of $\Delta f_{n,l,m} = 0.134$ d^{-1} was substituted in equation 7.4 and estimated the value of rotation period (P_{rot}). The rotation period is 6.19 days which means the rotational frequency is 0.161 d^{-1}. We observed a frequency value $f_3 = 0.159 \pm 0.004$ d^{-1} in table 2 which is closed to the value calculated above. Therefore, f_3 is determined as the rotational frequency of KIC 9700322. This result also confirmed that the rotational frequency is much smaller than the pulsation frequency of DDS.
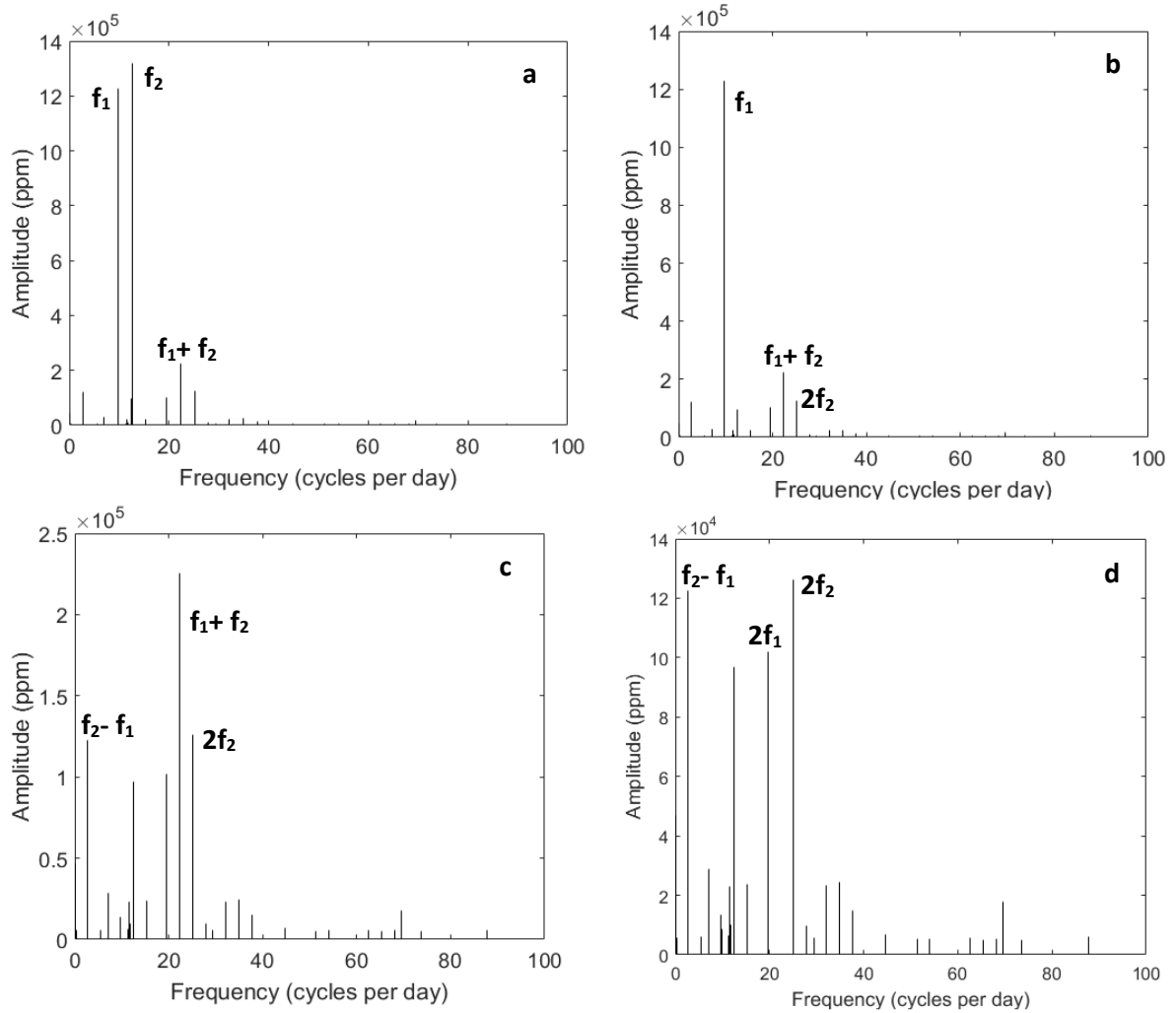
Figure 7.6 Amplitude spectra of KIC 9700322. Frequencies, combinations and harmonics are marked. The panels a, b, c and d show the remaining frequencies after pre-whitening the dominant frequency.

Table 7.3. The oscillation frequencies of KIC 9700322.

	Frequency (d^{-1}) ±0.002	Amplitude (ppm)	Identification
f_1	9.792	1227651.58	Fundamental
f_2	12.569	1319764.29	1st Overtone
f_3	0.159	4583.00	Rotation
f_4	0.0121	46826.81	
f_5	11.316	6348.07	Quintuplet
f_6	11.455	5775.80	Quintuplet
f_7	11.589	22978.14	Quintuplet
f_8	11.719	10042.14	Quintuplet
f_9	11.858	5230.76	Quintuplet
f_{10}	0.026	11464.82	$2f_4$
f_{11}	2.775	122446.58	f_2-f_1
f_{12}	5.550	5982.86	$2f_2-2f_1$
f_13	7.016	28803.27	$2f_1-f_2$
f_{14}	9.781	13594.57	$f_1+f_2-f_3$
f_{15}	9.792	8693.03	$f_1+f_2-f_3+2f_4$
f_{16}	12.545	96857.34	f_2-2f_4
f_{17}	12.569	67945.97	f_2-f_4
f_{18}	12.582	14856.26	f_2+f_4
f_{19}	15.345	23618.59	$2f_2-f_1$
f_{20}	19.585	102097.16	$2f_1$
f_{21}	22.361	225738.91	f_1+f_2
f_{22}	25.137	126096.23	$2f_2$
f_{23}	27.914	9578.32	$3f_2-f_1$
f_{24}	29.377	5754.46	$3f_1$
f_{25}	32.153	23401.58	$2f_1+f_2$
f_{26}	34.929	24567.54	f_1+2f_2
f_{27}	37.705	14988.67	$3f_2$
f_{28}	44.723	6819.39	$2f_1+2f_2$
f_{29}	62.541	5842.42	$5f_2$

7.5 KIC 9845907

The full data set of KIC 9845907 from quarter 8.1 (Q8.1) through quarter 9.3 (Q9.3) was obtained from the KASOC. This star was observed in 171 days resulting 253831 flux values. The frequency analysis was done using Period04 in the range of 0 d^{-1} to 100 d^{-1} in the step size of 0.0008 d^{-1}. The dominant pulsation frequencies of the KIC 9845907 are shown in Figure 7.7 and listed in the Table 7.4. The mean relative density $(\frac{\rho}{\rho_\odot})$ of 0.34±0.06 revealed that this star has a maximum radius of 1.94 ± 0.09 R$_\odot$ for the upper ceiling of mass 2.5 M$_\odot$.
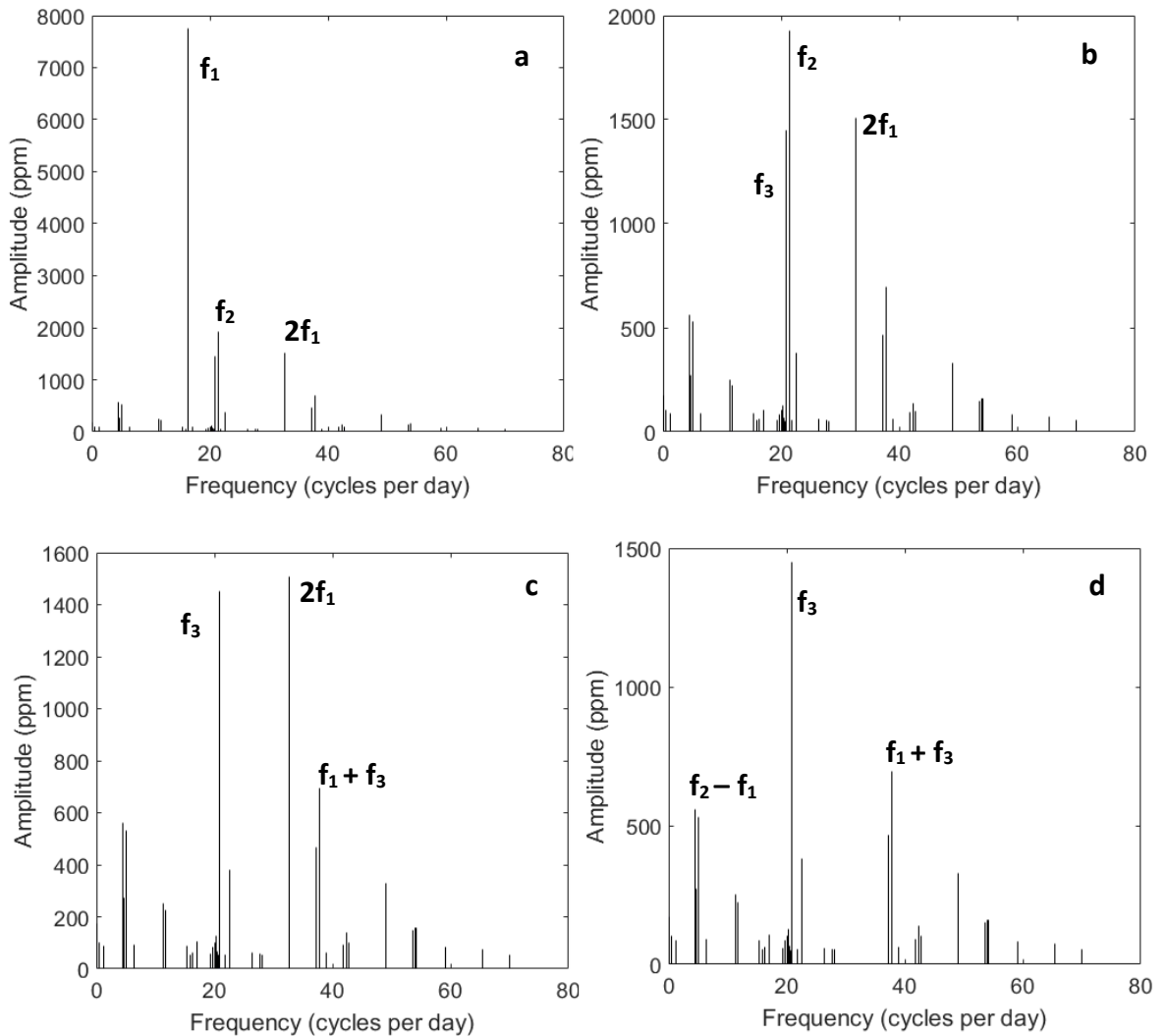
Figure 7.7. Amplitude spectra of KIC 9845907. The dominant modes and the combinations are shown. The panels a, b, c and d show the remaining frequencies after pre-whitening the dominant frequency.

143

Table 7.4. The oscillation frequencies of KIC 9845907.

	Frequency (d^{-1}) ±0.002	Amplitude (ppm)	Identification
f_1	17.597	10496.36	Fundamental
f_2	22.850	2636.76	1st Overtone
f_3	28.210	530.07	2nd Overtone
f_6	27.010	685.87	
f_4	0.065	450.92	
f_5	13.831	195.37	
f_7	1.693	151.43	f_2-f_1
f_8	13.898	136.75	f_3+f_4
f_9	26.880	192.45	f_6-2f_4
f_{10}	26.945	156.26	f_6-f_4
f_{11}	28.956	226.29	$f_6 + 3f_4$
f_{12}	29.736	448.16	$2f_5 -f_6 + f_4$
f_{13}	29.797	163.88	$2f_5 -f_6 + 2f_4$
f_{14}	31.363	1181.84	$f_1+f_5 -f_4$
f_{15}	31.428	2209.07	$f_1 + f_5$
f_{16}	31.493	1993.26	$f_1 + f_5 + f_4$
f_{17}	35.195	572.34	$2f_1$
f_{18}	49.025	176.29	$f_1 + f_2$
f_{19}	49.090	125.97	$f_1 + f_2 + f_4$
f_{20}	59.471	393.34	$4f_5 -2f_6 +2f_4$
f_{21}	61.164	324.04	$2f_1 + f_2 - 2f_4$
f_{22}	62.856	315.41	$2f_1 + 2f_5$

7.6 KIC 11754974

The full data set of KIC 11754974 from quarter 6.1 (Q6.1) through quarter 7.1 (Q7.1) was obtained from the KASOC. Total data points of 172917, spanning a total time of 120 days, after normalization, the pulsation frequencies were determined by the same method as in Section previous sections. The oscillation frequencies were searched in the range of 0 d^{-1} to 100 d^{-1} in the step size of 0.0008 d^{-1}. The independent modes of pulsation frequencies and the combinations of the KIC 11754974 are shown in Figure 7.8 and listed in the Table 7.5. The determined relative density using the period-density relationship of KIC 11754974 ($\frac{\rho}{\rho_\odot}$) is 0.29 ± 0.01. The upper limit of the radius is 1.86 ± 0.02 $R_\odot$ for the standard upper mass of 2.5 $M_\odot$ of DSS stars.
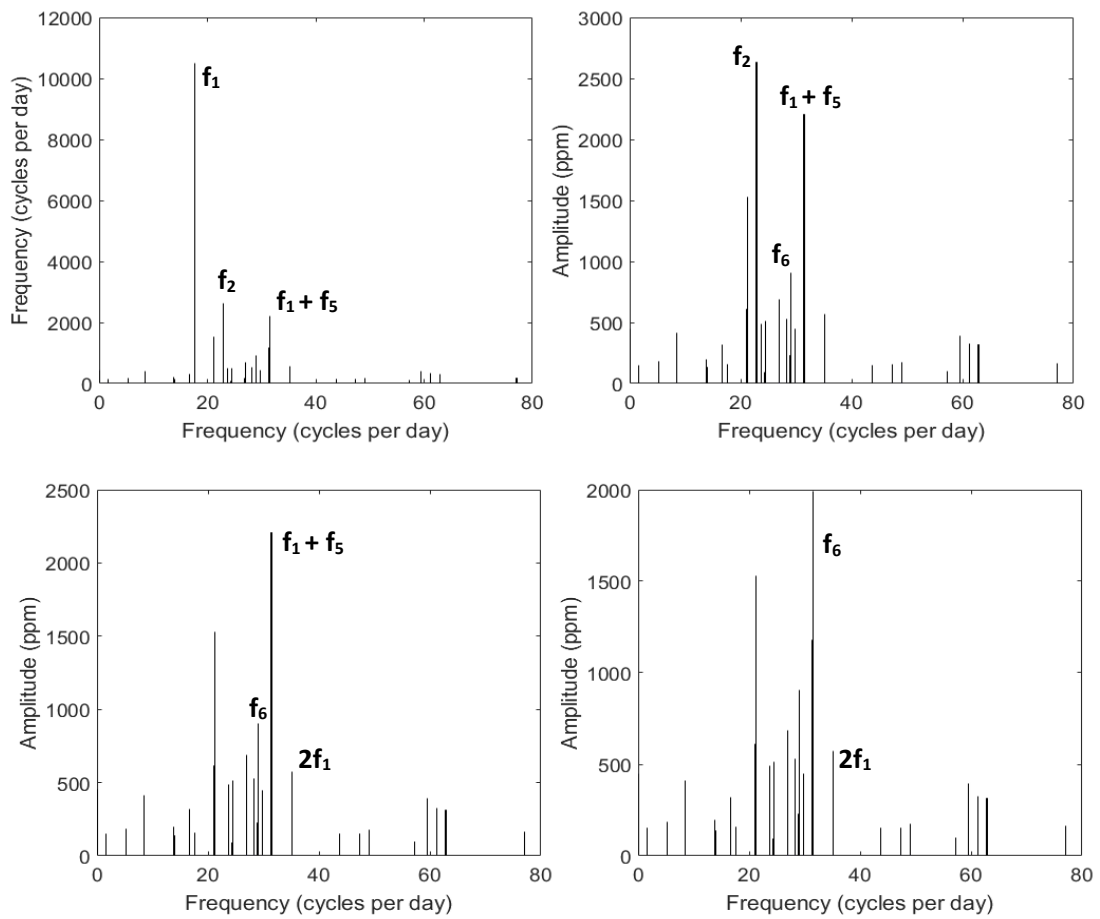
Figure 7.8. Amplitude spectra of KIC 11754974. The dominant modes and the combinations are shown. The panels a, b, c and d show the remaining frequencies after pre-whitening the dominant frequency.

Table 7.5. The oscillation frequencies of KIC 11754974.

	Frequency (d^{-1}) ±0.0002	Amplitude (ppm)	Identification
f_1	16.3451	7752.21	Fundamental
f_2	21.3997	1925.44	1st Overtone
f_3	20.9067	1450.81	
f_4	20.9441	992.40	
f_5	22.6610	381.06	
f_6	19.7839	85.08	Quintuplet
f_7	20.0194	102.61	Quintuplet
f_8	20.2437	125.27	Quintuplet
f_9	20.4562	68.22	Quintuplet
f_{10}	20.6560	51.71	Quintuplet
f_{11}	0.4921	102.97	f_2-f_3
f_{12}	1.2605	86.04	f_5-f_2
f_{13}	4.5624	559.64	f_3-f_1
f_{14}	4.5990	271.40	f_4-f_1
f_{15}	5.0546	532.20	f_2-f_1
f_{16}	6.3159	90.36	f_5-f_1
f_{17}	11.2905	251.95	$2f_1-f_2$
f_{18}	11.7461	69.57	$2f_1-f_4$
f_{19}	11.7826	224.09	$2f_1-f_3$
f_{20}	15.8530	54.36	$f_1-f_3-f_2$
f_{21}	26.4542	60.32	$2f_2-f_1$
f_{22}	27.6356	56.36	$3f_1-f_2$
f_{23}	28.1277	53.22	$3f_1 - f_3$
f_{24}	32.6902	1505.81	$2f_1$
f_{25}	37.2518	467.73	$f_1 + f_3$
f_{26}	37.2900	391.97	$f_1 + f_4$
f_{27}	37.7447	695.09	$f_1 + f_2$
f_{28}	39.0061	63.36	$f_1 + f_5$
f_{29}	41.8151	58.96	$2f_3$
f_{30}	41.8533	92.22	$f_4 + f_3$
f_{31}	42.3072	137.90	$f_2 + f_3$
f_{32}	42.7993	102.06	$2f_2$
f_{33}	49.0353	329.11	$3f_1$
f_{34}	53.5969	149.79	$2f_1 + f_3$
f_{35}	53.6351	96.23	$2f_1 + f_4$
f_{36}	54.0898	158.53	$2f_1 + f_2$
f_{37}	59.1444	83.70	$2f_2 + f_1$
f_{38}	65.3804	74.84	$4f_1$

7.7 Discussion

Five DSS observed by the Kepler mission were subjected to frequency analysis within the range of 0 - 100 d^{-1}. The frequency tables revealed that the independent modes are condensed in within the range of 5 - 30 d^{-1}. These frequencies are mostly identified as low degree p - modes (Kurtz et al., 2014). All five stars show combinations and harmonics of radial and non-radial modes. Generally, independent modes at higher frequencies are rare in DDS. The frequency tables of these five stars also indicate the non-availability of independent modes at higher frequencies. The detected higher frequencies are either harmonics or combinations of independent modes. In general, DSS have prominent radial mode along with non radial modes. In mode identification, the simplest mode is the fundamental radial mode which represents by $l = 0$ and $n = 1$. The overtones of this fundamental are represented by $n = 2, 3$, etc. The frequency of fundamental radial mode ($n = 1$) is known as f_1. In this mode, the star swells and contracts, heats and cools in spherical symmetry. The standing wave creates with the core as a node and the surface as a moving anti-node.

The first overtone radial mode (f_2) frequency which corresponds to $n = 2$, has one radial node that is a concentric shell within the star. As we are thinking in terms of the radial displacement, this shell is a non-moving node; the motions above and below the node are in anti-phase.

KIC 8623953 does not show any prominent fundamental radial node as none of the higher amplitudes modes are consistent with the characteristics of fundamental radial node. In fact, non-radial modes only occur for n ≥ 1, so that in the case of the $l = 1$ dipole mode, there is at least one radial node within the star (Aerts et al., 2010). Therefore, it is rather unusual to present non-radial modes without a fundamental radial mode in KIC8623953.

The ratios in the first overtone to the fundamental in the DSS are a direct consequence of the sound speed gradient in them, hence the temperature and (in some places) chemical composition gradients. Thus, just by observing two pulsation frequencies, we have had our first look into the interiors of KIC 9700322, KIC 11754974 and KIC 9845907. The frequency f_1, is the radial fundamental mode for the three stars, KIC 9700322, KIC 11754974 and KIC 9845907. Therefore, the frequency ratio of fundamental (f_1) and 1st harmonic (f_2) were calculated for all three stars, KIC

9700322, KIC 11754974 and KIC 9845907. The ratios, f_1/f_2, for KIC 9700322, KIC 11754974 and KIC 9845907 are 0.779, 0.763 and 0.779 respectively. These values were close to the expected frequency ratio of fundamental and first overtone radial pulsation of DSS (Stellingwerf, 1979). Furthermore, the frequency ratio f_2/f_3, 1st overtone (f_2=22.854 day^{-1}) and 2nd overtone (f_3=28.214 day^{-1}) of KIC 9845907 is 0.81 which close to the expected frequency ratio of 1st overtone and 2nd overtone for the radial pulsation of DSS.

In the frequency spectrum of KIC 9700322 and KIC 11754974, we can identify the equidistant frequency pattern of peaks with several components that depends on the value of l. These five peaks (quintuplet) for $l = 2$ is given by the equation $m = 2l + 1$. Therefore $l = 2$ mode, there are five peaks possible as -2, -1, 0, +1 and +2 where the central peak is denoted as $m = 0$.

In KIC 9700322, a quintuplet was found (f_5, f_6, f_7, f_8 and f_9 in Table 7.3) around the two dominant modes and the average spacing between the frequencies in quintuplet is 0.134 day^{-1}. Similarly, KIC 11754974 consists of a quintuplet (f_6, f_7, f_8, f_9 and f_{10} in Table 7.5) and the average spacing between the frequencies is 0.2180 day^{-1}. This value is identified as the frequency splitting ($\Delta v_{n,l,m}$) in equation 7.3. The rotation period (P_{rot}) and rotation frequencies can be calculated by using this frequency splitting.

For the star KIC 9700322, the frequency splitting of $\Delta v_{n,l,m} = 0.134$ d^{-1} was substituted in equation 7.4 and estimated the value of rotation period (P_{rot}). The rotation period is 6.19 days and which means the rotational frequency is 0.1614 day^{-1}. We observed a frequency value $f_3 = 0.159$ d^{-1} in table 2 which is closed to the value calculated above. Therefore, f_3 is determined as the rotational frequency of KIC 9700322. This result also confirmed that the rotational frequency is much smaller than the pulsation frequency of DDS. Similarly, for KIC 11754974, the value $\Delta v_{n,l,m}$ is 0.218 d^{-1} and the rotation period (P_{rot}) is 3.83 days and the rotational frequency was 0.260 d^{-1}. But this frequency could recover from the power spectra of KIC 11754974. The rotation period and the estimated upper limit of radius result in the projected rotational velocity v sin (i) of 24 km/s and 25 km/s for KIC 9700322 and KIC 11754974, respectively.

The detected frequencies of KIC 9700322 (Breger, et al., 2011), KIC 11754974 and KIC 9845907 show simple linear combinations. These combinations are entirely caused by radial modes of f_1 and f_2 and the rotational frequency. Therefore the availability of more combinations provides the presence of independent modes. These combinations help in identifying the radial modes.

The frequency f_2 of the target KIC 4077032 was identified as the fundamental radial node and f_2/f_n (where n = 1, 2, 3, etc.) ratios were calculated to check for the 1st or 2nd overtones. None of the ratios were consistent with the ranges mentioned in this paragraph to conclude the unavailability of overtone frequencies in KIC 4077032.

This analysis presented combination frequencies, the quintuplets ($l = 2$ mode) and the estimations of relative densities for all five DDS. In addition, the rotation periods were determined as 6.19 days and 3.83 days for The KIC 9700322 and KIC 11754974, respectively. The values of relative densities $\frac{\rho}{\rho\odot}$ were determined as 0.07±0.01, 0.10±0.04, 0.29±0.01 and 0.34±0.06 for KIC 4077032, KIC 9700322, KIC 11754974 and KIC 9845907, respectively. The mathematical relationship introduced by Suárez et al., (2014) can be used to estimate the relative densities of DDS for known large frequency separations. The large frequency separations of KIC 9700322, KIC 9700322 and KIC 11754974 given by their corresponding frequency tables used to estimate the relative densities as an alternative method. These densities are consistent with the values calculated using equation 7.2 with the pulsation constants. The KIC 9700322 and KIC 11754974 contain radial and non-radial pulsation while KIC 9845907 is only a radial pulsator.

The pulsation constant (Q) was determined for the fundamental radial mode of KIC 9845907 as 0.0216 which is less than the acceptable range of $0.0327 \leq Q \leq 0.0332$ (Fitch, 1981). Breger and Montgomery (2000) pointed out that the DSS have more diverse range of Q for the fundamental and overtones typically $0.015 - 0.035$. The uncertainties of input parameters in equation 7.1 are overall 25%. Therefore, the determination of Q value depends on the accuracy of stellar parameters such as T_{eff}, log (g), M_{bol}. With the commission of GAIA mission (Brown et al., 2016, 2018) the

stellar parallex could be determined with unprecedented accuracy, hence the M_{bol} has minimized. The stellar parameters of all five Kepler targets were summarized in Table 7.6.

Table 7.6. The stellar parameters of five KIC Delta Scuti stars. The asterisk (∗) marked values were determined in this analysis. Breger et al., (2011) and Murphy et al., (2013) are refereed for KIC 9700322 and KIC 11754974 respectively. Other values are taken from KASOC Delta Scuti stars catalogue. The determination of maximum radius in this analysis is based on the upper ceiling of the stellar mass of 2.5 $M_\odot$ for Delta Scuti stars.

Star	T_{eff} (K)	Log (g)	R ($R_\odot$)	Fe/H	ρ ($\rho_\odot$)	v sin(i) (Km/s)	Fundamental Radial Frequency (d^{-1})	Pulsation constant (Q)	Pulsation status
KIC 4077032	6789	4.047	1.772 3.15±0.06*	-0.275	0.07±0.01*	17	8.038*	0.033*	Radial and non radial
KIC 8623953	7725	3.738	2.818 3.14±0.06*	-0.118	0.08±0.01*		27.257*	0.011*	Radial and non radial
KIC 9700322	6700	3.700	2.9±0.3*	-0.500	0.10±0.04*	19	9.792*	0.026*	Radial and non radial
KIC 9845907	7936	4.029	1.954 1.94±0.09*	-0.039	0.34±0.06*		17.597*	0.022*	Radial
KIC 11754974	7110	3.862	2.425 1.86±0.06*	-0.500	0.29±0.01*	25	16.345*	0.023*	Radial and non radial

Chapter 8

Results and Discussion

The advent of space-based photometry has made theoretical predictions with asteroseismology more realistic. The observational results are being validated through different theoretical models and have updated the physics of pulsations, including the stellar interior rotation, chemical peculiarities, angular momentum transport, etc. Among these investigations, the particular group of stars, Delta Scuti stars, plays a vital role as they are more diverse in stellar pulsations. The stellar interior structure of the Delta Scuti stars is fully exploited by discovering more frequencies in their amplitude spectra.

The dissertation includes both ground and space-based observations of DSS. The multi-site campaign observed SZ Lyn in UBVR bands, as discussed in Chapter 2. The inclusion of the space-based photometry, TESS, reinforces the asteroseismic analysis of SZ Lyn. The contrast of data analysis techniques of ground and space is well experienced throughout the investigation. The preparation of raw data of ground-based observation is time-consuming with the initial corrections, while the space-based data is ready for analysis after few correction steps. Though the space-based data are good in quality and extended in the period, the data reduction experience is missing because the initial corrections are made through automated pipelines. Therefore, the importance of ground-based observations is emphasized in photometry despite the vast advantages of space-based photometry. There is also a point that space-based photometry is usually in one band while multi-band observation can be done from the ground. The scope of analysis is broad in multi-band photometry. Therefore, the validity of multi-band, multi-site ground-based photometry is equally appreciated with the space-based data.

Initially, the orbital parameters of SZ Lyn were determined using all available maxima of light curves, including the present observations. The Levenberg-Marquardt least-squares fitting to the O – C resulted in semi-major axis (a sin i), eccentricity (e) and orbital period (P_{orbit}) as $(1.4\pm0.1)\times10^{8}$ km, 0.18 ± 0.07 and 1187 ± 15 days, respectively (Adassuriya et al., 2018).

Gazeas et al. (2004) identified the SZ Lyn as a radial pulsator without any non-radial modes. The high precision and high duty cycle TESS data of SZ Lyn revealed the availability of non-radial p-modes and possible g-mode (Adassuriya et al., 2020). This observation further confirmed the simultaneous occurrence of pressure and gravity modes in DSS (Kurtz et al., 2014).

The frequency spectrum of SZ Lyn has combinations and harmonics of fundamental radial mode and non-radial modes. However, the common occurrence of overtones of fundamental was not seen in SZ Lyn. In addition, rotational splitting or frequency spacing could not discover in the amplitude spectra obtained by high temporal resolution TESS data. Therefore, mode identification using echelle diagrams, rotationally split multiplets, and period spacing patterns (Aerts, 2019) are impossible for SZ Lyn. Nevertheless, the ground-based observation of UBVR photometry provides amplitudes of the oscillation frequencies in different pass bands, and hence the amplitude ratio method was performed. In this method, the observed amplitudes were compared with the theoretical amplitudes. The computation of theoretical amplitudes provides the inclusion of a wide range of stellar parameters into the model convergence process. This model convergence leads to determine the stellar parameters of SZ Lyn.

The pulsation models were produced using TDC non-adiabatic models (Dupret et al. 2003) and linear non-adiabatic models (Pamyatnykh 1999b; Dziembowski 1977). Evolutionary sequences were computed using MESA and overlapped the models to provide further insight into the stellar parameters. These models were discussed in Chapters 4 and 5. The theoretical results were highly dependent on input parameters, and hence the model dependency significantly affected the determination of stellar parameters. Different combinations of stellar parameters can approach the observation results in several paths. Therefore, these combinations cause the analysis more robust in asteroseismology. Nevertheless, the stellar parameters of SZ Lyn were discussed, considering all the possible models with the perturbation effects of input parameters. Therefore, the behavior of the models was considered by perturbing the input parameters. AlphaTg code determines the flux derivatives and limb darkening derivatives for any T_{eff} and log (g). Hence, the error contribution from flux and limb darkening derivatives to the theoretical amplitudes is minimized. However, the

perturbation of T_{eff} on eigen values f_T and ψ_T is significant and hence changes the theoretical amplitudes considerably (Dupret et al., 2005). The temperature component (T_2) discussed in Chapter 3 has a significant contribution to theoretical amplitudes. Thus, the best model was perturbed by the observational uncertainty of ± 150 K. This uncertainty propagates to the non-adiabatic parameters, f_T and ψ_T, and observed, a considerable deviation in the theoretical amplitudes.

The uncertainty included stellar parameters of SZ Lyn are given below. The temperature of SZ Lyn is converged to 7500 K $\leq T_{eff} \leq$ 7800 K, resulting in concluding that SZ Lyn is close to the blue edge. Similarly, the investigation of the model dependency on Z and α_{MLT} determined $0.014 \leq Z \leq 0.02$ and $1.7 \leq \alpha_{MLT} \leq 2.0$ for SZ Lyn. The log (g) = 3.81±0.06 dex is considered as the average of all the pulsation models (Adassuriya et al., 2020).

The evolutionary sequences were computed using MESA to obtain an independent value for the mass of SZ Lyn. Placing TDC models and HELAS models in the HR diagram allowed us to compare the models with the evolutionary tracks of stars between 1.7 - 2.0 $M_\odot$, Z = 0.01 - 0.02, and different values for overshooting. The evolutionary tracks assume that these ranges of mass, metallicity and overshooting encompass the possible values for SZ Lyn. The results show that TDC Model 2 with mass 1.9 $M_\odot$ is compatible with stars in these ranges at the Hertzsprung gap phase of M = 1.8 $M_\odot$ (Z=0.01) and M = 1.9 $M_\odot$ (Z=0.02), or at the last phase of central hydrogen burning (main sequence) of M = 2.0 $M_\odot$ (Z=0.02) model in Figure 5.3. Though it is hard to determine the exact single model, the mass can be defined as 1.9 $\pm$ 0.1 $M_\odot$ through the stellar pulsation modes, which align with the observations (Adassuriya et al., 2020).

It is a fact that the evolutionary sequences are highly sensitive to metallicity (Z), as seen in Figure 5.3. The higher the metallicity, the more efficient the κ - mechanism and hence the significant decrease in luminosity occurred in the evolutionary tracks. The higher sensitivity of the models to the metallicity shifts the evolutionary tracks to

the low luminosity region. Consequently, the observation error box and the best TDC Model 2 (1.9 M$_\odot$) are located in the main sequence phase of the M = 2.0 M$_\odot$ model of the evolution. This inconsistency cannot be avoided unless the metallicity (Z) is accurately known through very high resolution spectroscopic observation of SZ Lyn. In this process the pulsation models of SZ Lyn were evaluated with an appropriate set of evolutionary sequences with different stellar parameters. However, it is vital to have more individual observations of DSS, with a similar analysis, to better understand the behavior of these parameters.

The H-β line profiles show the blue and red shift with the same phase of fundamental radial frequency. Therefore, the high amplitude radial pulsation can be seen even in low resolution spectra of SZ Lyn. In addition, a similar Doppler shift with much lower amplitude is also weakly characterized in the time series spectroscopy providing a clue of the presence of another frequency which may be non-radial mode discovered in Section 3.4.3.

In addition to the extensive analysis of ground and space-based data of SZ Lyn, few Kepler DSS are investigated in Chapter 7. The DSS is a more diverse group of pulsating stars characterizing the frequency spectra with hybrid, rotation, and chemical peculiarities signatures. The five stars presented here are different from one another in the frequency analysis. KIC 4077032, identified as a hybrid pulsator (Niemczura et al., 2015), shows the nature of γ Dor and Delta Scuti. In general, the fundamental radial mode results in the highest amplitude peak of the amplitude spectra. The KIC 4077032 deviates from the normality producing 14.482 d^{-1} as the highest and 8.038 d^{-1} as the second highest, showing the characteristics of fundamental radial mode (see Table 7.1). Another strange target, KIC 8623953, was observed without a prominent radial mode in its power spectra. The pulsation constant (Q) is calculated for all dominant modes, and none of these are found within the acceptable range of Q of the fundamental radial mode. However, it revealed that the typical range of the pulsation constant (Q) is only one indication of the presence of fundamental, and overtones modes and the ranges given are inconsistent for the more diverse group of DSS.

The KIC 9700322, KIC 9845907, and KIC 11754974 show prominent radial fundamental mode, overtones, and non-radial components. The KIC 9700322 and KIC 11754974 show very strong rotational multiplets used to determine the spherical degree l of the mode. All five Kepler targets have linear combination frequencies and harmonics, while SZ Lyn showed 12 harmonics of its fundamental radial mode. The harmonics are the representations of non-sinusoidal components of the light curve. Therefore, the existing 12 harmonics in SZ Lyn indicate the highly asymmetrical nature of its light curve.

The average densities of the five targets are diverse, as seen in Table 7.6. The less-dense means the sound waves penetrate deep and the time period of the fundamental mode is large, conversely, denser means the fundamental radial period is less. This fact is clearly seen except for target KIC 8623953. However, the frequency of the highest amplitude, $f_1 = 27.257$ d^{-1} in KIC 8623953, could not confirm as the radial fundamental due to these inconsistencies. Therefore, KIC 8623953 should be subjected to deep asteroseismic analysis to find out the oscillation modes.

Chapter 9

Conclusions

Mode identification of a HADS star, SZ Lyn, is presented using multi-band photometry. Consequently, the physical parameters of SZ Lyn were determined through stellar modeling. The SZ Lyn was previously identified as a pure radial oscillator. The presence of non-radial p-modes found in this analysis classifies SZ Lyn as a non-radial oscillator. Furthermore, evidence of a medium order g-mode is also found in SZ Lyn.

The mode identification process strongly depends on theoretical models. Therefore, a robust analysis of these models with appropriate uncertainties of input parameters should be followed to determine the accurate stellar parameters. In addition to the primary stellar parameters, T_{eff}, log (g), and mass, the model-dependent approach of asteroseismology provides a better understanding of mixing length parameter (α_{MLT}), overshooting parameter (f_{over}), and metallicity (Z) of SZ Lyn.

The selected Kepler targets of DSS show the diversity of the group and emphasize the importance of analyzing them individually with multi-band photometry. In addition, the Kepler DSS provides evidence that the parameters of these individual targets deviate from the general terms of DSS. Therefore, some of the general terms of DSS should be statistically redefined.

This dissertation underlines the importance of multi-band photometry through the analysis of stellar models. Therefore, this opportunity is used to emphasize the validity and significance of multi-band, multi-site, ground-based photometry over space-based photometry. The importance of a multi-band space-based future mission for photometry is also pointed out.

Suggestions for further studies

The Kepler and TESS missions revolutionized space-based photometry with an unprecedented way of understanding pulsation stars with very high accuracy and high duty cycle time-series photometry. This space-based photometry leads to identifying modes using different techniques such as rotational splitting, period spacing, and echelle diagram. Since, the space-based observations are limited to one band (instrumental pass band of the mission), in the absence of rotational splitting, period spacing in particular targets makes the mode identification more difficult. This analysis shows that Kepler targets, KIC 4077032, KIC 8623953, and SZ Lyn, it is found that neither of the characteristics mentioned above is seen in their power spectra. Therefore, multi-site, multi-band ground-based observations are also important for such targets. Hence, amplitude ratio and phase difference techniques are still helpful to identify the oscillation modes.

Studies of stellar rotation and angular momentum transport are important for a complete understanding of stellar evolution (Pinsonneault, 1997; Tayar & Pinsonneault, 2013). The stellar evolution is also closely connected to the stellar dynamo process, and contributes to our understanding of the origin of the magnetic fields in the universe (Kurtz et al., 2014). Recently, Kepler Mission data have revealed core rotation in two red giant stars 5–10 times faster than the surface rotation (Beck et al., 2012; Deheuvels et al., 2012). Therefore, a strong mechanism for angular momentum transport must be acting before stars become red giants, probably in the dominant main-sequence phase. Yet little is known of the internal rotation and angular momentum transport of stars. In order to investigate the interior structure, the interior sensitive gravity wave should be recovered in low frequency region of the power spectra. Therefore, the Kepler and TESS data should be analyzed focusing on the low frequency region (less than 5 d^{-1} or 58 µHz).

The theoretical modeling of the observation is a vital phase of any analysis. The state-of-art theoretical pulsation codes, HELAS (linear non-adiabatic pulsation code, Pamyatnykh, 1999), MAD code (Dupret 2001), The Li`ege Oscillation Code (Scuflaire, et al., 2008), and FILOU oscillation code (Suárez and Goupil, 2008) were

introduced and have been extensively used in literature. In addition, MESA stellar evolution code (Paxton et al., 2010, 2013, 2015, 2019) is being used with unlimited customization of stellar parameters. However, the resulting models from different codes show inconsistencies where the different sets of stellar parameters will converge to the observations. Therefore, it is necessary to perform the appropriateness of models produced by different codes that ultimately try to approach the observational results.

Introducing the high resolution spectrographs with sensitive detectors has a significant impact on empirical mode identification. From an observational point of view, it is challenging to obtain spectra covering the overall oscillation period of the multi-periodic stars, with a high resolving power (typically above 40000) and with a high signal-to-noise ratio (typically above 200), for a good temporal resolution in the sense of the integration time to the oscillation period. The possibility of this nature of observations is limited. Therefore, it is a necessity to allocate more time to ground-based high resolution spectroscopy for asteroseismology.

List of publications came out of this study

Peer reviewed journals

1. **Adassuriya, J**., Ganesh, S., Gutiérrez, J.L., Handler, G., Joshi, S., Jayaratne, K.P.S.C. and Baliyan, K.S., 2020. Asteroseismology of SZ Lyn using multiband high time resolution photometry from ground and space. *Monthly Notices of the Royal Astronomical Society*, *502*(1), pp.541-555.
   DOI: https://doi.org/10.1093/mnras/staa3923

2. **Adassuriya, J**., Jayaratne, K. P. S. C., Cooray, P. T. L. V. and Attygalle, M. L. C., 2020. Determination of oscillation frequencies and stellar properties of three Delta Scuti variable stars using Kepler data. *Journal of the National Science Foundation of Sri Lanka*, *48*(4), pp. 367-378.
   DOI: https://doi.org/10.4038/jnsfsr.v48i4.9145

3. **Adassuriya, J**., Jayaratne, K. P. S. C. and Ganesh, S., 2018. Light travel time effect of the binary orbit of SZ Lyn. *Journal of Sri Lanka Association for the Advancement of Science, 1*, pp. 40-49.

4. **J. Adassuriya,** J. A. N. S. S. Jayasinghe, and K. P. S. C. Jayaratne. Identify variable stars from kepler data using machine learning. Submitted: July, 2021. *European Journal of Applied Physics.*

Manuscript prepared for submission

5. **J. Adassuriya**, K. Sellahewa, K. P. S. C. Jayaratne and S. Ganesh. AlphaTg:Code for flux derivatives and limb darkening integrals for asteroseismology, *Astronomy and Computing.*

Conference Abstracts

6. **J. Adassuriya** and K. P. S. C. Jayaratne, 2020. Oscillation frequencies of two Delta Scuti stars; KIC 4077032 and KIC 8623953, *76th Annual Sessions, Sri Lanka Assocoation for the Advancement of Science*, pp. 78.

7. **Janaka Adassuriya**, Shashikiran Ganesh and Chandana Jayaratne, 2018. Asteroseismology of SZ Lyn using very high time resolution photometry in BVR bands. *Physics of Oscillating Stars (PHOST), Banyuls-sur-mer, France, 2-7 September 2018.*
   DOI: https://doi.org/10.5281/zenodo.1463699

8. **Adassuriya J**., Asteroseismology of Delta Scuti Stars, 2020. *International Workshop on Space Science (IWSS 2020), 18-21 May 2020, Rajkot, India.*

9. **J. Adassuriya**, K. P. S. C. Jayaratne, P. T. L. Cooray, and M. L. Attygalle, 2018. Determination of oscillation frequencies of Delta Scuti star KIC 1162150. *Annual Research Symposium, University of Colombo,* pp. 219.

10. **J. Adassuriya**, K. P. S. Chandana Jayaratne, S. Ganesh, 2018. Orbital elements of SZ Lyn, 74th Annual Sessions, Sri Lanka Association for the Advancement of Science, pp. 66.

11. **J. Adassuriya**, K. P. S. C. Jayaratne, S. Ganesh, 2017. Light curve analysis of CC Andromeda. *Annual Research Symposium, University of Colombo*, pp. 257.

Awards

1. *Orbital Elements of SZ Lyn*, Best oral presentation section E1 - Physical Sciences, 74th Annual Session 2018, Sri Lanka Association for the Advancement of Science.

2. *Asteroseismology of Delta Scuti Star*, 3rd Place, oral presentation.
   International Workshop on Space Science, 18 - 21 May 2020, Rajkot, India.
   Department of Physics, School of Science, RK University, Rajkot, India.

3. Indian Science Research Fellowship (ISRF), 2016. Department of Space, Government of India.

List of References

Aerts, C., De Pauw, M. & Waelkens, C. (1992). Mode identification of pulsating stars from line profile variations with the moment method. an example-The Beta Cephei star Delta Ceti. *Astronomy and Astrophysics*, *266*, pp.294-306.

Aerts, C. (1996). Mode identification of pulsating stars from line-profile variations with the moment method: a more accurate discriminant. *Astronomy and Astrophysics*, *314*, pp.115-122.

Aerts, C., Christensen-Dalsgaard, J. & Kurtz, W. D. (2010). *Asteroseismology*. Springer Dordrecht Hedielberg, London.

Aerts, C. and De Cat, P. (2003). β Cep stars from a spectroscopic point of view. *Space Science Reviews*, *105*(1-2), 453 - 492.

Aerts, C., De Cat, P., Peeters, E., Decin, L., De Ridder, J., Kolenberg, et al. (1999). Selection of a sample of bright southern Slowly Pulsating B Stars for long-term photometric and spectroscopic monitoring. *Astronomy and astrophysics*, *343*, 872 - 882.

Aerts, C. & Waelkens, C. (1993). Line Profile Variations of Rotating Pulsating Stars. *Astronomy and Astrophysics*, *273*, 135.

Aerts, C. (2019). Probing the interior physics of stars through asteroseismology. *arXiv preprint arXiv:1912.12300*.

Alania, I. F. (1972). Spectral Class and Metal-Abundance Index Determination for 20 RR Lyrae Stars at Light Maximum. *Information Bulletin on Variable Stars*, *702*.

Asplund, M., Grevesse, N., Sauval, A. J. & Scott, P. (2009). The chemical composition of the Sun. *Annual review of astronomy and astrophysics*, *47*.

Balona, L. A., Dziembowski, W.A. and Pamyatnykh, A. (1997). The structure of the instability strip and mode identification for β Cep stars in three young open clusters. *Monthly Notices of the Royal Astronomical Society*, *289*(1), pp.25-36.

Balona, L. A. (1986). Mode identification from line profile variations. *Monthly Notices of the Royal Astronomical Society*, *219*(1), pp.111-129.

Balona, L. A. (1986). Mode identification from line profile variations–II. A quantitative least-squares algorithm. *Monthly Notices of the Royal Astronomical Society*, *220*(3), pp.647-656.

Balona, L. A. & Evers, E. A. (1999). Mode identification and asteroseismology of δ Scuti stars. *Monthly Notices of the Royal Astronomical Society*, *302*(2), 349-361.

Balona, L. A. & Dziembowski, W. A. (2011). Kepler observations of δ Scuti stars. *Monthly Notices of the Royal Astronomical Society*, *417*(1), 591-601.

Balona, L. A., Lenz, P., Antoci, V., Bernabei, S., Catanzaro, G., Daszyńska-Daszkiewicz, J., et al. (2012). Kepler observations of the high-amplitude δ Scuti star V2367 Cyg. *Monthly Notices of the Royal Astronomical Society*, *419*(4), pp.3028-3038.

Balona, L. A., Holdsworth, D.L. and Cunha, M.S. (2019). High frequencies in TESS A–F main-sequence stars. *Monthly Notices of the Royal Astronomical Society*, *487*(2), pp.2117-2132.

Baker, N. & Kippenhahn, R. (1962). The Pulsations of Models of delta Cephei Stars. With 17 Figures in the Text. *Zeitschrift fur Astrophysik*, *54*, 114.

Baker, N. & Kippenhahn, R. (1965). The pulsations of models of i Cephei stars. *Publications of Goddard Space Flight Center*, 11.

Barning, F. J. (1963). The numerical analysis of the light-curve of 12 Lacertae. *Bulletin of the Astronomical Institutes of the Netherlands*, *17*, p.22.

Bardin, C. and Imbert, M. (1981). Radial velocities of the dwarf cepheid SZ Lyn at high temporal resolution. *Astronomy and Astrophysics*, *98*, pp.198-202.

Barnes III, T. G. and Moffett, T.J. (1975). Photometric properties and evidence of duplicity for SZ Lyncis. *The Astronomical Journal*, *80*, pp.48-55.

Beck, P. G., Montalban, J., Kallinger, T., De Ridder, J., Aerts, C., García, R.A., et al. (2012). Fast core rotation in red-giant stars as revealed by gravity-dominated mixed modes. *Nature*, *481*(7379), 55-57.

Binnendijk, L. (1968). Photoelectric observations of SZ Lyncis. *The Astronomical Journal*, *73*, pp. 29-31.

Bloomfield, P. (2004). *Fourier analysis of time series: an introduction*. John Wiley & Sons.

Böhm-Vitense, E. (1992). *Introduction to Stellar Astrophysics: Volume 3* (Vol. 3). Cambridge University Press, Cambridge.

Bowman, D. M. (2017). *Amplitude Modulation of Pulsation Modes in Delta Scuti Stars*. Springer.

Bowman, D. M. and Kurtz, D. W. (2018). Characterizing the observational properties of δ Sct stars in the era of space photometry from the Kepler mission. *Monthly Notices of the Royal Astronomical Society*, *476*(3), 3169-3184.

Brassard, P., Fontaine, G. and Wesemael, F. (1995). The modeling of energy distributions and light curves of ZZ Ceti stars. 1: Basic theory and semianalytic expressions for the emergent flux. *The Astrophysical Journal Supplement Series*, *96*, pp.545-580.

Breger, M. and Bregman, J.N. (1975). Period-luminosity-color relations and pulsation modes of pulsating variable stars. *The Astrophysical Journal*, *200*, pp.343-353.

Breger, M., Lenz, P., Antoci, V., Guggenberger, E., Shobbrook, R. R., Handler, G., et al. (2005). Detection of 75+ pulsation frequencies in the δ Scuti star FG Virginis. *Astronomy & Astrophysics*, *435*(3), 955-965.

Breger, M. & Lenz, P. (2008). 44 Tau: Examination of amplitude variability and combination frequencies. *CoAst*, *157*, 292.

Breger, M. & Hiesberger, F. (1999). The multiperiodic δ Scuti star 4 Canum Venaticorum: 1997 APT photometry. *Astronomy and Astrophysics Supplement Series*, *135*(3), 547-553.

Breger, M. & Montgomery, M. H. (2001). Book Review: Delta Scuti and related stars: reference handbook and proceedings of the 6th Vienna Workshop in astrophysics/Astronomical Society of the Pacific, 2000. *The Observatory*, *121*, 122.

Breger, M., Balona, L., Lenz, P., Hollek, J.K., Kurtz, D.W., Catanzaro, G., et al. (2011). Regularities in frequency spacings of δ Scuti stars: the Kepler star KIC 9700322. *Monthly Notices of the Royal Astronomical Society*, *414*(2), 1721-1731.

Breger, M., Stich, J., Garrido, R., Martin, B., Jiang, S.Y., Li, Z. P., et al. (1993). Nonradial pulsation of the delta-scuti star Bu-Cancri in the praesepe cluster. *Astronomy and Astrophysics*, *271*, 482.

Breger, M., Handler, G., Garrido, R., Audard, N., Zima, W., Paparó, M., et al. (1999). 30+ frequencies for the delta Scuti variable 4 Canum Venaticorum: results of the 1996 multisite campaign. *Astronomy and Astrophysics*, *349*, 225-235.

Breger, M., Zima, W., Handler, G., Poretti, E., Shobbrook, R. R., Nitta, A., et al. (1998). The Delta Scuti star FG Vir. III. The 1995 multisite campaign and the detection of 24 pulsation frequencies. *Astronomy and Astrophysics*, *331*, 271-279.

Briquet, M. & Aerts, C. (2003). A new version of the moment method, optimized for mode identification in multiperiodic stars. *Astronomy & Astrophysics*, *398*(2), pp.687-696.

Brown, A. G., Vallenari, A., Prusti, T., De Bruijne, J. H. J., Mignard, F., Drimmel, R., et al. (2016). Gaia Data Release 1-Summary of the astrometric, photometric, and survey properties. *Astronomy & Astrophysics*, *595*, A2.

Brown, A. G., Vallenari, A., Prusti, T., De Bruijne, J. H. J., Babusiaux, C., Bailer-Jones, C. A. L., et al. (2018). Gaia Data Release 2-Summary of the contents and survey properties. *Astronomy & astrophysics*, *616*, A1.

Brown, T. M., Latham, D. W., Everett, M. E. & Esquerdo, G.A. (2011). Kepler input catalog: photometric calibration and stellar classification. *The Astronomical Journal*, *142*(4), p.112.

Castelli, F. & Kurucz, R. L. (2004). New grids of ATLAS9 model atmospheres. *arXiv preprint astro-ph/0405087*.

Christensen-Dalsgaard, J. (1976). On isolated stars in non-radial oscillation. *Monthly Notices of the Royal Astronomical Society*, *174*, 87-90.

Christensen-Dalsgaard, J., Däppen, W., Ajukov, S.V., Anderson, E.R., Antia, H.M., Basu, S., et al. (1996). The current state of solar modeling. *Science*, *272*(5266), 1286-1292.

Claret, A. (2000). A new non-linear limb-darkening law for LTE stellar atmosphere models. Calculations for-5.0<= log [M/H]<=+ 1, 2000 K<= Teff<= 50000 K at several surface gravities. *Astronomy and Astrophysics*, *363*, 1081-1190.

Cox, A. N. ed., (2015). *Allen's astrophysical quantities*. Springer. Los Alamos.

Cugier, H. & Daszyńska, J. (2001). Spectroscopic nonadiabatic observables in Cephei models. *Astronomy & Astrophysics*, *377*(1), pp.113-122.

Daszyńska-Daszkiewicz, J., Dziembowski, W.A., Pamyatnykh, A.A. and Goupil, M.J. (2002). Photometric amplitudes and phases of nonradial oscillation in rotating stars. *Astronomy & Astrophysics*, *392*(1), pp.151-159.

Daszyńska-Daszkiewicz, J. & Walczak, P. (2009). Constraints on opacities from complex asteroseismology of B-type pulsators: the β Cephei star θ Ophiuchi. *Monthly Notices of the Royal Astronomical Society*, *398*(4), 1961-1969.

Davison, C. (1936). Great earthquakes. Thomas Murby and Company, London.

Deheuvels, S., García, R.A., Chaplin, W.J., Basu, S., Antia, H.M., Appourchaux, T., et al. (2012). Seismic evidence for a rapidly rotating core in a lower-giant-branch star observed with Kepler. *The astrophysical journal*, *756*(1), 19.

De Pauw, M., Aerts, C. and Waelkens, C. (1993). Mode identification of pulsating stars from line profile variations with the moment method. A theoretical study of the accuracy of the method. *Astronomy and astrophysics*, *280*, pp.493-507.

De Ridder, J., Dupret, M. A., Neuforge, C. and Aerts, C. (2002). Influence of non-adiabatic temperature variations on line profile variations of slowly rotating β Cephei stars and SPBs-II. Simulations of line profile time series. *Astronomy & Astrophysics*, *385*(2), 572-584.

Dupret, M. A. (2001). Nonradial nonadiabatic stellar pulsations: A numerical method and its application to a β Cephei model. *Astronomy & Astrophysics*, *366*(1), 166-173.

Dupret, M. A., De Ridder, J., De Cat, P., Aerts, C., Scuflaire, R., Noels, A. et al. (2003). A photometric mode identification method, including an improved non-adiabatic treatment of the atmosphere. *Astronomy & Astrophysics*, *398*(2), 677-685.

Dupret, M. A., Grigahcene, A., Garrido, R., De Ridder, J., Scuflaire, R. and Gabriel, M. (2005). Time-dependent convection seismic study of δ Sct stars. *Monthly Notices of the Royal Astronomical Society*, *361*(2), 476-486.

Dupret, M. A., Grigahcene, A., Garrido, R., Gabriel, M. and Scuflaire, R. (2005). Convection-pulsation coupling-II. Excitation and stabilization mechanisms in δ Sct and γ Dor stars. *Astronomy & Astrophysics*, *435*(3), 927-939.

Dupret, M. A., Grigahcene, A., Garrido, R., Gabriel, M. & Scuflaire, R. (2004). Theoretical instability strips for δ Scuti and γ Doradus stars. *Astronomy & Astrophysics*, *414*(2), L17-L20.

Dziembowski, W. (1977). Light and radial velocity variations in a nonradially oscillating star. *AcA*, *27*, 203-211.

Dziembowski, W. (1977). Oscillations of giants and supergiants. *Acta Astronomica*, *27*, 95-126.

Dziembowski, W. A. & Pamyatnykh, A. A. (1993). The opacity mechanism in B-type stars–I. Unstable modes in β Cephei star models. *Monthly Notices of the Royal Astronomical Society*, *262*(1), pp.204-212.

Eddington, A. S. and Eddington, A. S. (1988). *The internal constitution of the stars*. Cambridge University Press, Cambridge.

Fernley, J. A., Jameson, R. F. and Sherrington, M. R. (1984). BVJHK observations of the dwarf Cepheid SZ Lynx. *Monthly Notices of the Royal Astronomical Society*, *208*(4), pp.853-863.

Fitch, W. S. (1981). LO, 1, 2, and 3 pulsation constants for evolutionary models of delta-scuti stars. *The Astrophysical Journal*, *249*, 218.

Ganesh, S., Baliyan, K.S., Chandra, S., Joshi, U.C., Kalyaan, A. & Mathur, S.N. (2013). Automated telescope for variability studies. In *Astronomical Society of India Conference Series* (Vol. 9, p. 99).

Garrido, R., Garcia-Lobo, E. & Rodriguez, E. (1990). Modal discrimination of pulsating stars by using Stromgren photometry. *Astronomy and Astrophysics, 234,* 262-268.

Garrido, R. (2000). Photometric modal discrimination in Delta Scuti and Gamma Doradus stars. *arXiv preprint astro-ph/0001064*.

García, R.A., Hekker, S., Stello, D., Gutiérrez-Soto, J., Handberg, R., Huber, D., et al. (2011). Preparation of Kepler light curves for asteroseismic analyses. *Monthly Notices of the Royal Astronomical Society: Letters, 414*(1), pp.L6-L10.

Gaspani, A. (1998). Neural Techniques for Low Height Photometry of Variable Stars. In *29th Conference on Variable Star Research* (p. 96).

Gazeas, K. D., Niarchos, P. G. & Boutsia, K. A. (2004). SZ Lyn: New BVRI CCD observations and improved pulsational and orbital elements. *Communications in Asteroseismology, 144,* 26-34.

Gilliland, R. L., Jenkins, J. M., Borucki, W. J., Bryson, S. T., Caldwell, D. A., Clarke, B. D., et al. (2010). Initial characteristics of Kepler short cadence data. *The Astrophysical Journal Letters, 713*(2), L160.

Goupil, M. J., Dziembowski, W. A., Pamyatnykh, A. A. and Talon, S. (2000). Rotational Splitting of delta Scuti Stars. In *Delta Scuti and Related Stars,Vol. 210,* 267.

Grigahcène, A., Antoci, V., Balona, L., Catanzaro, G., Daszyńska-Daszkiewicz, J., Guzik, J. A., et al. (2010). Hybrid γ Doradus-δ Scuti pulsators: New insights into the physics of the oscillations from Kepler observations. *The Astrophysical Journal Letters, 713*(2), L192.

Guzik, J. A., Garcia, J. A. & Jackiewicz, J. (2019). Properties of 249 δ Scuti Variable Star Candidates Observed During the NASA K2 Mission. *Frontiers in Astronomy and Space Sciences, 6,* 40.

Handler, G. (2012). Asteroseismology. *arXiv preprint arXiv:1205.6407*.

Hartman, J. D. & Bakos, G. Á. (2016). VARTOOLS: A program for analyzing astronomical time-series data. *Astronomy and Computing, 17,* 1-72.

Heynderickx, D., Waelkens, C. & Smeyers, P. (1994). A photometric study of beta Cephei stars. II. Determination of the degrees L of pulsation modes. *Astronomy and Astrophysics Supplement Series, 105,* 447-480.

Hoffmeister, C. (1949). Verzeichnis von 1440 neuen veranderlichen Sternen MIT Angaben uber die Art ihres Lichtwechsels. *Berlin*.

Houdek, G. & Dupret, M. A. (2015). Interaction between convection and pulsation. *Living Reviews in Solar Physics*, *12*(1), 8.

Iglesias, C. A. & Rogers, F. J. (1996). Updated OPAL opacities. *The astrophysical journal*, *464*, 943.

Irwin, J. B. (1952). The Determination of a Light-Time Orbit. *The Astrophysical Journal*, *116*, p.211.

Jenkins, J. M., Twicken, J.D., McCauliff, S., Campbell, J., Sanderfer, D., Lung, D., et al. (2016). August. The TESS science processing operations center. In *Software and Cyberinfrastructure for Astronomy IV* (Vol. 9913, p. 99133E). International Society for Optics and Photonics.

Johnson, H. L., Mitchell, R. I., Iriarte, B. & Wisniewski, W. Z. (1966). UBVRIJKL photometry of the bright stars. *CoLPL*, *4*, 99-110.

Kendall, M. & Ord, J.K. (1990). Time Series, I Edward Arnold. *Sevenoaks, Kent, Great Britain*, pp.51-52.

Kern, J. W., Reed, M. D., Baran, A. S., Telting, J. H. & Østensen, R. H. (2018). Asteroseismic analysis of the pulsating subdwarf B star KIC 11558725: an sdB+ WD system with divergent frequency multiplets and mode trapping observed by Kepler. *Monthly Notices of the Royal Astronomical Society*, *474*(4), 4709-4716.

Kuschnig, R., Weiss, W.W., Gruber, R., Bely, P.Y. & Jenkner, H. (1997). Microvariability survey with the hubble space telescope fine guidance sensors. Exploring the instrumental properties. *Astronomy and Astrophysics*, *328*, pp.544-550.

Kurtz, D. W., Saio, H., Takata, M., Shibahashi, H., Murphy, S. J. & Sekii, T. (2014). Asteroseismic measurement of surface-to-core rotation in a main-sequence A star, KIC 11145123. *Monthly Notices of the Royal Astronomical Society*, *444*(1), 102-116.

Kurtz, D.W., Shibahashi, H., Murphy, S.J., Bedding, T.R. & Bowman, D.M. (2015). A unifying explanation of complex frequency spectra of γ Dor, SPB and Be stars: combination frequencies and highly non-sinusoidal light curves. *Monthly Notices of the Royal Astronomical Society*, *450*(3), pp.3015-3029.

Kurucz, R. L. (1993). VizieR online data catalog: model atmospheres (Kurucz, 1979). *VizieR online data catalog*, pp.VI-39.

Langford, W. R. (1976). *Intermediate-Band Photometry of Short Period Dwarf Cepheid Variables*. Brigham Young University.

Ledoux, P. & Walraven, T. (1958). Variable stars. In *Astrophysics II: Stellar Structure/Astrophysik II: Sternaufbau* 353-604. Springer, Berlin, Heidelberg.

Ledoux, P. (1951). The Nonradial Oscillations of Gaseous Stars and the Problem of Beta Canis Majoris. *Astrophysical Journal*, *114*, 373-384.

Lenz, P. & Breger, M. (2005). Period04 user guide. *Communications in Asteroseismology*, *146*, 53-136.

Lin-Jia, L. and Sheng-Bang, Q. (2013). Observations and Orbital Analysis of the High-Amplitude Delta Scuti Star SZ Lyncis: The Unusual Orbital Precession. *Publications of the Astronomical Society of Japan*, *65*(6).

Lomb, N. R. (1976). Least-squares frequency analysis of unequally spaced data. *Astrophysics and space science*, *39*(2), 447-462.

Luo, A. L., Zhao, Y. H., Zhao, G., Deng, L. C., Liu, X. W., Jing, Y. P., et al. (2015). The first data release (DR1) of the LAMOST regular survey. *Research in Astronomy and Astrophysics*, *15*(8), 1095.

Luri, X., Brown, A. G. A., Sarro, L. M., Arenou, F., Bailer-Jones, C. A. L., Castro-Ginard, et al. (2018). Gaia data release 2-using gaia parallaxes. *Astronomy & Astrophysics*, *616*, A9.

Maeder A. (2009). *Physics, Formation and Evolution of Rotating Stars,* 371-448, Springer.

Massey, P. and Davis, L. E. (1992). A User's Guide to Stellar CCD photometry with IRAF. *NOAO Laboratory*.

McNamara, D. (1997). Luminosities of SX Phoenicis, large-amplitude Delta Scuti, and RR Lyrae stars. *Publications of the Astronomical Society of the Pacific*, *109*(741), 1221.

Moffett, T. J., Barnes III, T. G., Fekel Jr, F.C., Jefferys, W. H. and Achtermann, J. M. (1988). Orbital and photometric properties of SZ Lyncis. *The Astronomical Journal*, *95*, pp.1534-1542.

Molnár, L., Kolláth, Z., Szabó, R., Bryson, S., Kolenberg, K., Mullally, F. and Thompson, S. E. (2012). Nonlinear asteroseismology of RR Lyrae. *The Astrophysical Journal Letters*, *757*(1), p.L13.

Murphy, S. J., Pigulski, A., Kurtz, D.W., Suárez, J.C., Handler, G., Balona, L. A., et al. (2013). Asteroseismology of KIC 11754974: a high-amplitude SX Phe pulsator in a 343-d binary system. *Monthly Notices of the Royal Astronomical Society*, *432*(3), 2284-2297.

Niemczura, E., Murphy, S. J., Smalley, B., Uytterhoeven, K., Pigulski, A., Lehmann, H., et al. (2015). Spectroscopic survey of Kepler stars. I. HERMES/Mercator

observations of A-and F-type stars. *Monthly Notices of the Royal Astronomical Society*, *450*(3), 2764-2783.

Oelkers, R. J. and Stassun, K. G. (2018). Precision Light Curves from TESS Full-frame Images: A Different Imaging Approach. *The Astronomical Journal*, *156*(3), 132.

Oke, J.B. (1974). Absolute spectral energy distributions for white dwarfs. *The Astrophysical Journal Supplement Series*, *27*, p.21.

Osaki, Y. (1971). Non-Radial Oscillations and the Beta Canis Majoris Phenomenon. *Publications of the Astronomical Society of Japan*, *23*, p.485.

Pamyatnykh, A. A. (1999). Pulsational instability domains in the upper main sequence. *Acta Astronomica*, *49*, 119-148.

Paparó, M., Szeidl, B. and Mahdy, H. A. (1988). The high amplitude Delta Scuti star SZ Lyncis revisited. *Astrophysics and space science*, *149*(1), pp.73-82.

Paparó, M., Kolláth, Z., Shobbrook, R. R., Matthews, J. M., Antoci, V., Benkő, J. M., et al. (2018). The Delta Scuti star 38 Eri from the ground and from space. *Monthly Notices of the Royal Astronomical Society*, *477*(4), 4362-4379.

Pápics, P. I., Briquet, M., Baglin, A., Poretti, E., Aerts, C., Degroote, P., et al. (2012). Gravito-inertial and pressure modes detected in the B3 IV CoRoT target HD 43317. *Astronomy & Astrophysics*, *542*, p.A55.

Paxton, B., Bildsten, L., Dotter, A., Herwig, F., Lesaffre, P. and Timmes, F. (2010). Modules for experiments in stellar astrophysics (MESA). *The Astrophysical Journal Supplement Series*, *192*(1), 3.

Paxton, B., Cantiello, M., Arras, P., Bildsten, L., Brown, E. F., Dotter, A., et al., (2013). Modules for experiments in stellar astrophysics (MESA): planets, oscillations, rotation, and massive stars. *The Astrophysical Journal Supplement Series*, *208*(1), 4.

Paxton, B., Marchant, P., Schwab, J., Bauer, E. B., Bildsten, L., Cantiello, M., et al. (2015). Modules for experiments in stellar astrophysics (MESA): binaries, pulsations, and explosions. *The Astrophysical Journal Supplement Series*, *220*(1), 15.

Paxton, B., Smolec, R., Schwab, J., Gautschy, A., Bildsten, L., Cantiello, M., et al. (2019). Modules for experiments in stellar astrophysics (MESA): Pulsating variable stars, rotation, convective boundaries, and energy conservation. *The Astrophysical Journal Supplement Series*, *243*(1), 10.

Pinsonneault, M. (1997). Mixing in stars. *Annual Review of Astronomy and Astrophysics*, *35*(1), 557-605.

Reed, M. D., Baran, A., Quint, A. C., Kawaler, S. D., O'Toole, S. J., Telting, J., et al. (2011). First Kepler results on compact pulsators–VIII. Mode identifications via period spacings in g-mode pulsating subdwarf B stars. *Monthly Notices of the Royal Astronomical Society*, *414*(4), 2885-2892.

Ricker, G. R., Winn, J. N., Vanderspek, R., Latham, D. W., Bakos, G. Á., Bean, J. L., et al. (2014). Transiting exoplanet survey satellite. *Journal of Astronomical Telescopes, Instruments, and Systems*, *1*(1), p.014003.

Rodríguez, E. & Breger, M. (2001). δ Scuti and related stars: Analysis of the R00 Catalogue. *Astronomy & Astrophysics*, *366*(1), pp.178-196.

Rogers, F. J., Swenson, F. J. & Iglesias, C. A. (1996). OPAL equation-of-state tables for astrophysical applications. *The Astrophysical Journal, 456*, 902.

Rogers, F. J. & Iglesias, C. A. (1998). Opacity of stellar matter. *Space science reviews*, *85*(1-2), 61-70.

Scargle, J. D. (1982). Studies in astronomical time series analysis. II-Statistical aspects of spectral analysis of unevenly spaced data. *The Astrophysical Journal, 263*, 835-853.

Seaton, M. J. (2005). Opacity Project data on CD for mean opacities and radiative accelerations. *Monthly Notices of the Royal Astronomical Society: Letters*, *362*(1), pp.L1-L3.

Scuflaire, R., Théado, S., Montalbán, J., Miglio, A., Bourge, P.O., Godart, M., et al. (2008). CLÉS, Code Liégeois d'Évolution Stellaire. *Astrophysics and Space Science*, *316*(1-4), 83-91.

Shapley, H. (1914). On the nature and cause of Cepheid variation. *The Astrophysical Journal, 40*, 448.

Smith, J. A., Tucker, D. L., Kent, S., Richmond, M. W., Fukugita, M., Ichikawa, T., et al (2002). The ugriz standard-star system. *The Astronomical Journal, 123*(4), p.2121.

Stellingwerf, R. F. (1979). Pulsation in the lower Cepheid strip. I-Linear survey. *The Astrophysical Journal, 227*, 935-942.

Street, R. A., Pollacco, D. L., Fitzsimmons, A., Keenan, F. P., Horne, K., Kane, S., et al. (2002). Superwasp: wide angle search for planets. *arXiv preprint astro-ph/0208233*.

Suárez, J. C., Garrido, R. & Goupil, M.J. (2006). The role of rotation on Petersen diagrams. The period ratios. *Astronomy & Astrophysics*, *447*(2), pp.649-653.

Suárez, J. C., Hernández, A. G., Moya, A., Rodrigo, C., Solano, E., Garrido, R. et al. (2014). Measuring mean densities of δ Scuti stars with asteroseismology-Theoretical properties of large separations using TOUCAN. *Astronomy & Astrophysics*, *563*, A7.

Suárez, J. C. & Goupil, M. J. (2008). FILOU oscillation code. *Astrophysics and Space Science*, *316*(1-4), 155-161.

Tassoul, M. (1980). Asymptotic approximations for stellar nonradial pulsations. *The Astrophysical Journal Supplement Series*, *43*, pp.469-490.

Tassoul, M. (1990). Second-order asymptotic approximations for stellar nonradial acoustic modes. *The Astrophysical Journal*, *358*, pp.313-327.

Tayar, J. and Pinsonneault, M.H. (2013). Implications of rapid core rotation in red giants for internal angular momentum transport in stars. *The Astrophysical Journal Letters*, *775*(1), L1.

Tian, Z. J., Bi, S. L., Yang, W. M., Chen, Y. Q., Liu, Z. E., Liu, K., et al. (2014). Asteroseismic analysis of solar-like star KIC 6225718: constraints on stellar parameters and core overshooting. *Monthly Notices of the Royal Astronomical Society*, *445*(3), 2999-3008.

Ulrich, R. K. (1970). Convective Energy Transport in Stellar Atmospheres. II: Model Atmosphere Calculation. *Astrophysics and Space Science*, *7*, 183-200.

Uytterhoeven, K., Moya, A., Grigahcène, A., Guzik, J. A., Gutiérrez-Soto, J., Smalley, B., et al. (2011). The Kepler characterization of the variability among A-and F-type stars-I. General overview. *Astronomy & Astrophysics*, *534*, A125.

Van Genderen, A. M. (1967). Variations in the period and in the light-curve of SZ Lyncis. *Bulletin of the Astronomical Institutes of the Netherlands*, *19*, p.74.

Viskum, M., Kjeldsen, H., Bedding, T. R., Dall, T. H., Baldry, I. K., Bruntt, H. (1998). Oscillation mode identifications and models for the delta Scuti star FG Virginis. *arXiv preprint astro-ph/9804218*.

Watson, R.D. (1988). Contributing factors to flux changes in nonradial stellar pulsations. *Astrophysics and space science*, *140*(2), pp.255-290.

Zechmeister, M. & Kürster, M. (2009). The generalised Lomb-Scargle periodogram-a new formalism for the floating-mean and Keplerian periodograms. *Astronomy & Astrophysics*, *496*(2), 577-584.

Zhao, G., Zhao, Y. H., Chu, Y. Q., Jing, Y. P. and Deng, L. C. (2012). LAMOST spectral survey—An overview. *Research in Astronomy and Astrophysics*, *12*(7), 723.

Zhevakin, S. A. (1963). Physical basis of the pulsation theory of variable stars. *Annual Review of Astronomy and Astrophysics*, *1*(1), 367-400.

Zima, W. (2006). A new method for the spectroscopic identification of stellar non-radial pulsation modes-I. The method and numerical tests. *Astronomy & Astrophysics*, *455*(1), 227-234.

Zima, W., Wright, D., Bentley, J., Cottrell, P. L., Heiter, U., Mathias, P., et al. (2006). A new method for the spectroscopic identification of stellar non-radial pulsation modes-II. Mode identification of the δ Scuti star FG Virginis. *Astronomy & Astrophysics*, *455*(1), 235-246.

Zima, W. (2008). FAMIAS User Manual. *Communications in Asteroseismology, 155*, pp.17-121.

Appendix A

Two TDC models

M/M_sun = 1.90 T_{eff} =   7557.1   Log (L/L_sun) = 1.3221
Log g = 3.8612   R/R_sun = 2.6770   age (y)   = 1.0962E+09
X   = 0.72   Z   = 0.014   alphaconv   = 1.70   overshoot = 0.20

l	n	freq(c/d)	f_T	psi_T	f_g	psi_g
0	1	9.66E+00	4.28E+00	1.12E+02	1.47E+01	1.80E+02
0	2	1.25E+01	4.57E+00	1.07E+02	2.31E+01	1.80E+02
0	3	1.55E+01	4.46E+00	1.07E+02	3.47E+01	1.80E+02
0	4	1.86E+01	4.27E+00	1.18E+02	4.92E+01	1.80E+02
0	5	2.17E+01	4.56E+00	1.35E+02	6.61E+01	1.80E+02
0	6	2.47E+01	5.61E+00	1.51E+02	8.50E+01	1.80E+02
0	7	2.77E+01	7.29E+00	1.61E+02	1.06E+02	1.80E+02
0	8	3.09E+01	9.41E+00	1.66E+02	1.31E+02	1.80E+02
0	9	3.41E+01	1.18E+01	1.69E+02	1.60E+02	1.80E+02
0	10	3.74E+01	1.42E+01	1.71E+02	1.92E+02	1.80E+02
1	-17	1.49E+00	3.74E-01	3.12E+02	2.30E+00	1.80E+02
1	-15	1.65E+00	2.42E-01	2.22E+02	2.37E+00	1.80E+02
1	-14	1.79E+00	4.83E-01	1.87E+02	2.43E+00	1.80E+02
1	-12	2.02E+00	8.70E-01	1.72E+02	2.56E+00	1.80E+02
1	-12	2.02E+00	8.70E-01	1.72E+02	2.56E+00	1.80E+02
1	-11	2.23E+00	1.15E+00	1.66E+02	2.68E+00	1.80E+02
1	-10	2.49E+00	1.42E+00	1.61E+02	2.85E+00	1.80E+02
1	-9	2.67E+00	1.57E+00	1.58E+02	2.97E+00	1.80E+02
1	-8	3.00E+00	1.81E+00	1.54E+02	3.22E+00	1.80E+02
1	-7	3.50E+00	2.11E+00	1.48E+02	3.66E+00	1.80E+02
1	-6	3.91E+00	2.32E+00	1.44E+02	4.08E+00	1.80E+02
1	-5	4.53E+00	2.60E+00	1.39E+02	4.79E+00	1.80E+02
1	-4	5.74E+00	3.09E+00	1.31E+02	6.46E+00	1.80E+02
1	-3	7.23E+00	3.64E+00	1.23E+02	9.08E+00	1.80E+02
1	-2	8.94E+00	4.11E+00	1.15E+02	1.28E+01	1.80E+02
1	-1	9.97E+00	4.32E+00	1.12E+02	1.55E+01	1.80E+02
1	1	1.28E+01	4.58E+00	1.06E+02	2.43E+01	1.80E+02
1	2	1.59E+01	4.44E+00	1.08E+02	3.62E+01	1.80E+02
1	3	1.83E+01	4.29E+00	1.16E+02	4.73E+01	1.80E+02
1	4	1.98E+01	4.30E+00	1.24E+02	5.51E+01	1.80E+02
1	5	2.27E+01	4.82E+00	1.41E+02	7.19E+01	1.80E+02
1	6	2.58E+01	6.14E+00	1.55E+02	9.22E+01	1.80E+02
1	7	2.89E+01	8.05E+00	1.63E+02	1.15E+02	1.80E+02
1	8	3.21E+01	1.03E+01	1.68E+02	1.42E+02	1.80E+02
1	9	3.55E+01	1.28E+01	1.70E+02	1.73E+02	1.80E+02
1	10	3.88E+01	1.52E+01	1.71E+02	2.07E+02	1.80E+02
2	-29	1.56E+00	3.75E+00	3.41E+02	2.33E+00	1.80E+02

2	-26	1.72E+00	2.83E+00	3.36E+02	2.40E+00	1.80E+02
2	-24	1.84E+00	2.25E+00	3.32E+02	2.46E+00	1.80E+02
2	-22	2.00E+00	1.63E+00	3.26E+02	2.54E+00	1.80E+02
2	-21	2.08E+00	1.36E+00	3.22E+02	2.58E+00	1.80E+02
2	-20	2.19E+00	1.01E+00	3.15E+02	2.65E+00	1.80E+02
2	-19	2.29E+00	7.72E-01	3.06E+02	2.71E+00	1.80E+02
2	-18	2.40E+00	5.40E-01	2.89E+02	2.78E+00	1.80E+02
2	-17	2.56E+00	3.87E-01	2.46E+02	2.89E+00	1.80E+02
2	-16	2.69E+00	4.47E-01	2.11E+02	2.98E+00	1.80E+02
2	-15	2.83E+00	6.05E-01	1.89E+02	3.08E+00	1.80E+02
2	-14	3.06E+00	9.04E-01	1.72E+02	3.27E+00	1.80E+02
2	-13	3.31E+00	1.18E+00	1.63E+02	3.48E+00	1.80E+02
2	-12	3.47E+00	1.35E+00	1.59E+02	3.63E+00	1.80E+02
2	-11	3.82E+00	1.68E+00	1.53E+02	3.97E+00	1.80E+02
2	-10	4.26E+00	2.02E+00	1.47E+02	4.46E+00	1.80E+02
2	-9	4.58E+00	2.23E+00	1.43E+02	4.83E+00	1.80E+02
2	-8	5.09E+00	2.54E+00	1.39E+02	5.51E+00	1.80E+02
2	-7	5.92E+00	2.97E+00	1.32E+02	6.75E+00	1.80E+02
2	-6	6.64E+00	3.29E+00	1.27E+02	7.97E+00	1.80E+02
2	-5	7.51E+00	3.62E+00	1.23E+02	9.64E+00	1.80E+02
2	-4	8.96E+00	4.07E+00	1.16E+02	1.29E+01	1.80E+02
2	-3	1.02E+01	4.33E+00	1.12E+02	1.60E+01	1.80E+02
2	-2	1.16E+01	4.51E+00	1.08E+02	2.03E+01	1.80E+02
2	-1	1.28E+01	4.57E+00	1.07E+02	2.43E+01	1.80E+02
2	0	1.43E+01	4.54E+00	1.07E+02	2.99E+01	1.80E+02
2	1	1.63E+01	4.41E+00	1.09E+02	3.81E+01	1.80E+02
2	2	1.84E+01	4.29E+00	1.17E+02	4.80E+01	1.80E+02
2	3	2.12E+01	4.47E+00	1.32E+02	6.28E+01	1.80E+02
2	4	2.42E+01	5.37E+00	1.48E+02	8.12E+01	1.80E+02
2	5	2.72E+01	6.98E+00	1.59E+02	1.03E+02	1.80E+02
2	6	3.04E+01	9.07E+00	1.65E+02	1.27E+02	1.80E+02
2	7	3.30E+01	1.10E+01	1.68E+02	1.50E+02	1.80E+02
2	8	3.39E+01	1.17E+01	1.69E+02	1.58E+02	1.80E+02
2	9	3.71E+01	1.40E+01	1.71E+02	1.89E+02	1.80E+02
2	10	4.05E+01	1.62E+01	1.72E+02	2.24E+02	1.80E+02
3	-42	1.52E+00	8.23E+00	3.45E+02	2.32E+00	1.80E+02
3	-40	1.60E+00	7.54E+00	3.44E+02	2.35E+00	1.80E+02
3	-38	1.69E+00	6.82E+00	3.42E+02	2.39E+00	1.80E+02
3	-37	1.72E+00	6.52E+00	3.41E+02	2.40E+00	1.80E+02
3	-36	1.77E+00	6.15E+00	3.40E+02	2.43E+00	1.80E+02
3	-35	1.83E+00	5.73E+00	3.39E+02	2.45E+00	1.80E+02
3	-34	1.88E+00	5.39E+00	3.38E+02	2.48E+00	1.80E+02
3	-33	1.93E+00	5.08E+00	3.36E+02	2.50E+00	1.80E+02
3	-32	1.99E+00	4.70E+00	3.35E+02	2.54E+00	1.80E+02
3	-31	2.05E+00	4.40E+00	3.34E+02	2.57E+00	1.80E+02
3	-30	2.11E+00	4.06E+00	3.32E+02	2.60E+00	1.80E+02

3	-29	2.19E+00	3.64E+00	3.30E+02	2.65E+00	1.80E+02
3	-28	2.26E+00	3.33E+00	3.28E+02	2.69E+00	1.80E+02
3	-27	2.32E+00	3.05E+00	3.26E+02	2.73E+00	1.80E+02
3	-26	2.41E+00	2.68E+00	3.23E+02	2.79E+00	1.80E+02
3	-25	2.49E+00	2.40E+00	3.21E+02	2.84E+00	1.80E+02
3	-24	2.58E+00	2.07E+00	3.17E+02	2.91E+00	1.80E+02
3	-23	2.71E+00	1.68E+00	3.12E+02	3.00E+00	1.80E+02
3	-22	2.81E+00	1.43E+00	3.07E+02	3.07E+00	1.80E+02
3	-21	2.91E+00	1.17E+00	2.99E+02	3.15E+00	1.80E+02
3	-20	3.07E+00	8.49E-01	2.84E+02	3.28E+00	1.80E+02
3	-19	3.21E+00	6.65E-01	2.65E+02	3.40E+00	1.80E+02
3	-18	3.36E+00	5.83E-01	2.36E+02	3.53E+00	1.80E+02
3	-17	3.58E+00	6.86E-01	2.00E+02	3.74E+00	1.80E+02
3	-16	3.78E+00	8.74E-01	1.82E+02	3.93E+00	1.80E+02
3	-15	3.95E+00	1.07E+00	1.71E+02	4.12E+00	1.80E+02
3	-14	4.27E+00	1.41E+00	1.60E+02	4.48E+00	1.80E+02
3	-13	4.62E+00	1.74E+00	1.52E+02	4.90E+00	1.80E+02
3	-12	4.84E+00	1.93E+00	1.49E+02	5.18E+00	1.80E+02
3	-11	5.30E+00	2.28E+00	1.43E+02	5.80E+00	1.80E+02
3	-10	5.91E+00	2.69E+00	1.36E+02	6.74E+00	1.80E+02
3	-9	6.38E+00	2.95E+00	1.32E+02	7.51E+00	1.80E+02
3	-8	7.00E+00	3.26E+00	1.28E+02	8.64E+00	1.80E+02
3	-7	8.05E+00	3.70E+00	1.22E+02	1.08E+01	1.80E+02
3	-6	8.98E+00	4.00E+00	1.17E+02	1.29E+01	1.80E+02
3	-5	9.51E+00	4.15E+00	1.15E+02	1.43E+01	1.80E+02
3	-4	1.05E+01	4.36E+00	1.12E+02	1.71E+01	1.80E+02
3	-3	1.20E+01	4.53E+00	1.08E+02	2.15E+01	1.80E+02
3	-2	1.33E+01	4.57E+00	1.07E+02	2.61E+01	1.80E+02
3	-1	1.53E+01	4.49E+00	1.08E+02	3.39E+01	1.80E+02
3	0	1.66E+01	4.40E+00	1.11E+02	3.96E+01	1.80E+02
3	1	1.85E+01	4.30E+00	1.17E+02	4.82E+01	1.80E+02
3	2	1.95E+01	4.31E+00	1.22E+02	5.34E+01	1.80E+02
3	3	2.21E+01	4.66E+00	1.37E+02	6.80E+01	1.80E+02
3	4	2.52E+01	5.83E+00	1.52E+02	8.79E+01	1.80E+02
3	5	2.83E+01	7.66E+00	1.62E+02	1.11E+02	1.80E+02
3	6	3.16E+01	9.92E+00	1.67E+02	1.37E+02	1.80E+02
3	7	3.49E+01	1.24E+01	1.70E+02	1.67E+02	1.80E+02
3	8	3.83E+01	1.48E+01	1.71E+02	2.01E+02	1.80E+02
3	9	4.00E+01	1.60E+01	1.72E+02	2.19E+02	1.80E+02
4	-57	1.46E+00	1.31E+01	3.49E+02	2.29E+00	1.80E+02
4	-54	1.54E+00	1.22E+01	3.48E+02	2.32E+00	1.80E+02
4	-50	1.66E+00	1.10E+01	3.46E+02	2.37E+00	1.80E+02
4	-49	1.69E+00	1.07E+01	3.45E+02	2.39E+00	1.80E+02
4	-48	1.72E+00	1.03E+01	3.44E+02	2.40E+00	1.80E+02
4	-46	1.79E+00	9.68E+00	3.43E+02	2.44E+00	1.80E+02
4	-46	1.79E+00	9.68E+00	3.43E+02	2.44E+00	1.80E+02

4	-45	1.83E+00	9.28E+00	3.42E+02	2.46E+00	1.80E+02
4	-44	1.88E+00	8.90E+00	3.41E+02	2.48E+00	1.80E+02
4	-43	1.92E+00	8.62E+00	3.40E+02	2.50E+00	1.80E+02
4	-42	1.96E+00	8.24E+00	3.39E+02	2.52E+00	1.80E+02
4	-41	2.02E+00	7.84E+00	3.38E+02	2.55E+00	1.80E+02
4	-40	2.06E+00	7.51E+00	3.37E+02	2.58E+00	1.80E+02
4	-39	2.11E+00	7.15E+00	3.36E+02	2.60E+00	1.80E+02
4	-38	2.17E+00	6.76E+00	3.35E+02	2.64E+00	1.80E+02
4	-37	2.22E+00	6.45E+00	3.34E+02	2.67E+00	1.80E+02
4	-36	2.28E+00	6.07E+00	3.33E+02	2.70E+00	1.80E+02
4	-35	2.35E+00	5.63E+00	3.31E+02	2.75E+00	1.80E+02
4	-34	2.42E+00	5.27E+00	3.29E+02	2.79E+00	1.80E+02
4	-33	2.48E+00	4.96E+00	3.28E+02	2.83E+00	1.80E+02
4	-32	2.56E+00	4.56E+00	3.26E+02	2.89E+00	1.80E+02
4	-31	2.63E+00	4.25E+00	3.24E+02	2.94E+00	1.80E+02
4	-30	2.70E+00	3.90E+00	3.22E+02	2.99E+00	1.80E+02
4	-29	2.81E+00	3.47E+00	3.19E+02	3.07E+00	1.80E+02
4	-28	2.89E+00	3.16E+00	3.17E+02	3.14E+00	1.80E+02
4	-27	2.97E+00	2.87E+00	3.14E+02	3.20E+00	1.80E+02
4	-26	3.09E+00	2.48E+00	3.10E+02	3.30E+00	1.80E+02
4	-25	3.19E+00	2.19E+00	3.06E+02	3.38E+00	1.80E+02
4	-24	3.31E+00	1.86E+00	3.01E+02	3.49E+00	1.80E+02
4	-23	3.47E+00	1.49E+00	2.92E+02	3.63E+00	1.80E+02
4	-22	3.59E+00	1.25E+00	2.83E+02	3.75E+00	1.80E+02
4	-21	3.72E+00	1.03E+00	2.71E+02	3.88E+00	1.80E+02
4	-20	3.93E+00	8.30E-01	2.47E+02	4.09E+00	1.80E+02
4	-19	4.11E+00	7.97E-01	2.21E+02	4.29E+00	1.80E+02
4	-18	4.29E+00	8.82E-01	2.00E+02	4.50E+00	1.80E+02
4	-17	4.56E+00	1.12E+00	1.79E+02	4.83E+00	1.80E+02
4	-16	4.83E+00	1.37E+00	1.66E+02	5.16E+00	1.80E+02
4	-15	5.03E+00	1.58E+00	1.60E+02	5.44E+00	1.80E+02
4	-14	5.42E+00	1.93E+00	1.51E+02	5.98E+00	1.80E+02
4	-13	5.88E+00	2.31E+00	1.44E+02	6.68E+00	1.80E+02
4	-12	6.16E+00	2.52E+00	1.40E+02	7.15E+00	1.80E+02
4	-11	6.67E+00	2.86E+00	1.35E+02	8.04E+00	1.80E+02
4	-10	7.43E+00	3.28E+00	1.28E+02	9.49E+00	1.80E+02
4	-9	8.08E+00	3.58E+00	1.24E+02	1.09E+01	1.80E+02
4	-8	8.69E+00	3.81E+00	1.21E+02	1.22E+01	1.80E+02
4	-7	9.37E+00	4.03E+00	1.17E+02	1.39E+01	1.80E+02
4	-6	1.02E+01	4.25E+00	1.14E+02	1.62E+01	1.80E+02
4	-5	1.16E+01	4.47E+00	1.10E+02	2.01E+01	1.80E+02
4	-4	1.24E+01	4.54E+00	1.09E+02	2.28E+01	1.80E+02
4	-3	1.29E+01	4.56E+00	1.08E+02	2.47E+01	1.80E+02
4	-2	1.53E+01	4.50E+00	1.08E+02	3.37E+01	1.80E+02
4	-1	1.60E+01	4.45E+00	1.09E+02	3.69E+01	1.80E+02
4	0	1.91E+01	4.31E+00	1.21E+02	5.16E+01	1.80E+02

4	1	1.96E+01	4.33E+00	1.23E+02	5.43E+01	1.80E+02
4	2	2.18E+01	4.60E+00	1.35E+02	6.63E+01	1.80E+02
4	3	2.27E+01	4.85E+00	1.41E+02	7.19E+01	1.80E+02
4	4	2.59E+01	6.22E+00	1.55E+02	9.30E+01	1.80E+02
4	5	2.91E+01	8.21E+00	1.63E+02	1.17E+02	1.80E+02
4	6	3.25E+01	1.06E+01	1.68E+02	1.45E+02	1.80E+02
4	7	3.59E+01	1.31E+01	1.70E+02	1.76E+02	1.80E+02
4	8	3.93E+01	1.55E+01	1.72E+02	2.12E+02	1.80E+02

M/M_sun = 2.00   T$_{eff}$ = 7521.7   Log (L/L_sun) = 1.4250
Log g = 3.7724   R/R_sun = 3.0419   age (y)   = 1.0101E+09
X   = 0.72   Z   = 0.014   alphaconv   = 1.70   overshoot = 0.20

l	n	freq(c/d)	f_T	psi_T	f_g	psi_g
0	1	8.16E+00	4.48E+00	1.16E+02	1.46E+01	1.80E+02
0	2	1.05E+01	4.87E+00	1.09E+02	2.30E+01	1.80E+02
0	3	1.31E+01	4.83E+00	1.09E+02	3.47E+01	1.80E+02
0	4	1.58E+01	4.61E+00	1.18E+02	4.92E+01	1.80E+02
0	5	1.84E+01	4.81E+00	1.35E+02	6.62E+01	1.80E+02
0	6	2.10E+01	5.77E+00	1.52E+02	8.52E+01	1.80E+02
0	7	2.36E+01	7.47E+00	1.63E+02	1.07E+02	1.80E+02
0	8	2.62E+01	9.70E+00	1.70E+02	1.32E+02	1.80E+02
0	9	2.90E+01	1.22E+01	1.74E+02	1.61E+02	1.80E+02
0	10	3.18E+01	1.48E+01	1.76E+02	1.93E+02	1.80E+02
1	-5	4.69E+00	3.08E+00	1.35E+02	6.16E+00	1.80E+02
1	-4	5.46E+00	3.45E+00	1.29E+02	7.64E+00	1.80E+02
1	-3	7.35E+00	4.22E+00	1.19E+02	1.22E+01	1.80E+02
1	-2	8.36E+00	4.52E+00	1.15E+02	1.52E+01	1.80E+02
1	-1	9.33E+00	4.73E+00	1.12E+02	1.85E+01	1.80E+02
1	1	1.09E+01	4.89E+00	1.09E+02	2.44E+01	1.80E+02
1	2	1.35E+01	4.80E+00	1.10E+02	3.65E+01	1.80E+02
1	3	1.61E+01	4.61E+00	1.20E+02	5.10E+01	1.80E+02
1	4	1.80E+01	4.73E+00	1.32E+02	6.31E+01	1.80E+02
1	5	1.95E+01	5.12E+00	1.42E+02	7.39E+01	1.80E+02
1	6	2.19E+01	6.32E+00	1.56E+02	9.28E+01	1.80E+02
1	7	2.45E+01	8.26E+00	1.66E+02	1.16E+02	1.80E+02
1	8	2.73E+01	1.07E+01	1.72E+02	1.43E+02	1.80E+02
1	9	3.01E+01	1.32E+01	1.75E+02	1.73E+02	1.80E+02
1	10	3.30E+01	1.58E+01	1.77E+02	2.08E+02	1.80E+02
2	-9	4.62E+00	2.80E+00	1.38E+02	6.03E+00	1.80E+02
2	-8	5.30E+00	3.20E+00	1.33E+02	7.31E+00	1.80E+02
2	-7	5.74E+00	3.44E+00	1.29E+02	8.22E+00	1.80E+02
2	-6	6.63E+00	3.87E+00	1.24E+02	1.03E+01	1.80E+02
2	-5	7.66E+00	4.27E+00	1.19E+02	1.31E+01	1.80E+02
2	-4	8.27E+00	4.46E+00	1.16E+02	1.49E+01	1.80E+02
2	-3	9.14E+00	4.67E+00	1.13E+02	1.78E+01	1.80E+02
2	-2	1.05E+01	4.86E+00	1.10E+02	2.27E+01	1.80E+02
2	-1	1.21E+01	4.89E+00	1.09E+02	2.96E+01	1.80E+02
2	0	1.36E+01	4.80E+00	1.11E+02	3.70E+01	1.80E+02
2	1	1.50E+01	4.68E+00	1.15E+02	4.46E+01	1.80E+02
2	2	1.62E+01	4.61E+00	1.21E+02	5.18E+01	1.80E+02
2	3	1.81E+01	4.75E+00	1.33E+02	6.39E+01	1.80E+02
2	4	2.05E+01	5.56E+00	1.49E+02	8.16E+01	1.80E+02
2	5	2.31E+01	7.15E+00	1.61E+02	1.03E+02	1.80E+02

2	6	2.58E+01	9.34E+00	1.69E+02	1.28E+02	1.80E+02
2	7	2.86E+01	1.19E+01	1.73E+02	1.57E+02	1.80E+02
2	8	3.14E+01	1.44E+01	1.76E+02	1.89E+02	1.80E+02
2	9	3.36E+01	1.64E+01	1.78E+02	2.15E+02	1.80E+02
3	-12	4.86E+00	2.63E+00	1.40E+02	6.46E+00	1.80E+02
3	-11	5.40E+00	3.03E+00	1.35E+02	7.51E+00	1.80E+02
3	-10	5.84E+00	3.31E+00	1.31E+02	8.45E+00	1.80E+02
3	-9	6.35E+00	3.60E+00	1.28E+02	9.62E+00	1.80E+02
3	-8	7.21E+00	4.02E+00	1.22E+02	1.18E+01	1.80E+02
3	-7	7.76E+00	4.24E+00	1.20E+02	1.34E+01	1.80E+02
3	-6	8.18E+00	4.38E+00	1.18E+02	1.47E+01	1.80E+02
3	-5	9.26E+00	4.67E+00	1.14E+02	1.82E+01	1.80E+02
3	-4	1.03E+01	4.82E+00	1.11E+02	2.19E+01	1.80E+02
3	-3	1.11E+01	4.89E+00	1.10E+02	2.54E+01	1.80E+02
3	-2	1.23E+01	4.89E+00	1.09E+02	3.07E+01	1.80E+02
3	-1	1.32E+01	4.83E+00	1.10E+02	3.51E+01	1.80E+02
3	0	1.56E+01	4.65E+00	1.18E+02	4.81E+01	1.80E+02
3	1	1.66E+01	4.63E+00	1.23E+02	5.44E+01	1.80E+02
3	2	1.87E+01	4.88E+00	1.37E+02	6.78E+01	1.80E+02
3	3	2.01E+01	5.37E+00	1.46E+02	7.84E+01	1.80E+02
3	4	2.13E+01	5.98E+00	1.53E+02	8.79E+01	1.80E+02
3	5	2.40E+01	7.82E+00	1.64E+02	1.11E+02	1.80E+02
3	6	2.68E+01	1.02E+01	1.71E+02	1.37E+02	1.80E+02
3	7	2.96E+01	1.28E+01	1.74E+02	1.68E+02	1.80E+02
3	8	3.25E+01	1.54E+01	1.77E+02	2.02E+02	1.80E+02
4	-16	4.83E+00	2.21E+00	1.48E+02	6.42E+00	1.80E+02
4	-15	5.05E+00	2.42E+00	1.45E+02	6.82E+00	1.80E+02
4	-14	5.41E+00	2.74E+00	1.40E+02	7.54E+00	1.80E+02
4	-13	5.86E+00	3.08E+00	1.35E+02	8.48E+00	1.80E+02
4	-12	6.15E+00	3.28E+00	1.32E+02	9.14E+00	1.80E+02
4	-11	6.77E+00	3.67E+00	1.27E+02	1.07E+01	1.80E+02
4	-10	7.39E+00	3.99E+00	1.23E+02	1.23E+01	1.80E+02
4	-9	7.77E+00	4.15E+00	1.21E+02	1.34E+01	1.80E+02
4	-8	8.17E+00	4.31E+00	1.19E+02	1.46E+01	1.80E+02
4	-7	9.18E+00	4.61E+00	1.15E+02	1.79E+01	1.80E+02
4	-6	1.00E+01	4.78E+00	1.12E+02	2.11E+01	1.80E+02
4	-5	1.05E+01	4.84E+00	1.11E+02	2.30E+01	1.80E+02
4	-4	1.14E+01	4.89E+00	1.10E+02	2.64E+01	1.80E+02
4	-3	1.33E+01	4.84E+00	1.11E+02	3.53E+01	1.80E+02
4	-2	1.37E+01	4.81E+00	1.11E+02	3.74E+01	1.80E+02
4	-1	1.49E+01	4.70E+00	1.15E+02	4.41E+01	1.80E+02
4	0	1.64E+01	4.64E+00	1.22E+02	5.26E+01	1.80E+02
4	1	1.82E+01	4.79E+00	1.34E+02	6.47E+01	1.80E+02
4	2	1.92E+01	5.04E+00	1.40E+02	7.17E+01	1.80E+02
4	3	2.19E+01	6.34E+00	1.56E+02	9.27E+01	1.80E+02
4	4	2.40E+01	7.92E+00	1.65E+02	1.11E+02	1.80E+02

4	5	2.47E+01	8.37E+00	1.66E+02	1.17E+02	1.80E+02
4	6	2.75E+01	1.09E+01	1.72E+02	1.45E+02	1.80E+02
4	7	3.04E+01	1.35E+01	1.75E+02	1.77E+02	1.80E+02
4	8	3.34E+01	1.61E+01	1.78E+02	2.13E+02	1.80E+02

Appendix B

O – C of SZ Lyn. The all available T_{max} (HJD) in literature and observation are included.

Source	T_{max}(Observed)	Cycles	E	T_{max} (Calculated)	O-C
	2451907.465400	114349.161168	114349	2451907.445974	0.019426
	2451966.524400	114839.135401	114839	2451966.508079	0.016321
	2451967.368300	114846.136692	114846	2451967.351824	0.016476
	2452003.407200	115145.128079	115145	2452003.391762	0.015438
	2452032.335100	115385.124111	115385	2452032.320140	0.014960
	2452053.429400	115560.129841	115560	2452053.413750	0.015650
	2452202.646700	116798.089035	116798	2452202.635968	0.010732
	2452209.519200	116855.105712	116855	2452209.506458	0.012742
	2452263.638900	117304.101774	117304	2452263.626633	0.012267
	2452308.356400	117675.093879	117675	2452308.345084	0.011316
	2452321.735780	117786.093921	117786	2452321.724459	0.011321
	2452343.795630	117969.110194	117969	2452343.782348	0.013282
	2452374.412700	118223.120173	118223	2452374.398215	0.014485
	2452410.332700	118521.125125	118521	2452410.317618	0.015082
	2452628.505800	120331.165884	120331	2452628.485805	0.019995
	2452658.639390	120581.164743	120581	2452658.619533	0.019857
	2452721.322000	121101.201718	121101	2452721.297686	0.024314
	2452774.359500	121541.219469	121541	2452774.333046	0.026454
	2452775.323700	121549.218811	121549	2452775.297326	0.026374
	2452776.288200	121557.220643	121557	2452776.261605	0.026595
	2452785.687100	121635.197222	121635	2452785.663328	0.023772
	2452983.484400	123276.193179	123276	2452983.461115	0.023285
	2453011.566000	123509.168008	123509	2453011.545749	0.020251
	2453028.445900	123649.209594	123649	2453028.420637	0.025263
	2453051.582500	123841.158964	123841	2453051.563339	0.019161
	2453052.428500	123848.177677	123848	2453052.407084	0.021416
AAVSO	2453064.720089	123950.153019	123950	2453064.701645	0.018444
	2453064.722520	123950.173190	123950	2453064.701645	0.020875
	2453070.386000	123997.159412	123997	2453070.366785	0.019215
	2453079.669300	124074.176933	124074	2453079.647973	0.021327
	2453090.399200	124163.195957	124163	2453090.375580	0.023620
	2453094.378000	124196.205481	124196	2453094.353232	0.024768
	2453096.422900	124213.170691	124213	2453096.402326	0.020574
	2453099.436100	124238.169257	124238	2453099.415699	0.020401
	2453119.325800	124403.181203	124403	2453119.303959	0.021841
	2453125.352000	124453.176677	124453	2453125.330704	0.021296
	2453129.330300	124486.182053	124486	2453129.308356	0.021944
	2453132.342600	124511.173153	124511	2453132.321729	0.020871
	2453145.360100	124619.170911	124619	2453145.339499	0.020601
	2453338.813180	126224.125691	126224	2453338.798030	0.015150
	2453395.585280	126695.126997	126695	2453395.569972	0.015308

	2453397.273400	126709.132234	126709	2453397.257461	0.015939
	2453397.393300	126710.126967	126710	2453397.377996	0.015304
	2453409.568900	126811.140026	126811	2453409.552022	0.016878
	2453409.687400	126812.123143	126812	2453409.672557	0.014843
	2453416.557750	126869.121983	126869	2453416.543047	0.014703
	2453644.734800	128762.159029	128762	2453644.715631	0.019169
	2453644.854400	128763.151273	128763	2453644.836166	0.018234
	2453721.757100	129401.163115	129401	2453721.737439	0.019661
AAVSO	2453728.743728	129459.126635	129459	2453728.728464	0.015264
AAVSO	2453728.864365	129460.127486	129460	2453728.848999	0.015367
AAVSO	2453731.033101	129478.120081	129478	2453731.018627	0.014474
AAVSO	2453742.365195	129572.135120	129572	2453742.348909	0.016287
	2453745.623900	129599.170481	129599	2453745.603351	0.020549
AAVSO	2453745.739792	129600.131959	129600	2453745.723886	0.015906
	2453758.761870	129708.167700	129708	2453758.741656	0.020214
	2453758.885410	129709.192631	129709	2453758.862191	0.023219
	2453759.606040	129715.171231	129715	2453759.585401	0.020639
	2453759.726920	129716.174094	129716	2453759.705936	0.020984
	2453759.847130	129717.171399	129717	2453759.826470	0.020660
	2453759.967920	129718.173515	129718	2453759.947005	0.020915
	2453761.535200	129731.176221	129731	2453761.513959	0.021241
	2453766.237200	129770.185667	129770	2453766.214821	0.022379
	2453773.589100	129831.179614	129831	2453773.567450	0.021650
	2453798.419550	130037.181759	130037	2453798.397642	0.021908
	2453801.673300	130064.176013	130064	2453801.652084	0.021216
	2453808.305200	130119.196588	130119	2453808.281504	0.023696
AAVSO	2453829.639279	130296.191608	130296	2453829.616183	0.023095
	2453840.607700	130387.189487	130387	2453840.584860	0.022840
	2453853.626200	130495.195541	130495	2453853.602630	0.023570
	2453871.588100	130644.213780	130644	2453871.562332	0.025768
	2453890.631800	130802.207012	130802	2453890.606848	0.024952
	2453981.879900	131559.233337	131559	2453981.851775	0.028125
	2454009.844300	131791.235834	131791	2454009.815874	0.028426
	2454015.870300	131841.229649	131841	2454015.842619	0.027681
	2454058.781100	132197.232735	132197	2454058.753047	0.028053
	2454067.580000	132270.231504	132270	2454067.552096	0.027904
	2454067.701500	132271.239511	132271	2454067.672631	0.028869
AAVSO	2454074.809009	132330.205902	132330	2454074.784190	0.024818
AAVSO	2454074.929256	132331.203512	132331	2454074.904725	0.024530
	2454085.299900	132417.242026	132417	2454085.270727	0.029173
	2454085.420500	132418.242566	132418	2454085.391262	0.029238
AAVSO	2454087.704991	132437.195508	132437	2454087.681426	0.023566
AAVSO	2454110.728620	132628.207628	132628	2454110.703593	0.025026
AAVSO	2454110.850025	132629.214851	132629	2454110.824128	0.025897
AAVSO	2454110.971783	132630.224993	132630	2454110.944663	0.027119
AAVSO	2454117.720052	132686.211006	132686	2454117.694618	0.025434

AAVSO	2454117.955602	132688.165211	132688	2454117.935688	0.019914
AAVSO	2454117.960523	132688.206035	132688	2454117.935688	0.024834
AAVSO	2454120.730628	132711.187801	132711	2454120.707991	0.022637
AAVSO	2454120.853706	132712.208902	132712	2454120.828526	0.025180
AAVSO	2454131.578200	132801.183076	132801	2454131.556133	0.022067
AAVSO	2454131.818700	132803.178349	132803	2454131.797203	0.021497
AAVSO	2454131.940900	132804.192163	132804	2454131.917738	0.023162
AAVSO	2454133.750965	132819.209101	132819	2454133.725761	0.025204
AAVSO	2454133.873237	132820.223511	132820	2454133.846296	0.026941
AAVSO	2454134.593706	132826.200774	132826	2454134.569506	0.024200
AAVSO	2454134.716723	132827.221366	132827	2454134.690041	0.026682
AAVSO	2454134.837328	132828.221946	132828	2454134.810575	0.026752
AAVSO	2454135.677983	132835.196318	132835	2454135.654320	0.023663
AAVSO	2454135.921976	132837.220573	132837	2454135.895390	0.026587
AAVSO	2454136.884449	132845.205580	132845	2454136.859669	0.024780
AAVSO	2454137.604800	132851.181869	132851	2454137.582878	0.021922
AAVSO	2454137.728204	132852.205676	132852	2454137.703413	0.024791
AAVSO	2454137.847700	132853.197053	132853	2454137.823948	0.023752
AAVSO	2454146.766282	132927.188749	132927	2454146.743532	0.022751
AAVSO	2454146.887989	132928.198468	132928	2454146.864066	0.023922
AAVSO	2454147.612371	132934.208201	132934	2454147.587276	0.025095
AAVSO	2454147.730309	132935.186650	132935	2454147.707811	0.022498
AAVSO	2454152.794480	132977.200797	132977	2454152.770277	0.024203
AAVSO	2454154.602716	132992.202557	132992	2454154.578301	0.024415
AAVSO	2454154.846079	132994.221585	132994	2454154.819371	0.026709
	2454185.340100	133247.210704	133247	2454185.314703	0.025397
	2454186.426700	133256.225520	133256	2454186.399517	0.027183
	2454191.368800	133297.226920	133297	2454191.341448	0.027352
	2454191.488900	133298.223311	133298	2454191.461983	0.026917
	2454197.395000	133347.222394	133347	2454197.368194	0.026806
AAVSO	2454200.648671	133374.215989	133374	2454200.622636	0.026034
	2454202.336100	133388.215497	133388	2454202.310125	0.025975
	2454203.420800	133397.214550	133397	2454203.394939	0.025861
	2454208.602700	133440.205414	133440	2454208.577940	0.024760
AAVSO	2454218.608929	133523.220609	133523	2454218.582338	0.026591
	2454222.585700	133556.213300	133556	2454222.559990	0.025710
	2454223.427800	133563.199657	133563	2454223.403734	0.024066
	2454261.636500	133880.192469	133880	2454261.613301	0.023199
	2454366.860500	134753.167775	134753	2454366.840277	0.020223
	2454394.825700	134985.176908	134985	2454394.804376	0.021324
	2454414.833400	135151.167823	135151	2454414.813171	0.020229
WASP	2454418.694403	135183.200062	135183	2454418.670289	0.024114
WASP	2454419.657007	135191.186165	135191	2454419.634568	0.022439
WASP	2454420.623903	135199.207874	135199	2454420.598847	0.025056
WASP	2454420.747115	135200.230079	135200	2454420.719382	0.027733
WASP	2454427.613780	135257.198352	135257	2454427.589872	0.023908

WASP	2454427.735768	135258.210407	135258	2454427.710407	0.025361
WASP	2454436.650861	135332.173151	135332	2454436.629990	0.020871
WASP	2454436.770997	135333.169845	135333	2454436.750525	0.020472
WASP	2454438.580814	135348.184723	135348	2454438.558549	0.022266
WASP	2454438.701256	135349.183950	135349	2454438.679084	0.022172
	2454479.559100	135688.154992	135688	2454479.540418	0.018682
	2454484.620000	135730.141998	135730	2454484.602884	0.017116
WASP	2454491.495486	135787.183451	135787	2454491.473374	0.022112
WASP	2454501.377809	135869.170678	135869	2454501.357237	0.020573
WASP	2454501.501434	135870.196314	135870	2454501.477772	0.023663
WASP	2454501.623241	135871.206867	135871	2454501.598307	0.024935
WASP	2454502.462810	135878.172228	135878	2454502.442051	0.020759
WASP	2454502.581990	135879.160979	135879	2454502.562586	0.019404
WASP	2454504.388706	135894.150131	135894	2454504.370610	0.018096
	2454506.680000	135913.159515	135913	2454506.660773	0.019227
	2454511.501600	135953.161205	135953	2454511.482169	0.019431
AAVSO	2454511.620291	135954.145908	135954	2454511.602704	0.017587
	2454511.622400	135954.163404	135954	2454511.602704	0.019696
AAVSO	2454511.739429	135955.134319	135955	2454511.723239	0.016190
	2454511.742000	135955.155647	135955	2454511.723239	0.018761
	2454512.465800	135961.160547	135961	2454512.446449	0.019351
	2454513.669000	135971.142717	135971	2454513.651798	0.017202
	2454520.781500	136030.150518	136030	2454520.763357	0.018143
WASP	2454524.398228	136060.156170	136060	2454524.379405	0.018824
WASP	2454524.519266	136061.160343	136061	2454524.499940	0.019327
WASP	2454526.448261	136077.163960	136077	2454526.428498	0.019763
AAVSO	2454529.819719	136105.134764	136105	2454529.803476	0.016244
WASP	2454530.428461	136110.185097	136110	2454530.406150	0.022311
WASP	2454530.549869	136111.192345	136111	2454530.526685	0.023184
WASP	2454532.353593	136126.156671	136126	2454532.334709	0.018884
WASP	2454532.475042	136127.164251	136127	2454532.455244	0.019798
WASP	2454534.403471	136143.163182	136143	2454534.383802	0.019669
WASP	2454535.367813	136151.163704	136151	2454535.348081	0.019732
WASP	2454536.454206	136160.176801	136160	2454536.432896	0.021311
WASP	2454539.346635	136184.173410	136184	2454539.325733	0.020902
WASP	2454539.466847	136185.170732	136185	2454539.446268	0.020579
WASP	2454544.408063	136226.164792	136226	2454544.388200	0.019863
WASP	2454544.526998	136227.151518	136227	2454544.508735	0.018263
WASP	2454547.420596	136251.157830	136251	2454547.401572	0.019024
AAVSO	2454744.858400	137889.171278	137889	2454744.837755	0.020645
AAVSO	2454749.799200	137930.161893	137930	2454749.779686	0.019514
AAVSO	2454749.920200	137931.165751	137931	2454749.900221	0.019979
AAVSO	2454876.840200	138984.138703	138984	2454876.823481	0.016719
AAVSO	2454902.756100	139199.146123	139199	2454902.738487	0.017613
	2455114.910900	140959.256949	140959	2455114.879929	0.030971
	2455163.848400	141365.259658	141365	2455163.817102	0.031298

	2455167.704500	141397.251220	141397	2455167.674219	0.030281
	2455167.827100	141398.268352	141398	2455167.794754	0.032346
	2455167.945400	141399.249811	141399	2455167.915289	0.030111
	2455189.523400	141578.268487	141578	2455189.491038	0.032362
	2455191.451900	141594.268001	141594	2455191.419597	0.032303
	2455191.572200	141595.266052	141595	2455191.540131	0.032069
	2455191.693100	141596.269081	141596	2455191.660666	0.032434
	2455206.759000	141721.261085	141721	2455206.727530	0.031470
AAVSO	2455209.646400	141745.215971	141745	2455209.620368	0.026032
	2455209.651900	141745.261601	141745	2455209.620368	0.031532
	2455210.738000	141754.272269	141754	2455210.705182	0.032818
	2455212.665100	141770.260168	141770	2455212.633741	0.031359
	2455259.552400	142159.253697	142159	2455259.521821	0.030579
	2455259.552400	142159.253697	142159	2455259.521821	0.030579
	2455301.618200	142508.246366	142508	2455301.588504	0.029696
AAVSO	2455301.618200	142508.246366	142508	2455301.588504	0.029696
	2455301.618200	142508.246366	142508	2455301.588504	0.029696
AAVSO	2455301.738800	142509.246906	142509	2455301.709039	0.029761
	2455301.740100	142509.257691	142509	2455301.709039	0.031061
	2455301.740100	142509.257691	142509	2455301.709039	0.031061
	2455303.426900	142523.251977	142523	2455303.396528	0.030372
	2455303.426900	142523.251977	142523	2455303.396528	0.030372
	2455304.513700	142532.268452	142532	2455304.481342	0.032358
	2455304.513700	142532.268452	142532	2455304.481342	0.032358
	2455310.419500	142581.265046	142581	2455310.387553	0.031947
	2455310.419500	142581.265046	142581	2455310.387553	0.031947
AAVSO	2455310.421000	142581.277490	142581	2455310.387553	0.033447
	2455310.539800	142582.263097	142582	2455310.508088	0.031712
	2455310.539800	142582.263097	142582	2455310.508088	0.031712
AAVSO	2455310.540700	142582.270564	142582	2455310.508088	0.032612
	2455478.801200	143978.218841	143978	2455478.774822	0.026378
AAVSO	2455478.803600	143978.238753	143978	2455478.774822	0.028778
	2455507.489000	144216.222918	144216	2455507.462131	0.026869
	2455507.489000	144216.222918	144216	2455507.462131	0.026869
	2455507.609500	144217.222629	144217	2455507.582665	0.026835
	2455507.609500	144217.222629	144217	2455507.582665	0.026835
AAVSO	2455512.909600	144261.194122	144261	2455512.886202	0.023398
AAVSO	2455525.803900	144368.169769	144368	2455525.783437	0.020463
	2455525.808800	144368.210421	144368	2455525.783437	0.025363
	2455525.808800	144368.210421	144368	2455525.783437	0.025363
	2455570.647000	144740.203896	144740	2455570.622423	0.024577
	2455570.647100	144740.204726	144740	2455570.622423	0.024677
AAVSO	2455583.537800	144847.150506	144847	2455583.519659	0.018141
	2455583.544900	144847.209410	144847	2455583.519659	0.025241
	2455583.544900	144847.209410	144847	2455583.519659	0.025241
AAVSO	2455583.659500	144848.160172	144848	2455583.640194	0.019306

	2455583.665200	144848.207461	144848	2455583.640194	0.025006
	2455587.642500	144881.204541	144881	2455587.617846	0.024654
	2455587.642500	144881.204541	144881	2455587.617846	0.024654
	2455587.763300	144882.206740	144882	2455587.738381	0.024919
	2455587.883900	144883.207280	144883	2455587.858916	0.024984
	2455588.607400	144889.209690	144889	2455588.582125	0.025275
	2455588.607400	144889.209690	144889	2455588.582125	0.025275
	2455588.727300	144890.204423	144890	2455588.702660	0.024640
	2455588.848300	144891.208281	144891	2455588.823195	0.025105
	2455588.968800	144892.207992	144892	2455588.943730	0.025070
	2455591.381000	144912.220451	144912	2455591.354428	0.026572
	2455591.381000	144912.220451	144912	2455591.354428	0.026572
	2455591.500000	144913.207717	144913	2455591.474963	0.025037
	2455591.621000	144914.211576	144914	2455591.595498	0.025502
AAVSO	2455601.621900	144997.182559	144997	2455601.599895	0.022005
	2455601.623900	144997.199152	144997	2455601.599895	0.024005
	2455601.623900	144997.199152	144997	2455601.599895	0.024005
AAVSO	2455626.570800	145204.167407	145204	2455626.550622	0.020178
AAVSO	2455626.688800	145205.146376	145205	2455626.671157	0.017643
AAVSO	2455626.811600	145206.165168	145206	2455626.791691	0.019909
	2455629.347500	145227.203886	145227	2455629.322925	0.024575
	2455629.347500	145227.203886	145227	2455629.322925	0.024575
AAVSO	2455630.670100	145238.176641	145238	2455630.648809	0.021291
AAVSO	2455630.789000	145239.163077	145239	2455630.769343	0.019657
AAVSO	2455631.633800	145246.171835	145246	2455631.613088	0.020712
AAVSO	2455631.760600	145247.223813	145247	2455631.733623	0.026977
AAVSO	2455639.589500	145312.175120	145312	2455639.568392	0.021108
AAVSO	2455639.710800	145313.181468	145313	2455639.688927	0.021873
	2455639.711500	145313.187275	145313	2455639.688927	0.022573
	2455639.711500	145313.187275	145313	2455639.688927	0.022573
AAVSO	2455644.657400	145354.220201	145354	2455644.630858	0.026542
	2455654.657800	145437.187036	145437	2455654.635256	0.022544
AAVSO	2455663.576400	145511.178878	145511	2455663.554839	0.021561
AAVSO	2455663.701200	145512.214262	145512	2455663.675374	0.025826
	2455838.835500	146965.190002	146965	2455838.812598	0.022902
AAVSO	2455838.836500	146965.198298	146965	2455838.812598	0.023902
AAVSO	2455859.811000	147139.210126	147139	2455859.785672	0.025328
AAVSO	2455859.930700	147140.203199	147140	2455859.906207	0.024493
AAVSO	2455875.839500	147272.188198	147272	2455875.816816	0.022684
	2455875.839700	147272.189858	147272	2455875.816816	0.022884
AAVSO	2455879.815200	147305.172004	147305	2455879.794468	0.020732
AAVSO	2455879.937700	147306.188307	147306	2455879.915002	0.022698
AAVSO	2455888.855300	147380.171852	147380	2455888.834586	0.020714
AAVSO	2455890.905400	147397.180203	147397	2455890.883679	0.021721
	2455890.906900	147397.192647	147397	2455890.883679	0.023221
AAVSO	2455921.759800	147653.159155	147653	2455921.740616	0.019184

	2455921.763700	147653.191511	147653	2455921.740616	0.023084
AAVSO	2455921.880800	147654.163014	147654	2455921.861151	0.019649
AAVSO	2455932.608200	147743.161297	147743	2455932.588758	0.019442
	2455932.611900	147743.191993	147743	2455932.588758	0.023142
AAVSO	2455932.728000	147744.155200	147744	2455932.709293	0.018707
AAVSO	2455935.620900	147768.155715	147768	2455935.602131	0.018769
	2455935.626900	147768.205493	147768	2455935.602131	0.024769
AAVSO	2455936.585900	147776.161695	147776	2455936.566410	0.019490
AAVSO	2455958.522000	147958.151294	147958	2455958.503764	0.018236
	2455958.527000	147958.192776	147958	2455958.503764	0.023236
AAVSO	2455958.642100	147959.147686	147959	2455958.624299	0.017801
AAVSO	2455961.539500	147983.185535	147983	2455961.517137	0.022363
AAVSO	2455962.502100	147991.171603	147991	2455962.481416	0.020684
AAVSO	2455969.490000	148049.145679	148049	2455969.472441	0.017559
AAVSO	2455969.612800	148050.164471	148050	2455969.592976	0.019824
	2455969.616500	148050.195168	148050	2455969.592976	0.023524
	2455995.653300	148266.205616	148266	2455995.628516	0.024784
AAVSO	2456012.648100	148407.200453	148407	2456012.623938	0.024162
AAVSO	2456024.702600	148507.208824	148507	2456024.677429	0.025171
AAVSO	2456026.632200	148523.217465	148523	2456026.605988	0.026212
AAVSO	2456036.635300	148606.206700	148606	2456036.610385	0.024915
AAVSO	2456340.631500	151128.266077	151128	2456340.599428	0.032072
AAVSO	2456381.617300	151468.298686	151468	2456381.581298	0.036002
AAVSO	2456574.954200	153072.289596	153072	2456574.919294	0.034906
AAVSO	2456604.841600	153320.245977	153320	2456604.811951	0.029649
AAVSO	2456604.963200	153321.254813	153321	2456604.932486	0.030714
AAVSO	2456615.810900	153411.251147	153411	2456615.780628	0.030272
Abu	2456639.314210	153606.242872	153606	2456639.284935	0.029275
Abu	2456664.266980	153813.259827	153813	2456664.235662	0.031318
Abu	2456664.388930	153814.271567	153814	2456664.356197	0.032733
Abu	2456684.277140	153979.271151	153979	2456684.244457	0.032683
Abu	2456686.208060	153995.290742	153995	2456686.173015	0.035045
Abu	2456686.324750	153996.258843	153996	2456686.293550	0.031200
Abu	2456693.313830	154054.242709	154054	2456693.284575	0.029255
Abu	2456693.427670	154055.187165	154055	2456693.405110	0.022560
AAVSO	2456705.482500	154155.198274	154155	2456705.458601	0.023899
AAVSO	2456722.359300	154295.214142	154295	2456722.333488	0.025812
AAVSO	2456728.385400	154345.208786	154345	2456728.360234	0.025166
AAVSO	2456728.506000	154346.209326	154346	2456728.480769	0.025231
AAVSO	2456728.626500	154347.209037	154347	2456728.601304	0.025196
AAVSO	2456745.381000	154486.210261	154486	2456745.355656	0.025344
AAVSO	2456757.435900	154586.221950	154586	2456757.409147	0.026753
AAVSO	2456763.343700	154635.235136	154635	2456763.315358	0.028342
AAVSO	2456763.465200	154636.243143	154636	2456763.435893	0.029307
AAVSO	2456952.823100	156207.222870	156207	2456952.796236	0.026864
AAVSO	2456952.942500	156208.213455	156208	2456952.916771	0.025729

AAVSO	2456966.925300	156324.219680	156324	2456966.898821	0.026479
AAVSO	2457022.728400	156787.181821	156787	2457022.706484	0.021916
AAVSO	2457022.851300	156788.201443	156788	2457022.827019	0.024281
AAVSO	2457084.442000	157299.179549	157299	2457084.420358	0.021642
AAVSO	2457093.604800	157375.197360	157375	2457093.581011	0.023789
AAVSO	2457314.918000	159211.289493	159211	2457314.883106	0.034894
AAVSO	2457327.810600	159318.251036	159318	2457327.780341	0.030259
AAVSO	2457327.935000	159319.283102	159319	2457327.900876	0.034124
AAVSO	2457355.655600	159549.262948	159549	2457355.623906	0.031694
AAVSO	2457355.775700	159550.259340	159550	2457355.744441	0.031259
AAVSO	2457355.895700	159551.254902	159551	2457355.864975	0.030725
AAVSO	2457411.824800	160015.262383	160015	2457411.793174	0.031626
AAVSO	2457424.597400	160121.228364	160121	2457424.569874	0.027526
AAVSO	2457435.570500	160212.265061	160212	2457435.538551	0.031949
AAVSO	2457436.537500	160220.287633	160220	2457436.502830	0.034670
AAVSO	2457436.656300	160221.273239	160221	2457436.623365	0.032935
AAVSO	2457436.777800	160222.281246	160222	2457436.743900	0.033900
AAVSO	2457436.898400	160223.281786	160223	2457436.864435	0.033965
AAVSO	2457437.500200	160228.274531	160228	2457437.467109	0.033091
AAVSO	2457437.619100	160229.260967	160229	2457437.587644	0.031456
AAVSO	2457438.581000	160237.241227	160237	2457438.551924	0.029076
AAVSO	2457439.548100	160245.264629	160245	2457439.516203	0.031897
Handler	2457480.657556	160586.323135	160586	2457480.618607	0.038949
Handler	2457480.778713	160587.328290	160587	2457480.739142	0.039570
Handler	2457482.707622	160603.331199	160603	2457482.667701	0.039921
Handler	2457491.746205	160678.318460	160678	2457491.707819	0.038386
Handler	2457492.711029	160686.322984	160686	2457492.672098	0.038931
AAVSO	2457494.638600	160702.314790	160702	2457494.600657	0.037943
Handler	2457494.639019	160702.318264	160702	2457494.600657	0.038362
Handler	2457495.724968	160711.327684	160711	2457495.685471	0.039497
Handler	2457496.688438	160719.320970	160719	2457496.649750	0.038688
Handler	2457497.652530	160727.319413	160727	2457497.614030	0.038500
Handler	2457499.701318	160744.316878	160744	2457499.663123	0.038195
Handler	2457503.678944	160777.316660	160777	2457503.640775	0.038169
AAVSO	2457681.950400	162256.319352	162256	2457681.911907	0.038493
AAVSO	2457686.771000	162296.312745	162296	2457686.733303	0.037697
AAVSO	2457686.890500	162297.304159	162297	2457686.853838	0.036662
AAVSO	2457696.895100	162380.305838	162380	2457696.858236	0.036864
AAVSO	2457701.716200	162420.303379	162420	2457701.679632	0.036568
AAVSO	2457701.836400	162421.300601	162421	2457701.800167	0.036233
AAVSO	2457701.956600	162422.297822	162422	2457701.920702	0.035898
AAVSO	2457736.667100	162710.268336	162710	2457736.634756	0.032344
AAVSO	2457736.788000	162711.271365	162711	2457736.755291	0.032709
AAVSO	2457761.855100	162919.236842	162919	2457761.826552	0.028548
AAVSO	2457768.848700	162977.258207	162977	2457768.817577	0.031123
AAVSO	2457768.971000	162978.272851	162978	2457768.938112	0.032888

AAVSO	2457803.683600	163266.260787	163266	2457803.652166	0.031434
AAVSO	2457803.803600	163267.256349	163267	2457803.772701	0.030899
AAVSO	2457828.755300	163474.264427	163474	2457828.723427	0.031873
AAVSO	2457844.667200	163606.275145	163606	2457844.634035	0.033165
AAVSO	2458021.611300	165074.265621	165074	2458021.579283	0.032017
AAVSO	2458035.836300	165192.281224	165192	2458035.802403	0.033897
AAVSO	2458035.955200	165193.267660	165193	2458035.922938	0.032262
AAVSO	2458041.498700	165239.258485	165239	2458041.467543	0.031157
AAVSO	2458079.705000	165556.231386	165556	2458079.677110	0.027890
AAVSO	2458079.825200	165557.228607	165557	2458079.797645	0.027555
AAVSO	2458079.944700	165558.220021	165558	2458079.918180	0.026520
AAVSO	2458090.671700	165647.214985	165647	2458090.645787	0.025913
AAVSO	2458090.790800	165648.203081	165648	2458090.766322	0.024478
AAVSO	2458090.913000	165649.216895	165649	2458090.886857	0.026143

Appendix C

```
[root@Adassuriya SZLyn]# vartools -i All_V -oneline -ascii \-LS
0.01 0.2 1 50 1
/usr/local/vartools/VARTOOLS1.3/EXAMPLES/OUTDIRSZLyn whiten clip
5. 1
Name                = All_V
LS_Period_1_0       =      0.12052725
Log10_LS_Prob_1_0   = -779.78713
LS_SNR_1_0          =     96.27185
LS_Period_2_0       =      0.06026703
Log10_LS_Prob_2_0   = -460.08563
LS_SNR_2_0          =     68.94339
LS_Period_3_0       =      0.04018029
Log10_LS_Prob_3_0   = -113.81514
LS_SNR_3_0          =     30.72882
LS_Period_4_0       =      0.08071648
Log10_LS_Prob_4_0   =  -95.19800
LS_SNR_4_0          =     20.93324
LS_Period_5_0       =      0.14845224
Log10_LS_Prob_5_0   =  -70.67430
LS_SNR_5_0          =     15.79490
LS_Period_6_0       =      0.19969732
Log10_LS_Prob_6_0   =  -84.00067
LS_SNR_6_0          =     17.15492
LS_Period_7_0       =      0.09667096
Log10_LS_Prob_7_0   =  -68.34635
LS_SNR_7_0          =     14.95352
LS_Period_8_0       =      0.07080986
Log10_LS_Prob_8_0   =  -66.43799
LS_SNR_8_0          =     14.98224
LS_Period_9_0       =      0.13257697
Log10_LS_Prob_9_0   =  -45.52205
LS_SNR_9_0          =     10.35208
LS_Period_10_0      =      0.19606179
Log10_LS_Prob_10_0  =  -45.91533
LS_SNR_10_0         =      9.50278
LS_Period_11_0      =      0.09650471
Log10_LS_Prob_11_0  =  -44.03894
LS_SNR_11_0         =      9.83806
LS_Period_12_0      =      0.12427836
Log10_LS_Prob_12_0  =  -38.11672
LS_SNR_12_0         =      8.89698
LS_Period_13_0      =      0.05377706
Log10_LS_Prob_13_0  =  -42.00527
LS_SNR_13_0         =     10.63778
LS_Period_14_0      =      0.07574482
Log10_LS_Prob_14_0  =  -29.59113
LS_SNR_14_0         =      8.47694
LS_Period_15_0      =      0.04697881
Log10_LS_Prob_15_0  =  -23.80775
LS_SNR_15_0         =      7.46239
LS_Period_16_0      =      0.02841793
```

```
Log10_LS_Prob_16_0  =   -22.00448
LS_SNR_16_0         =     7.57579
LS_Period_17_0      =      0.19530757
Log10_LS_Prob_17_0  =   -20.34264
LS_SNR_17_0         =     6.66007
LS_Period_18_0      =      0.03434429
Log10_LS_Prob_18_0  =   -20.76925
LS_SNR_18_0         =     7.16381
LS_Period_19_0      =      0.06199826
Log10_LS_Prob_19_0  =   -20.61875
LS_SNR_19_0         =     7.54592
LS_Period_20_0      =      0.02186640
Log10_LS_Prob_20_0  =   -17.42304
LS_SNR_20_0         =     7.16499
LS_Period_21_0      =      0.03084666
Log10_LS_Prob_21_0  =   -17.53910
LS_SNR_21_0         =     7.48927
LS_Period_22_0      =      0.09048494
Log10_LS_Prob_22_0  =   -17.08415
LS_SNR_22_0         =     7.26310
LS_Period_23_0      =      0.19700370
Log10_LS_Prob_23_0  =   -20.28247
LS_SNR_23_0         =     7.80026
LS_Period_24_0      =      0.13875378
Log10_LS_Prob_24_0  =   -22.11898
LS_SNR_24_0         =     8.77045
LS_Period_25_0      =      0.19477238
Log10_LS_Prob_25_0  =   -18.95842
LS_SNR_25_0         =     7.47839
LS_Period_26_0      =      0.09605261
Log10_LS_Prob_26_0  =   -19.85478
LS_SNR_26_0         =     7.98721
LS_Period_27_0      =      0.02094376
Log10_LS_Prob_27_0  =   -18.64031
LS_SNR_27_0         =     8.42012
LS_Period_28_0      =      0.02429053
Log10_LS_Prob_28_0  =   -15.97689
LS_SNR_28_0         =     7.91133
LS_Period_29_0      =      0.19595369
Log10_LS_Prob_29_0  =   -14.15512
LS_SNR_29_0         =     7.04306
LS_Period_30_0      =      0.03476082
Log10_LS_Prob_30_0  =   -14.31615
LS_SNR_30_0         =     7.73511
LS_Period_31_0      =      0.07543399
Log10_LS_Prob_31_0  =   -11.32991
LS_SNR_31_0         =     6.93863
LS_Period_32_0      =      0.19943584
Log10_LS_Prob_32_0  =   -11.35605
LS_SNR_32_0         =     6.74990
LS_Period_33_0      =      0.14330430
Log10_LS_Prob_33_0  =   -13.84113
LS_SNR_33_0         =     8.05031
LS_Period_34_0      =      0.19936126
Log10_LS_Prob_34_0  =   -41.91632
LS_SNR_34_0         =    20.04932
```

```
LS_Period_35_0       =        0.19624223
Log10_LS_Prob_35_0 =   -20.61033
LS_SNR_35_0          =        9.82514
LS_Period_36_0       =        0.10062137
Log10_LS_Prob_36_0 =   -17.44732
LS_SNR_36_0          =        9.01236
LS_Period_37_0       =        0.19045802
Log10_LS_Prob_37_0 =   -11.44640
LS_SNR_37_0          =        6.29059
LS_Period_38_0       =        0.02214389
Log10_LS_Prob_38_0 =   -9.55092
LS_SNR_38_0          =        5.64230
LS_Period_39_0       =        0.02096353
Log10_LS_Prob_39_0 =   -9.94436
LS_SNR_39_0          =        6.02317
LS_Period_40_0       =        0.03319274
Log10_LS_Prob_40_0 =   -10.88140
LS_SNR_40_0          =        7.01609
LS_Period_41_0       =        0.19977216
Log10_LS_Prob_41_0 =   -10.33587
LS_SNR_41_0          =        6.63460
LS_Period_42_0       =        0.07045424
Log10_LS_Prob_42_0 =   -9.36588
LS_SNR_42_0          =        6.37090
LS_Period_43_0       =        0.01982934
Log10_LS_Prob_43_0 =   -7.87233
LS_SNR_43_0          =        5.94567
LS_Period_44_0       =        0.04730606
Log10_LS_Prob_44_0 =   -7.93473
LS_SNR_44_0          =        6.41777
LS_Period_45_0       =        0.04098186
Log10_LS_Prob_45_0 =   -7.29211
LS_SNR_45_0          =        5.96326
LS_Period_46_0       =        0.03800335
Log10_LS_Prob_46_0 =   -8.10354
LS_SNR_46_0          =        6.86557
LS_Period_47_0       =        0.13828586
Log10_LS_Prob_47_0 =   -8.54905
LS_SNR_47_0          =        6.91342
LS_Period_48_0       =        0.19039000
Log10_LS_Prob_48_0 =   -25.80184
LS_SNR_48_0          =        16.51787
LS_Period_49_0       =        0.09917068
Log10_LS_Prob_49_0 =   -19.77131
LS_SNR_49_0          =        13.85323
LS_Period_50_0       =        0.19609785
Log10_LS_Prob_50_0 =   -10.53803
LS_SNR_50_0          =        8.05614
```

===== Killharm routine for harmonic remove from light curves of SZ Lyn =======

```
[root@localhost SZLyn]# vartools -i szlyn_V_Hdler -oneline -LS
0.01 0.2 0.1 1 0 -Killharm ls 3 0 1  /usr/local/vartools/vartools-
1.34/EXAMPLES/OUTDIR_SZLyn
Name                                   = szlyn_V_Hdler
LS_Period_1_0                          = 0.12054509      // Determine
the Fundamental period
Log10_LS_Prob_1_0                      = -288.97060
LS_Periodogram_Value_1_0               =    0.86677
LS_SNR_1_0                             = 524.43728
Killharm_Mean_Mag_1                    =    0.85496
Killharm_Period_1_1                    =      0.12054509
Killharm_Per1_Fundamental_Sincoeff_1 =   0.23127      // Fitting
the fundamental period
Killharm_Per1_Fundamental_Coscoeff_1 =   0.02376
Killharm_Per1_Harm_2_Sincoeff_1        = -0.07530      // Fitting
the first harmonic
Killharm_Per1_Harm_2_Coscoeff_1        =   0.03334
Killharm_Per1_Harm_3_Sincoeff_1        =   0.01707      // Fitting
the second harmonic
Killharm_Per1_Harm_3_Coscoeff_1        = -0.02593
Killharm_Per1_Harm_4_Sincoeff_1        = -0.00205      // Fitting
the third harmonic
Killharm_Per1_Harm_4_Coscoeff_1        =   0.01209
Killharm_Per1_Amplitude_1              =   0.52874


[root@localhost SZLyn]# vartools -i handler_rm4harmonic -oneline -
LS 0.05 0.1 0.01 20 1 /usr/local/vartools/vartools-
1.34/EXAMPLES/OUTDIR_SZLyn whiten clip 5. 1
Name                       = handler_rm4harmonic
LS_Period_1_0              =      0.09694279
Log10_LS_Prob_1_0          =    -10.48415
LS_Periodogram_Value_1_0   =    0.08761
LS_SNR_1_0                 =    12.09793
LS_Period_2_0              =      0.06020112
Log10_LS_Prob_2_0          =    -8.24305
LS_Periodogram_Value_2_0   =    0.07541
LS_SNR_2_0                 =    11.16717
LS_Period_3_0              =      0.09725208
Log10_LS_Prob_3_0          =    -10.13376
LS_Periodogram_Value_3_0   =    0.08736
LS_SNR_3_0                 =    15.61191
LS_Period_4_0              =      0.06033167
Log10_LS_Prob_4_0          =    -8.01945
LS_Periodogram_Value_4_0   =    0.07398
LS_SNR_4_0                 =    14.80155
LS_Period_5_0              =      0.05032952
Log10_LS_Prob_5_0          =    -0.32144
LS_Periodogram_Value_5_0   =    0.02270
LS_SNR_5_0                 =    3.75402
LS_Period_6_0              =      0.06523590
Log10_LS_Prob_6_0          =    -0.33673
```

```
LS_Periodogram_Value_6_0    =      0.02284
LS_SNR_6_0                  =      3.89901
LS_Period_7_0               =      0.09835446
Log10_LS_Prob_7_0           =     -0.05964
LS_Periodogram_Value_7_0    =      0.01932
LS_SNR_7_0                  =      3.37716
LS_Period_8_0               =      0.06541852
Log10_LS_Prob_8_0           =     -0.00033
LS_Periodogram_Value_8_0    =      0.01565
LS_SNR_8_0                  =      2.63939
LS_Period_9_0               =      0.05150607
Log10_LS_Prob_9_0           =     -0.00000
LS_Periodogram_Value_9_0    =      0.01370
LS_SNR_9_0                  =      2.20463
LS_Period_10_0              =      0.05843490
Log10_LS_Prob_10_0          =     -0.00000
LS_Periodogram_Value_10_0 =      0.01209
LS_SNR_10_0                 =      1.86811
LS_Period_11_0              =      0.05043815
Log10_LS_Prob_11_0          =      0.00000
LS_Periodogram_Value_11_0 =      0.01041
LS_SNR_11_0                 =      1.44260
LS_Period_12_0              =      0.06131949
Log10_LS_Prob_12_0          =     -0.00000
LS_Periodogram_Value_12_0 =      0.01096
LS_SNR_12_0                 =      1.58996
LS_Period_13_0              =      0.09600294
Log10_LS_Prob_13_0          =      0.00000
LS_Periodogram_Value_13_0 =      0.00993
LS_SNR_13_0                 =      1.43429
LS_Period_14_0              =      0.07750451
Log10_LS_Prob_14_0          =      0.00000
LS_Periodogram_Value_14_0 =      0.00719
LS_SNR_14_0                 =      0.88901
LS_Period_15_0              =      0.09627451
Log10_LS_Prob_15_0          =      0.00000
LS_Periodogram_Value_15_0 =      0.00752
LS_SNR_15_0                 =      1.16637
LS_Period_16_0              =      0.05021201
Log10_LS_Prob_16_0          =      0.00000
LS_Periodogram_Value_16_0 =      0.00717
LS_SNR_16_0                 =      1.07786
LS_Period_17_0              =      0.07387051
Log10_LS_Prob_17_0          =      0.00000
LS_Periodogram_Value_17_0 =      0.00658
LS_SNR_17_0                 =      0.95610
LS_Period_18_0              =      0.09138298
Log10_LS_Prob_18_0          =      0.00000
LS_Periodogram_Value_18_0 =      0.00678
LS_SNR_18_0                 =      1.09482
LS_Period_19_0              =      0.06100150
Log10_LS_Prob_19_0          =      0.00000
LS_Periodogram_Value_19_0 =      0.00586
LS_SNR_19_0                 =      0.83444
LS_Period_20_0              =      0.05008217
Log10_LS_Prob_20_0          =      0.00000
```

```
LS_Periodogram_Value_20_0 =      0.00509
LS_SNR_20_0               =      0.63576


[root@localhost SZLyn]# vartools -i All_V -oneline -LS 0.01 0.2
0.1 1 0 -Killharm ls 3 0 1  /usr/local/vartools/vartools-
1.34/EXAMPLES/OUTDIR_SZLyn
Name                                  = All_V
LS_Period_1_0                         =      0.12052588
Log10_LS_Prob_1_0                     = -1679.93904
LS_Periodogram_Value_1_0              =      0.81727
LS_SNR_1_0                            =  205.44015
Killharm_Mean_Mag_1                   =  11.00680
Killharm_Period_1_1                   =      0.12052588
Killharm_Per1_Fundamental_Sincoeff_1 =  -0.17881
Killharm_Per1_Fundamental_Coscoeff_1 =  -0.13934
Killharm_Per1_Harm_2_Sincoeff_1      =  -0.05167
Killharm_Per1_Harm_2_Coscoeff_1      =  -0.05815
Killharm_Per1_Harm_3_Sincoeff_1      =  -0.02162
Killharm_Per1_Harm_3_Coscoeff_1      =  -0.01899
Killharm_Per1_Harm_4_Sincoeff_1      =  -0.00462
Killharm_Per1_Harm_4_Coscoeff_1      =  -0.00950
Killharm_Per1_Amplitude_1            =   0.51338


[root@localhost SZLyn]# vartools -i V_rm4harmonic -oneline -LS
0.05 0.1 0.1 20 1 /usr/local/vartools/vartools-
1.34/EXAMPLES/OUTDIR_SZLyn whiten clip 5. 1
Name                      = V_rm4harmonic
LS_Period_1_0             =      0.09309943
Log10_LS_Prob_1_0         = -206.13515
LS_Periodogram_Value_1_0  =    0.09110
LS_SNR_1_0                =    0.81868
LS_Period_2_0             =      0.07654859
Log10_LS_Prob_2_0         =  -71.00114
LS_Periodogram_Value_2_0  =    0.07344
LS_SNR_2_0                =    0.51210
LS_Period_3_0             =      0.06820478
Log10_LS_Prob_3_0         =  -44.18203
LS_Periodogram_Value_3_0  =    0.04804
LS_SNR_3_0                =    0.13236
LS_Period_4_0             =      0.08903862
Log10_LS_Prob_4_0         =  -46.21794
LS_Periodogram_Value_4_0  =    0.04999
LS_SNR_4_0                =    0.18990
LS_Period_5_0             =      0.05532899
Log10_LS_Prob_5_0         =  -27.82190
LS_Periodogram_Value_5_0  =    0.03220
LS_SNR_5_0                =   -0.07649
LS_Period_6_0             =      0.07694024
Log10_LS_Prob_6_0         =  -19.04864
LS_Periodogram_Value_6_0  =    0.02360
LS_SNR_6_0                =   -0.20460
LS_Period_7_0             =      0.06725737
Log10_LS_Prob_7_0         =  -13.91359
LS_Periodogram_Value_7_0  =    0.01853
LS_SNR_7_0                =   -0.27174
```

```
LS_Period_8_0             =       0.09979539
Log10_LS_Prob_8_0         =    -13.70406
LS_Periodogram_Value_8_0  =       0.01832
LS_SNR_8_0                =      -0.26040
LS_Period_9_0             =       0.08632999
Log10_LS_Prob_9_0         =     -9.36576
LS_Periodogram_Value_9_0  =       0.01402
LS_SNR_9_0                =      -0.32126
LS_Period_10_0            =       0.09999287
Log10_LS_Prob_10_0        =     -6.93640
LS_Periodogram_Value_10_0 =       0.01160
LS_SNR_10_0               =      -0.35376
LS_Period_11_0            =       0.07649586
Log10_LS_Prob_11_0        =     -7.34441
LS_Periodogram_Value_11_0 =       0.01200
LS_SNR_11_0               =      -0.33548
LS_Period_12_0            =       0.05086125
Log10_LS_Prob_12_0        =     -2.80425
LS_Periodogram_Value_12_0 =       0.00747
LS_SNR_12_0               =      -0.40680
LS_Period_13_0            =       0.08609228
Log10_LS_Prob_13_0        =     -2.11772
LS_Periodogram_Value_13_0 =       0.00678
LS_SNR_13_0               =      -0.41366
LS_Period_14_0            =       0.06748684
Log10_LS_Prob_14_0        =     -3.34786
LS_Periodogram_Value_14_0 =       0.00801
LS_SNR_14_0               =      -0.38901
LS_Period_15_0            =       0.09775317
Log10_LS_Prob_15_0        =     -0.64072
LS_Periodogram_Value_15_0 =       0.00525
LS_SNR_15_0               =      -0.43019
LS_Period_16_0            =       0.08564209
Log10_LS_Prob_16_0        =     -0.85015
LS_Periodogram_Value_16_0 =       0.00548
LS_SNR_16_0               =      -0.42275
LS_Period_17_0            =       0.06527111
Log10_LS_Prob_17_0        =     -0.00041
LS_Periodogram_Value_17_0 =       0.00381
LS_SNR_17_0               =      -0.45049
LS_Period_18_0            =       0.05760697
Log10_LS_Prob_18_0        =     -0.04430
LS_Periodogram_Value_18_0 =       0.00429
LS_SNR_18_0               =      -0.44284
LS_Period_19_0            =       0.08121203
Log10_LS_Prob_19_0        =     -0.00000
LS_Periodogram_Value_19_0 =       0.00349
LS_SNR_19_0               =      -0.45357
LS_Period_20_0            =       0.09785724
Log10_LS_Prob_20_0        =     -0.21152
LS_Periodogram_Value_20_0 =       0.00468
LS_SNR_20_0               =      -0.42954
```

```
[root@localhost SZLyn]# vartools -i WASP_SZLyn_lc -oneline -LS
0.01 0.2 0.1 1 0 -Killharm ls 3 0 1  /usr/local/vartools/vartools-
1.34/EXAMPLES/OUTDIR_SZLyn
Name                                    = WASP_SZLyn_lc
LS_Period_1_0                           =      0.12053312
Log10_LS_Prob_1_0                       = -712.19718
LS_Periodogram_Value_1_0                =      0.68091
LS_SNR_1_0                              =    474.13330
Killharm_Mean_Mag_1                     =    9.24027
Killharm_Period_1_1                     =      0.12053312
Killharm_Per1_Fundamental_Sincoeff_1 =   0.20583
Killharm_Per1_Fundamental_Coscoeff_1 = -0.10295
Killharm_Per1_Harm_2_Sincoeff_1         =  -0.01004
Killharm_Per1_Harm_2_Coscoeff_1         =   0.08106
Killharm_Per1_Harm_3_Sincoeff_1         =  -0.02215
Killharm_Per1_Harm_3_Coscoeff_1         =  -0.01452
Killharm_Per1_Harm_4_Sincoeff_1         =   0.01120
Killharm_Per1_Harm_4_Coscoeff_1         =  -0.00465
Killharm_Per1_Amplitude_1               =   0.52595

[root@localhost SZLyn]# vartools -i WASP_rm4harmonic -oneline -LS
0.05 0.1 0.1 20 1 /usr/local/vartools/vartools-
1.34/EXAMPLES/OUTDIR_SZLyn whiten clip 5. 1
Name                        = WASP_rm4harmonic
LS_Period_1_0               =      0.08371957
Log10_LS_Prob_1_0           =  -11.73376
LS_Periodogram_Value_1_0    =    0.02011
LS_SNR_1_0                  =    2.08115
LS_Period_2_0               =      0.09264751
Log10_LS_Prob_2_0           =   -6.45199
LS_Periodogram_Value_2_0    =    0.01681
LS_SNR_2_0                  =    1.57881
LS_Period_3_0               =      0.07990269
Log10_LS_Prob_3_0           =   -4.68610
LS_Periodogram_Value_3_0    =    0.01404
LS_SNR_3_0                  =    1.27822
LS_Period_4_0               =      0.09323754
Log10_LS_Prob_4_0           =   -3.55365
LS_Periodogram_Value_4_0    =    0.01226
LS_SNR_4_0                  =    1.09976
LS_Period_5_0               =      0.09368216
Log10_LS_Prob_5_0           =   -2.78375
LS_Periodogram_Value_5_0    =    0.01104
LS_SNR_5_0                  =    0.95728
LS_Period_6_0               =      0.09601114
Log10_LS_Prob_6_0           =   -4.05926
LS_Periodogram_Value_6_0    =    0.01305
LS_SNR_6_0                  =    1.31850
LS_Period_7_0               =      0.09204510
Log10_LS_Prob_7_0           =   -2.07483
LS_Periodogram_Value_7_0    =    0.00993
LS_SNR_7_0                  =    0.86384
LS_Period_8_0               =      0.06656462
Log10_LS_Prob_8_0           =   -2.19484
LS_Periodogram_Value_8_0    =    0.01012
LS_SNR_8_0                  =    0.90877
```

```
LS_Period_9_0              =      0.09748666
Log10_LS_Prob_9_0          =     -1.62164
LS_Periodogram_Value_9_0   =      0.00920
LS_SNR_9_0                 =      0.74583
LS_Period_10_0             =      0.07560241
Log10_LS_Prob_10_0         =     -1.43053
LS_Periodogram_Value_10_0  =      0.00890
LS_SNR_10_0                =      0.67490
LS_Period_11_0             =      0.08959073
Log10_LS_Prob_11_0         =     -2.03677
LS_Periodogram_Value_11_0  =      0.00987
LS_SNR_11_0                =      0.83610
LS_Period_12_0             =      0.09503012
Log10_LS_Prob_12_0         =     -0.95912
LS_Periodogram_Value_12_0  =      0.00813
LS_SNR_12_0                =      0.53162
LS_Period_13_0             =      0.08339139
Log10_LS_Prob_13_0         =     -0.41216
LS_Periodogram_Value_13_0  =      0.00714
LS_SNR_13_0                =      0.42106
LS_Period_14_0             =      0.09856471
Log10_LS_Prob_14_0         =     -0.14926
LS_Periodogram_Value_14_0  =      0.00650
LS_SNR_14_0                =      0.35281
LS_Period_15_0             =      0.05245747
Log10_LS_Prob_15_0         =     -0.51523
LS_Periodogram_Value_15_0  =      0.00734
LS_SNR_15_0                =      0.45910
LS_Period_16_0             =      0.05909919
Log10_LS_Prob_16_0         =     -1.31062
LS_Periodogram_Value_16_0  =      0.00870
LS_SNR_16_0                =      0.68265
LS_Period_17_0             =      0.09144830
Log10_LS_Prob_17_0         =     -0.11887
LS_Periodogram_Value_17_0  =      0.00640
LS_SNR_17_0                =      0.35056
LS_Period_18_0             =      0.09224577
Log10_LS_Prob_18_0         =     -1.33141
LS_Periodogram_Value_18_0  =      0.00874
LS_SNR_18_0                =      0.69716
LS_Period_19_0             =      0.05228651
Log10_LS_Prob_19_0         =     -0.01655
LS_Periodogram_Value_19_0  =      0.00583
LS_SNR_19_0                =      0.26713
LS_Period_20_0             =      0.05549850
Log10_LS_Prob_20_0         =     -0.00681
LS_Periodogram_Value_20_0  =      0.00567
LS_SNR_20_0                =      0.23151
```

IRAF photometry

```
vocl> lpar imexamine
        input = "SZLyn"          images to be examined
        frame = 1                display frame
        image = "ab"             image name
     (output = "")               output root image name
   (ncoutput = 101)              Number of columns in image output
   (nloutput = 101)              Number of lines in image output
    (logfile = "gausspara.log")  logfile
    (keeplog = yes)              log output results
     (defkey = "a")              default key for cursor list input
  (autoredraw = yes)             automatically redraw graph
   (allframes = yes)             use all frames for displaying new images
     (nframes = 0)               number of display frames (0 to autosense)
      (ncstat = 5)               number of columns for statistics
      (nlstat = 5)               number of lines for statistics
    (graphcur = "")              graphics cursor input
    (imagecur = "")              image display cursor input
         (wcs = "logical")       Coordinate system
     (xformat = "")              X axis coordinate format
     (yformat = "")              Y axis coordinate format
    (graphics = "stdgraph")      graphics device
     (display = "display(image='$1',frame=$2)") display command template
 (use_display = yes)             enable direct display interaction
        (mode = "ql")
```

```
vocl> lpar daofind
        image = ""              Input image(s)
      (output = "default")      The output coordinates list(s) (default: image.
     (starmap = "")             The output density enhancement image(s)
      (skymap = "")             The output sky image(s)
    (datapars = "")             Data dependent parameters
    (findpars = "")             Object detection parameters
    (boundary = "nearest")      Boundary extension (constant, nearest, reflect,
    (constant = 0.)             Constant for constant boundary extension
 (interactive = no)             Interactive mode ?
   (icommands = "")             Image cursor: [x y wcs] key [cmd]
   (gcommands = "")             Graphics cursor: [x y wcs] key [cmd]
      (wcsout = )_.wcsout)       The output coordinate system (logical,tv,physic
       (cache = )_.cache)        Cache the image pixels ?
      (verify = )_.verify)      Verify critical parameters in non-interactive m
      (update = )_.update)      Update critical parameters in non-interactive m
     (verbose = )_.verbose)     Print messages in non-interactive mode ?
    (graphics = )_.graphics)    Graphics device
     (display = )_.display)     Display device
        (mode = "ql")

 vocl> lpar datapars
       (scale = 1.)             Image scale in units per pixel
     (fwhmpsf = 3.9800000190735) FWHM of the PSF in scale units
    (emission = yes)            Features are positive ?
       (sigma = 17.497999191284) Standard deviation of background in counts
     (datamin = INDEF)          Minimum good data value
     (datamax = INDEF)          Maximum good data value
       (noise = "poisson")      Noise model
     (ccdread = "")             CCD readout noise image header keyword
        (gain = "GAIN")         CCD gain image header keyword
    (readnoise = 6.)            CCD readout noise in electrons
       (epadu = INDEF)          Gain in electrons per count
```
201

```
      (exposure = "EXPTIME")       Exposure time image header keyword
       (airmass = "AIRMASS")       Airmass image header keyword
        (filter = "")              Filter image header keyword
       (obstime = "UT")            Time of observation image header keyword
         (itime = INDEF)           Exposure time
      (xairmass = INDEF)           Airmass
       (ifilter = "INDEF")         Filter
         (otime = "INDEF")         Time of observation
          (mode = "ql")
```

vocl> **lpar centerpars**
```
  (calgorithm = "centroid")       Centering algorithm
         (cbox = 5.)               Centering box width in scale units
   (cthreshold = 0.)               Centering threshold in sigma above background
    (minsnratio = 1.)              Minimum signal-to-noise ratio for centering alg
     (cmaxiter = 10)               Maximum number of iterations for centering algo
     (maxshift = 1.)               Maximum center shift in scale units
        (clean = no)               Symmetry clean before centering ?
       (rclean = 1.)               Cleaning radius in scale units
        (rclip = 2.)               Clipping radius in scale units
       (kclean = 3.)               Rejection limit in sigma
      (mkcenter = no)              Mark the computed center on display ?
         (mode = "ql")
```

 vocl> **lpar fitskypars**
```
  (salgorithm = "centroid")       Sky fitting algorithm
      (annulus = 10.)              Inner radius of sky annulus in scale units
     (dannulus = 12.)              Width of sky annulus in scale units
     (skyvalue = 0.)               User sky value
     (smaxiter = 10)               Maximum number of sky fitting iterations
      (sloclip = 0.)               Lower clipping factor in percent
      (shiclip = 0.)               Upper clipping factor in percent
      (snreject = 50)              Maximum number of sky fitting rejection iterati
     (sloreject = 3.)              Lower K-sigma rejection limit in sky sigma
```

```
    (shireject = 3.)              Upper K-sigma rejection limit in sky sigma
       (khist = 3.)               Half width of histogram in sky sigma
     (binsize = 0.10000000149012) Binsize of histogram in sky sigma
      (smooth = no)               Boxcar smooth the histogram
       (rgrow = 0.)               Region growing radius in scale units
      (mksky = no)                Mark sky annuli on the display
         (mode = "ql")

 vocl> lpar photpars
    (weighting = "constant")      Photometric weighting scheme for wphot
    (apertures = "8.14")          List of aperture radii in scale units
        (zmag = 0.)               Zero point of magnitude scale
     (mkapert = no)               Draw apertures on the display
         (mode = "ql")

 vocl> lpar phot
        image = "20161113195515-166-RA.fits" The input image(s)
      skyfile = ""                The input sky file(s)
       (coords = "coordinate")    The input coordinate files(s) (default: image.c
       (output = "default")       The output photometry file(s) (default: image.m
     (plotfile = "")              The output plots metacode file
     (datapars = "")              Data dependent parameters
   (centerpars = "")              Centering parameters
   (fitskypars = "")              Sky fitting parameters
     (photpars = "")              Photometry parameters
  (interactive = no)              Interactive mode ?
     (radplots = no)              Plot the radial profiles in interactive mode ?
     (icommands = "")             Image cursor: [x y wcs] key [cmd]
     (gcommands = "")             Graphics cursor: [x y wcs] key [cmd]
        (wcsin = )_.wcsin)        The input coordinate system (logical,tv,physica
       (wcsout = )_.wcsout)       The output coordinate system (logical,tv,physic
        (cache = )_.cache)        Cache the input image pixels in memory ?
       (verify = yes)             Verify critical parameters in non-interactive m
       (update = yes)             Update critical parameters in non-interactive m
```
203

```
        (verbose = yes)              Print messages in non-interactive mode ?
     (graphics = "stdgraph")         Graphics device
      (display = "stdimage")         Display device
          (mode = "ql")
```

IRAF spectroscopy

```
kpnoslit> lpar apall
         input =                     List of input images
         nfind =                     Number of apertures to be found automatically
       (output = "")                 List of output spectra
    (apertures = "")                 Apertures
       (format = "multispec")        Extracted spectra format
   (references = "")                 List of aperture reference images
     (profiles = "")                 List of aperture profile images\n
  (interactive = yes)                Run task interactively?
         (find = yes)                Find apertures?
      (recenter = yes)               Recenter apertures?
        (resize = yes)               Resize apertures?
          (edit = yes)               Edit apertures?
         (trace = yes)               Trace apertures?
      (fittrace = yes)               Fit the traced points interactively?
       (extract = yes)               Extract spectra?
        (extras = yes)               Extract sky, sigma, etc.?
        (review = yes)               Review extractions?\n
          (line = INDEF)             Dispersion line
          (nsum = 10)                Number of dispersion lines to sum or median\n\n
         (lower = -5.)               Lower aperture limit relative to center
         (upper = 5.)                Upper aperture limit relative to center
     (apidtable = "")                Aperture ID table (optional)\n\n# DEFAULT BACKG
    (b_function = "chebyshev")       Background function
       (b_order = 1)                 Background function order
      (b_sample = "-10:-6,6:10")     Background sample regions
    (b_naverage = -3)                Background average or median
     (b_niterate = 0)                Background rejection iterations
```

```
(b_low_reject = 3.)          Background lower rejection sigma
(b_high_rejec = 3.)          Background upper rejection sigma
     (b_grow = 0.)           Background rejection growing radius\n\n# APERTU
      (width = 5.)           Profile centering width
     (radius = 10.)          Profile centering radius
  (threshold = 0.)           Detection threshold for profile centering\n\n#
     (minsep = 5.)           Minimum separation between spectra
     (maxsep = 100000.)      Maximum separation between spectra
      (order = "increasing") Order of apertures\n\n# RECENTERING PARAMETERS\n
  (aprecenter = "")          Apertures for recentering calculation
     (npeaks = INDEF)        Select brightest peaks
      (shift = yes)          Use average shift instead of recentering?\n\n#
     (llimit = INDEF)        Lower aperture limit relative to center
     (ulimit = INDEF)        Upper aperture limit relative to center
     (ylevel = 0.1)          Fraction of peak or intensity for automatic wid
       (peak = yes)          Is ylevel a fraction of the peak?
        (bkg = yes)          Subtract background in automatic width?
     (r_grow = 0.)           Grow limits by this factor
  (avglimits = no)           Average limits over all apertures?\n\n# TRACING
     (t_nsum = 10)           Number of dispersion lines to sum
     (t_step = 10)           Tracing step
    (t_nlost = 3)            Number of consecutive times profile is lost bef
 (t_function = "legendre")   Trace fitting function
    (t_order = 2)            Trace fitting function order
   (t_sample = "*")          Trace sample regions
  (t_naverage = 1)           Trace average or median
   (t_niterate = 0)          Trace rejection iterations
(t_low_reject = 3.)          Trace lower rejection sigma
(t_high_rejec = 3.)          Trace upper rejection sigma
     (t_grow = 0.)           Trace rejection growing radius\n\n# EXTRACTION
 (background = "none")       Background to subtract
     (skybox = 1)            Box car smoothing length for sky
    (weights = "none")       Extraction weights (none|variance)
       (pfit = "fit1d")      Profile fitting type (fit1d|fit2d)
```

```
        (clean = no)              Detect and replace bad pixels?
   (saturation = INDEF)           Saturation level
    (readnoise = "0.")            Read out noise sigma (photons)
        (gain = "1.")             Photon gain (photons/data number)
      (lsigma = 4.)               Lower rejection threshold
      (usigma = 4.)               Upper rejection threshold
     (nsubaps = 1)                Number of subapertures per aperture
        (mode = "ql")

kpnoslit> lpar identify
      images =                    Images containing features to be identified
       crval =                    Approximate coordinate (at reference pixel)
       cdelt =                    Approximate dispersion
     (section = "middle line")    Section to apply to two dimensional images
    (database = "database")       Database in which to record feature data
   (coordlist = "linelists$idhenear.dat") User coordinate list
       (units = "")               Coordinate units
        (nsum = "10")             Number of lines/columns/bands to sum in 2D imag
       (match = -3.)              Coordinate list matching limit
 (maxfeatures = 50)               Maximum number of features for automatic identi
      (zwidth = 100.)             Zoom graph width in user units
       (ftype = "emission")       Feature type
      (fwidth = 4.)               Feature width in pixels
     (cradius = 5.)               Centering radius in pixels
   (threshold = 0.)               Feature threshold for centering
      (minsep = 2.)               Minimum pixel separation
    (function = "spline3")        Coordinate function
       (order = 1)                Order of coordinate function
      (sample = "*")              Coordinate sample regions
     (niterate = 0)               Rejection iterations
   (low_reject = 3.)              Lower rejection sigma
  (high_reject = 3.)              Upper rejection sigma
        (grow = 0.)               Rejection growing radius
    (autowrite = no)              Automatically write to database
```

```
    (graphics = "stdgraph")      Graphics output device
      (cursor = "")              Graphics cursor input
     (aidpars = "")              Automatic identification algorithm parameters
        (mode = "ql")

  kpnoslit> lpar refspectra
       input =                   List of input spectra
      answer =                   Accept assignment?
  (references = "*.imh")         List of reference spectra
   (apertures = "")              Input aperture selection list
      (refaps = "")              Reference aperture selection list
   (ignoreaps = yes)             Ignore input and reference apertures?
      (select = "interp")        Selection method for reference spectra
        (sort = "jd")            Sort key
       (group = "ljd")           Group key
        (time = no)              Is sort key a time?
    (timewrap = 17.)             Time wrap point for time sorting
    (override = no)              Override previous assignments?
     (confirm = yes)             Confirm reference spectrum assignments?
      (assign = yes)             Assign the reference spectra to the input spect
    (logfiles = "STDOUT,logfile") List of logfiles
     (verbose = no)              Verbose log output?
        (mode = "ql")

  kpnoslit> **lpar dispcor**
       input =                   List of input spectra
      output =                   List of output spectra
    (linearize = yes)            Linearize (interpolate) spectra?
    (database = "database")      Dispersion solution database
       (table = "")              Wavelength table for apertures
          (w1 = INDEF)           Starting wavelength
          (w2 = INDEF)           Ending wavelength
          (dw = INDEF)           Wavelength interval per pixel
          (nw = INDEF)           Number of output pixels
```

```
         (log = no)            Logarithmic wavelength scale?
        (flux = yes)           Conserve total flux?
       (blank = 0.)            Output value of points not in input
    (samedisp = no)            Same dispersion in all apertures?
      (global = no)            Apply global defaults?
   (ignoreaps = no)            Ignore apertures?
     (confirm = no)            Confirm dispersion coordinates?
    (listonly = no)            List the dispersion coordinates only?
     (verbose = yes)           Print linear dispersion assignments?
     (logfile = "")            Log file
        (mode = "ql")

kpnoslit> lpar continuum
        input = "szlyn18cal"    Input images
       output = "szlyn18con"    Output images
          ask = "yes"
       (lines = "*")           Image lines to be fit
       (bands = "1")           Image bands to be fit
        (type = "ratio")       Type of output
     (replace = no)            Replace rejected points by fit?
   (wavescale = yes)           Scale the X axis with wavelength?
    (logscale = no)            Take the log (base 10) of both axes?
    (override = no)            Override previously fit lines?
    (listonly = no)            List fit but don't modify any images?
    (logfiles = "logfile")     List of log files
 (interactive = yes)           Set fitting parameters interactively?
      (sample = "*")           Sample points to use in fit
    (naverage = 1)             Number of points in sample averaging
    (function = "spline3")     Fitting function
       (order = 2)             Order of fitting function
  (low_reject = 2.)            Low rejection in sigma of fit
 (high_reject = 1.)            High rejection in sigma of fit
    (niterate = 10)            Number of rejection iterations
        (grow = 1.)            Rejection growing radius
```

```
  (markrej = yes)              Mark rejected points?
(graphics = "stdgraph")        Graphics output device
  (cursor = "")                Graphics cursor input
    (mode = "ql")
```

IRAF Scripts

```
===== Display list of images ====================================

list="flist"
while(fscan(list,s1)!=EOF){
display(s1)
}

==== Write results of imexamine task to a log files for list of
images ======

list="B.list"
while(fscan(list,s1)!=EOF){
display(s1)
imexamine(s1,keeplog+) // write imexamine results into logfile,
prior to this text file should create in the folder //
}

=== Photometry of list of images and write to a text file =======

list="list"
while ( fscan(list,s1) != EOF)
{ display ((s1),1
tvmark 1 image_cord.coo
print((s1))
phot ( (s1),coords="image_cord.coo",output=s1//".mag.1")
del image_cord.coo
txdump((s1)//".mag.1", "XCENTER,YCENTER,ID","yes",
>"image_cord.coo")
!wc image_cord.coo
}

====== Read header values and write to a text file ==============

list="3B.list'
while(fscan(list,s1)!=EOF){
imgets((s1),"JD")
s2=(imgets.value)
print((s2),>>"JDlist")
}

==== Do imexamine and write outpt to a text file for a set of
images =====

list="C2011B.list"
imexamine.keeplog=yes
imexamine.logfile="center.log"
while(fscan(list,s1)!=EOF){
display((s1),zscale-,zrange-,z1=0,z2=1000)
imexam((s1))
}
```

```
list="40.list"
imexamine.keeplog=yes
imexamine.logfile="gausspara40.log"
while(fscan(list,s1)!=EOF){
display(s1)
imexam((s1))
}

=========== Rename set of images =============================

list="V.list"
while(fscan(list,s1)!= EOF){
for (i=1; i<=552; i+=1)
if (i < 10)
rename(s1, "sz00"//i)
s2="sz00"//i
else if (i < 100)
rename(s1, "sz0"//i)
s2="sz0"//i
else (i < 553)
rename(s1, "sz"//i)
s2="sz"//i
print(s2)

}

====== Read coordinates from a list of files and shift the image
pixels =====

list="center.log"
real a,b
while(fscan(list,s1,x,y)!=EOF){
a=306.38-x
b=489.31-y
imshift((s1),"shifted"//(s1),a,b)
disp("shifted"//(s1))
}
```